Title
Shaking Table Evaluation of Reinforced Concrete Bridge Columns Repaired using Fiber Reinforced Polymer Jackets

Author
Kumar, Pardeep

Publication Date
2014

Peer reviewed|Thesis/dissertation

Shaking Table Evaluation of Reinforced Concrete Bridge Columns Repaired using Fiber Reinforced Polymer Jackets

By

Pardeep Kumar

A dissertation submitted in partial satisfaction of the

requirements for the degree of

Doctor of Philosophy

in

Engineering – Civil and Environmental Engineering

in the

Graduate Division

of the

University of California, Berkeley

Committee in charge

Professor Khalid M. Mosalam, Chair
Professor Jack P. Moehle
Professor Jon Wilkening

Fall 2014

Shaking Table Evaluation of Reinforced Concrete Bridge Columns Repaired using Fiber Reinforced Polymer Jackets

by

Pardeep Kumar

Abstract

Shaking Table Evaluation of Reinforced Concrete Bridge Columns Repaired using Fiber Reinforced Polymer Jackets

by

Pardeep Kumar

Doctor of Philosophy in Engineering – Civil and Environmental Engineering

University of California, Berkeley

Professor Khalid M. Mosalam, Chair

After an earthquake event it is the responsibility of the engineers to decide if the bridge structure is safe for the traffic flow, requires repair or needs to be replaced completely depending on the damage level. Effective, economical and timely repair of Reinforced Concrete (RC) bridges after a seismic event is crucial to avoid traffic congestion and lengthy detours. Fiber Reinforced Polymer (FRP) composite laminates are one of few options with several advantages. Use of FRP jackets in structural engineering is gaining interest in applications such as strengthening weak structural elements, improving the existing structure capacity to resist increased loads due to change in use of structure and retrofitting structural elements for seismic upgrades. The study presents shaking table experimental investigation to evaluate the use of FRP for repairing RC bridge columns with circular cross-sections.

Two ¼-scale RC columns were tested in as-built configuration. Both tests had identical geometry and reinforcement details except for the spacing of the transverse reinforcing bars. One column had closely spaced hoops satisfying code requirements and the other had larger spacing, representing a shear-critical column. The test specimens were subjected to a series of horizontal and vertical excitations on a shaking table and experienced moderate to high damage. The damaged columns were subsequently repaired with unidirectional FRP composite laminates and subjected to the same set of earthquake excitations. The obtained experimental data showed that the repaired columns achieved higher strength and ductility with lower residual displacements compared to the as-built ones contributing to the resiliency of the bridge system.

A three-dimensional (3D) Finite Element (FE) model was developed and calibrated using the experimental test results. A bilinear confined concrete model was adopted to model the constitutive relationship of the FRP confined concrete without explicitly modeling the FRP composite jacket. Due to variability of the material properties, several calibration parameters were studied to develop a reliable FE model. The results of the dynamic FE analysis showed great potential for 3D modeling of the repaired test specimens. From this study, it is concluded that the used FRP composite laminates represent a viable solution for the effective and rapid repair of damaged RC bridge columns. A parametric study was conducted to evaluate the horizontal force, deformation, and confining strain response of the retrofitted RC bridge columns

using the computational model. The response of the FE models with different number of FRP plies in the jacket was investigated. The analytical results suggested that increasing the number of FRP plies in the jacket significantly changed the confining strains response of the confined cross-section but the global force-deformation was not significantly affected.

Table of Contents

List of Figures

List of Tables

Chapter 1. Introduction

1.1 GENERAL

Bridges are essential lifelines representing an important part of the infrastructure in any urban society. They provide effective alternatives for travel and transportation around the natural terrains. This contributes to spatial efficacy and faster commute. Bridge designs must ensure safety and enhance comfort of commuters and economy of the region in modern societies. Among all the components of a bridge system, columns are the most critical from structural point of view and therefore require comparatively precise design guidelines and construction procedures. In areas with high seismic activities, bridge columns are expected to perform well and effectively resist the earthquake loads in addition to the dead and live loads. Recent code design approaches focus on assuring adequate performance of structures during and after an earthquake.

The ability of bridge columns to support the loads after an earthquake is crucial for sustainable dispatch and distribution, i.e. robust and rapid response to a potential disaster before it turns into a real disaster, of emergency aids to affected communities and for evacuation procedures. In case of large nonlinear deformations and damage, the bridge columns require rapid and effective repair of damaged zones. Research activities have been focused on various damage detection and repair methods. This study explores the effectiveness of repairing Reinforced Concrete (RC) bridge columns damaged after earthquake shaking using Fiber Reinforced Polymer (FRP) composite jackets. FRP composite jackets have various advantages and have proven to be very effective in Structural Engineering applications. Being light weight, they do not induce any additional dead load or inertia forces to the repaired structure. They are easily adaptable to various cross-sectional shapes and sizes and require comparatively shorter application and curing time.

In RC bridge columns, shear failure is a brittle mode and is therefore undesirable. Various factors, e.g. due to type of loading, may result in lowered shear capacity of bridge columns. Adequate shear capacity of a RC bridge column during a seismic event is a crucial criterion for the acceptable performance of a bridge system. In designing RC structures, contribution from concrete and transverse reinforcing steel resist the applied shear loads. Reconnaissance of the bridge columns after earthquakes, e.g. San Fernando (1971), Lome Prieta (1989) and Northridge (1994), suggested the importance of confining reinforcement in the flexure and shear response of RC bridge columns and the design codes were updated with new guidelines for effectively confining the bridge columns [38], [19], [46]. Recent observations from earthquake data and post-earthquake reconnaissance efforts, e.g. Kalamata (1986), Northridge (1994) and Kobe (1995), have revealed that detrimental effects occur due to seismic loading especially when ground motions have significant horizontal and vertical components,

typically found in near-fault ground motion [10], [29], [41], [65]. Concrete being weak in tension fracture when the vertical component of ground motion causes axial tension in the column cross-sections. This results in rapid degradation of the shear capacity of the RC bridge column [35], [53], [59]. An effective repair of RC bridge columns should be able to restore the structural capacity to resist both flexure and shear stresses.

Various post-earthquake measures of repairing and retrofitting the damaged bridge column had been studied and tested by many researchers [8], [14], [22], [36]. Effectiveness of a repair method depends on the cost, time and its contribution to performance enhancement. FRP composites are being studied as a viable option in that regards. FRP composites are light weight, high strength, and their ease of application give them a significant practical advantage over the other repair methods, e.g. steel jacketing [3], [13], [43], [44], [64], external pre-stressing [8], [55], [63], concrete jacketing [22], [47], etc. In the past three decades, the FRP repair and strengthening technique has been extensively used in practice and evaluated by many experimental research activities focusing on improving the confining properties, ductility and strength [9], [40], [42], [49]-[52], [54]. However, very limited experimental research has given attention to assessing the validity of FRP repair of RC bridge columns using the dynamic testing with shaking [28], [60]. To the best of author's knowledge no such dynamic load assessment exists in the literature considering the realistic combined effect of lateral and vertical ground motion excitations.

1.2 FIBER REINFORCED POLYMERS

FRP is a composite material generally comprised of unidirectional or woven fibers embedded in a layer of polymer resin matrix. The fibers act as reinforcement providing strength and stiffness to the composite lamina and the resin (tough but brittle) holds the fiber system together and transfer the stresses from one lamina to another. Typically used polymer resins are epoxies, polyesters, vinylesters; and typically used fibers are carbon, glass, boron or aramid. Even though brittle, the FRP composites behave linear-elastically under axial loads and usually have high magnitude of rupture strain. The use of either unidirectional or woven FRP lamina depends on the application and the associated force path. Repair and retrofit of structures using FRP composite jackets have several advantages over the other conventional strengthening techniques, e.g. steel jacketing, concrete jacketing, external prestressing, etc. FRP materials are relatively thin and light weight which is ideal for areas with limited access without adding much to the static dead weight of the structural system or the dynamic inertia forces. Due to their ease in handling and installation, FRP composites can be installed on various shapes (square, rectangular, or circular) of structural element with minimum alteration to the actual geometry.

Unidirectional FRP sheets are made of unidirectional fibers embedded in the polymer matrix. The strength and stiffness of unidirectional FRP lamina in the direction of fibers are significantly higher than those in the perpendicular directions. In case of woven FRP sheets, they have significant strength and stiffness in two or more directions (2D or 3D). In Structural Engineering applications, the time and cost of repair and/or retrofit is quite crucial. Three most common approaches used for the retrofitting and/or repair of the structural systems using FRP are: pre-fabricated shells, machine wrapping, and wet layup process. In the current study, unidirectional Glass-Fiber Reinforced Polymers (GFRP) and Carbon-Fiber Reinforced Polymers

(CFRP) embedded in epoxy resin matrix were installed on the reduced-scale bridge column test specimens using wet layup process for subsequent shaking table assessment.

1.2.1 Glass-Fiber Reinforced Polymers

GFRP consist of glass fabric embedded in the polymer matrix. GFRP are of high strength, easy to handle in the field, and are relatively cheaper. Different variations of GFRP are available depending on the chemical configuration of the fiber material. The two main types of GFRP lamina used in the Structural Engineering applications are: E-Glass FRP and S-Glass FRP. E-Glass FRP are alkali-free and have higher resistance to chemical action of the environment. S-Glass FRP have relatively higher strength than E-Glass FRP and are more expensive than the E-Glass alternatives. Due to the competitive cost and adequate strength, E-Glass FRP are the most commonly used FRP composites in the Structural Engineering applications, including one of the tests conducted in this study.

1.2.2 Carbon-Fiber Reinforced Polymers

CFRP consist of carbon fibers held by polymer resin matrix. Compared to GFRP, carbon fibers have higher strength, stiffness, and fatigue and chemical resistance. CFRP are more expensive and have lower failure strain than GFRP. However, due to excellent fire-resistance (little to no change in tensile strength up to temperature of more than 1832ºF [5], ability to withstand harsh environment, i.e. requiring relatively less frequent inspections, CFRP composites are highly popular in Structural Engineering applications and also used in repairing two specimens in this study.

1.2.3 Epoxy Resin

Epoxy resins are thermosetting polymer resins with sufficient curing time to facilitate the application to the FRP lamina on site. Once cured, epoxy resin cannot be reheated and melted. This (to some extent) helps protect the reinforcing fibers from fire and environmental damage. Epoxy resins adhere well with the GFRP and CFRP and have relatively low degree of curing shrinkage. Moreover, epoxy resins are cheap, easy to apply, and dimensionally stable. Use of epoxy as an adequate repair of cracked concrete has been successfully demonstrated by researchers [18], [23]. Epoxy resin is used for repairing all test specimens in this study.

1.2.4 Wet Layup Process

The wet layup process is the most common in-situ method of installing the FRP jackets on the structural system and was also used in this study for repairing the test specimens (Figure 1.1). Fabric generally comes in rolls and is laid on the surface with a layer of polymer resin (Figure 1.1a). Another layer of resin is applied on top of the fiber roll using paint roller until the FRP surface is completely drenched and dripping (Figure 1.1b and Figure 1.1c). The FRP sheets are then applied over the surface to be repaired (the bridge column curved surface in this case) and smoothened using the paint roller to release any trapped air (Figure 1.1d). The system is then allowed to cure (depending on the curing time of the polymer resin).

Figure 1.1 Wet layup process: (a) CFRP roll; (b) application of epoxy; (c) CFRP soaked in epoxy resin; (d) wrapping of the column specimens.

1.3 LITERATURE REVIEW

From the structural performance point of view, various studies have demonstrated that FRP jackets improve the confinement effects, ductility and flexural and shear capacities of the structural members [25], [27], [30], [52]. Xiao et al. (1999) [62] conducted an experimental investigation to study the effectiveness of prefabricated composite jacket retrofit in enhancing the seismic shear strength performance of existing circular RC bridge column specimens. The study compared the performance of three ½-scale bridge column specimens: one as-built and two retrofitted with pre-fabricated composite jackets. Based on the experimental results the authors concluded that the hysteretic response of the retrofitted test specimens was significantly better than the as-built one. More specifically, the study showed that the hysteretic loops of the retrofitted test specimens were stable even at displacement ductility of 10.

Ilki et al. (2006) [27] studied the effect of FRP-confinement in different cross-section shapes under uniaxial compression. The experimental results showed that FRP-confinement was effective in delaying the longitudinal bar buckling in sections with inadequate steel confinement, in strengthening columns constructed with low strength concrete, and in improving the compressive strength and axial deformation of the test specimens. Saadatmanesh et al. (1994, 1997a, b) [49] – [51] conducted theoretical and experimental studies on concrete columns repaired CFRP and GFRP laminates. They concluded that the flexural strength and ductility of the columns repaired with FRP laminates were higher than the original column specimens. Lam and Teng (2003) [30] proposed a design-oriented, bilinear compressive stress-strain model based on experimental data from adequately FRP-confined concrete sections. In this model, the strength of FRP-confined concrete increases until it reaches the rupture point of the FRP-confining medium, after which the failure of the specimen is brittle. Despite that, the overall ductility of FRP-confined columns is significantly higher than that of conventionally designed RC columns.

Most of the experimental studies performed so far have focused on the behavior of FRP-confined RC column sections with or without confining transverse steel reinforcement, under uniaxial or bidirectional loading. Seismic performance of the FRP-repair of structural member is also gaining interests of the researchers [15], [25], [57]. This study presents the shaking table performance of two ¼-sclaed RC test specimens, with flexure-shear damage, repaired and retrofitted using FRP composites. The experimental investigations explored the efficacy of FRP jacket repair during combined horizontal and vertical ground motions.

1.4 RESEARCH OBJECTIVE

The main objective of this study is to evaluate the seismic performance of repaired RC bridge columns using unidirectional FRP jackets with shear and flexure damage prior to the repair. This study presents results of shaking table experiments on two repaired ¼-scale RC bridge column specimens. The two columns were subjected to a series of horizontal and vertical ground motions in as-built configurations. The as-built specimens had moderate to high damage at the completion of the loading protocol. The specimens were subsequently repaired using unidirectional CFRP and GFRP composite jackets and re-tested under the same set of ground motions. A three-dimensional (3D) computational model was developed and calibrated with the experimental results. The same model was used to conduct a parametric study to investigate the analytical response of retrofitted “virtual” test specimens, particularly the effect of the jacket thickness on the global and local response parameters.

1.5 DISSERTATION FORMAT

In Chapter 2 the design of prototype and as-built test specimens is discussed. The simple steps for the design and application of the FRP composites to repair the damaged test specimens are discussed. The chapter then details the material properties of the test specimens.

In Chapter 3, the detailed test setup of the repaired specimens on the shake table is discussed followed by details of the instrumentation and the ground motion data chosen for testing.

In Chapter 4, the global response of the shake table test is presented. Test conducted to measure the stiffness and time period of the test specimens are discussed. Impact of repair on the response quantities like shear and axial force, displacements and bending moments is presented.

In Chapter 5, the local response measured at sections along the column height of the repaired and as-built test specimens is compared. Confining strain measured on the surface of the FRP jackets are discussed to compare the effectiveness of the two FRP jackets under similar ground motion loading.

In Chapter 6, a detailed discussion of the computational study performed and calibrated using the experimental results, is presented. 3D FE models of the test specimens were developed and used for the analysis to conduct a parametric study of retrofitted column specimens.

In Chapter 7, a summary of the experimental and analytical results and their conclusions is presented and future extensions are suggested.

Chapter 2. Details of Test Specimens

2.1 GENERAL DESCRIPTION

An experimental study was conducted to investigate the effect of vertical ground motions on shear demand and capacity of two as-built ¼-scale RC circular bridge column specimens. Both test specimens had identical geometry and reinforcement details except their volumetric confinement ratios. Test specimen SP1 had closely spaced transverse reinforcement than the test specimen SP2. Axial load ratio was 6.8% of the nominal axial load capacity for both test specimens for a nominal compressive concrete strength, $f_c' = 3.9$ ksi (26.89 MPa). The as-built test specimens were subjected to a series of horizontal and vertical base excitations on the shaking table. After testing, damaged test specimens were repaired using unidirectional GFRP (for SP1) and CFRP (for SP2) composite sheets. Testing of the repaired specimens was carried out using the same sets of horizontal and vertical ground motions used for testing the as-built test specimens.

2.2 PROTOTYPE DETAILS

The Plumas Arboga Overhead was chosen as the prototype for the two as-built test specimens. Figure 2.1a shows the cross-section of bridge column with overlapping spirals. The bridge is a three-span bridge with single column bents having interior span of 190 ft (57.91 m) and exterior span of 133 ft (40.54 m). Aspect ratio, i.e. height to diameter ratio, of the prototype is 3.58 along the weak axis and 5.78 along the strong axis. A modified effective circular cross-section was chosen for the experimental study (Figure 2.1b). Test specimens were ¼-scale version of the prototype bridge system with aspect ratio of 3.5, close to the aspect ratio of prototype along the weak-axis. More details about prototype and modifications to design the effective circular cross-section are given in Lee (2011) [33].

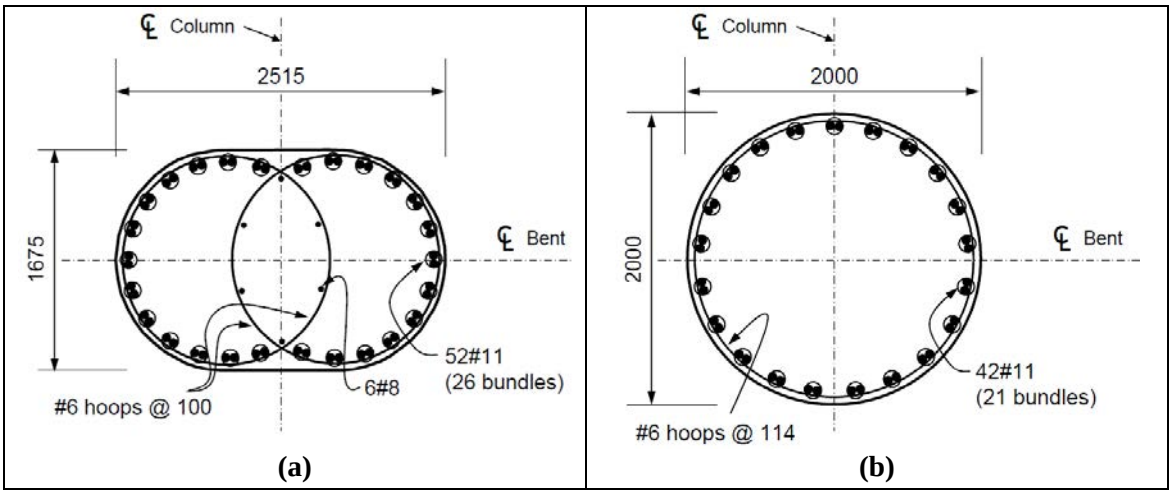

Figure 2.1 Plumas Arboga overhead prototype (BIRIS, Caltrans): (a) original cross-section of column; (b) effective cross-section of column (all dimensions in mm).

2.3 GEOMETRY AND REINFORCEMENT DETAILS

The test specimens' configuration had three components cast monolithically: rigid footing, cantilever column, and the mass block. All components of the test specimens were cast monolithically from the same batch of concrete in the upright position. The test specimens rested on four load cells attached at the four corners of the footing. The load cells were then firmly connect to the shake table. The mass block on top of the test specimens was attached to assembly of the concrete slabs, hollow steel beams, and the lead blocks. The configuration of mass block attachments was chosen to mimic the scaled version of the superstructure mass supported by the bridge column. Following sections discussed each of the test specimen components in details.

2.3.1 Cantilever Columns

Design of the test specimens was based on ACI and Caltrans bridge design codes [1], [2], [4]. Figure 2.2 shows the elevation and section view of the test specimens. The cantilever column had a diameter of 20 in (508 mm) and clear height of 70 in (1778 mm). The longitudinal reinforcement consisted of 16 #5, ASTM A706, Grade 60 steel bars distributed uniformly around the perimeter, corresponding to the longitudinal steel ratio (ρ_l) of 1.56%. #2 deformed steel reinforcement hoops were provided at a center-to-center spacing of 2 in (50.8 mm) and 3 in (76.2mm) in the test specimens SP1 and SP2, respectively. The clear cover thickness of concrete was 1.0 in (25.4 mm). The hoop spacing of SP1 resulted in transverse confinement ratio of 0.55%, higher than the specified minimum value of 0.47% by the code [2]. Specimen SP2 had transverse reinforcement ratio of 0.36%, representing a shear-critical column. Both test specimens SP1 and SP2 had their transverse hoop reinforcement extended into the foundation and the top blocks as shown in Figure 2.2. The center-to-center spacing in these regions was kept equal to the spacing in the column region.

The ratios of hoop spacing to longitudinal reinforcing bar diameter were 3.2 and 4.8 for SP1 and SP2, respectively, sufficient to avoid any pre-mature buckling of the longitudinal bars. Minimum and maximum nominal shear strength of test specimen SP1 were 66.35 kips (295.14

KN) and 92.24 kips (410.30 KN), respectively. Test specimen SP2 had a maximum and minimum nominal shear strength of 76.74 kips (341.36 KN) and 50.85 kips (226.19 KN), respectively. These values were computed using a displacement ductility demand (μ_d) of 4.0, following procedures outlined in Section 3.6 of the Seismic Design Criteria [11], [12]. Maximum and minimum shear force computations were based on the contribution of concrete under maximum compression and maximum tension, respectively [33].

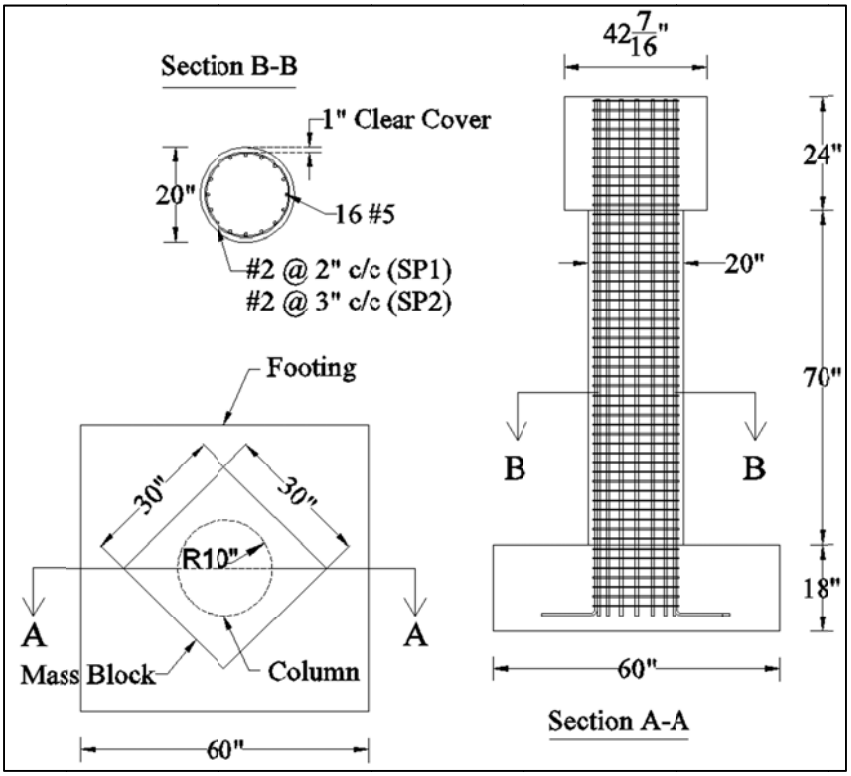

Figure 2.2 Section, elevation and top view of the as-built test specimens.

2.3.2 Concrete Footing

Cantilever column was supported by a 60 in × 60 in × 18 in (1524 mm × 1524 mm × 457.2 mm), rigid footing at its base. Figure 2.3 shows the geometric details of the concrete footing. Footing was designed symmetrically, to avoid any direct or punching shear failure during the testing. Depth of footing was based on the required development length of the longitudinal steel bars to avoid bar pullout/anchorage failure. Longitudinal and transverse reinforcements were extended into the footing and the top mass with the same configuration. Longitudinal bars were bent at 90^{o} at the end inside the footing to provide sufficient anchorage. During the test set-up four load cells were installed at the four corners under the footing to measure the base reaction forces. Post-tensioning rods were used to firmly attach footing and load cells with the shake table to avoid any tension (or decompression) under maximum expected overturning moment and to prevent sliding at maximum shear transfer relative to the shaking table. Self-weight of footing was about 5.7 kips (25.35 KN).

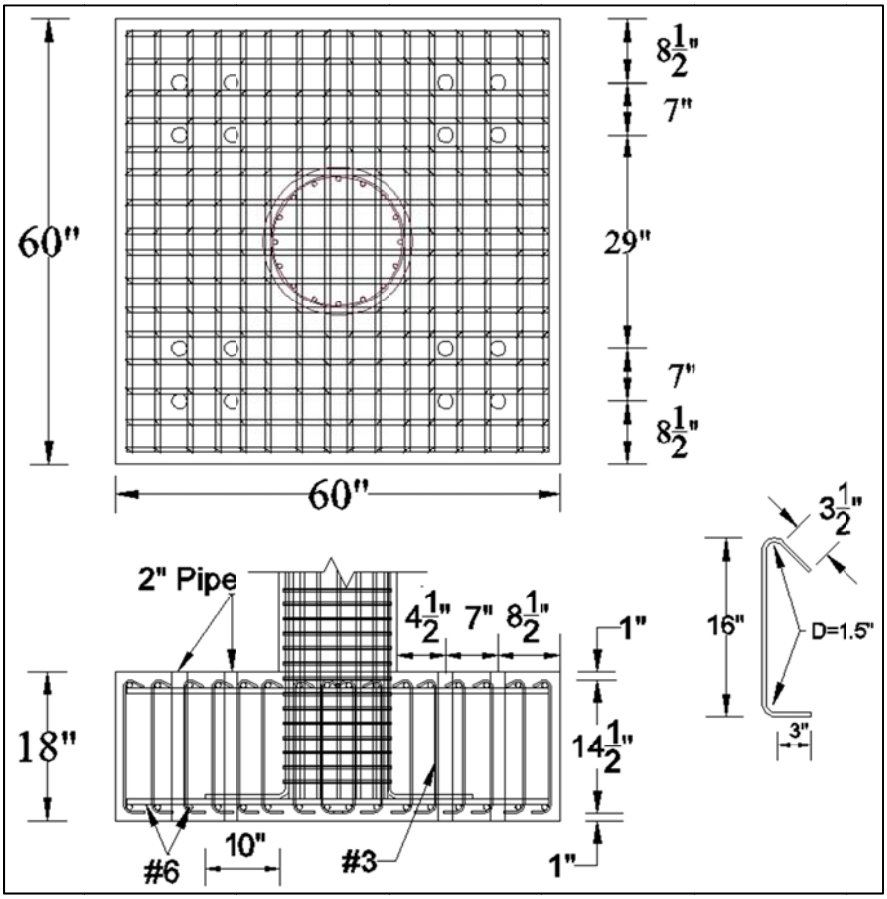

Figure 2.3 Top and elevation view of the concrete footing.

2.3.3 Mass Block

Top mass block was designed using minimum design criterion to avoid any form of flexural or shear failures during the shaking table testing (Figure 2.4). #4 steel reinforcing bars were used as the longitudinal reinforcement and #3 deformed steel reinforcing bars were used as hoop reinforcement. This block was formed mainly to attach additional superstructure mass at column top. Similar to the assembly for the repaired column tests, 8 PVC pipe holes running in each of the two perpendicular directions were made during the construction and to attach steel tubular beams with lead blocks (additional mass needed for scale-compensation).

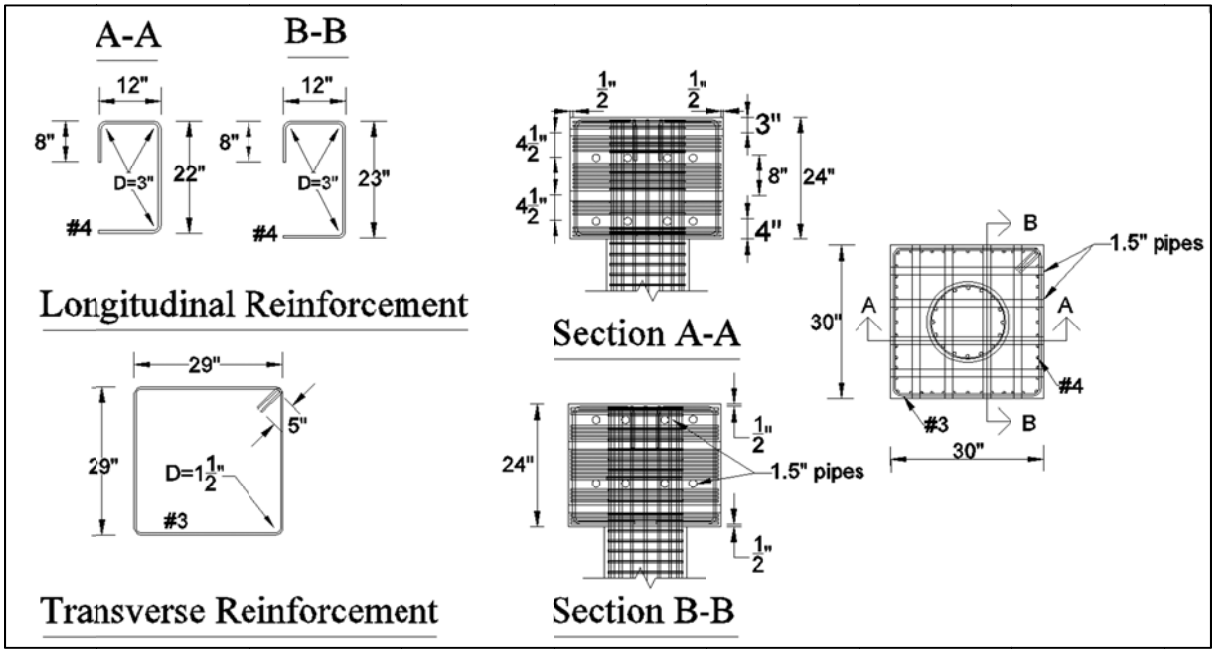

Figure 2.4 Section, elevation and top view of the mass blocks.

2.3.4 Superstructure Mass Configuration

Figure 2.5 shows both the top and elevation views of the test specimens. Total weight on the top of the specimens was 85.6 kips (380.77 KN) which provided the required axial load ratio of 6.8%. Four Hollow Steel Section (HSS) 12 in × 20 in × 0.5 in (304.8 mm × 508 mm × 12.7 mm), about 96 in (2438.4 mm) long, were attached on the four sides of the top block using post-tensioned rods through the 8 PVC pipe sections in the top mass block (Figure 2.5a). These steel beams supported the concrete slabs on top and hanging stacks of lead blocks to achieve the required values of the mass moment of inertia and location of the center of mass. Smaller size HSS tubes were attached at the top and bottom of the steel beams to support the loading elements.

Each beam was loaded with 4, 6, and 8 stacks lead blocks labeled as mass stacks M1, M2 and M3 in Figure 2.5b, respectively, carrying load of 9 kips (40 KN). On top of this lead mass configuration, two concrete slabs were attached to achieve the required axial load at the column base. Each slab was 120 in ×120 in ×14 in (3048 mm × 3048 mm × 356 mm) and weighed about 16.5 kips (73.4 KN). The top slabs were firmly connected to the HSS beams using post-tensioning steel rods. In addition, the lead block masses and steel beams were connected in a similar manner (Figure 2.5b). These post-tensioning rods were subjected to pre-stressing force high enough to avoid slippage between the connected elements.

The center of gravity of the superstructure mass was located at 4.45 in (113 mm) above the circular column and top block intersection. The mass moment of inertia of the test specimens was 47 slug-ft^2 (63.7 t-m^2). The superstructure mass configuration was chosen to match the quarter-scale values of the same parameters for the prototype bridge column. Pre-analysis of the test specimens showed that their lateral vibration period was comparable to that of the scaled version of the prototype bridge column. Figure 2.6 shows the test setup of as-built SP1 on shake table. In order to compare the response of the as-built and repaired specimens, same mass configuration was used in all the tests.

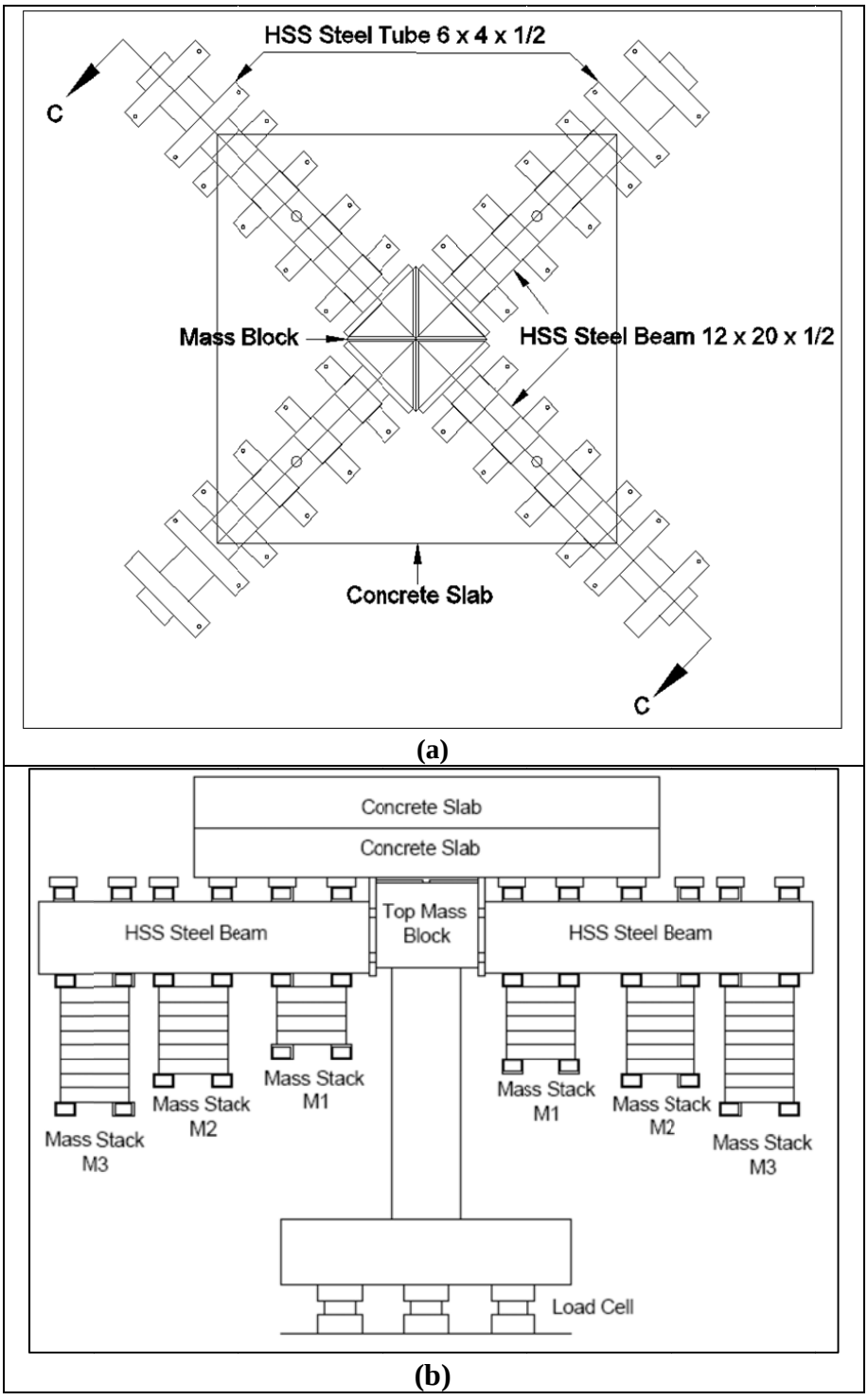

Figure 2.5 Superstructure mass configuration: (a) top view; (b) elevation view.

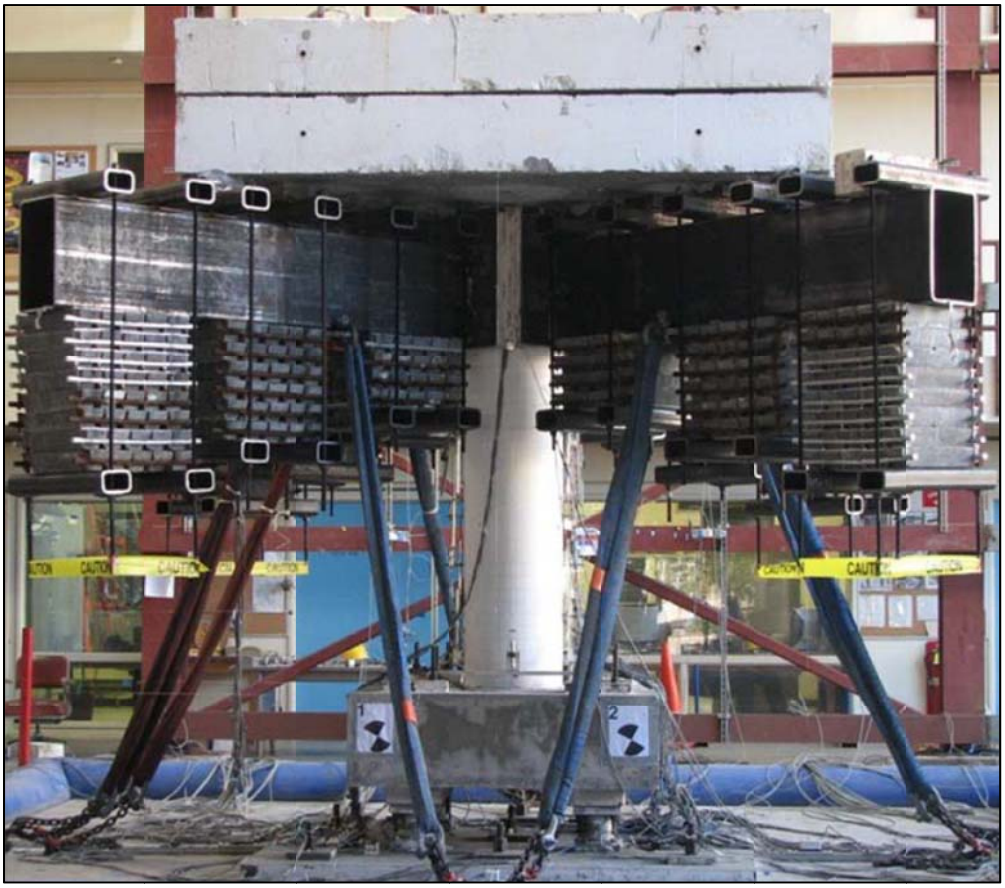

Figure 2.6 Test setup of as-built SP1.

2.4 REPAIR CALCULATIONS

The nominal design shear strength of the repaired test specimens ($V_{n,repaired}$) was computed as follows,

$$V_{n,repaired} = r_c V_C + r_s V_S + V_j \quad \textbf{(2.1)}$$

where V_C is the shear strength contribution of concrete, V_S is shear strength contribution of hoop steel, V_j is the shear strength contribution of the FRP jackets, r_c is the reduction factor of the concrete to the shear strength, and r_s is the reduction factor of the steel to the shear strength. As per the Seismic Design Criteria (SDC) [11], [12] the shear demand (V_{Demand}) of the RC member should be:

$$V_{Demand} \leq V_{Design} = \Phi V_{n,repaired} \quad \textbf{(2.2)}$$

where $\Phi = 0.85$ is factor of safety, based on the seismic design of the ductile RC members. Since the transverse confinement ratio of the as-built SP2 was less than the limit specified by AASHTO (2010) [2], the contribution of concrete and hoop steel to the design shear strength of the repaired SP2 was neglected. For the repair of the as-built SP1, the contribution of hoop steel and concrete (under tension) to the shear strength of the repaired SP1 was reduced by 50%. Shear demand was assumed as the maximum shear force measured in the as-built test specimens. The minimum design shear strength of the FRP jackets was computed as follows,

$$V_j \geq \frac{V_{demand}}{\Phi} - (r_c V_C + r_s V_S) \quad \textbf{(2.3)}$$

Based on Equation 2.3, the required design shear strength of the repaired SP1 and SP2 was about 76 kips and 95 kips, respectively. The required thickness of the FRP composite jackets [62] was computed as follows

$$t_{j,required} = \frac{V_j}{\frac{\pi}{2} \times \varepsilon_j \times E_j \times D \times \cot\theta} \quad \textbf{(2.4)}$$

where $t_{j,requires}$ is the required thickness of FRP jackets, ε_j is the design strain in the jacket, E_j is the elastic modulus of the FRP jackets, D is the diameter of the FRP confined section, and θ is the inclination of the compressive concrete strut with respect to the member axis. Seibel et al. (1997) [57], Caltrans (2006; 2010) [11], [12], and Vasooghi and Saiidi (2013) [60] recommended a 45º inclination of shear crack to column axis as an upper bound. Design strain of 0.4% was assumed to avoid failure of jacket under unexpected overloads due to large dilation strains and degradation of the aggregate-interlock action [42]. Based on the Equation 2.4 the as-built SP1 was repaired using 4 layers of GFRP composite jacket and the as-built SP2 was repaired using 2 layers of CFRP composite jackets.

The contribution of the core concrete to the shear strength capacity of the bridge column is different inside and outside the plastic hinge zone [2], [5]. Due to relatively higher shear-flexure cracking in the plastic hinge zone at high ductility, the aggregate interlock action is

comparatively less effective in contributing to concrete shear strength and more number of FRP jackets are required in the plastic hinge regions. The as-built test specimens experienced extensive shear and flexure cracking near the base and the top of the column specimens. It was assumed that the critical shear crack can extend to a distance of twice the diameter of the test specimens. During the shaking table tests the as-built test specimens were under double curvature and plastic hinge zones (region of relatively higher damage) near the ends of the cantilever column requiring the length of confinement repair to be about 4*D*. Total height of column was only 3.5*D*, thus entire column section was considered as a critical hinge region and was wrapped with composite jackets with same number of layers.

2.5 REPAIR PROCEDURE

Both as-built test specimens were subjected to the same set of horizontal and vertical ground motions. Both specimens developed shear and flexure cracks, damage being more in as-built test specimen SP2 compared to SP1, refer to Figure 2.7. Damaged specimens were then repaired and retrofitted with unidirectional FRP composite sheets by wet lay-up method.

Sounding hammer test was used to locate and mechanically remove lose and unsound concrete (Figure 2.8a). The exposed parts of reinforcing bars were cleaned of any rust using a wire brush. Using a drill machine, holes were drilled at adequate spacing carefully in the cracked regions and the surface was grinded lightly to remove the white paint (Figure 2.8b and Figure 2.8c). Injection ports were installed in all the drilled holes (Figure 2.8d). Several FRP Solutions Inc. products were used in the repair and retrofit of these columns as follows. BC020 bonding and corrosion protection system was applied on cleaned concrete and reinforcement surfaces. Voids wider than 0.75 in (19.1 mm) were patched using SM020 structural mortar and those smaller than 0.75 in (19.1 mm) were cap sealed using GS100 gel/paste epoxy system (Figure 2.9a). After the cap seal and patch material were cured, RN151 structural epoxy system was injected in all cracks. Multi-port injection system was used with relatively low pressure to prevent expansion and further damage to cracked concrete, Figure 2.9b. When injection resin was cured, specimen surfaces were grinded to remove cap seal material and injection ports.

Surface was then cleaned of any dust and debris and one coat of RN075 prime was applied on it as a primer. Four layers of E-Clad FRP composite system were installed on damaged specimen SP1 (Figure 2.9c). E-Clad is an FRP composite system comprised of FE261 unidirectional Advantex glass fiber fabric impregnated with RN075 structural epoxy system. Two layers of C-Clad FRP composite system were installed on damaged specimen SP2 (Figure 2.9d). C-Clad is an FRP composite system comprised of FC061 unidirectional carbon fiber fabric impregnated with RN075 structural epoxy system. PT006 temporary polyvinyl compression/curing tapes were wrapped on the installed composite sheets and were discarded after 2 weeks.

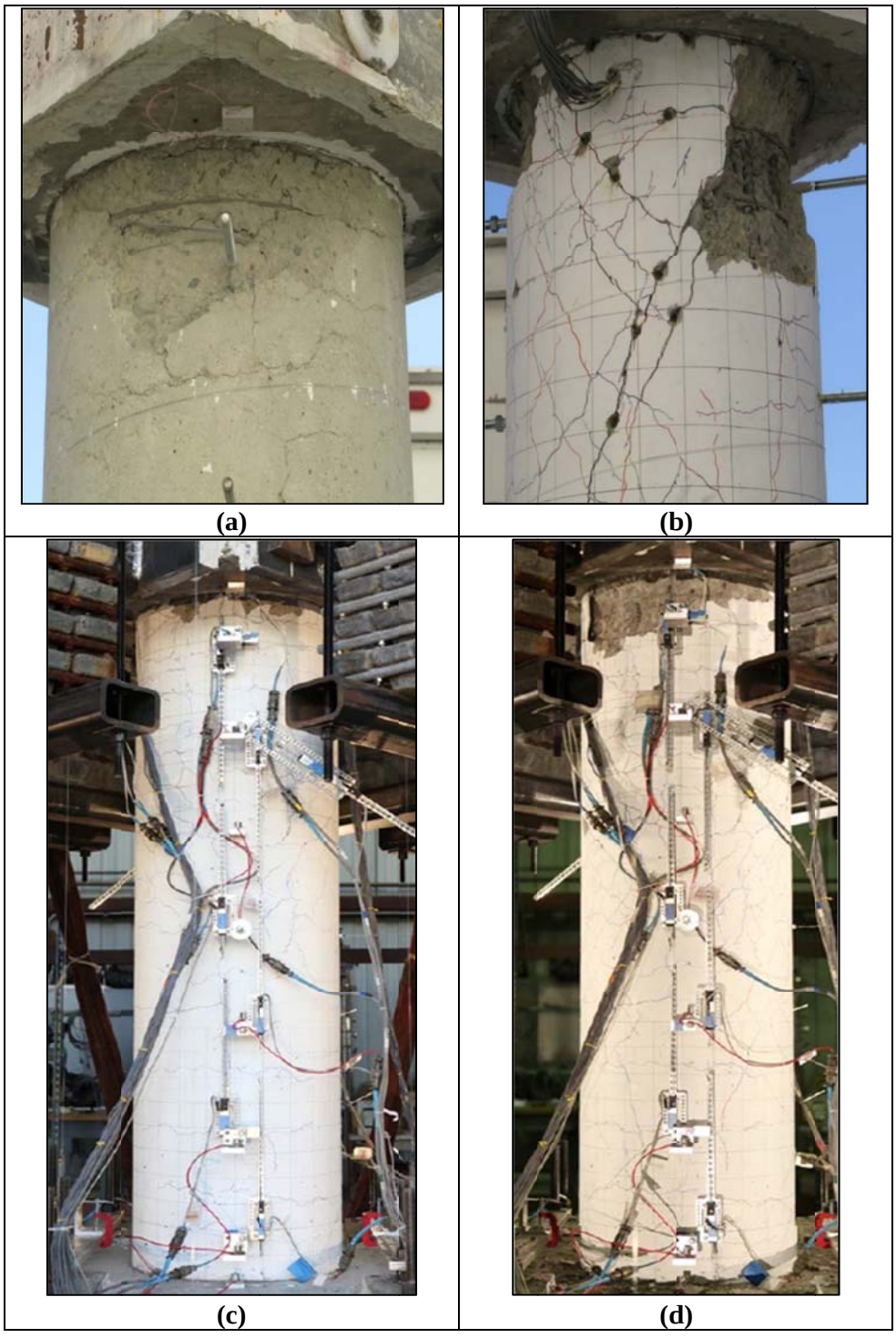

Figure 2.7 As-built test specimens after testing: (a) top damage state of SP1; (b) top damage state of SP2; (c) north view of damaged SP1; (d) north view of damaged SP2.

Figure 2.8 Repair of as-built test specimen (preparation stage): (a) hammer test to remove lose material; (b) hole-drilling in the cracked regions; (c) grinding of the surface paint; (d) Injection ports in damaged regions.

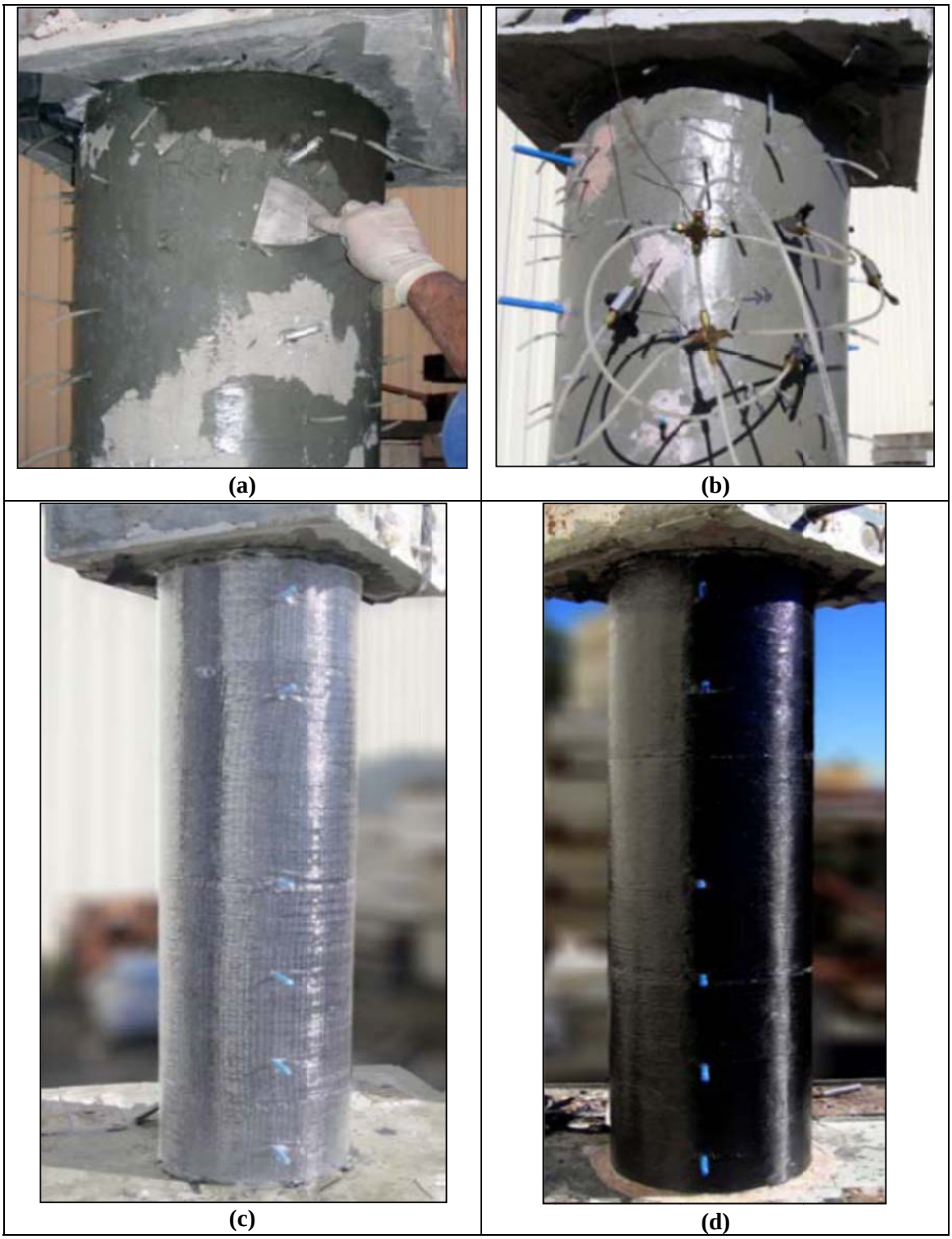

Figure 2.9 Repair of as-built test specimen (application stage): (a) cap sealing and surface repair; (b) multi-port injection system; (c) GFRP repaired SP1; (d) CFRP repaired SP2.

2.6 MATERIAL PROPERTIES

2.6.1 Concrete

Same batch of concrete ready mix was placed in both test specimens. 12, standard 6 in × 12 in (152.4 mm × 304.8 mm) cylindrical test specimens were taken from the same batch of concrete with which the two test specimens were cast. In all concrete mixes, the maximum size of the coarse aggregates was ¾ in (19.05 mm). The average density of concrete mix was 150.3 pcf (23.6 kN/m^3), which was the same as that of normal weight concrete. The cylindrical test specimens were tested at different time periods to access the strength gain of concrete. The average compressive strength of concrete (based on the standard cylindrical concrete test specimens) on the day of testing was 4.0 ksi (26.89 MPa) with corresponding peak strain of 0.28%. Figure 2.10 shows the stress-strain plots of the cylindrical test specimens tested at different number of days after casting.

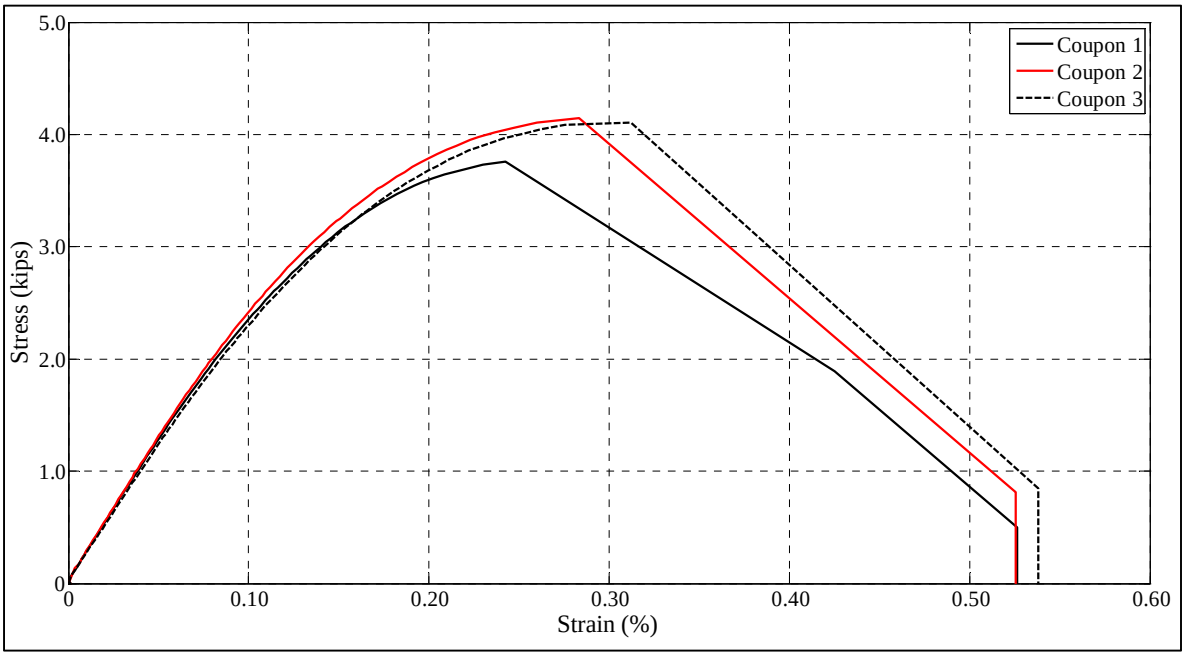

Figure 2.10 Compressive stress-strain plots of concrete cylindrical coupons on the day of testing.

2.6.2 Steel

16, #5 Grade 60 longitudinal steel bars, confirming to ASTM A706, were used as the longitudinal reinforcement in both test specimens SP1 and SP2. Two steel bar coupons were tested under monolithic tensile loading. The yield strength of the reinforcement was 77.4 ksi (533.7 MPa) and the ultimate stress at bar fracture was 105.06 ksi (724.4 MPa). Corresponding value of yield strain was 0.25% and strain measured at ultimate stress was 12.04%. #2 deformed bars hoops were used for providing the confinement. The hoops were lap welded at the ends. The yield and ultimate strength of the #2 deformed bars was 63.13 ksi (435.3 MPa) and 90.25 ksi (622.3 MPa) respectively, with yield strain of 0.22% and strain of 11.64% corresponding to ultimate tensile strength. #2 hoops coupons were straightened before the tensile testing. Figure 2.11 shows the stress-strain plots of the #5 and #2 reinforcing bars, respectively.

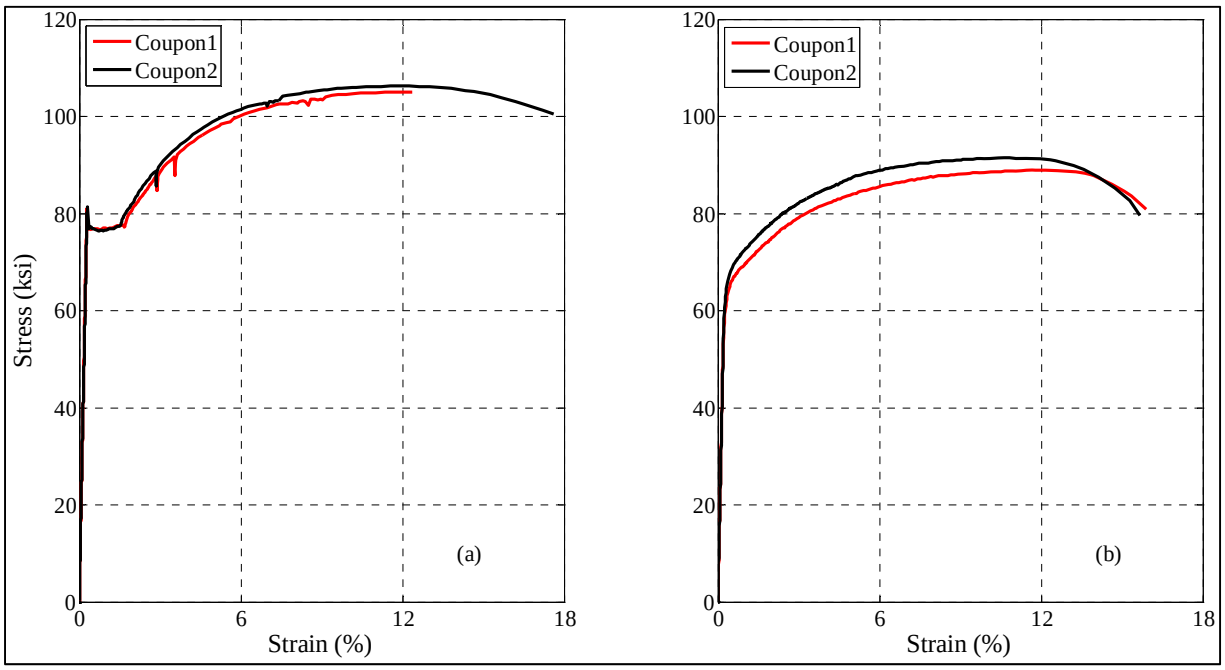

Figure 2.11 Stress-strain plots of steel coupons: (a) #5 bars for longitudinal reinforcement; (b) #2 bars for circular hoops.

2.6.3 Unidirectional Glass Fiber Fabric

Four layers of E-Clad FRP composite system were installed on the damaged SP1. E-Clad is an FRP composite system comprised of FE261 unidirectional Advantex glass fiber fabric impregnated with RN075 structural epoxy system to achieve a strong FRP composite laminate. Average laminate tensile strength of the GFRP composite sheet was 90.76 ksi (625.8 MPa) with an average tensile modulus of 3950 ksi (27.2 GPa) and corresponding rupture strain of 2.3%. Thickness of each ply was 0.04 in (1.0 mm).

2.6.4 Unidirectional Carbon Fiber Fabric

Two layers of C-Clad FRP composite system were installed on the damaged SP2. C-Clad is an FRP composite system comprised of FC061 unidirectional carbon fiber fabric impregnated with RN075 structural epoxy system. Average laminate tensile strength of the composite was 149 ksi (1027.3 MPa) with an average tensile modulus of 10100 ksi (69.6 GPa) and corresponding rupture strain of 1.2%. Single ply thickness for both laminates was 0.04 in (1.0 mm).

2.6.5 Patching Material

Structural Motor SM020 was used to fill the concrete cracks wider than 0.75 in (19.1 mm) and patch the damaged surface for proper application of composite layer. Based on the data provided by manufacturer, the structural motor had an average compressive and split tensile strength of 6.3 ksi (43.3 MPa) and 595 psi (4.1 MPa) , respectively, after 28 days. Modulus of elasticity based on the data from elastic zone of stress-strain plot was 2260 ksi (15.6 GPa). Bond strength of 0.5 ksi (3.45 MPa) was measured after 28 days with failure noticed in substrate (Appendix A).

Concrete cracks with the width less than 0.75 in (19.1 mm) were cap-sealed using GS100 gel/paste epoxy system. Compressive and tensile strength of the epoxy system was 10.5 ksi (72.4 MPa) and 7.2 ksi (49.64 MPa), respectively. Rupture strain of the epoxy system was about 0.85%. Average flexural strength measured after 14 days was 5.6 ksi (38.6 MPa) (Appendix A).

Chapter 3. Test Setup and Ground Motions

3.1 TEST SETUP

3.1.1 Introduction

The testing of all the test specimens was carried out using the Pacific Earthquake Engineering Research (PEER) Center shaking table facility, located at Richmond Field Station, Richmond, California. A stiff steel plate was attached to the shaking table to be able to center the test specimen on the table and reduce the impact of warping effect (out of plane bending) of the table surface during the ground motion excitation. Test specimens were subjected to a set of horizontal and vertical selected ground motions. This chapter discusses details of the test setup and the instrumentation used to measure the response during the loading protocol.

3.1.2 Description of Shake Table

The shaking table at Richmond Field Station is about 240 in × 240 in (6096 mm × 6096 mm) in horizontal plane and has six-degrees of freedom (three translational and three rotational). Total weight of empty shake table is about 100 kips (445 KN). Maximum limits of displacement, velocity and acceleration of empty shake table are given in Table ***3.1*** below. Due to high in-plane stiffness the natural frequency of the shake table in horizontal direction is above 20 Hz, thus making it easy to apply signals between 0-10Hz without any interference.

The shaking table is stiffened using heavy transverse steel ribs. Motion of the shaking table is controlled with a set of eight horizontal and four vertical hydraulic actuators, each of about 75 kips (333.62 KN) capacity, located underneath the table attached to the transverse ribs. To control the motion of actuators in the direction perpendicular to their primary direction of motion, swivel joints are provided at each end allowing for the end rotations. The length of each horizontal and vertical actuator is 126 in (3200 mm) and 104 in (2642 mm), respectively, measured from the end of swivel joint to the connection with ribs. An MTS control system is used to control the movement of the shaking table. Each of the 6 degrees of freedom can be programmed individually and run concurrently using the control system. With the actuator length variations and the control system, the horizontal and vertical components of input signal can be decoupled.

A stiff steel plate of dimensions 96 in × 96 in × 3.35 in (2438.4 mm × 2438.4 mm × 85.1 mm) was attached to the shaking table to center the test specimen on the table and reduce the warping effect (out of plane bending) of the table surface during the dynamic testing. The test specimens were attached to the steel plate with for load cells placed between the bottom of the

concrete footings and the top of the steel plate. 16, 7/8 in (22 mm) diameter threaded holes were drilled in the plate to attach the load cells to the steel plate. Another 9, 2.5 in (64 mm) diameter holes were drilled in the steel plate to connect it with the concrete shaking table. Plan of the steel base plate and location of the holes is shown in Figure 3.1. All test specimens had steel chain harness attached to the superstructure mass configuration of the test specimens and the shaking table. The steel chain harnesses were provided for the safety to hold the specimen in the event of collapse during shaking table testing. Figure 3.2 shows the test setup of the test specimens with superstructure mass and attached steel chain harnesses.

Table 3.1 Motion limits of empty shake table.

Parameter	Amplitude
Acceleration	About 3g along all the axes
Velocity	About 30 in/s (762 mm/s) along all the axis
Displacement	5 in (127 mm) along any horizontal direction (forward or backward)
	2 in (50.8 mm) along the vertical direction (up or down)

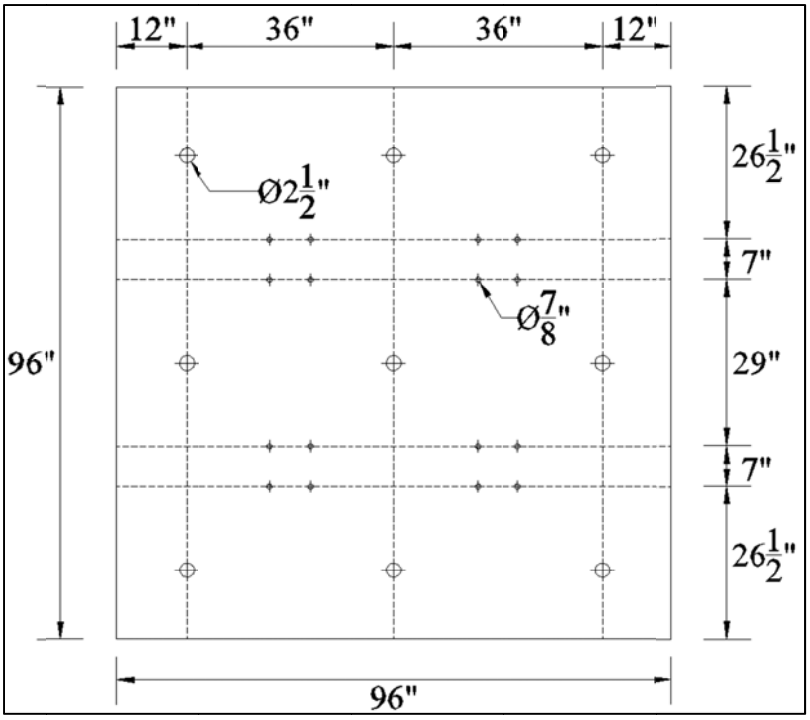

Figure 3.1 Plan of the steel base plate.

Figure 3.2 North-side view of the repaired SP2.

3.2 INSTRUMENTATION

3.2.1 Base Reaction Measurements

Four load cells were installed on the steel plate using post tensioning rods, through the 7/8 in (22.225 mm) holes (Figure 3.1). The test specimen assembly was attached on the top of the load cells. Data obtained from the load cells was used to compute the shear forces (longitudinal and transverse direction) and the axial load at the base of the footing. The measured force components by the load cells were directly added to obtain the base force in a particular direction (longitudinal or transverse) were directly added to obtain the horizontal shear in same direction. The load cell measurements were also used to measure the bending moments in the test specimens during the shaking table testing.

3.2.2 Acceleration Measurements

1D and 3D accelerometers were installed at the different locations on the test specimen set-up to measure the horizontal and vertical acceleration response during the shake table testing. Nine, 1-D accelerometers were installed along the column height to measure the vertical accelerations at different section heights (Figure 3.3a). Four, 3D accelerometers were installed at the corners of the top concrete slab to measure the accelerations at the top of the test specimens (Figure 3.3b). Four, 3D accelerometers were installed near the four corners of the base steel plate to measure the accelerations at the base of the test specimen (Figure 3.3c). One 3D accelerometer was installed on the East face of the mass block, just at the intersection of cantilever column and mass block, to measure the accelerations at the column top (Figure 3.3a).

3.2.3 Displacement Measurements

Twenty wire-potentiometers (WPs) were used to measure the horizontal and vertical displacements of the test specimens (Figure 3.4 and Figure 3.5). Four WPs were attached to the steel plate with target points (vertically above) on the concrete slab. These WPs were used to measure the vertical displacement of the test specimens with respect to the shaking table and the net rotation about the X- and Y- axis (horizontal). Eight WPs were installed on the South side frame with target points on the footing and the concrete slab, and along the column height to measure the displacements in the X-direction, as shown in Figure 3.4 and Figure 3.5a. Five inclined WP with target points on the West face of the test specimens were installed to measure any out-of-plane displacements and to verify the measured horizontal displacement data (Figure 3.5b).

3.2.4 Strain Measurements

The test specimens were instrumented both internally and externally using strain gauges, to measure the longitudinal and confining strains. Some the strain gauges, installed on the longitudinal and transverse reinforcing bars, were damaged during the tests of the as-built specimens and the repairing process (Figure 3.6). Strain gauges were installed on the longitudinal steel bars to measure the axial strains during the shake table test. Strains in the FRP composite jackets along the circumferential direction were measured using the external strain gauges. 32

horizontal strain gauges were installed on the FRP jackets of the repaired test specimens along the column height. Figure 3.7 shows the location and distribution of the jacket strain gauges.

3.2.5 Curvature Measurements

Total 14 linear vertical displacement transducers (LVDTs) were used to measure the average curvatures along the column height on the North and South face of the test specimen (Figure 3.8) Transducers were installed between two points of interest to measure relative vertical displacement. This relative change was measured on the North-South face of the test specimen at same section level. Average strain was computed as the ratio of the relative displacement to the initial distance between the two sections. The average curvature was computed as ratio of measured strain to the distance between the transducers on the North and South side (at same level) (Appendix C).

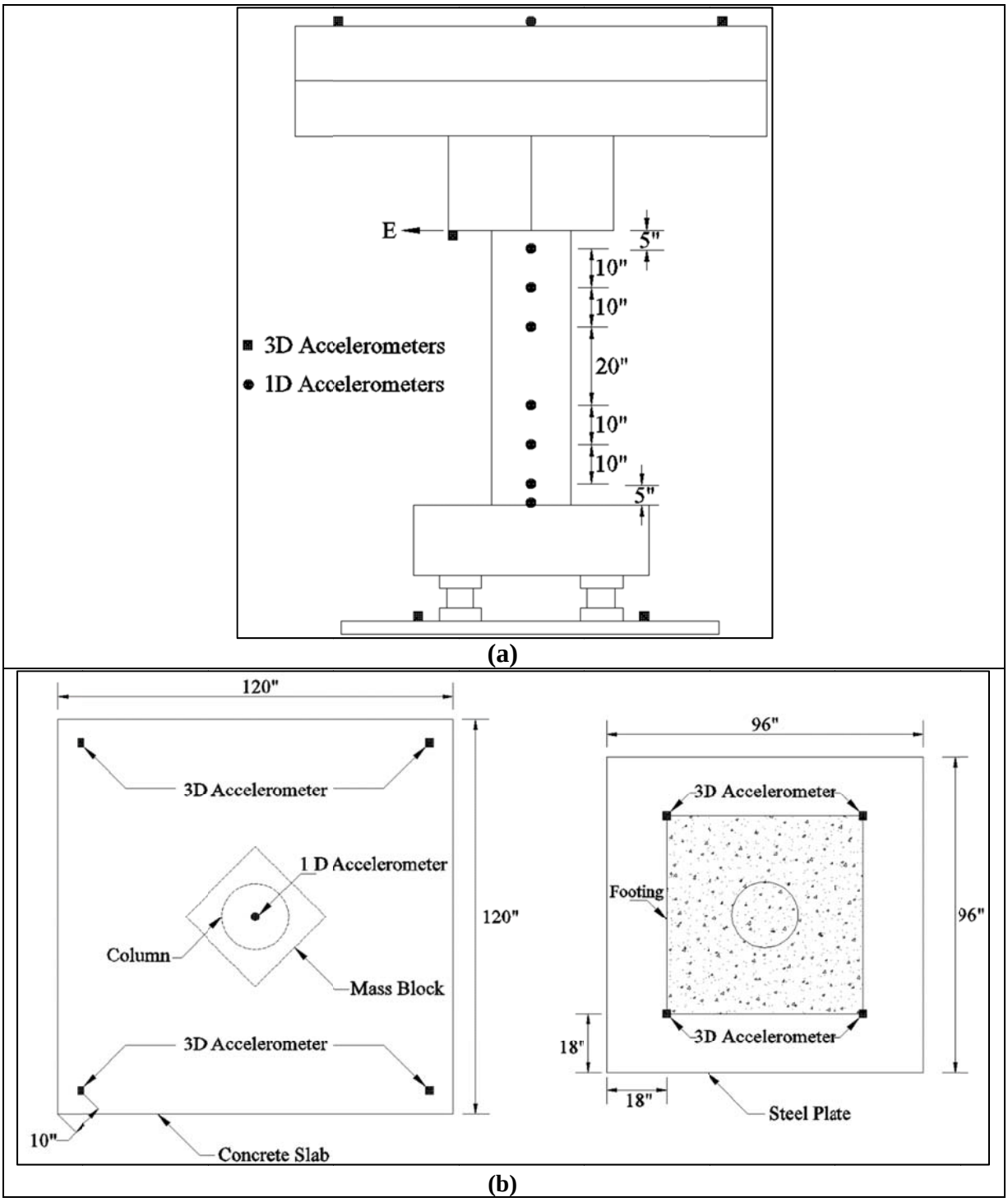

Figure 3.3 Accelerometers installed on the test specimens: (a) elevation view; (b) top view of the concrete slab and the steel plate.

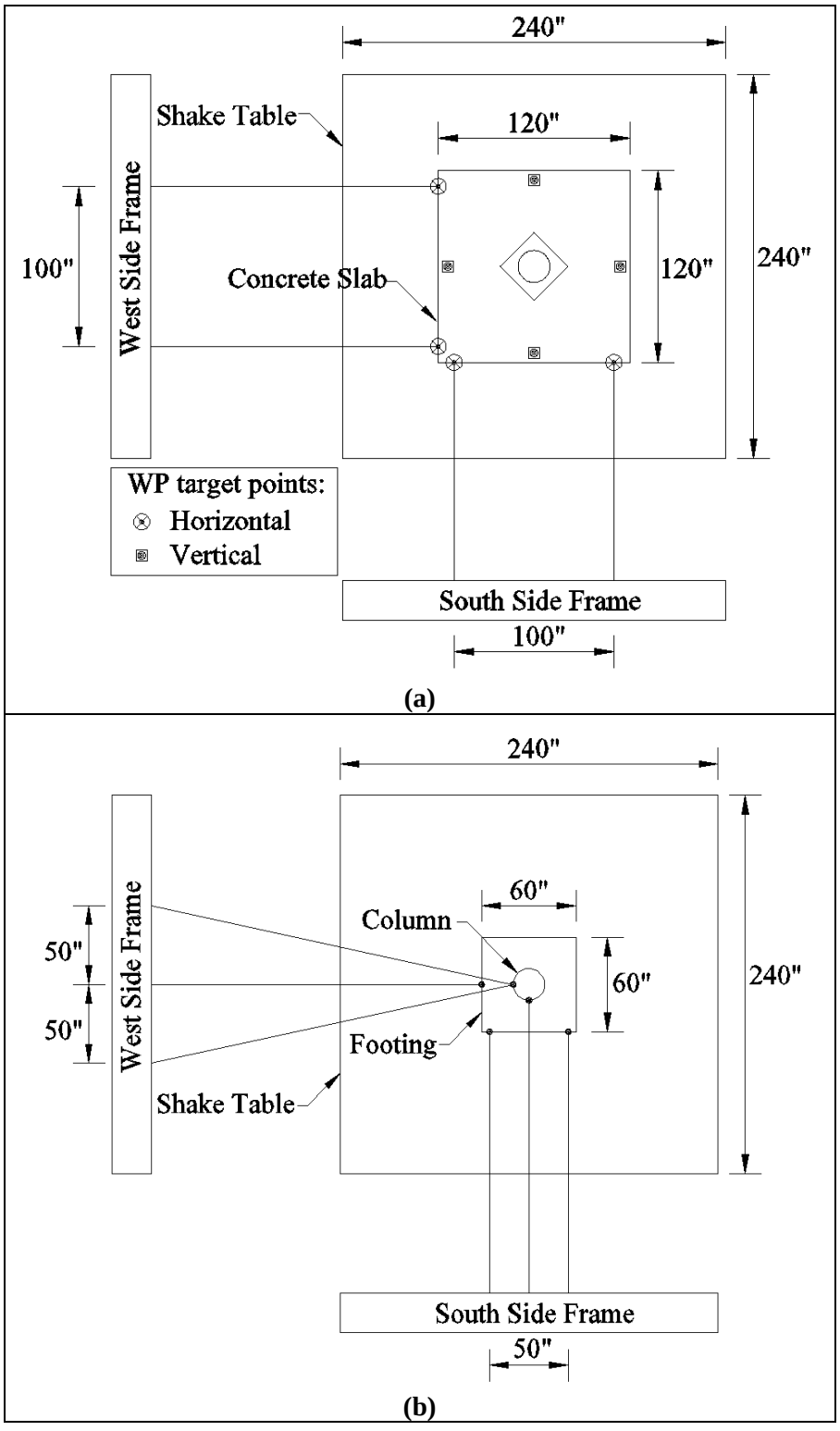

Figure 3.4 Top view of the WPs installed on: (a) the concrete slab; (b) the column and the footing.

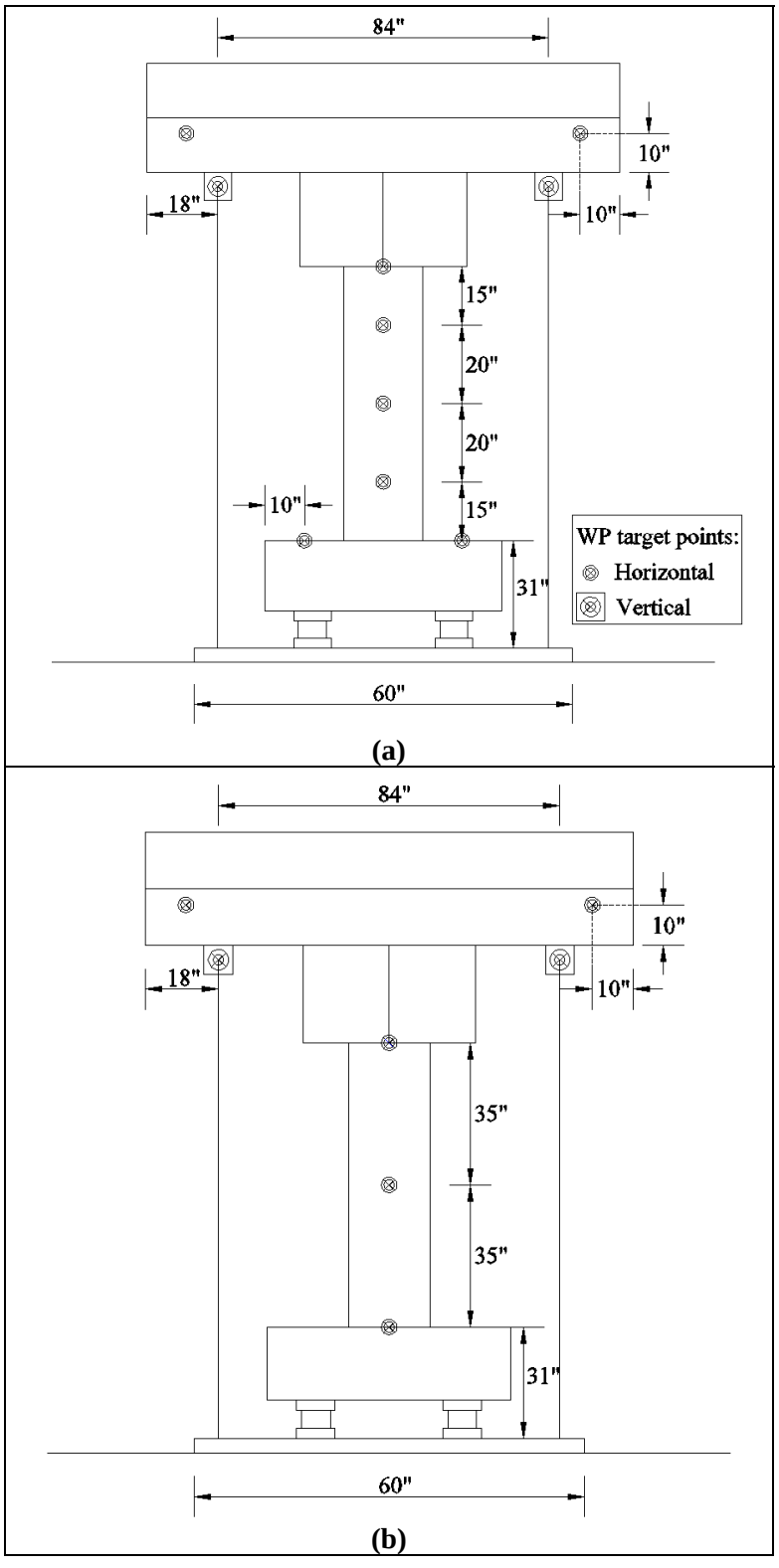

Figure 3.5 Elevation view of WPs from the: (a) South side; (b) West side.

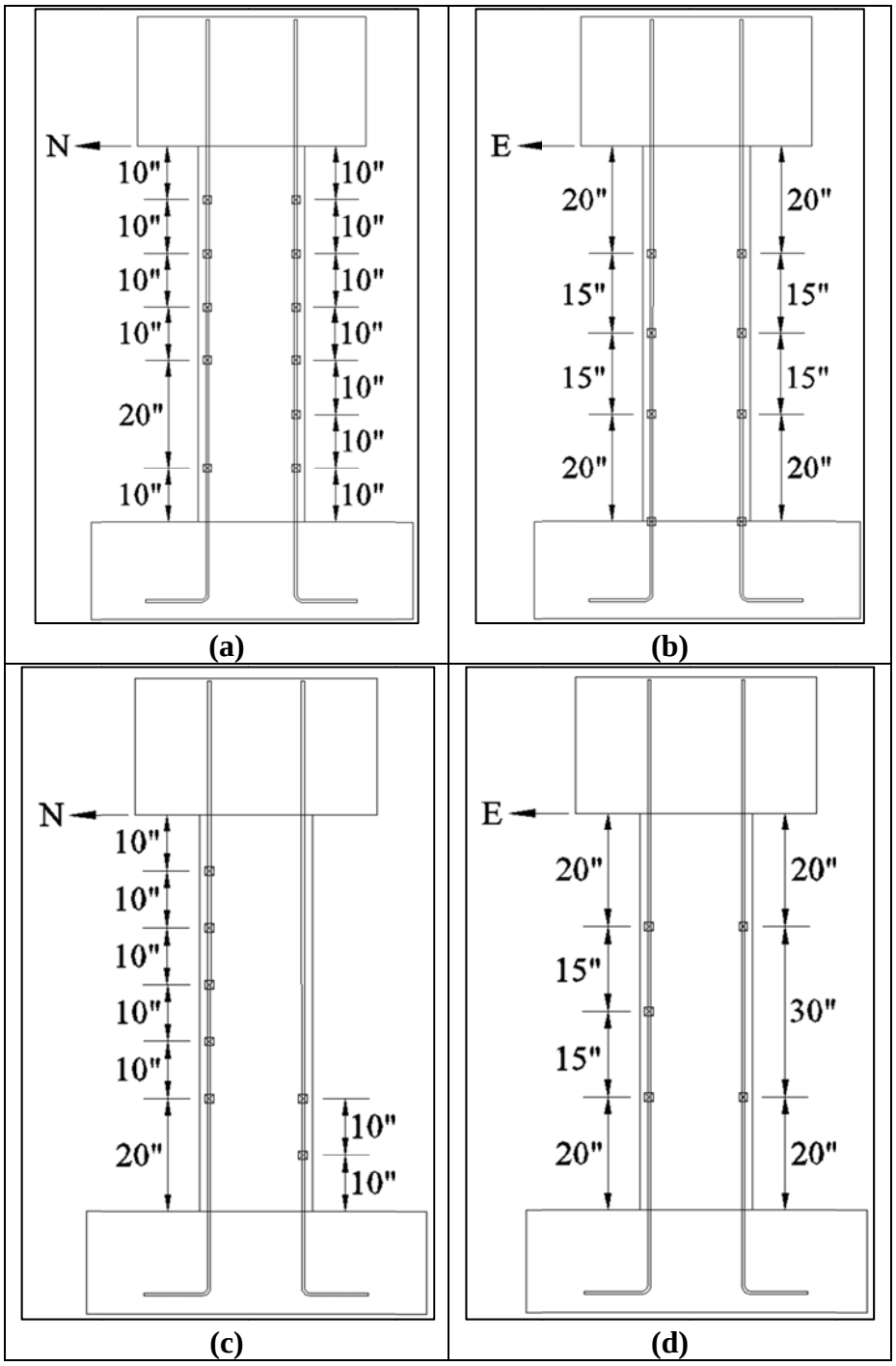

Figure 3.6 Longitudinal strain gauges: (a) North-South side of the repaired SP1; (b) East-West side of the repaired SP1; (c) North-South side of the repaired SP2; (b) East-West side of the repaired SP2.

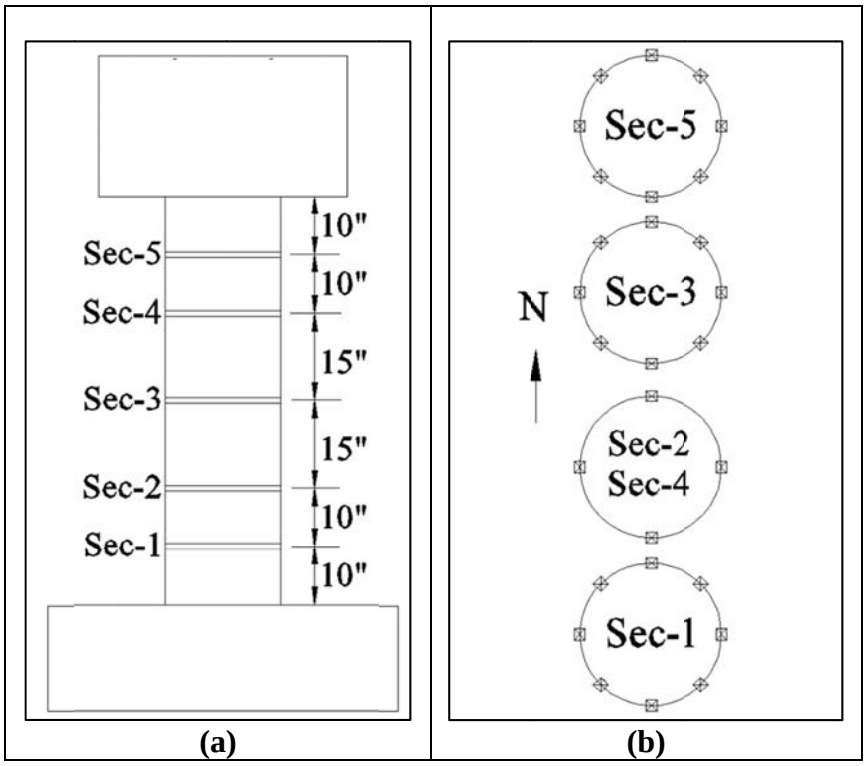

Figure 3.7 Strain gauges installed on the FRP jackets: (a) elevation view; (b) section details.

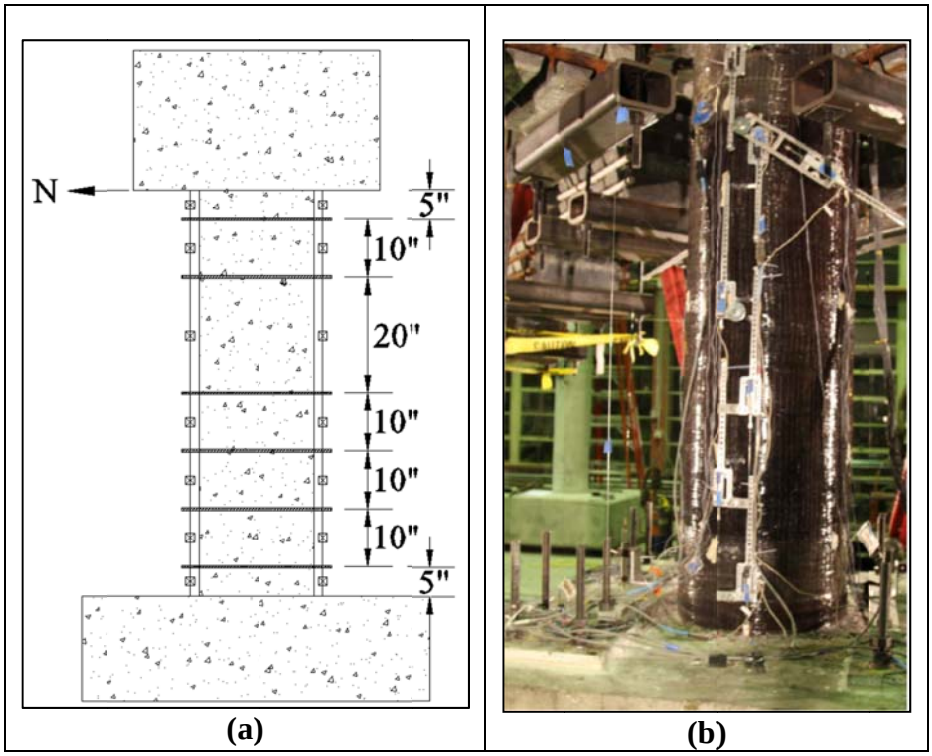

Figure 3.8 LDVTs: (a) North and South face of the test specimens; (b) on North face of the repaired SP2.

3.3 GROUND MOTIONS

The repaired test specimens were subjected to same set of the horizontal and vertical base excitations that were used for testing the as-built test specimens. The criterion and procedure of selecting the ground motions for the shaking table tests were discussed given in by Lee (2011) [33]. A summary of those details are presented in this section. The ground motions were selected from the PEER NGA database [20] based on three main criteria. First criteria was to choose the ground motions with magnitude of one (out of the two) horizontal components higher than 0.25g. The second criterion was based on the ratio of the pseudo-spectral acceleration corresponding to the peak vertical component (PSa_v) to those corresponding to the peak horizontal components (PSa_{h1}, PSa_{h2}). For the 20 pairs of periods T_h-T_v (T_v = 0.05 sec, 0.1 sec, 0.15 sec and 0.2 sec and T_h = 0.4 sec, 0.5 sec, 0.6 sec, 0.7 sec and 0.8 sec), PSa_v / PSa_{h1} or PSa_v / PSa_{h2} were calculated. If one of these two ratios were larger than 1.0 in at least 15 pairs, the ground motion was selected as one of the candidate. Third criteria was based on the time interval between the horizontal and vertical peak accelerations which affects the interaction of the horizontal and the vertical responses. Ground motions with interval shorter than the cut-off of 1 sec were chosen. After screening through these three criterion, ground motions with low frequency contents were also eliminated.

A fidelity test with the dummy mass replicating the weight and center of mass location of the test specimen was conducted at shaking table facility of Richmond Field Station. Due to the limitations of the shaking table it was difficult to reproduce the exact same input signals. Based on the results of fidelity test, the response spectra of the measured output signal was matched with that of the input signal. The ground motions with closest match in the required frequency ranges, for both horizontal and vertical components, were chosen as the final input signal for the loading protocol. The ground motion recorded at the Pacoima Dam station of 1994 Northridge earthquake (RSN 1051) was finalized as the input signal for dynamic testing. The Northridge earthquake occurred on January 17, 1994 in city of Los Angeles, California, had a moment magnitude of 6.69 and hypocenter depth of 17.5 km. The chosen ground motion data was obtained from the accelerometers installed on the left abutment of the Pacoima dam with peak acceleration of 1.5g. Most of the input testing signals included one horizontal and one vertical ground motion component. Out of the two measured horizontal components the one that produced bigger shear strength reduction due to the ground motion excitation was chosen [33].

Figure 3.9a and Figure 3.9b, show the two chosen unfiltered full-scale horizontal (X-direction) and vertical (Z-direction) components of the Northridge earthquake [20] Maximum value of horizontal component of ground motion was 1.585g towards the North side of the test specimen. To understand effect of tensile stress on behavior of test specimen, maximum of vertical component was directed upwards with a magnitude of 1.229g. Figure 3.9c and Figure 3.9d, show the cumulative energy (E_{cum}) plots based on the squared acceleration data ($a^2(t)$) over the entire ground motion period (T_g), computed using Equation 3.1. Input cumulative energy for the vertical component was almost half of the horizontal component.

$$E_{cum} = \int_0^{T_g} a^2(t)dt \tag{3.1}$$

Applied ground motions were scaled versions of the chosen signal with intensity scale factors (horizontal and vertical) increasing from 5% to 125% (Table 3.2). A scale of ¼ was used for the design of the test specimen and all ground motions were time compressed by a factor of 0.5. There extra ground motions with intensity scale of 25%, 50% and 125% were repeated but without the vertical excitation components. These ground motions were used to study the effect of the vertical ground motions components on the response of the test specimen. It is noted that EQ4 (25%-scale) and EQ6 (50%-scale) were not part of loading sequence for the as-built SP1. However, the repaired SP1 followed the complete sequence mentioned in Table 3.2. The test specimens (repaired or as-built) did not show any significant response nonlinearity during EQ4 and EQ6. Thus it was assumed that response of the repaired test specimens and their as-built counterparts could be compared during EQ4 and EQ6 with reasonable accuracy.

Figure **3.10** and Figure **3.11** compares the input and the output acceleration response of the repaired and the as-built test specimens. The output accelerations were computed at the table level. The acceleration data was measured during test EQ2 when the acceleration response of the test specimens was almost same. Due to limitations of the shake table a perfect match between the input signal and the table output was difficult. Table output was same for the repaired and as-built test specimens. Figure **3.10** a and Figure **3.10** b compare the cumulative energy ($\boldsymbol{E_{cum}}$) of the repaired and as-built SP1 along X- and Z-directions. Plotted values of $\boldsymbol{E_{cum}}$ corresponds to input in the test system, the shaking table and the test specimens. Ratio of maximum $\boldsymbol{E_{cum}}$ in X-direction to Z-direction was 2.5, compared to ratio of 2.0 obtained from the input signals. Figure **3.10** c and Figure **3.10** d show the pseudo acceleration ($\boldsymbol{S_a}$) spectra of the repaired and as-built SP1 in X- and Z-direction, assuming a damping of 2%. The measured and target $\boldsymbol{E_{cum}}$ for the test specimens SP2 was almost same with measured value being only 2% higher than the target maximum $\boldsymbol{E_{cum}}$in X-direction (Figure **3.11**a and Figure **3.11**b). The maximum value of $\boldsymbol{E_{cum}}$ in the Z-direction had a reduction of about 20% from the target value.

Table 3.2 Ground motions selected for testing of the repaired test specimens.

Test	Earthquake	Station	Scale Factor (%)	Components
EQ1	Northridge	Pacoima Dam	5	Horizontal and Vertical
EQ2	Northridge	Pacoima Dam	12.5	Horizontal and Vertical
EQ3	Northridge	Pacoima Dam	25	Horizontal and Vertical
EQ4	Northridge	Pacoima Dam	25	Horizontal Only
EQ5	Northridge	Pacoima Dam	50	Horizontal and Vertical
EQ6	Northridge	Pacoima Dam	50	Horizontal Only
EQ7	Northridge	Pacoima Dam	70	Horizontal and Vertical
EQ8	Northridge	Pacoima Dam	95	Horizontal and Vertical
EQ9	Northridge	Pacoima Dam	125	Horizontal and Vertical
EQ10	Northridge	Pacoima Dam	125	Horizontal Only
EQ11	Northridge	Pacoima Dam	125	Horizontal and Vertical

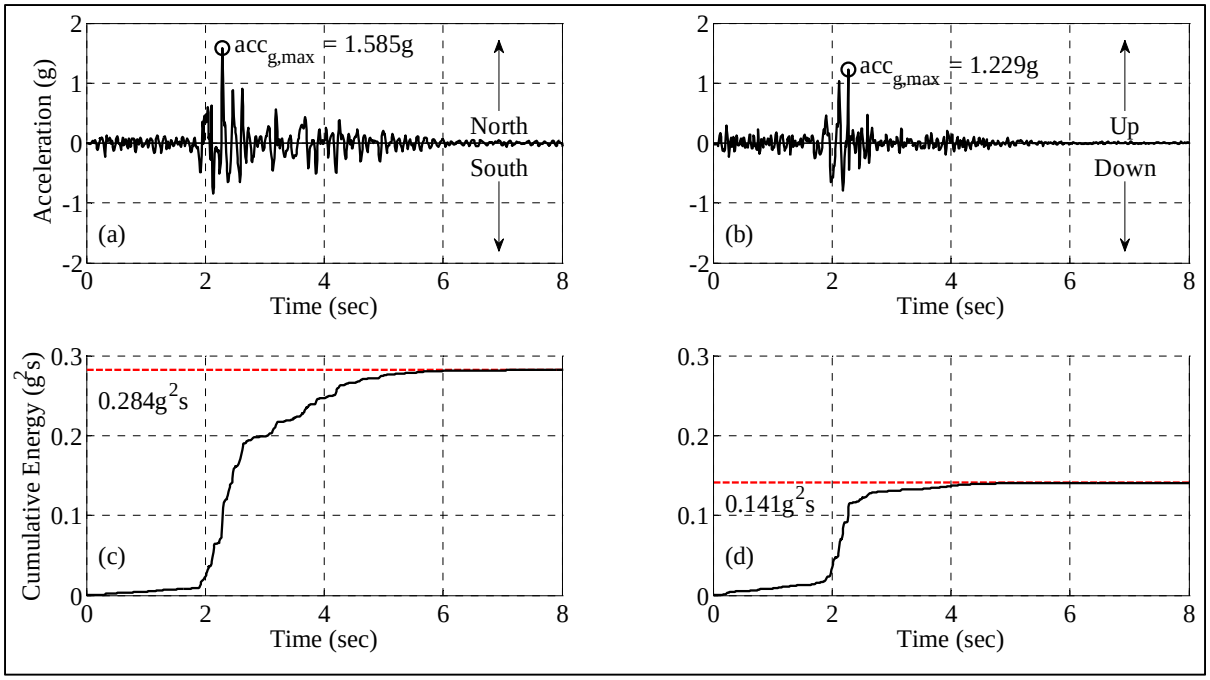

Figure 3.9 Full-scale Northridge earthquake: (a) unfiltered X-component; (b) unfiltered Z-component; (c) cumulative energy of X-component; (d) cumulative energy of Z-component.

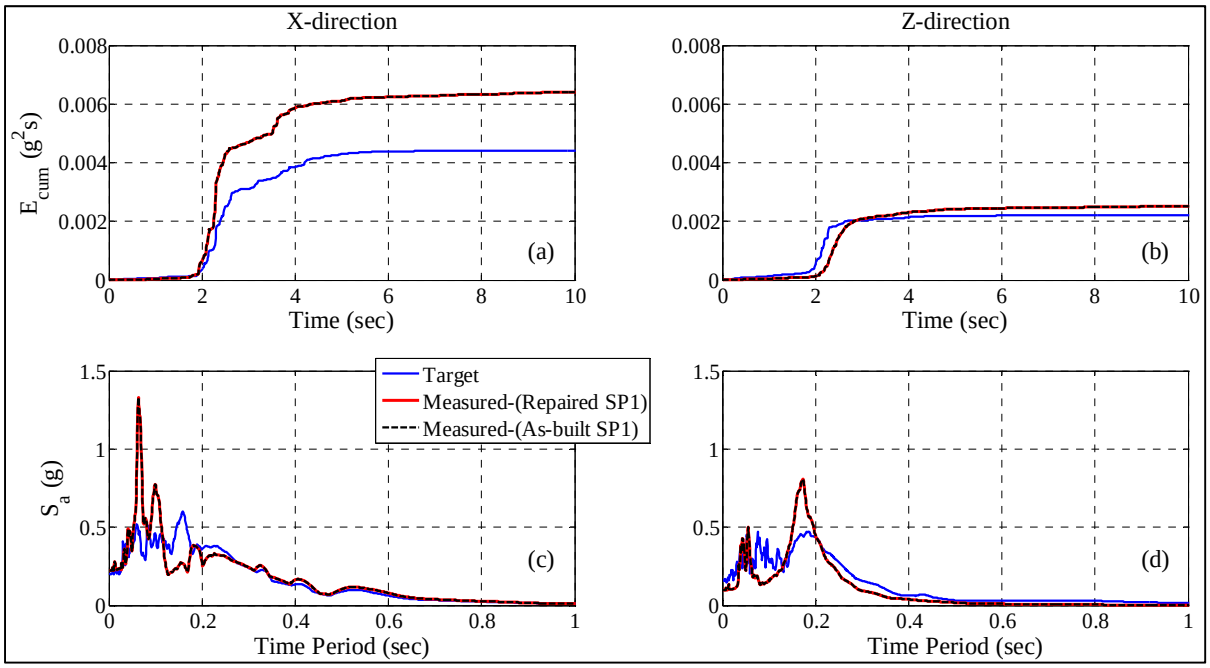

Figure 3.10 Comparison of the input and output acceleration parameters of the repaired and as-built SP1.

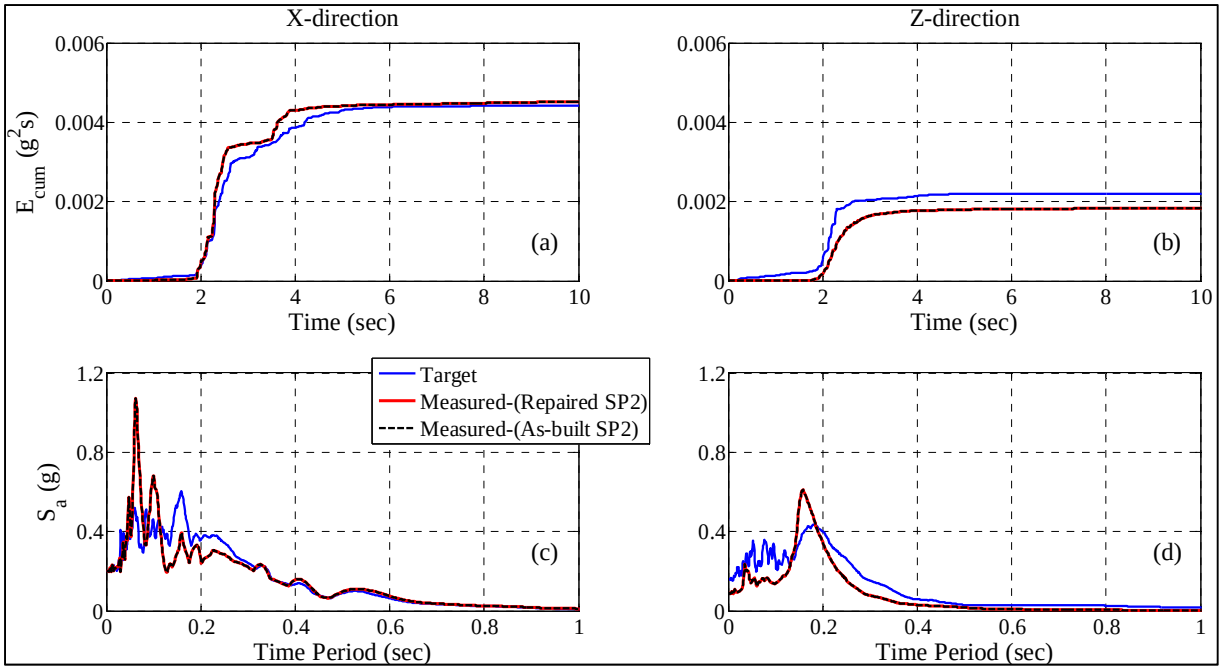

Figure 3.11 Comparison of the input and output acceleration parameters of the repaired and as-built SP2.

Chapter 4. Global Response

4.1 INTRODUCTION

This chapter details the global response of the repaired test specimens (SP1 and SP2) measured during the shaking table testing. Prior to the loading protocol discussed in Section 3.3, pull back and free vibration tests were conducted to determine the dynamic properties of the repaired test specimens. These tests and their results are discussed in Section 4.2 and Section 4.3. The main directly measured response quantities discussed in this chapter are the accelerations measured using accelerometers (Section 4.4), the shear and axial forces measured using load cells (Section 4.5), and the horizontal and vertical displacements measured using wire potentiometers (Section 4.6 and 4.7, respectively).

The derived response quantities, namely bending moments at the base and top of the column are discussed in Section 4.8. The input energy and dissipated hysteric energy of the test specimens are discussed in Section 4.9 along with the horizontal force-deformation response. Variation of these response parameters with the increase in the base excitation intensity provided important information regarding the strength and damage accumulation.

The height of the FRP jacket for the repaired test specimens that had a column height of 70 in (1778.0 mm) was 69.5 in (1765.3 mm) with 0.25 in (6.35 mm) gap at the intersection of the column with footing at the base, and a similar gap with the superstructure mass (concrete slab + steel beam configuration + concrete mass block) at the top. The FRP jackets remained intact during the entire loading protocol and no visual damage of the confined core was observed. The estimation of the possible damage was performed by comparing the global response parameter measured for the as-built test specimens with those obtained from the repaired counterparts.

4.2 PULLBACK TESTS

The lateral stiffness of the test specimens was computed as the ratio of the measured maximum force resisted during the dynamic test to the corresponding displacement at the column top. The lateral stiffness of the test specimens reduced during the loading protocol due to damage accumulation and cracking in the column section as they approached their shear capacities. In order to estimate the initial lateral stiffness of the repaired test specimens prior to the application of the dynamic loading protocol, four pullback tests were conducted. The lateral force was computed as the sum of the reaction components measured by the four load cells installed at the base of the test specimens in the direction of the applied loading. Displacement at the top of the test specimen was measured using the wire potentiometers and the linear direct current differential transformers (DCDTs). The absolute and relative displacements of the test specimens were defined as the displacement of the column top with respect to the stationary shaking table in the static configuration pullback test and with respect to the footing, respectively. Absolute and relative stiffness values of the test specimens were computed as the ratio of the maximum resisted lateral force to the corresponding absolute and relative top displacement, respectively.

Table ***4.1*** lists the measured absolute and relative stiffness of the test specimens. Due to axial flexibility of the load cells, the values of the relative and absolute stiffness of the test specimens differed. It is to be noted that the values of the average absolute and relative stiffness of the as-built SP1 were 119 kips/in (13.4 kN/m) and 148.7 kips/in (16.8 kN/m), respectively and those of the as-built SP2 were 82.5 kips/in (9.3 kN/m) and 102.1 kips/in (11.5 kN/m), respectively. Difference in the values of absolute and relative stiffness was due to the axial flexibility of the load cells [34]. Moreover, the average absolute and relative stiffness values of the repaired SP1 (Table ***4.1***) were respectively 52% and 48% of the as-built SP1. On the other hand, the average absolute and relative lateral stiffness values of the repaired SP2 (Table ***4.1***) were 73% and 69.5% of the as-built SP2, respectively.

Table 4.1 Stiffness of the repaired test specimens.

Pullback Test	Repaired SP1		Repaired SP2	
	Absolute Stiffness, kips/in (kN/m)	**Relative Stiffness, kips/in (kN/m)**	**Absolute Stiffness, kips/in (kN/m)**	**Relative Stiffness, kips/in (kN/m)**
Test 1	62.4 (7.3)	69.2 (7.8)	60.1 (6.9)	72.2 (8.2)
Test 2	60.2 (6.8)	73.0 (8.2)	57.4 (6.6)	69.4 (7.8)
Test 3	64.6 (7.3)	74.8 (8.4)	62.1 (7.0)	70.2 (7.9)
Test 4	62.1 (7.1)	70.3 (7.9)	60.3 (6.8)	72.3 (8.2)
Average	62.2 (7.0)	71.8 (8.1)	60.2 (6.8)	71.0 (8.0)

4.3 FREE VIBRATION TESTS

Free vibration tests were conducted to estimate the time periods and damping properties of the test specimens. The lateral time period of the repaired SP1 and SP2 was 0.53 sec and 0.51 sec, respectively. The periods of other modes of vibration were determined as well and summarized in Error! Reference source not found.**.** Figure 4.1 shows the relative top displacement histories of the test specimens measured with respect to the footing during a free vibration test. The rate of reduction of displacement history peaks was used to compute the damping ratio (ζ) of the test specimens as follows,

$$\zeta = \frac{A}{\sqrt{1 + A^2}} \tag{4.1}$$

$$A = \frac{1}{2\pi j} \times \ln\left(\frac{u_1}{u_{j+1}}\right) \tag{4.2}$$

where u_1 is the peak displacement measured during the first cycle and u_{j+1} is the peak displacement measured after j cycles. Table ***4.2*** lists the average damping ratio computed during the free vibration tests. The damping ratio of both test specimens was between 1.9% and 2.1% during the free vibration tests. Figure 4.1(a) and (b) show the average exponential decay curve (dashed line) fitted on the displacement peaks of the repaired test specimens measured towards the North and the South sides, based on the computed damping. The damping ratio that was computed based on the top displacement history response towards the North and South sides of the repaired SP2 was not exactly the same. This is attributed to the higher damage on the South side of the as-built SP2 than North side prior to repair. Figure 4.1(c) and (d) compare the measured and theoretical top displacement response of the test specimens. Theoretical displacement of the cantilever column was computed as follows [16],

$$u(t) = e^{-\zeta\omega_n t}\left(u(0) \times \cos(\omega_D t) + \frac{\dot{u}(0) + \zeta\omega_n u(0)}{\omega_D} \times \sin(\omega_D t)\right) \tag{4.3}$$

$$\omega_D = \omega_n\sqrt{1 - \zeta^2} \tag{4.4}$$

$$\omega_n = \frac{2\pi}{T_n} \tag{4.5}$$

where ω_n is the natural frequency of the test specimens, T_n natural time period of the test specimens, ω_D is the natural frequency of damped vibrations, $u(0)$ and $\dot{u}(0)$ are initial displacement and velocity of the test specimen at time zero. Initial velocity ($\dot{u}(0)$) of the test specimens was zero during the free vibration tests. Using the Fast Fourier Transform (FFT) amplitudes and the half-power bandwidth method [16], damping ratio values of 3.0~3.1% and 2.5~3.0% were computed for the repaired SP1 and SP2, respectively.

As previously mentioned, Table ***4.2*** lists the different modes of vibration time periods of the test specimens measured during the free vibration tests. The vertical period of the test specimens during the free vibration tests was obtained from the vertical acceleration spectra, which is an alternative way to the FFT to find the vibration periods. Figure 4.2 shows the vertical acceleration spectra obtained from the accelerometer data measured at the base of the repaired test specimens, using 3% damping ratio. Two prominent peaks were observed in the plotted

spectra (peak A and peak B), which correspond to the vertical and rotational vibration period of the test specimens, respectively. The rotational period of the repaired SP2 (0.086 sec) was higher than the rotational period of the repaired SP1 (0.084 sec). The vertical period of both repaired specimens was 0.032 sec.

Table 4.2 Free vibration test results.

Test Specimen	Test	Damping Ratio (%)	Lateral Time Period (sec)	Vertical Time Period (sec)	Rotational Time Period (sec)
Repaired SP1	1	2.01	0.53	0.032	0.084
	2	1.99	0.53	0.032	0.084
	3	2.03	0.53	0.032	0.084
Repaired SP2	1	2.05	0.51	0.032	0.086
	2	2.02	0.51	0.032	0.086
	3	1.98	0.52	0.032	0.086

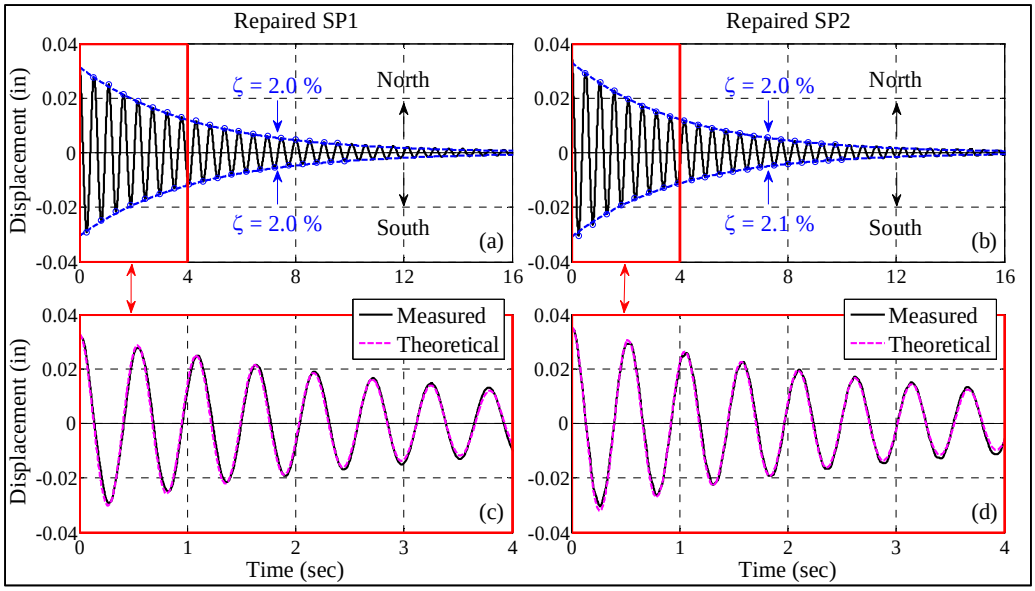

Figure 4.1 Displacement histories measured at the column's top during the first free vibration test.

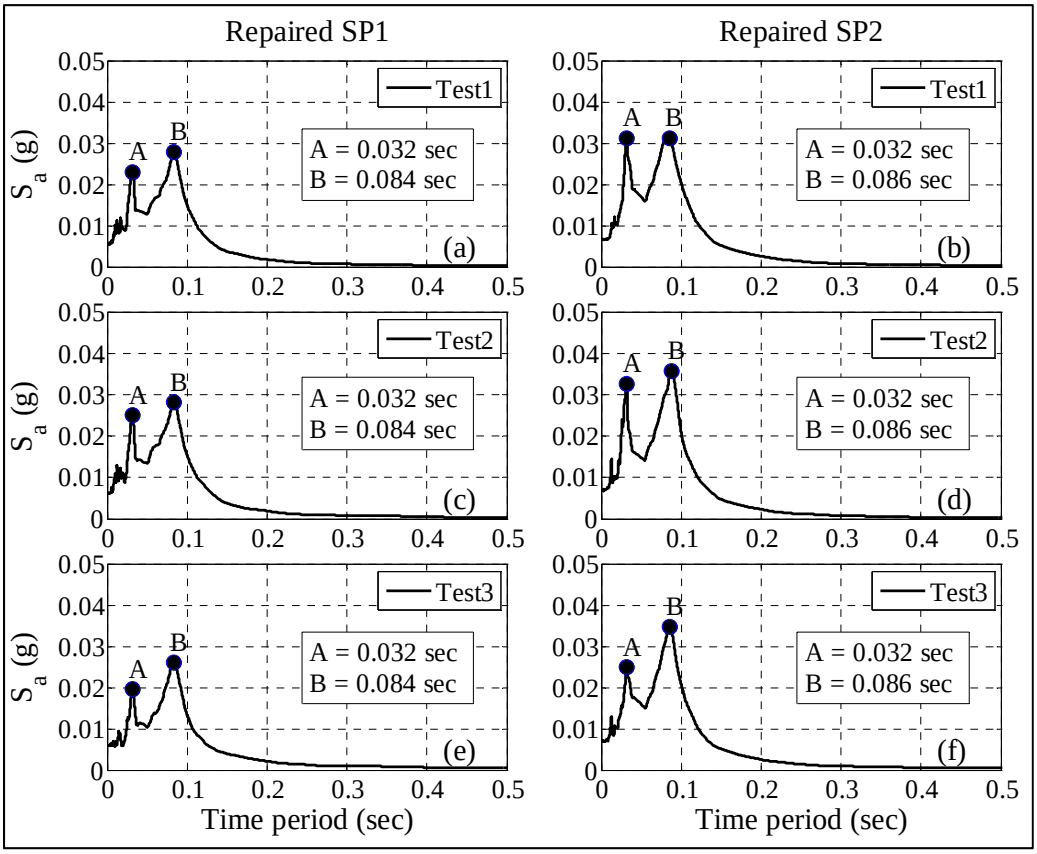

Figure 4.2 Vertical acceleration response spectra obtained during free vibration tests.

4.4 HORIZONTAL AND VERTICAL ACCELERATIONS RESPONSE

The horizontal and vertical acceleration responses of the repaired specimens were measured during the shaking table tests using the installed accelerometers. Total of nine 3D accelerometers were attached to the steel plate, the mass block, and on the top of the concrete slab to measure accelerations in X-, Y- and Z- directions. The average acceleration in the X-, Y- or Z-direction was computed as the arithmetic average of the accelerometers data measured in that particular direction. Moreover, nine 1D accelerometers were installed on the North face of the test specimens to measure the vertical accelerations along the column height. The detailed locations and orientation of accelerometers installed on the test specimens were previously discussed in Section 3.2.2. This section discusses the average accelerations measured in X- and Z- directions, whereas the accelerations measured in the Y-direction were significantly lower and not of interest. The strong component of the horizontal acceleration was directed towards the North side of the test specimens and the strong component of the vertical acceleration was in upward direction. For the accelerations sign convention, the positive sign was assigned to the acceleration data measured in the direction of the strong component. Thus, the horizontal accelerations towards the South and the vertical accelerations directed downwards were assigned negative signs (Appendix B).

Figure 4.3 and Figure 4.4 show the input and output acceleration time histories measured at the base of the repaired test specimens for EQ5 through EQ11. Due to the limitations of the shaking table, the input acceleration signal was not exactly achieved. However, the input and the measured acceleration data in the horizontal direction had a closer match than in the vertical direction. This is due to the higher stiffness of the shaking table in the horizontal direction (in-plane) than the vertical direction, and due to the interaction of the test specimens with the shaking table. During the 25%-, 50%- and 125%-scaled ground motions without the vertical ground motion component, the vertical acceleration component measured at the steel plate level was not zero. Relatively small accelerations were still obtained in the vertical direction because the vertical actuators had to resist the force generated by the interaction of the shaking table and the test specimens (e.g. overturning moments) during the horizontal ground motion testing while maintaining the vertical displacement to zero.

Figure 4.5 and Figure 4.6 compare the maximum output accelerations measured at the base of the repaired and as-built test specimens. The maximum magnitude of horizontal acceleration measured at the base of the repaired SP1 and SP2 during the entire loading protocol was 2.15g and 2.17g, respectively, which was measured during EQ10 (Figure 4.5a, b). The maximum magnitude of the vertical acceleration measured at the base of test specimens showed no particular trend (Figure 4.6). However, the magnitude of maximum vertical acceleration at the base of the repaired SP1 and SP2 during the entire loading protocol was 1.38g, which was measured during EQ9 (Figure 4.6). This is compared to maximum vertical accelerations of magnitude of 1.56g and 1.62g, respectively, at the base of the as-built SP1 and SP2, where the maximum magnitude was measured during EQ11. The acceleration response of the repaired specimens was closer to each other in terms of the magnitude and frequency of the output signal (Figure 4.3 and Figure 4.4).

Figure 4.7 and Figure 4.8 show the average X- and Z-accelerations at different heights of the specimens as obtained from the 3D accelerometers installed at the base level (steel plate accelerometers), column top (mass block level accelerometer) and superstructure level (concrete

block accelerometers). The acceleration response of the two repaired test specimens was almost the same. Figure 4.9 compares the maximum magnitude of X-accelerations measured at the three levels. The X-acceleration response varied along the height of the test specimens. The magnitude and frequency of the accelerations measured at the steel plate level were higher than those measured at the mass block and concrete slab level during the entire loading protocol. The difference in magnitude and frequency of accelerations measured at base and top level increased as the intensity of ground motion increased. This is attributed to the relatively lower lateral stiffness, in comparison to the axial stiffness, of the test specimens and the impact of the damage accumulation during the loading protocol. At the two top levels, the magnitude of X-acceleration measured at mass block level was higher than the average X-acceleration measured at the top of concrete slab (Figure 4.9). This is attributed to the interaction of the rotational and translational degrees of freedom at the top of the cantilever column. This was verified by comparing the measured X-acceleration with the derived X-acceleration data that considered the effect of the rotation of superstructure mass on the top of the concrete slab. Figure 4.10 shows the configuration of the test specimens under pure rotation of the superstructure mass. Rotation $\theta(t)$ of the superstructure mass at any time instant was computed from the data measured by the vertical wire potentiometers attached to the North and South ends of the concrete slab as follows,

$$\theta(t) = \frac{AA' - BB'}{D_{AB}} \tag{4.6}$$

where AA' and BB' are the vertical displacements measured using two vertical potentiometers installed on the steel plate with target points (A and B) on the concrete slab, and D_{AB} is the horizontal distance between A and B (Figure 4.10). The derived X-acceleration $a_d(t)$ was computed as follows,

$$a_d(t) = a_c(t) + \frac{d^2\theta}{dt^2} \times H_{CT} \tag{4.7}$$

where $a_c(t)$ is the acceleration measured at the mass block level using the 3D accelerometer, H_{CT} is the distance between the accelerometers installed at the concrete block level and the mass block level (Figure 9), and $\frac{d^2\theta}{dt^2}$ is the rotational acceleration of the superstructure mass obtained by double differentiating the rotation $\theta(t)$ of the superstructure mass. Figure 4.11 compares the measured average X-acceleration and the derived X-acceleration $a_d(t)$ time histories of the two repaired specimens at the concrete block level during EQ9 and EQ10.

The difference in the vertical acceleration ($a_z(t)$) response measured at the three instrumented levels was relatively low compared to the horizontal acceleration response due to the relatively higher stiffness of the repaired test specimens in the axial direction. However, the vertical accelerations measured at the concrete slab level were slightly higher than the vertical accelerations measured at the steel plate (base) level. This is attributed to the tensile forces measured in the test specimens during the 125%-scaled ground motions, which caused cracking of the core concrete. The difference in the maximum vertical acceleration ($a_z(t)$) measured at the steel plate (base) and the concrete slab level was higher in the repaired SP2 than repaired SP1. The repair of both tested as-built specimens focused on improving the confinement effect of the column sections. Thus, under tensile loads, the axial stiffness of the repaired specimens was affected by the amount of the original damage in the as-built specimens prior to the repair using

FRP jackets. Accordingly, the higher original damage in the as-built SP2 than that of the as-built SP1 led to the difference in the observed accelerations in the vertical direction.

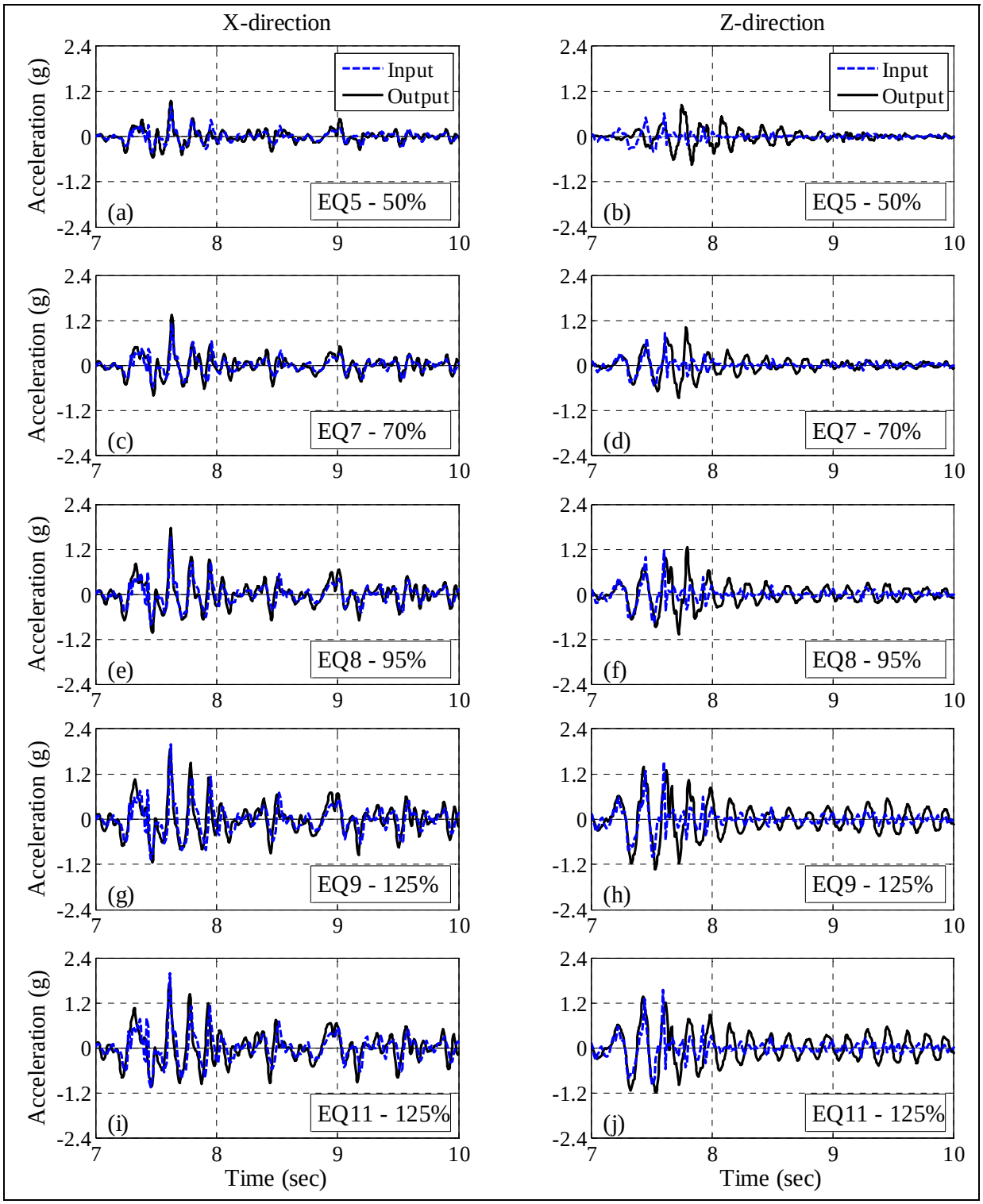

Figure 4.3 Acceleration time histories of repaired SP1.

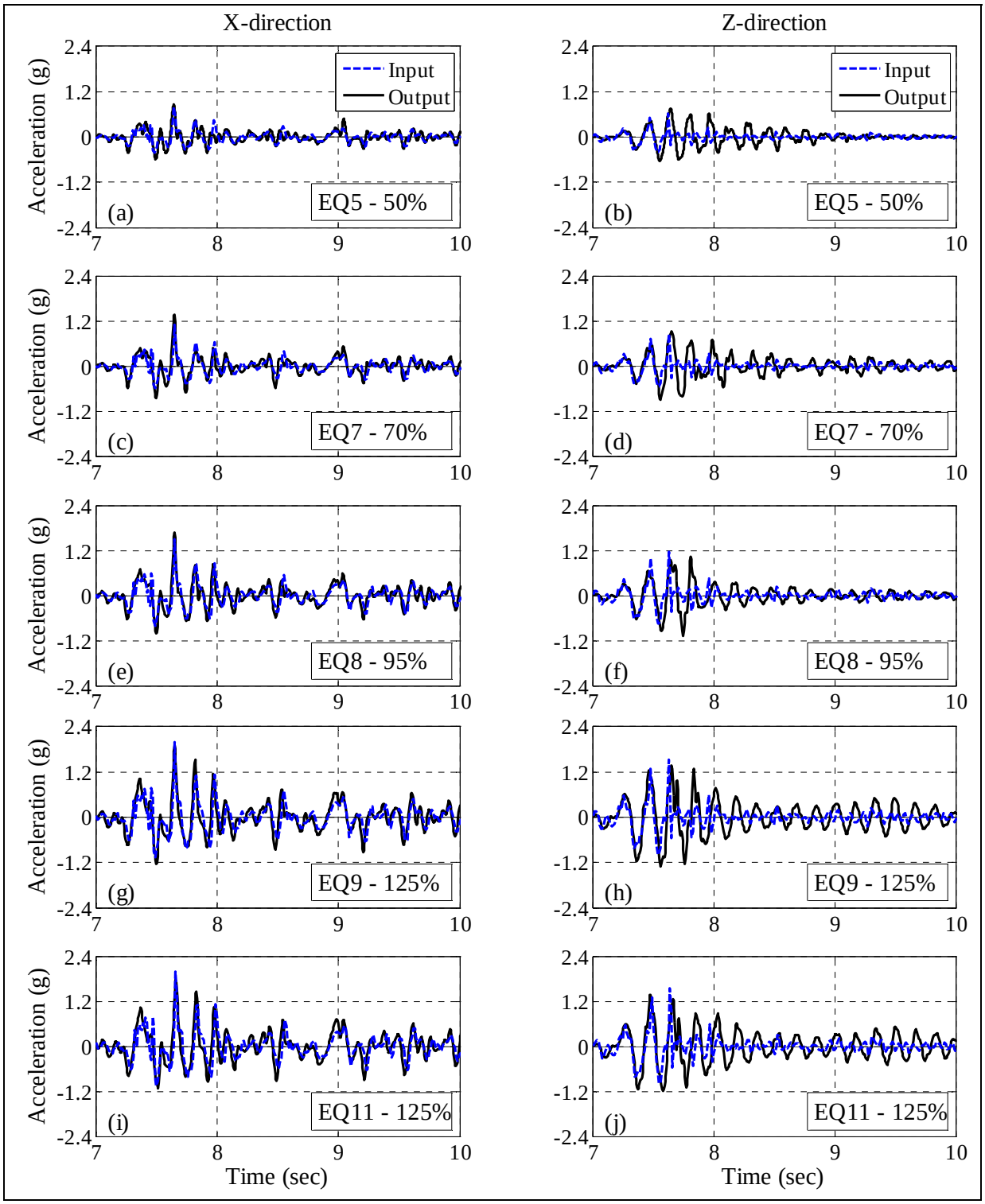

Figure 4.4 Acceleration time histories of repaired SP2.

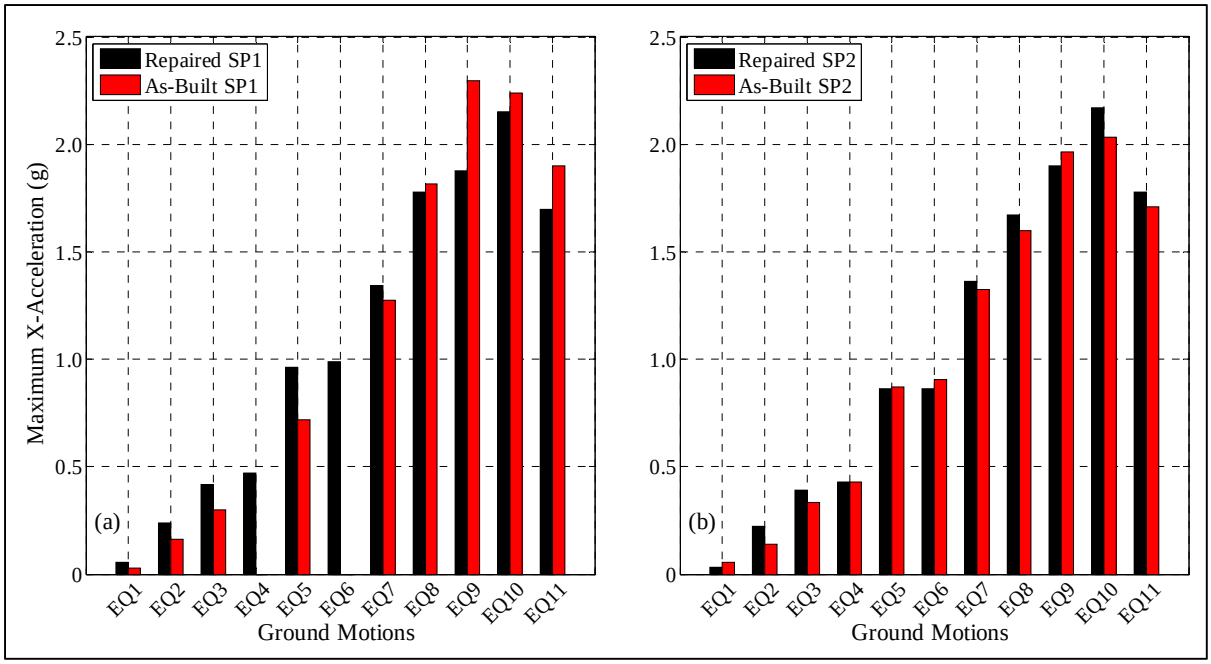

Figure 4.5 Maximum X-acceleration measured at the base (steel plate level) of test specimens.

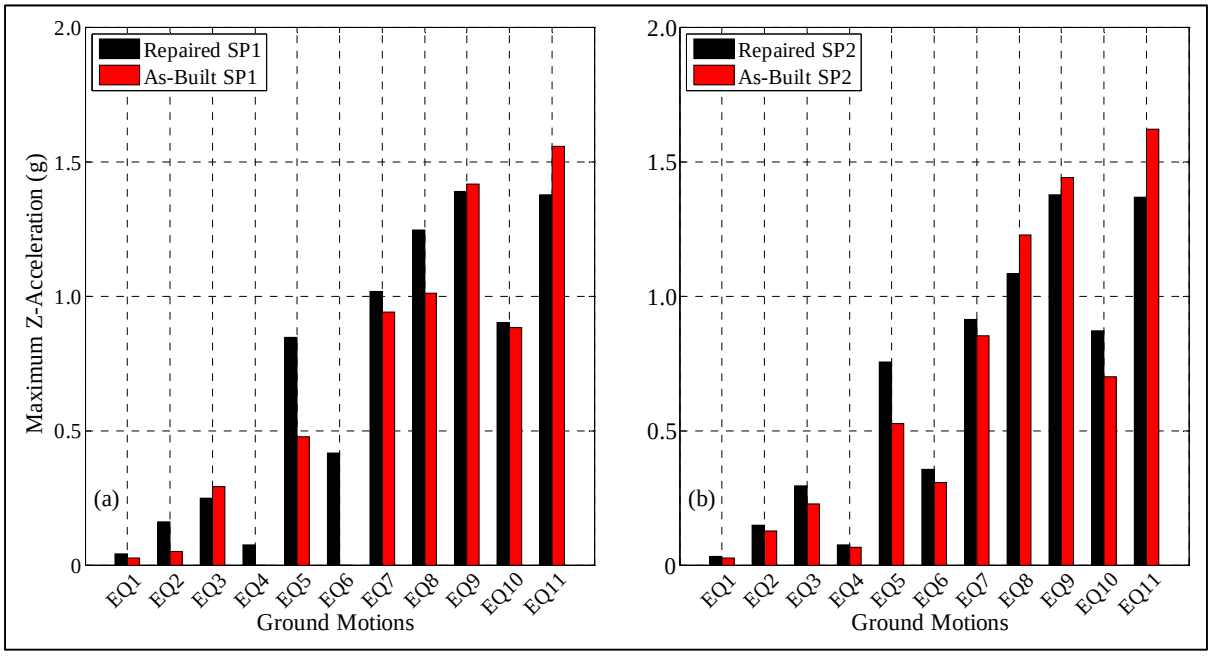

Figure 4.6 Maximum Z-acceleration measured at the base (steel plate level) of test specimens.

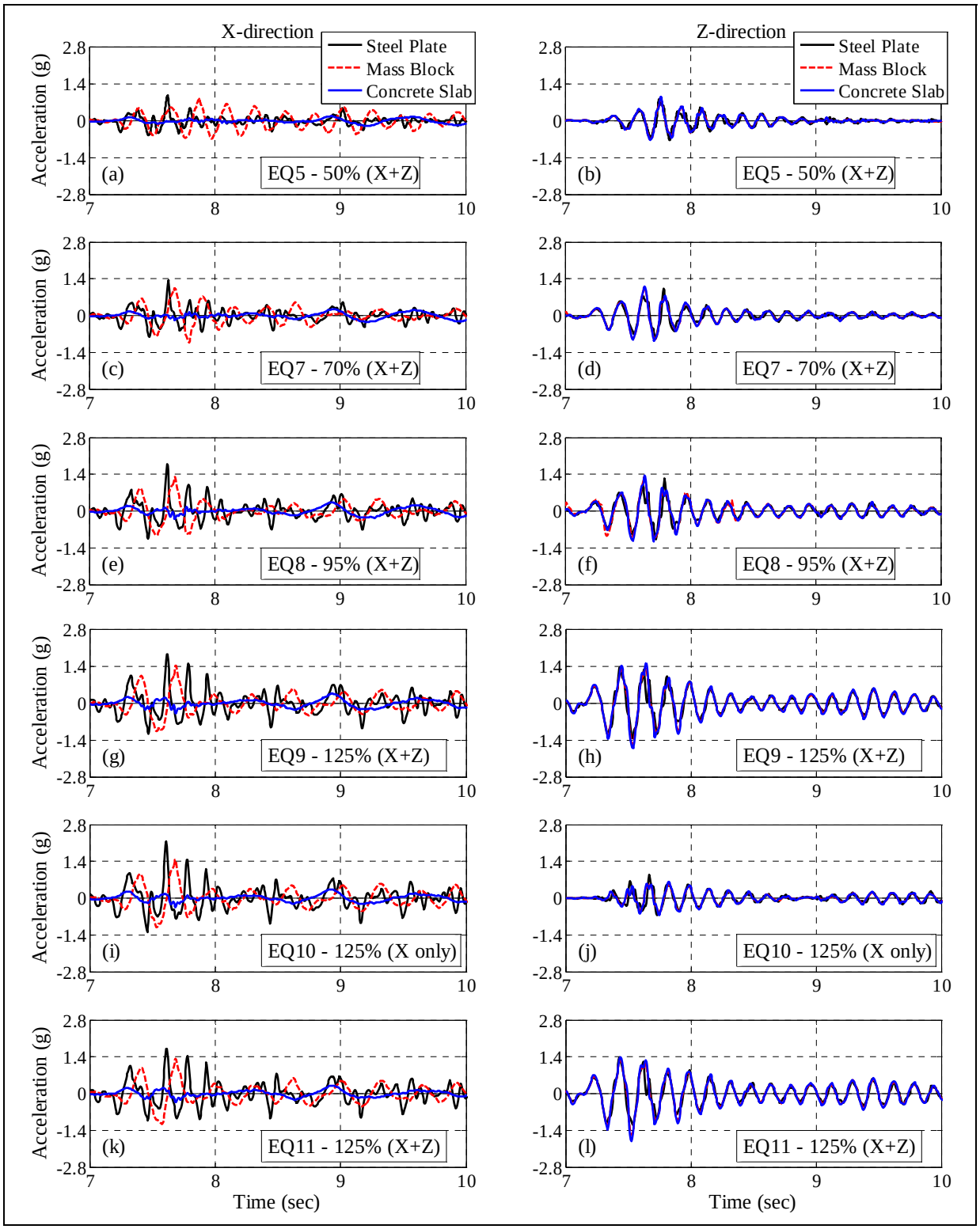

Figure 4.7 Acceleration time histories measured at base, column top and superstructure top level of repaired SP1.

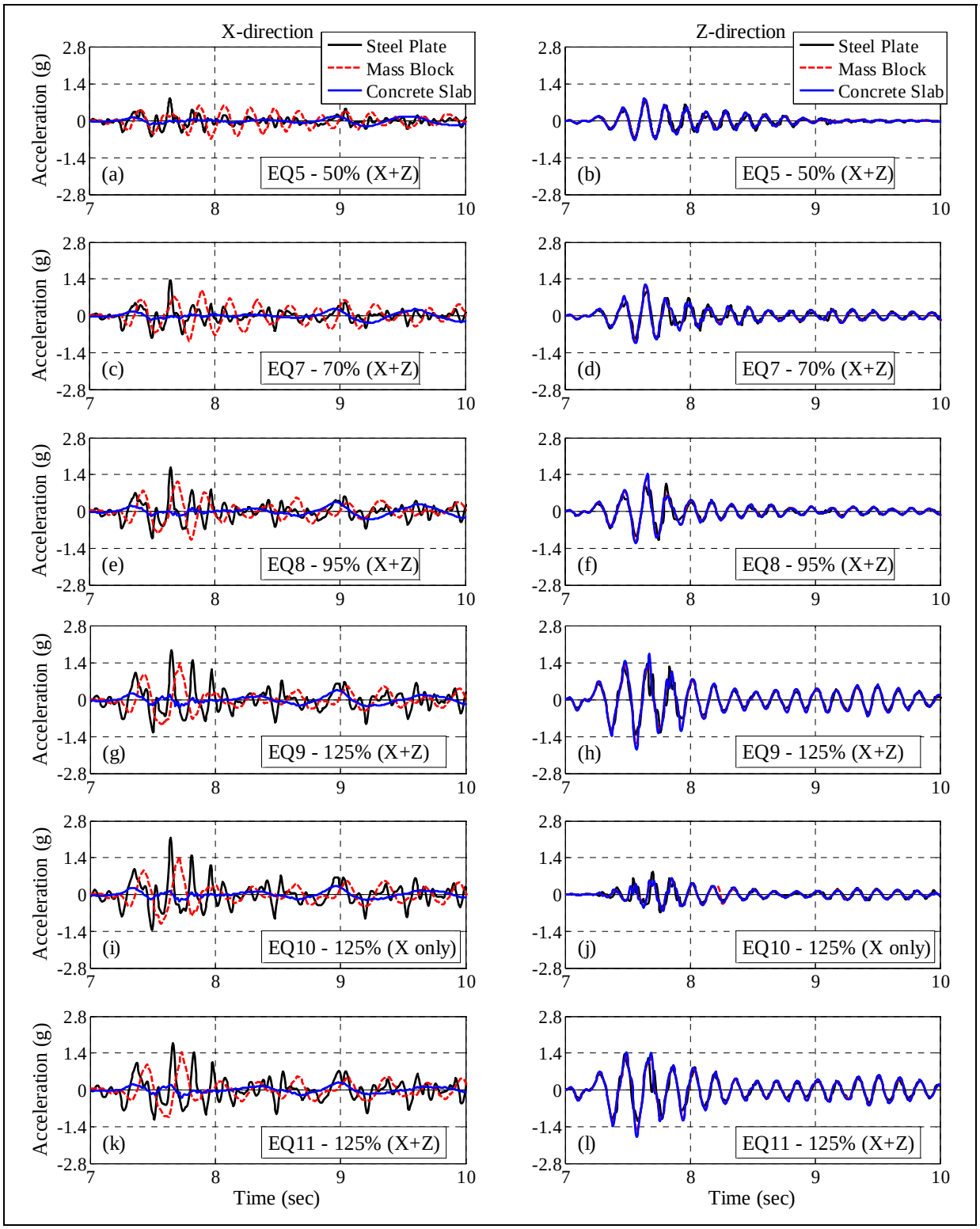

Figure 4.8 Acceleration time histories measured at base, column top and superstructure top level of repaired SP2.

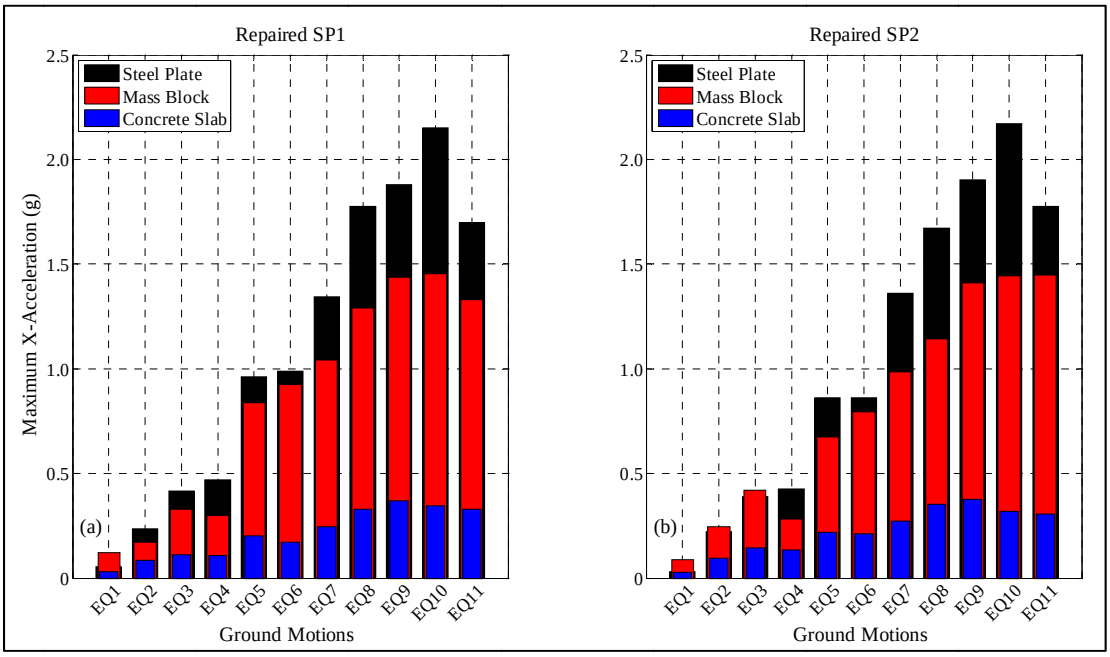

Figure 4.9 Maximum X-acceleration measured at the base, column top and top of the superstructure mass of repaired test specimens.

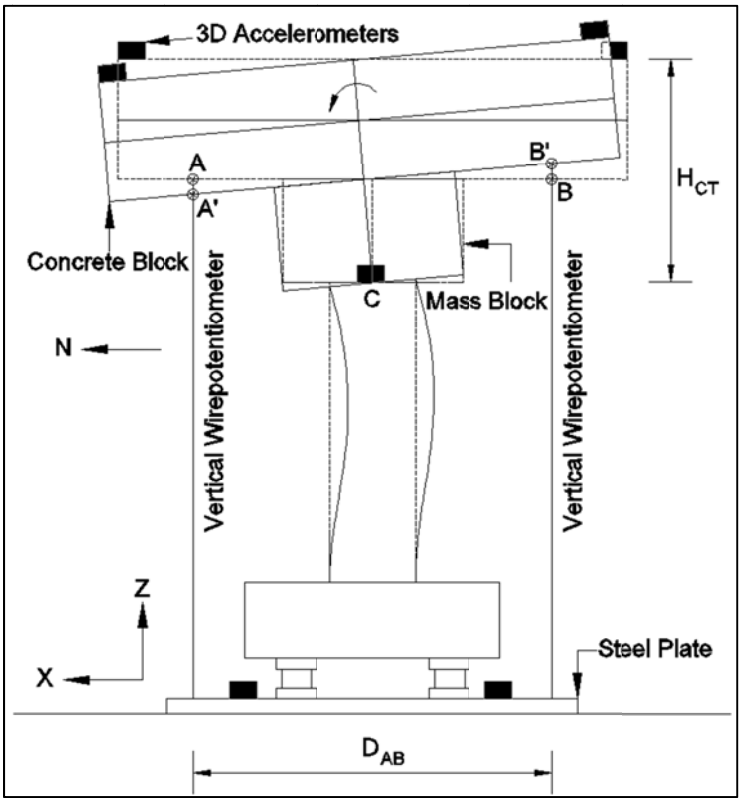

Figure 4.10 Rotation of the superstructure mass.

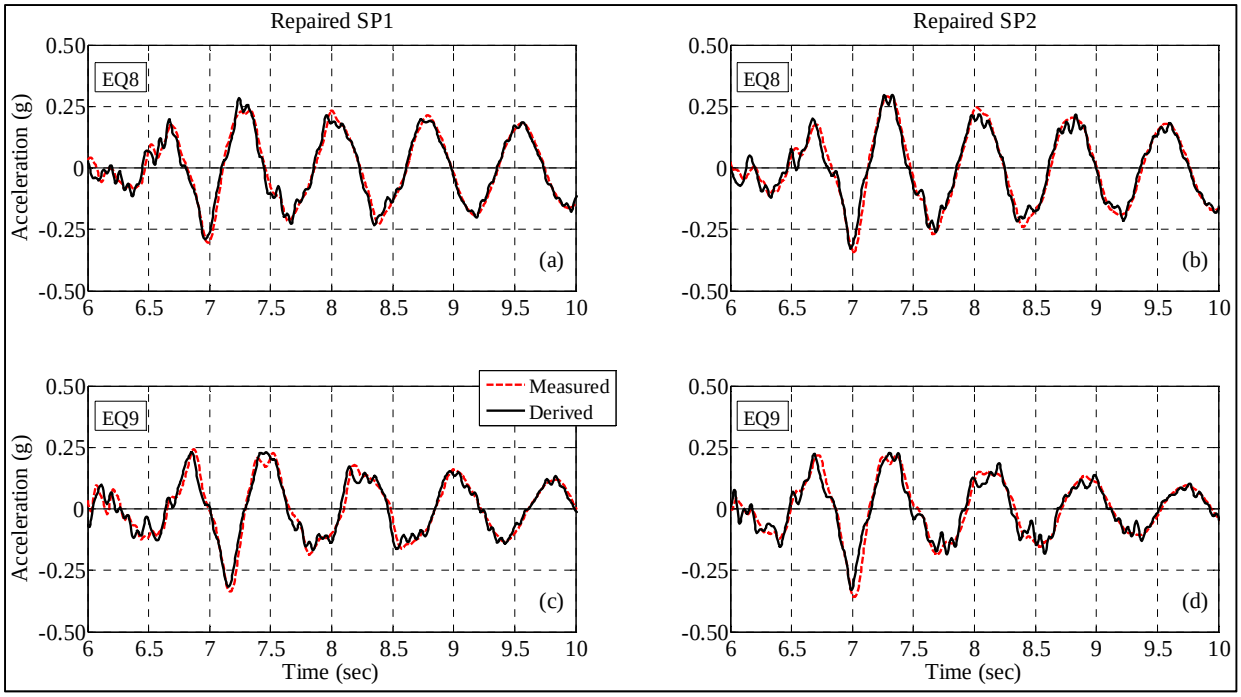

Figure 4.11 Comparison of the measured and derived acceleration history at the top of concrete slabs.

4.5 SHEAR AND AXIAL FORCES RESPONSE

The shear and axial forces measured at the base of the test specimens were computed by summing the X-, Y- and Z- reactions components measured by the four load cells. The applied ground motion components were in the X- and Z-directions only. Thus, the shear force response obtained in the Y-direction was significantly lower and is not discussed in this section. The dead gravity load of the test specimens measured before the seismic testing was about 95 kips (422.6 kN). The design shear capacity of the repaired specimens SP1 and SP2 was about 90 kips (400.3 kN) and 80 kips (355.9 kN), respectively. It is to be noted that for the sign convention, the shear forces measured towards the North and the axial loads under compression were assigned positive signs (Appendix B).

Figure 4.12 and Figure 4.13 compared the axial load and the shear force in the X-direction time histories of the repaired and the as-built test specimens SP1 and SP2, respectively, as measured during the 50%-, 70%- and 95%-scaled ground motions. It is noted from the figures that the axial load response of the repaired and the as-built SP1 was almost same, but the shear force response was different in terms of the magnitude and frequency. The rate of reduction of the shear force peaks, measured after the maximum shear force peak, was higher in the repaired SP1 than the as-built SP1. This difference in the shear force response of the repaired SP1 and the as-built SP1 reduced as the intensity of ground motion increased from 50% to 95%, due to the damage accumulation. Moreover, the axial load and shear force response of the repaired and as-built SP2 was almost similar during the 50%-, 70%- and 95%-scaled ground motions.

In addition, Figure 4.14 and Figure 4.15 compare the axial and shear force response of the repaired and as-built test specimens SP1 and SP2, respectively, during the 125%-scaled ground motions. Similar to the as-built test specimens, the repaired test specimens experienced tension during EQ9 and EQ11. However, the measured magnitude of the maximum tensile forces in the repaired test specimens was lower than the tensile forces measured in their as-built counterparts. Two tensile peaks were observed in the repaired test specimens during EQ9 and EQ11, and identified using dotted lines in Figure 4.14 and Figure 4.15. It is noted that the magnitude of the second tensile peak was higher than the first peak. Similarly, two significant positive shear peaks were observed at the base of both repaired test specimens during the 125%-scaled tests. The first positive shear peak was measured after the first tensile peak and the second positive shear peak, which was also the absolute maximum shear force, was measured after the second tensile force peak.

During EQ9, the magnitudes of the tensile force peaks measured in the repaired SP1 were 24.6 kips (109.2 kN) and 47.7 kips (212.2 kN), and the magnitudes of the tensile peaks measured in the repaired SP2 were 27.3 kips (121.7 kN) and 58.01 kips (258 kN). In the repaired SP1 and SP2, the magnitudes of the first positive shear peaks were almost the same (69.9 kips (310.9 kN)) followed by the second positive shear force peaks of magnitude 100.9 kips (448.9 kN) and 94.71 kips (421.2 kN), respectively. The magnitude of the first and the second tensile peak in the repaired SP2 was about 22% and 21% higher than the repaired SP1, respectively. However, the second shear peak of the repaired SP2 was only 6% less than the repaired SP1. Thus, the repaired SP2 was able to resist comparable shear forces to the repaired SP1 despite the higher magnitude of the tensile forces and the consequent relative damage to the concrete core. This is attributed to the higher shear strength contribution of the CFRP jacket than the GFRP jacket to the shear capacity of the repaired test specimens. The maximum magnitude of the shear force measured at

the base of repaired SP1 was almost the same during EQ9 and EQ10. On the other hand, the maximum shear resisted by the repaired SP2 increased by about 4.0 kips (17.8 kN) from EQ9 to EQ10.

During EQ11, the magnitude of the first and the second tensile peaks in the repaired SP1 was 25.24 kips (112.3 kN) and 51.92 kips (231.0 kN), respectively, which is about 2.6% and 8.9% higher than those measured during EQ9. Moreover, the magnitude of the first and the second positive shear force peaks measured at the base of the repaired SP1 were 67.12 kips (298.6 kN) and 96.21 kips (428 kN), respectively, which is about 4% and 4.7% less than those measured during EQ9. Similarly, for the repaired SP2, the magnitude of the first and second tensile peak were respectively about 25.9 kips (115.2 kN) and 49.3 kips (219.3 kN) during EQ11, which is about 5% and 15% less than the first and the second tensile peaks measured during EQ9. The maximum magnitude of the first and the second shear peak in the repaired SP2 were 67.3 kips (299.5 kN) and 90.23 kips (401.4 kN), respectively, i.e. a reduction of about 3% and 6% was observed compared to the first and the second shear measured during the repaired SP2 EQ9.

Next, the observed peak values during the repaired specimens' tests are compared to the as-built specimens' tests. For the as-built SP1 tests, the observed first and second positive shear peak were of magnitude 67.12 kips (298.6 kN) and 91.4 kips (406.5 kN), respectively during EQ9. It is noted from Figure 4.14 that the second shear peak, which was also the maximum shear force, in the as-built SP1 EQ9 test occurred before the two tensile force peaks. The tensile force peaks were 20.34 kips (90.5 kN) and 65.82 kips (292.8 kN) and represented by dotted line in Figure 4.14. Similar to the repaired SP1, the shear force measured in the as-built SP1 remained almost the same during EQ9 and EQ10. During EQ11, two tensile peaks of magnitude 17.66 kips (78.6 kN) and 57.86 kips (257.4 kN) were measured in the as-built SP1. The magnitude of the first and the second shear peak in the as-built SP1 were 70.89 kips and 80.12 kips (356.4 kN). However, the maximum shear force of magnitude 88.3 kips (392.8 kN) was measured towards the South end, i.e. had a negative sign. From EQ9 to EQ11, the magnitude of both of the maximum tensile force and the positive shear force peak of the as-built SP1 was reduced by almost 12%.

For the as-built SP2 during EQ9, the two tensile peaks of magnitude 18.41 kips (81.9 kN) and 61.55 kips (273.8 kN) were followed by the maximum shear force peak, which had a magnitude of 77.39 kips (344.2 kN). From EQ9 to EQ10, the maximum shear force measured in the as-built SP2 was increased by 4.5%. Similar to the as-built SP1 during EQ11, the maximum shear in the as-built SP2 test (77.24 kips (343.6 kN)) was measured towards the South side (negative). The maximum tensile force measured in the as-built SP2 EQ11 test was 63.11 kips (280.7 kN), i.e. about 2.5% higher than the maximum tensile force measured during EQ9.

The impact and effectiveness of the FRP jacket repair of the damaged as-built test specimens was more prominent during the 125%-scaled ground motions. The FRP jackets and repair work of the as-built test specimens aimed at improving the shear strength capacity of the column sections without any significant increase in the axial strength. Thus, the impact of the axial tensile loads on the concrete core of the repaired test specimens was a continuation from the final state that was reached during the testing of the as-built test specimens. Moreover, the repaired test specimens were successfully able to resist higher shear force than their as-built counterparts without any damage to the FRP jackets.

Another way of comparing the as-built and repaired test results is shown in Figure 4.16 and Figure 4.17. These two figures compare the maximum axial load and shear force measured at the base of both of the repaired and as-built test specimens for all loading cases. The maximum axial loads measured at the base of the repaired SP1 and SP2 followed a similar trend to the increased intensity of the input ground motion (Figure 4.16). Figure 4.17 shows that the maximum shear forces resisted by the repaired test specimens were higher than the maximum shear forces resisted by their as-built counterparts as previously mentioned. From EQ1 to EQ4, the maximum magnitude of the shear and axial forces measured at the base of repaired SP1 and SP2 was very close with only a difference of ±5 kips. As the intensity of the ground motion increased from 25% to 50%, the maximum axial load increased by 47% and 39% (Figure 4.16), while the shear force measured at the base increased by a factor of 3.0 and 2.1 for the repaired SP1 and SP2, respectively as shown in Figure 4.17. In the absence of the vertical component of the 50%-scaled ground motion, the maximum shear measured in the repaired SP1 and SP2 increased by 10% and 13%, respectively, while the maximum axial load was reduced by 54%.

The maximum shear force resisted by the repaired SP1 was 11% higher than the as-built SP1 during EQ9 despite the occurrence of the two tensile peaks in the repaired SP1 prior to reaching the maximum shear. During EQ11, the maximum tensile force measured in the repaired SP1 increased by 9%, and the maximum shear force was reduced by 5% compared to EQ9. The maximum tensile force and maximum shear measured at the base of as-built SP1 reduced by 12% and 13%, respectively compared to EQ9. This suggested that the vertical ground excitations had higher influence on the shear resisted by the as-built SP1 than the repaired SP1. This is attributed to the contribution of the GFRP jacket in enhancing the shear strength of the repaired SP1 irrespective of the damage that occurred in the core concrete as a result of the tensile forces.

On the other hand, for SP2, the maximum axial load and shear force measured at the base of the repaired SP2 increased by 12% and 45%, respectively, from EQ5 to EQ7. During EQ7, the magnitude of the maximum shear force measured at the base of the repaired SP2 and as-built SP2 was almost the same, and only the maximum axial load differed by 5% (Figure 4.16b and Figure 4.17b). Moreover, the responses of the repaired SP2 and as-built SP2 were similar during EQ8 (Figure 4.13), and the maximum axial load measured at the base was about twice the self-weight of the test specimens (~ 2g) as shown in Figure 4.16b. The peak shear force measured at the base of repaired SP2 increased by 15% as the ground motion intensity increased from 95% to 125%. The maximum tensile force measured in the repaired SP2 was about 25% higher than that measured in the repaired SP1 during EQ9, and the maximum shear resisted by the repaired SP2 was 4% less than that measured by repaired SP1. From EQ10 to EQ11, the maximum base shear force in repaired SP2 was reduced by 5%. The maximum tensile peak measured in repaired SP2, during EQ11, was 14% less than that measured during EQ9. Finally, the maximum tensile force measured in the as-built SP2 was almost similar during EQ9 and EQ11, while the maximum shear force (towards North) reduced by 13%.

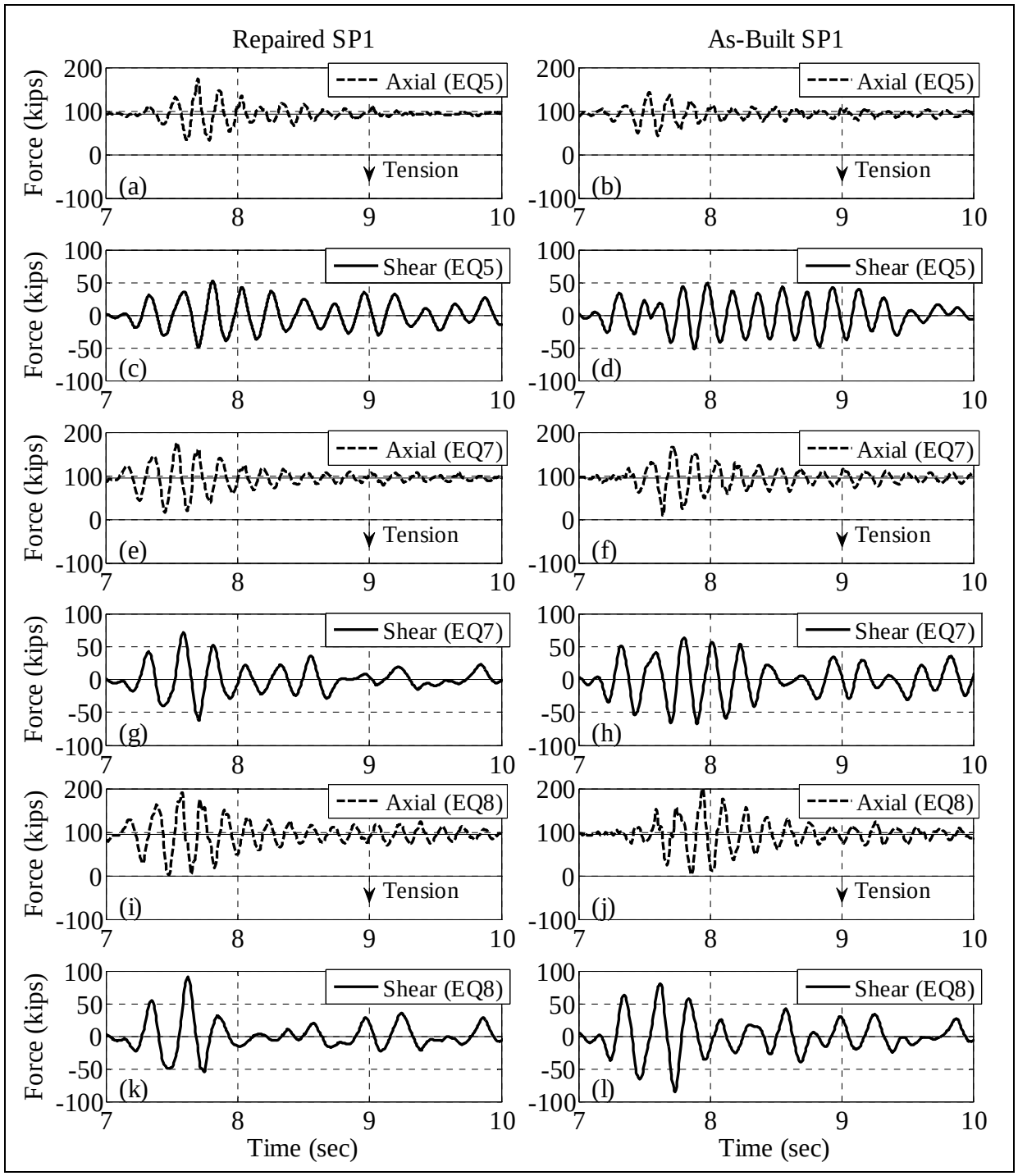

Figure 4.12 Axial load and shear force measured at the base of the repaired SP1 and as-built SP1 during 50%-, 70%- and 95%-scaled ground motions.

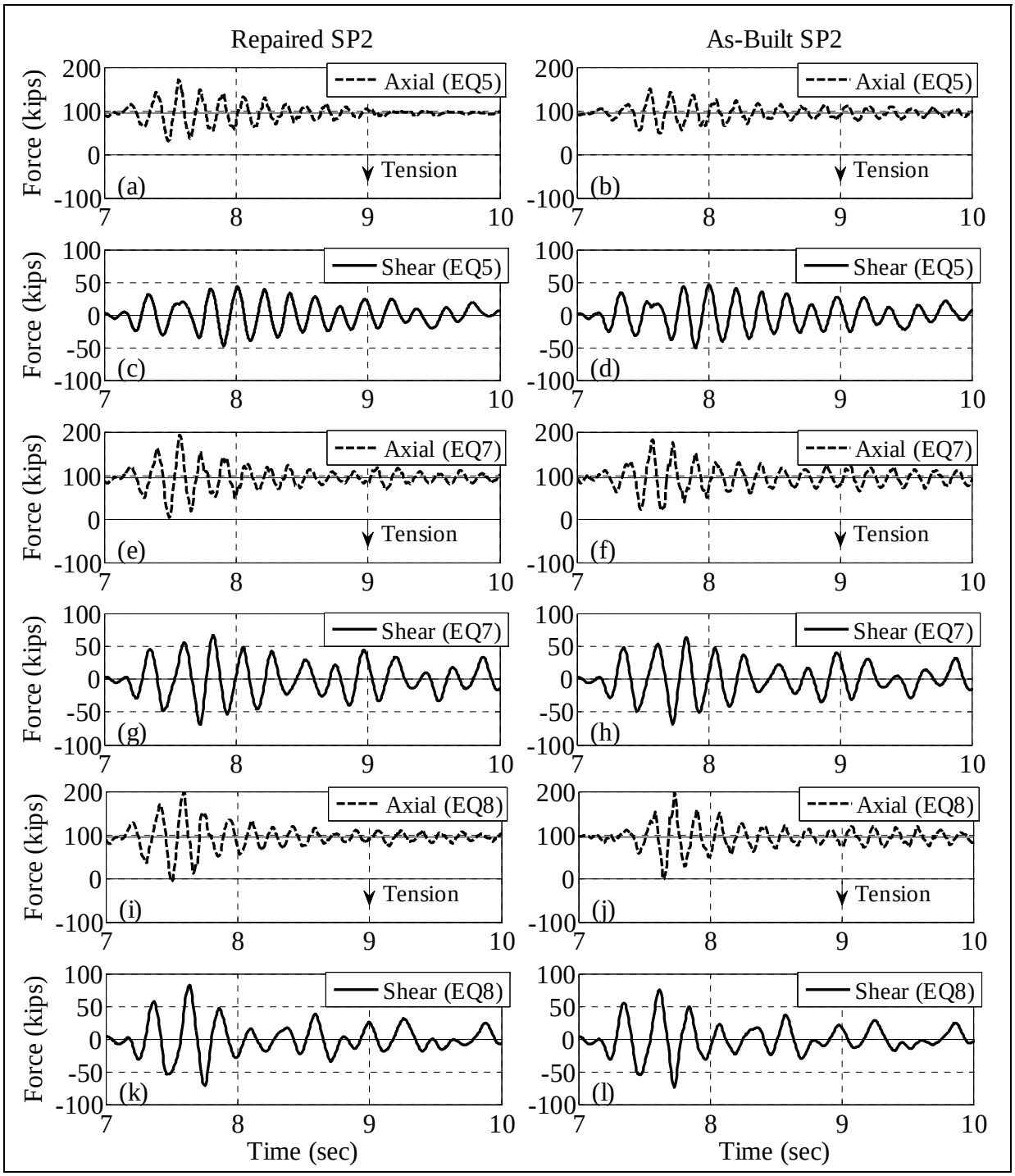

Figure 4.13 Axial load and shear force measured at the base of the repaired SP2 and as-built SP2 during 50%-, 70%- and 95%-scaled ground motions.

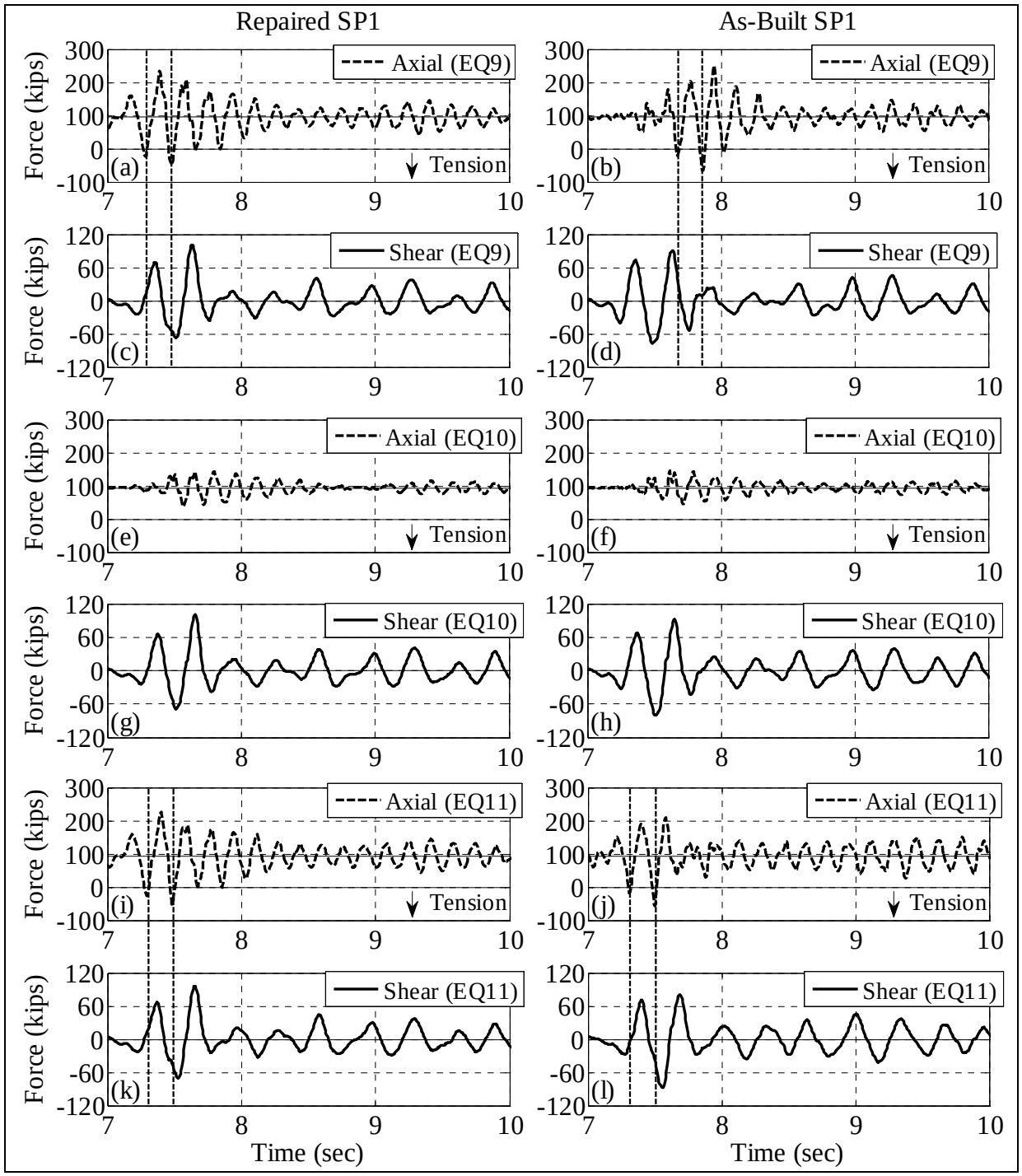

Figure 4.14 Axial load and shear force measured at the base of the repaired SP1 and as-built SP1 during 125%-scaled ground motions.

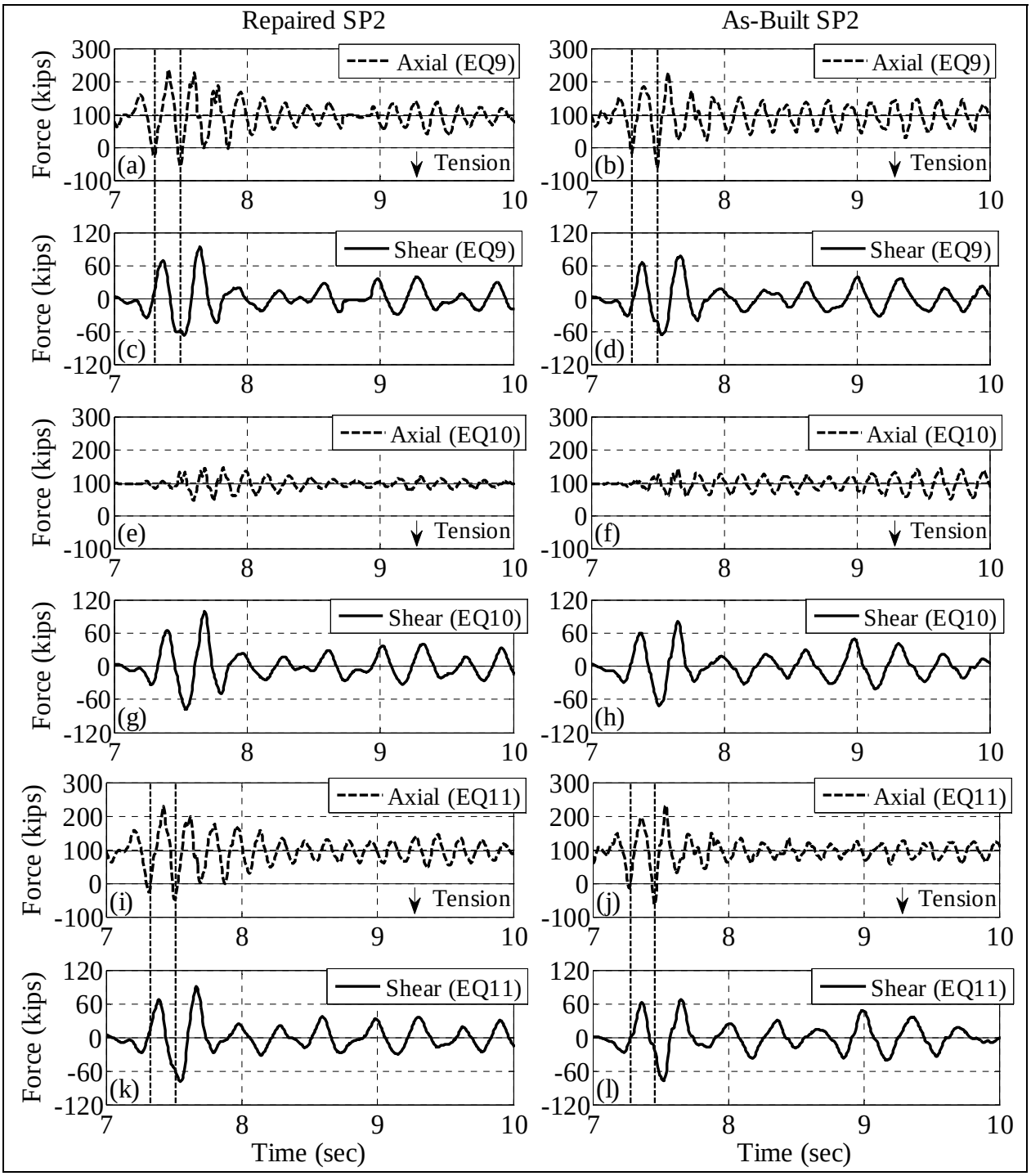

Figure 4.15 Axial load and shear force measured at the base of the repaired SP2 and as-built SP2 during 125%-scaled ground motions.

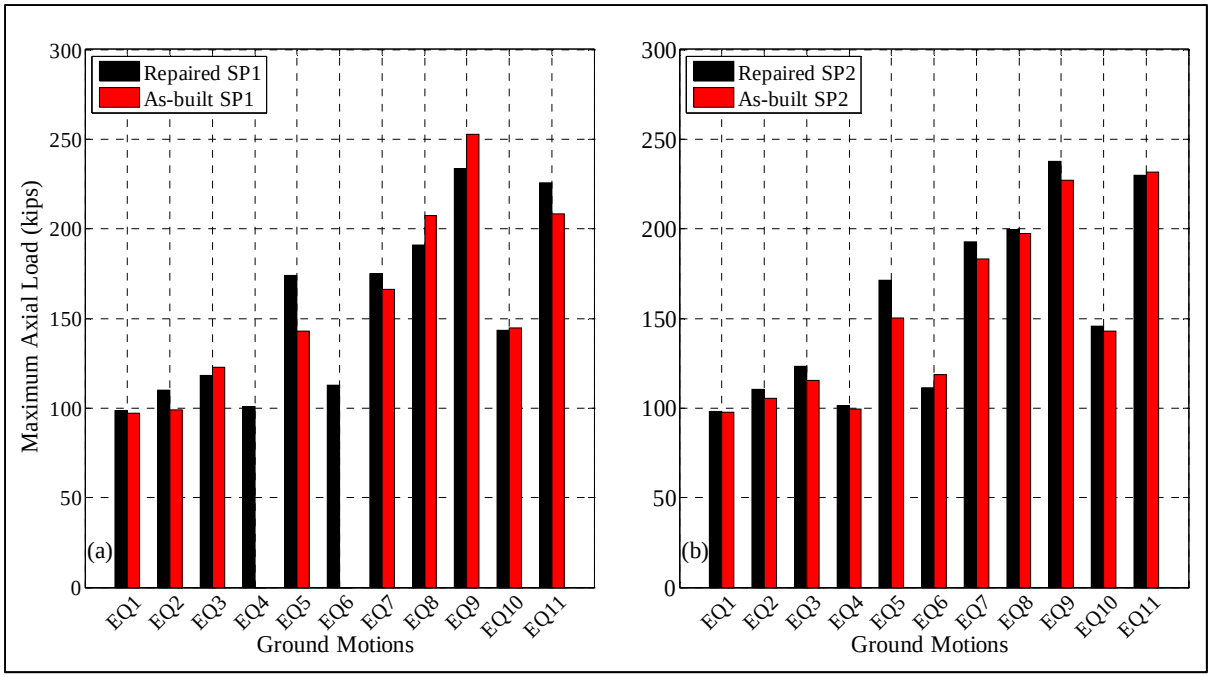

Figure 4.16 Maximum axial load measured at the base of test specimens.

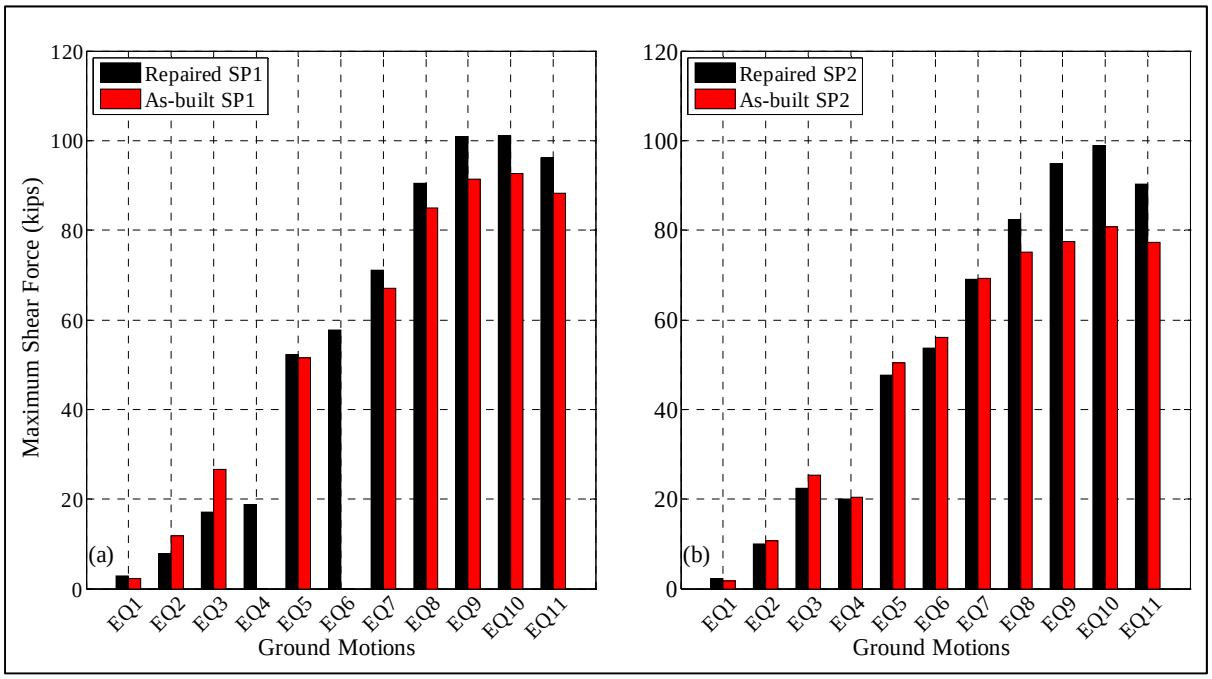

Figure 4.17 Maximum shear force measured at the base of test specimens.

4.6 HORIZONTAL DISPLACEMENT RESPONSE

Horizontal displacements in the X-direction (direction of loading) were measured using the wire potentiometers installed on the South side of the test setup. The details regarding the location and orientation of the wire potentiometers installed on the test specimens were previously discussed in Section 3.2.3. Horizontal displacement of the footing was obtained by averaging the wire potentiometer data measured near the two corners of the footing (Section 3.2). Four wire potentiometers with target points at 15 in (381 mm), 35 in (889 mm), 55in (1397 mm) and 70 in (1778 mm) above the column base were attached on the South face of the column specimen. The relative displacement at those target point locations was obtained by subtracting the average displacement data of the footing from the displacement data measured at the target points. This section focuses on the relative horizontal displacement (Δ_H) measured at the top of the cantilever column with respect to the footing. Additionally, the drift ratio (D.R.) of the test specimens was defined as the ratio of the obtained relative horizontal displacement (Δ_H) measured at the top of the column to the clear height of the cantilever column, which was 70 in (1778 mm). It is also to be noted that the design yield displacement (Δ_y) of the repaired test specimens was about 0.27 in (6.86 mm) as computed from the moment curvature analysis of the repaired sections.

Figure 4.18 shows the horizontal acceleration (a_x) and the relative displacement (Δ_H) time histories of the repaired test specimens measured during the 25%-scaled ground motions (EQ3 and EQ4). The horizontal displacement response of the test specimens could be divided into two main phases. During phase-I, the horizontal displacement response of the test specimens was influenced by the magnitude and the frequency of the ground motion peaks. However, during phase-II, the displacement response of the test specimens was similar to the free vibration displacement response of a damped single degree of freedom (SDOF) system. Thus, Phase-I refers to the strong part of the ground motion in the following discussion. From 5%- to 70%-scaled ground motions, the maximum magnitude of displacement was measured during the free vibration phase. As the intensity of ground motion increased to 95% and 125%, the maximum displacement was measured during the strong part of the ground motion (Phase-I). This shift is attributed to the increased damping of the test specimens due to damage accumulation, which suppressed the displacement magnitude during the free vibration phase. Based on the displacement response during the free vibration phase, the damping of the test specimens was computed from the 5%- through 95%-scaled ground motions using Equation 4.1 and 4.2 previously discussed. Figure 4.19 shows the plot of such damping ratios measured from 5%- through 95%-scaled ground motions. During the 125%-scaled ground motions, the response of the test specimens was highly nonlinear due to accumulation of damage caused by the higher intensity of the base excitation and the developed tensile forces in the column section. An average exponential curve fitting of the displacement data could not be attained in those big runs. Thus, the damping ratio during the 125%-scaled ground motions was not obtained or plotted in Figure 4.19. The computed damping ratio of the repaired and the as-built test specimens was not significantly different.

Figure 4.20 and Figure 4.21 show the maximum relative displacement ($\Delta_{H,max}$) measured at the top of the test specimens towards the North and the South side, respectively. Compared to the North side, the maximum displacement response on the South side was relatively linear. The maximum displacement ($\Delta_{H,max}$) measured towards the North end of the repaired test specimens was consistently higher than that measured towards the South end for almost all the ground motions. The difference between the maximum relative displacement ($\Delta_{H,max}$) magnitudes

measured towards the North and South side of the test specimens increased as the intensity of the base excitation increased. The relative top displacement (Δ_H) response of the repaired test specimens was almost symmetric during EQ1 through EQ6 with less than 10% difference in the magnitudes of the maximum displacement measured towards the North and the South side. Compared to the repaired SP1, the difference between the maximum top displacement ($\Delta_{H,max}$) measured to the North and the South side of repaired SP2 was higher during EQ7 through EQ11.

The relative displacements from the repaired specimens tests were also compared to the as-built specimens tests. Figure 4.22 and Figure 4.23 show the top horizontal displacement (Δ_H) time histories of the repaired and the as-built test specimens measured during the 50%-, 70%- and 95%-scaled ground motions. During the 50%-scaled ground motions, the top displacement of the repaired test specimens exceeded the design yield displacement magnitude (Δ_y). The maximum top displacement of repaired SP1 was $1.8\Delta_y$ and $1.7\Delta_y$ during EQ5 (Figure 4.22a) and EQ6, respectively. As previously mentioned, these maximum values were observed during the free vibration phase. The magnitude of the maximum top displacement of the repaired SP2 was lower than that of repaired SP1, with magnitudes $1.6\Delta_y$ and $1.4\Delta_y$ measured during EQ5 (Figure 4.23a) and EQ6, respectively. The damping ratio based on the free vibration displacement response of the repaired SP1 was about 2.28% and 2.35% during EQ5 and EQ6, respectively. It is to be noted that the damping of the repaired SP1 was only slightly higher than its as-built counterpart. The damping ratio of the as-built SP1 remained almost the same during the 50%-scale ground motions, while the damping ratio obtained from the repaired SP1 tests increased as noticed in Figure 4.19. This is attributed to the accumulated damage in repaired SP1 prior to the repair and the impact of yielding on the displacement response of the test specimens during EQ5. In addition, the damping ratio of the repaired SP2 was about 2.24% and 2.21% during EQ5 and EQ6, which was comparable to the as-built counterpart (Figure 4.19).

The displacement response of the repaired test specimens during EQ7 was similar to EQ5 (Figure 4.22(a, c) and Figure 4.23(a, c)). During EQ7, the maximum top displacement of the repaired SP1 and SP2 was $2.2\Delta_y$ and $2.3\Delta_y$, respectively. During EQ8, The maximum displacement measured at the top of repaired SP1 and repaired SP2 was $3.6\Delta_y$ and $2.9\Delta_y$, respectively. Thus, from EQ7 to EQ8, the maximum top of the repaired SP1 and SP2 increased by 66% and 27%, respectively. In these runs, the maximum displacement at the top of repaired test specimens was measured during strong part of the ground motion due to the relatively higher intensity of 95%-scaled ground motion. During EQ8, the damping ratio of the repaired specimens during the free vibration phase was about 2.9% (Figure 4.19). Due to higher damage and lower confinement ratio, the damping ratio of the as-built SP2 was higher than the other test specimens.

During the 125%-scaled ground motions (EQ9 and EQ11) of the as-built specimens, the specimens experienced tensile forces, which caused extensive cracking and spalling of the concrete in the plastic hinge regions (Lee, 2011). However, after the FRP jacket repair was applied, the damage and cracking of the repaired specimens after their tests was not visible. Figure 4.24 and Figure 4.25 show the displacement time histories measured during the 125%-scaled ground motions for SP1 and SP2, respectively. The close match between the displacement response of the repaired test specimens and their as-built counterparts indicated relatively higher cracking in the confined core of the repaired cross-sections during the 125%-scaled ground motion, i.e. minor effect of FRP confinement. Moreover, the free vibration response of the test specimens during the 125%-scaled ground motion was highly damped and the maximum

displacement was observed during the strong part of the ground motions (Phase-I). During EQ9, both repaired test specimens had a maximum displacement of $4.9\Delta_y$. In the absence of the vertical component of the 125%-scaled ground motion (EQ10), the displacement time history response of the repaired SP1 was almost similar to that of EQ9. On the other hand, the maximum displacement measured at the top of the repaired SP2 during EQ10 increased to $5.1\Delta_y$. The maximum displacement measured at the top of the repaired SP1 and SP2 during EQ11 was 1.4 in (35.7 mm) and 1.5 in (37.9 mm), respectively as noticed from Figure 4.24(e) and Figure 4.25(f). The maximum displacement measured at the top of the as-built SP1 and the as-built SP2 was 1.64 in (41.7 mm) and 1.4 in (35.7 mm), respectively during the loading protocol. The ultimate displacement ductility of the repaired SP1 and SP2 during EQ11 was 4.0 and 4.3, respectively. These obtained values for the ductility are slightly higher than the design displacement ductility limit of 4.0 required by the Caltrans SDC (2010). However, the maximum displacement ductility of the as-built SP1 and SP2 was 5.47 and 4.77, respectively.

The residual top displacement ($\Delta_{H,res}$) was defined as the relative lateral displacement of the column top at the end of each ground motion run with respect to the specimen footing. Moreover, the residual drift ratio (D.R.) was defined as the ratio of the residual displacement ($\Delta_{H,res}$) to the cantilever column height (70 in, (1778 mm)). Figure 4.26 shows the comparison of the residual displacements ($\Delta_{H,res}$) of the test specimens measured during the loading protocol. Despite the lesser damage along the column height, the residual D.R. of the as-built SP1 was higher than that of the as-built SP2. This is attributed to the fact that the residual displacement of the as-built SP1 was shifted towards the North during the entire loading protocol, while the residual displacement of the as-built SP2 was shifted towards the South from EQ1 to EQ6 then shifted towards the North from EQ7 to EQ11. Both repaired specimens followed a similar residual D.R. pattern to that of the as-built SP2. The residual displacement ($\Delta_{H,res}$) of the repaired SP1 and SP2 was 67% and 20% less than their as-built counterparts, respectively, after the completion of the entire loading protocol. Figure 4.27 shows the bar plot of the residual displacements ($\Delta_{H,res}$) of the test specimens (as-built and repaired) at the end of each ground motion, but normalized with respect to the absolute maximum lateral displacement ($\Delta_{H,max}$) during that ground motion run. The as-built specimens had much higher normalized residual displacements compared to the repaired ones after EQ5. Both repaired specimens had normalized residual displacement 10% or less in most of the runs. The increase of the earthquake intensity above EQ7 led to a steady increase of the normalized residual displacement for all the test specimens. However, the increase of the normalized residual displacement was slower for the repaired specimens than for the as-built counterparts. This indicates that the effectiveness of the investigated FRP repair technique to increase the resiliency of bridge columns when subjected to severe earthquake loading. Finally, at the end of EQ11, the residual displacement of the repaired SP1 and repaired SP2 was 0.109 in (2.759 mm) and 0.179 in (4.553 mm), respectively.

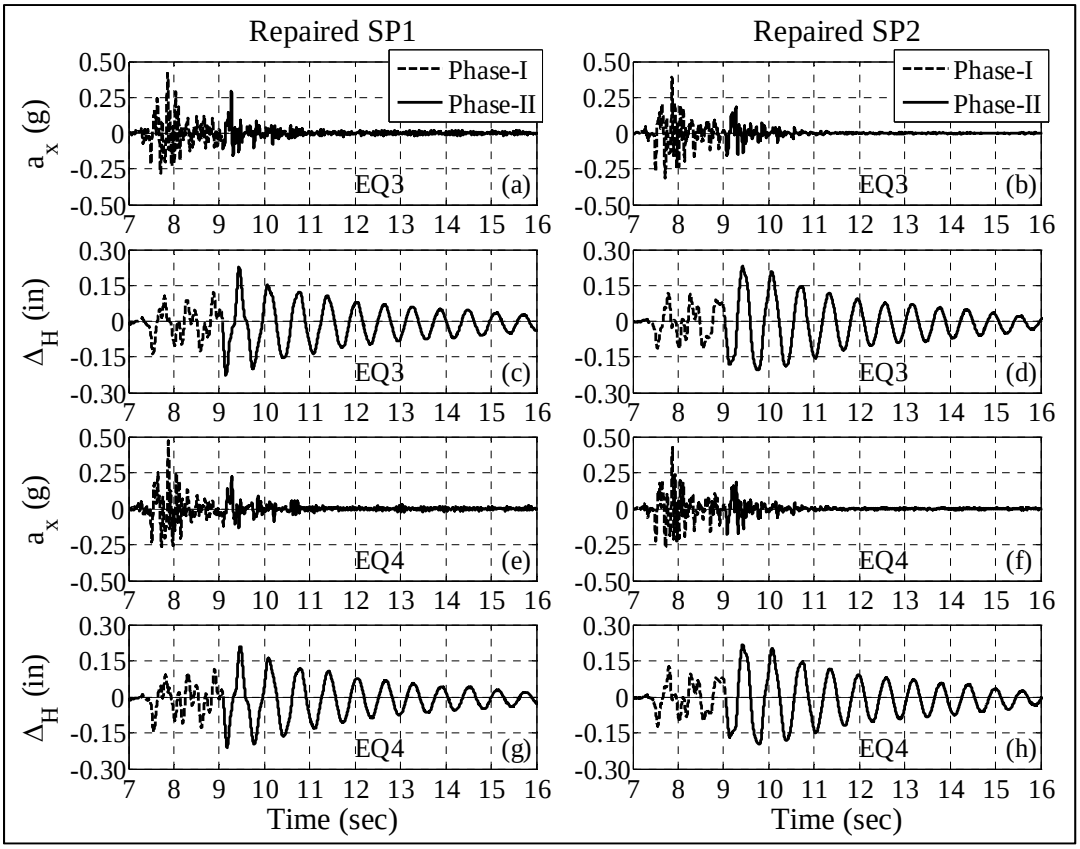

Figure 4.18 Acceleration and displacement time histories measured during 25%-scaled ground motions.

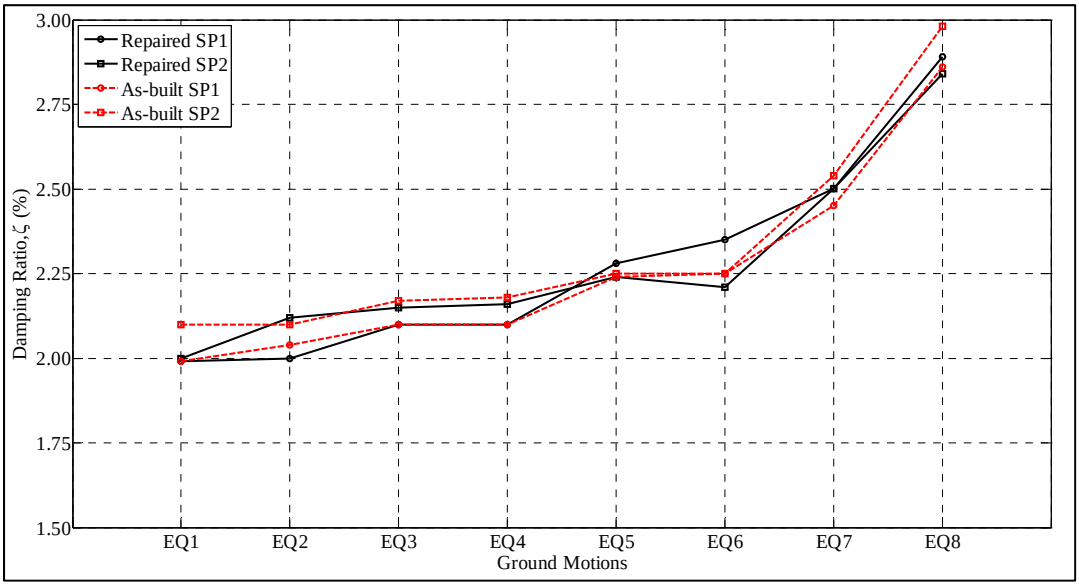

Figure 4.19 Damping ratio of the repaired and as-built test specimens.

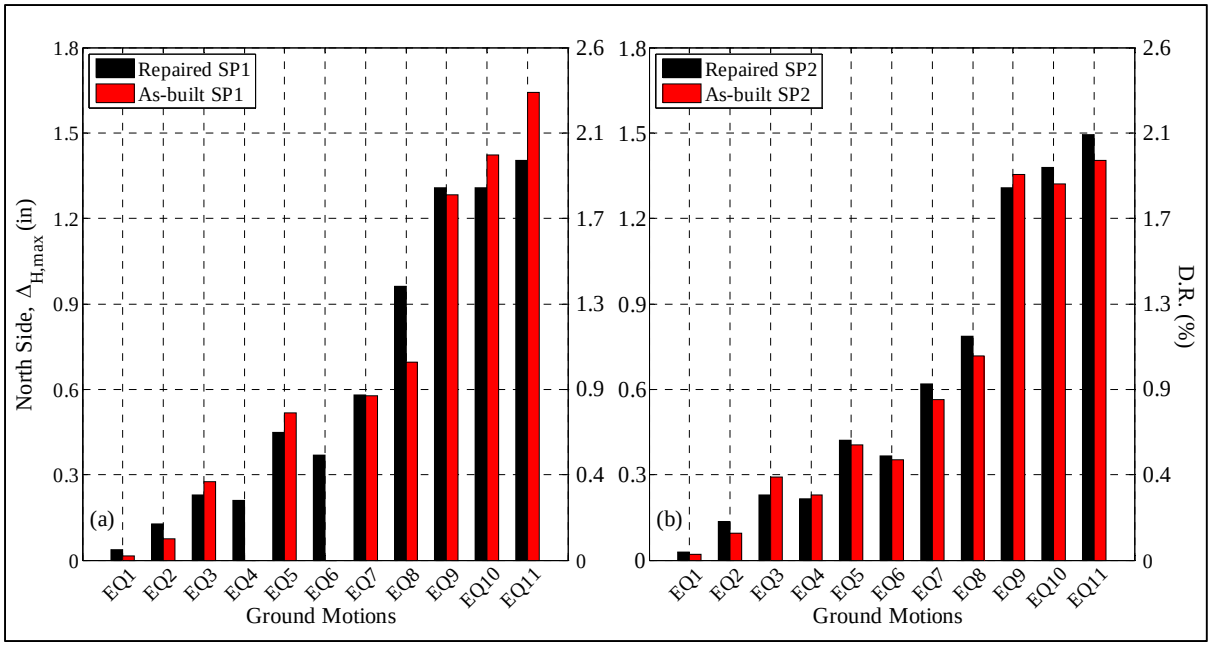

Figure 4.20 Maximum horizontal displacement ($\Delta_{H,max}$) response measured towards the North side of the test specimens.

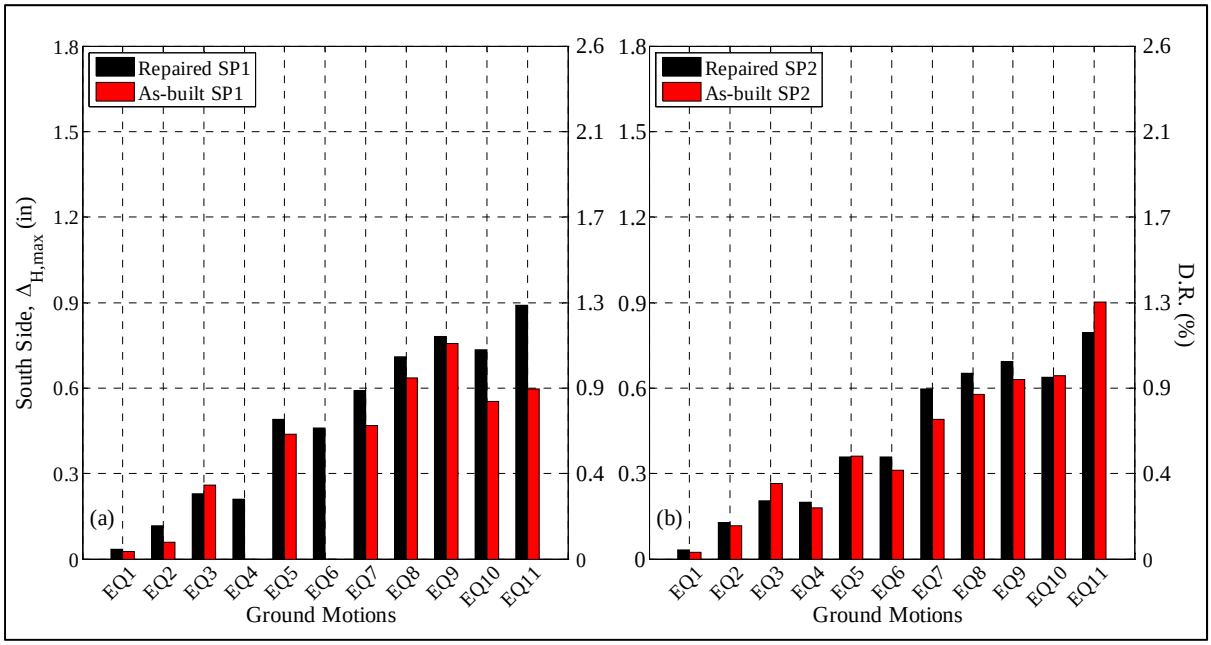

Figure 4.21 Maximum horizontal displacement ($\Delta_{H,max}$) response measured towards the South side of the test specimens.

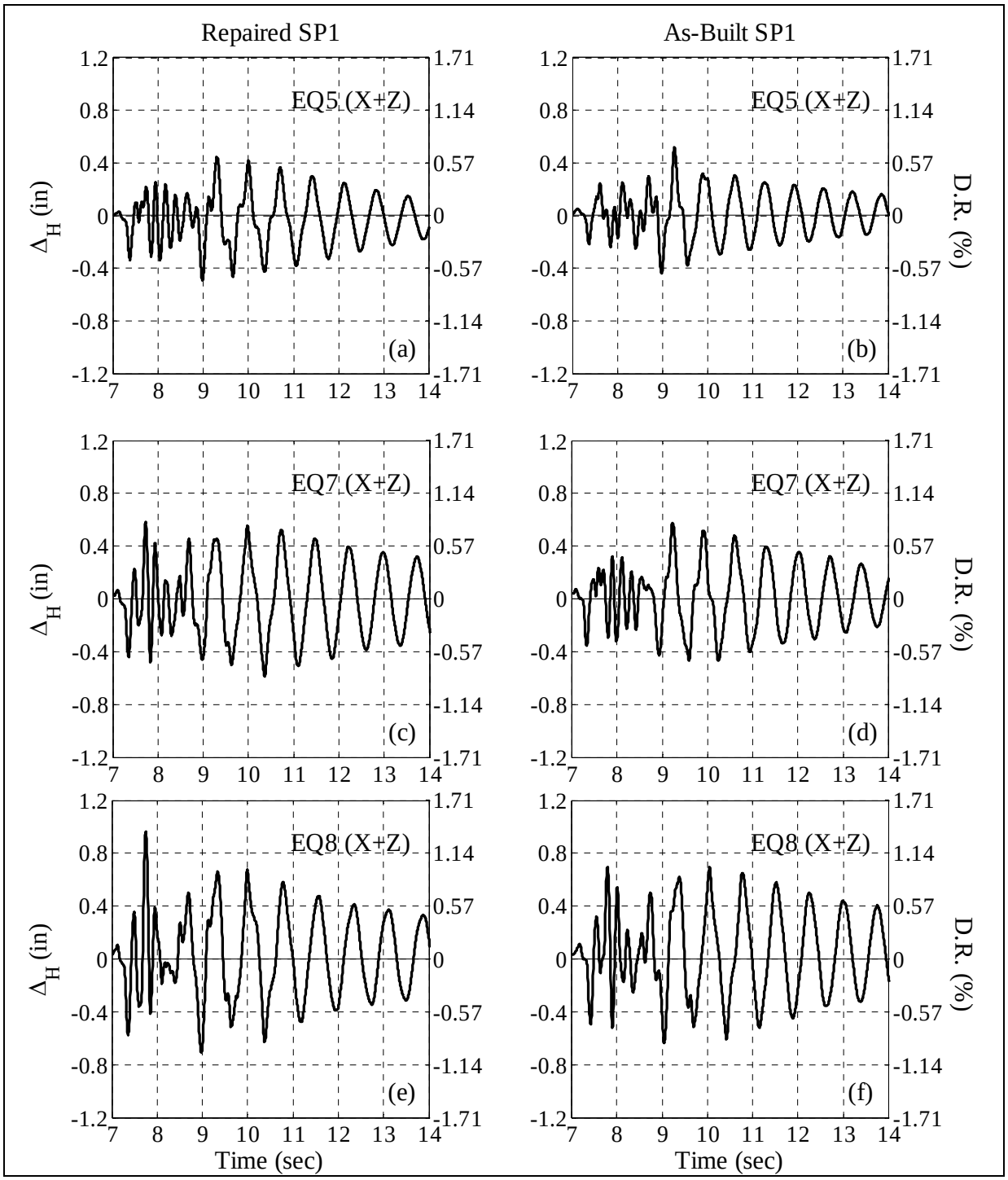

Figure 4.22 Top displacement (Δ_H) histories of repaired SP1 and as-built SP1 during 50%-, 70%- and 95%-scaled ground motions.

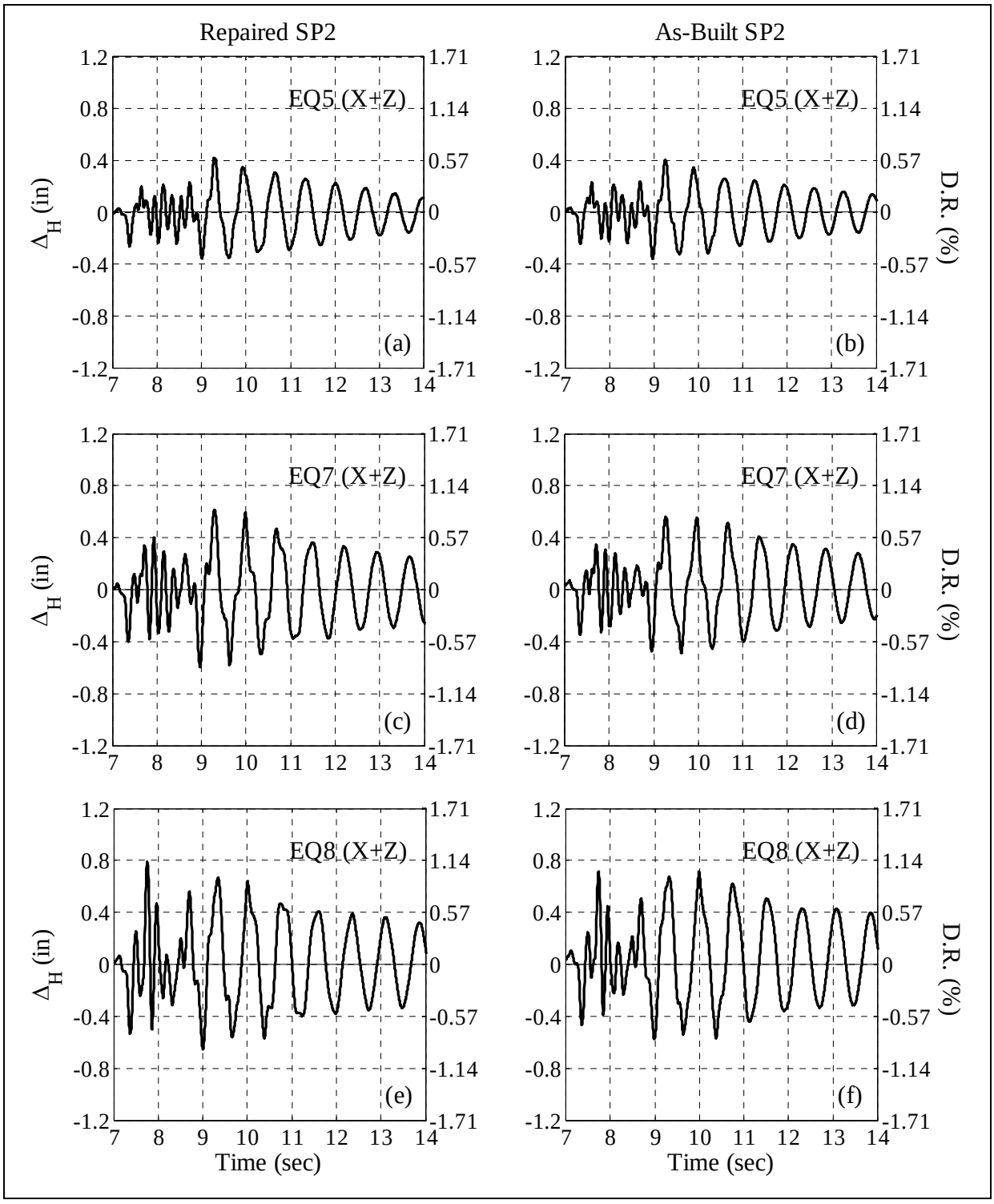

Figure 4.23 Top displacement (Δ_H) histories of the repaired SP2 and as-built SP2 measured during 50%-, 70%- and 95%-scaled ground motions.

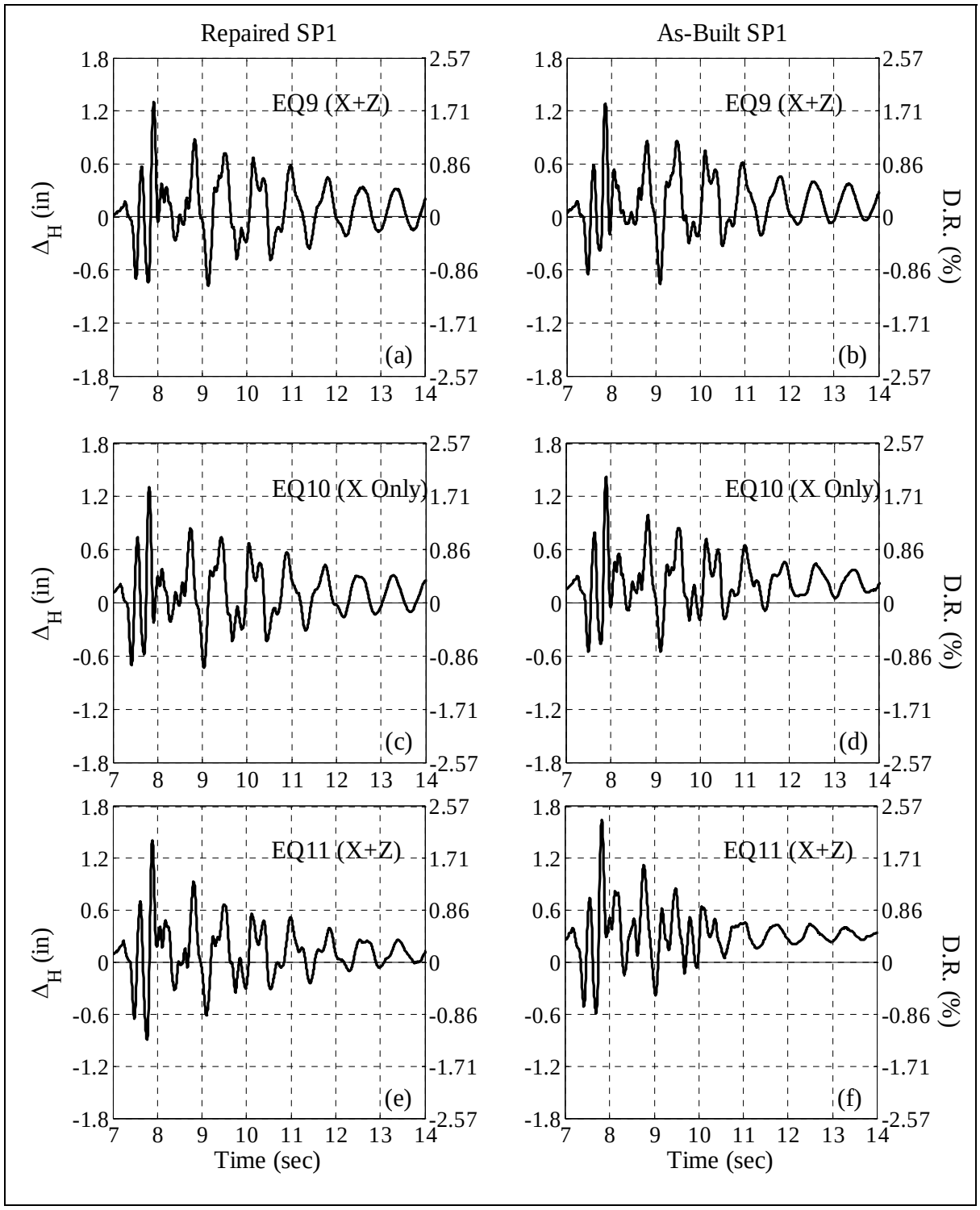

Figure 4.24 Top displacement (Δ_H) time histories of the repaired SP1 and the as-built SP1 during 125%-scaled ground motions.

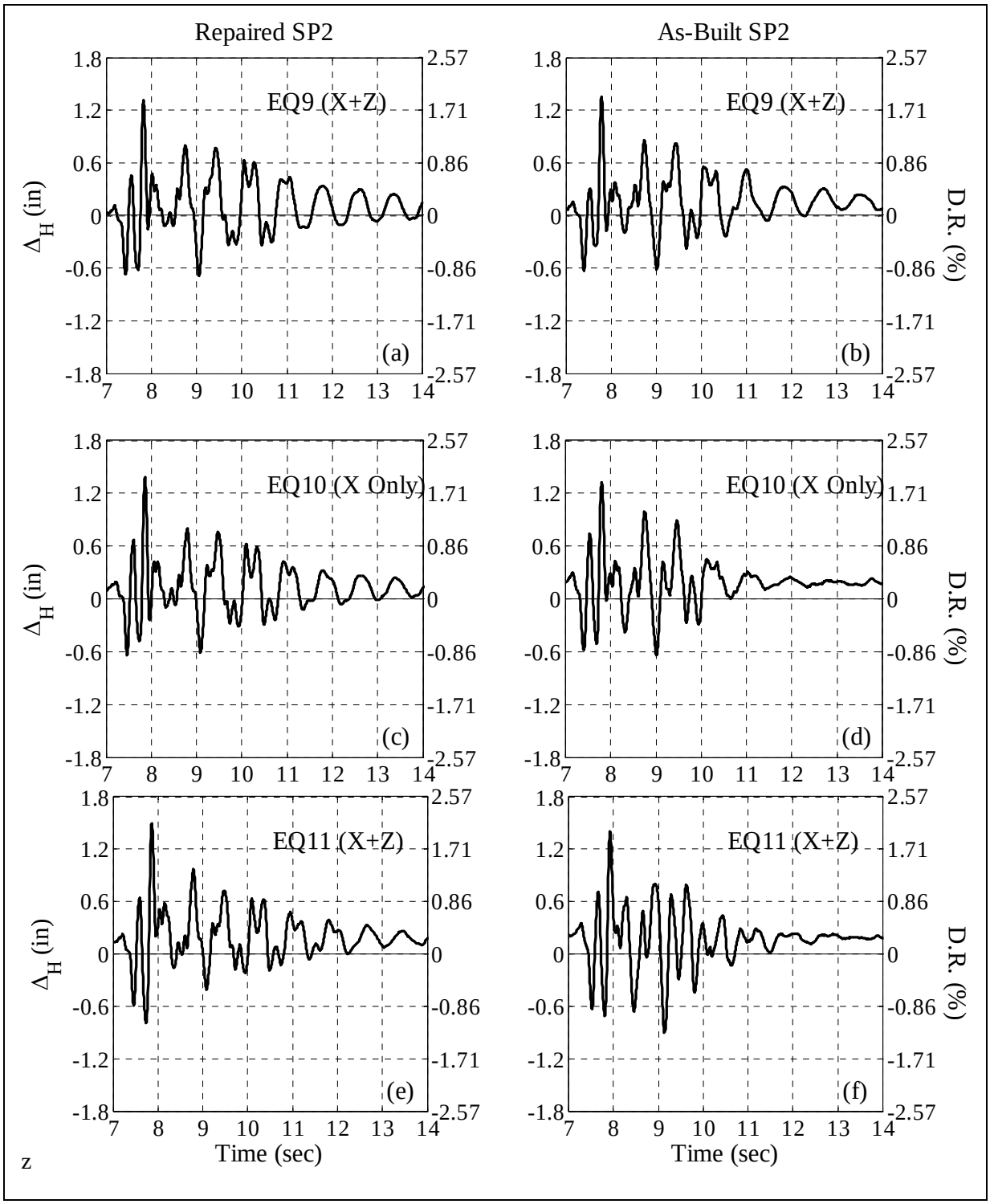

Figure 4.25 Top displacement (Δ_H) time histories of the repaired SP2 and the as-built SP2 during 125-scaled ground motions.

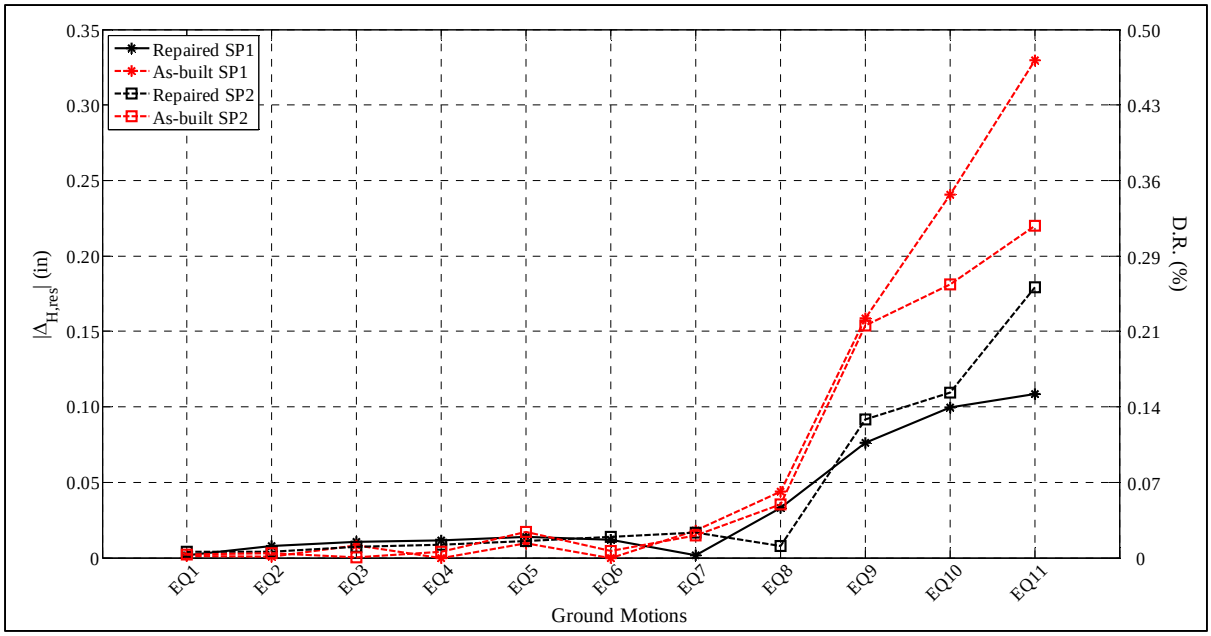

Figure 4.26 Absolute horizontal residual displacement ($\Delta_{H,res}$) of the repaired and as-built test specimens.

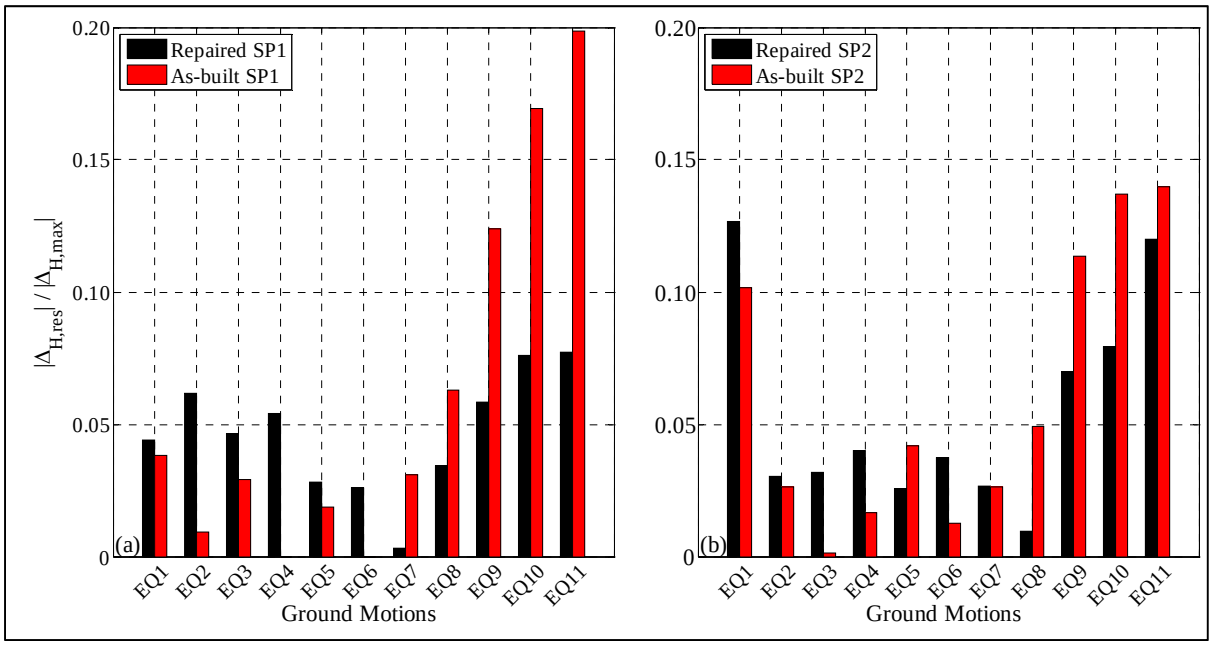

Figure 4.27 Normalized absolute horizontal residual displacement.

4.7 VERTICAL DISPLACEMENT AND TOP ROTATION RESPONSE

The vertical displacement (Δ_V) and top rotations (θ) were measured using the four vertical wire potentiometers attached at the steel plate level at one end, and targets at the four corners of concrete slabs from the other end (Section 3.2.3). The vertical displacement (Δ_V) was measured by averaging the data obtained from the four vertical wire potentiometers. The top rotation (θ) was defined as the ratio of the difference of the data measured from two vertical wire potentiometers installed on the opposite ends of concrete slab, North-South for rotation about Y-axis or East-West for rotation about X-axis, to the horizontal distance between them (120 in (3048 mm)). In this section, only the top rotation (θ) about the Y-axis is discussed as the rotation measured about the X-axis was less relevant and significantly lower. For the rotations sign convention, the top rotation was considered positive when the net vertical displacement of the North end of the concrete slab (superstructure mass configuration) was upwards (Appendix B).

The vertical displacement (Δ_V) of the repaired SP1 and SP2 increased from 0.005 in (0.13 mm) to 0.076 in (1.93 mm), and from 0.004 in (0.10 mm) to 0.05 in (1.27 mm), respectively. This increase corresponded to the ground motion intensity increased from 5% to 50%. The vertical displacement and the minimum axial load peaks were measured at the same time instant during the strong part of ground motions. Figure 4.28 and Figure 4.29 show the axial load (F_{Axial}) and the vertical displacements (Δ_V) time histories of the repaired and as-built test specimens measured during the 50%-, 70%- and 95%-scaled ground motions. It can be noticed that from EQ7 to EQ8, the maximum vertical displacement of the repaired SP1 and SP2 increased from 0.12 in to 0.19 in, and 0.10 in to 0.14 in, respectively. The residual vertical displacement (extension) of the repaired SP1 was higher than that of the repaired SP2, which resulted in higher magnitudes of vertical displacement (extension) of the repaired SP1 than repaired SP2 during the high intensity ground motions (EQ7 through EQ11).

Additionally, Figure 4.30 and Figure 4.31 show the axial load (F_{Axial}) and the vertical displacements (Δ_V) time histories of the repaired and as-built test specimens measured during the 125%-scaled ground motions. The vertical displacement response of the repaired test specimens was similar to their as-built counterparts during EQ11. With the exception of the 25%-scaled ground motions (EQ3 and EQ4), the maximum vertical displacement of the repaired test specimens were consistently higher than the as-built test specimens. The difference between the peak vertical displacements of the repaired SP1 and the as-built SP1 increased as the intensity of ground motion increased. In the absence of the vertical component of ground motion EQ10, the vertical displacement response of the repaired and the as-built SP1 was almost similar (Figure 4.30g, h). Similarly, the difference between the peak vertical displacement magnitudes of the repaired and the as-built SP2 increased with the increase in the ground motion intensity (Figure 4.31). It is also noted that the maximum vertical displacement of the repaired test specimens was observed after the maximum tensile force peak took place (dotted lines in Figure 4.30 and Figure 4.31).

The repair of the test specimens was done mainly to improve the shear strength capacity of the damaged as-built test specimens. The FRP jacket repair did not aim at improving the axial response of the test specimens. The repair of the test specimens was successful in maintaining the integrity of the column section, i.e. no rupture of the confining material took place, and accordingly, no spalling of the core and cover concrete was observed during the tests. Consequently, this reduced the net extension of the cantilever column that results from the

excessive opening of the cracks in concrete near the column top, which reduced the overall residual vertical displacement of the repaired SP1 compared to the as-built SP1 (Figure 4.32c). This behavior was not observed in case of the repaired and as-built SP2 during EQ10 and EQ11 where the residual vertical displacement of the repaired SP2 was higher than that of the as-built SP2 (Figure 4.32d). The residual vertical displacement of the as-built SP2 increased with each successive loading (EQ1 through EQ8). During the 125%-scaled ground motions, the residual vertical displacement of the as-built SP2 remained almost the same due to the increase in the damage at the top and base level besides the relatively higher residual rotation. At the end of the loading protocol, the repaired SP1 and SP2 stretched by 0.046 in (1.17 mm) and 0.054 in (1.37 mm) longer than their initial height (70 in (1778.0 mm)), respectively.

Figure 4.33 shows the absolute maximum and residual rotation measured at the top of the test specimens. The difference between the maximum rotation measured at the top of the repaired SP1 and the as-built SP1 was less than ±10% (Figure 4.33a). However, the residual top rotation of the as-built SP1 was higher than the repaired SP1. During EQ9 and EQ10, the residual top rotation of the repaired SP1 remained almost the same, and the residual top rotation of the as-built SP1 increased by 26%. At the end EQ11, the residual top rotation of as-built SP1 was 50% higher than the repaired SP1. The maximum top rotation of the repaired SP2 had a relatively higher magnitude than the as-built SP2, with a difference of 15% during EQ11. The residual top rotation of the repaired SP2 increased by 22% from EQ9 to EQ10, and 7% from EQ10 to EQ11. At the end of EQ11, the residual top rotation of the repaired SP2 was 12% higher than that of the as-built SP2.

The maximum magnitude of the top rotation was measured during the free vibration phase of the ground motions. Figure 4.34 and Figure 4.35 show the horizontal displacement and rotation time histories of the test specimens measured during the 50%-, 70%- and 95%-scaled ground motions. From EQ5 to EQ8, the top rotation response of the repaired and as-built SP1 was almost similar. The top rotation measured in the as-built SP2 was much lower than the repaired SP2 during the 50%-, 70%- and 95%-scaled ground motions. Figure 4.36 and Figure 4.37 show the horizontal displacement and rotation time histories of the test specimens measured during the 125%-scaled ground motions. The top rotation response of the repaired and the as-built SP1 was almost the same. The top rotations response of the as-built SP2 was highly damped compared to the repaired SP2. This is attributed to the relatively higher magnitude of residual drift and top rotation of the as-built test SP2. The maximum magnitude of the top rotation of both repaired test specimens was about 0.028 rad.

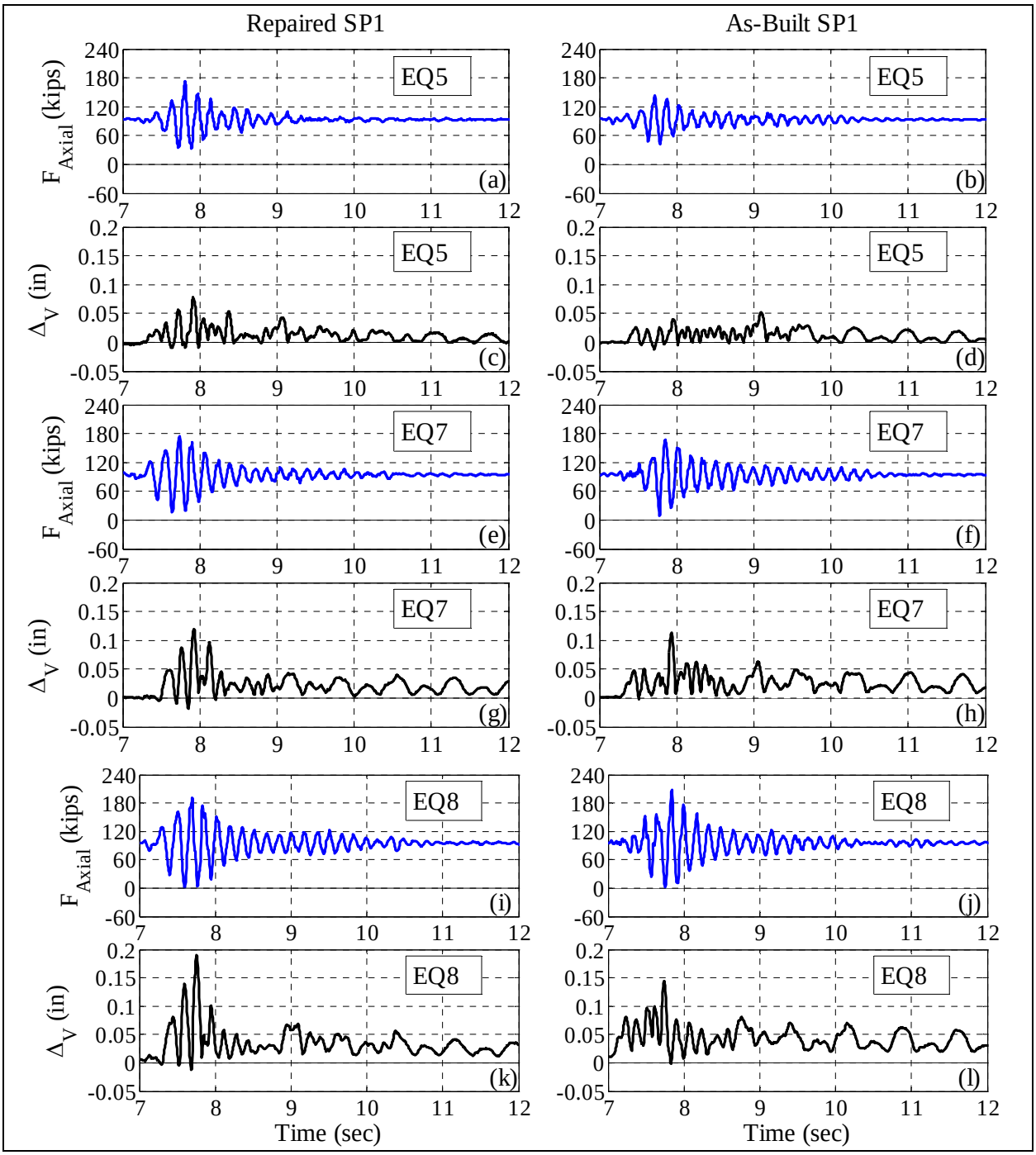

Figure 4.28 Axial load and vertical displacement time histories measured during 50%-, 70%- and 95%-scaled ground motions.

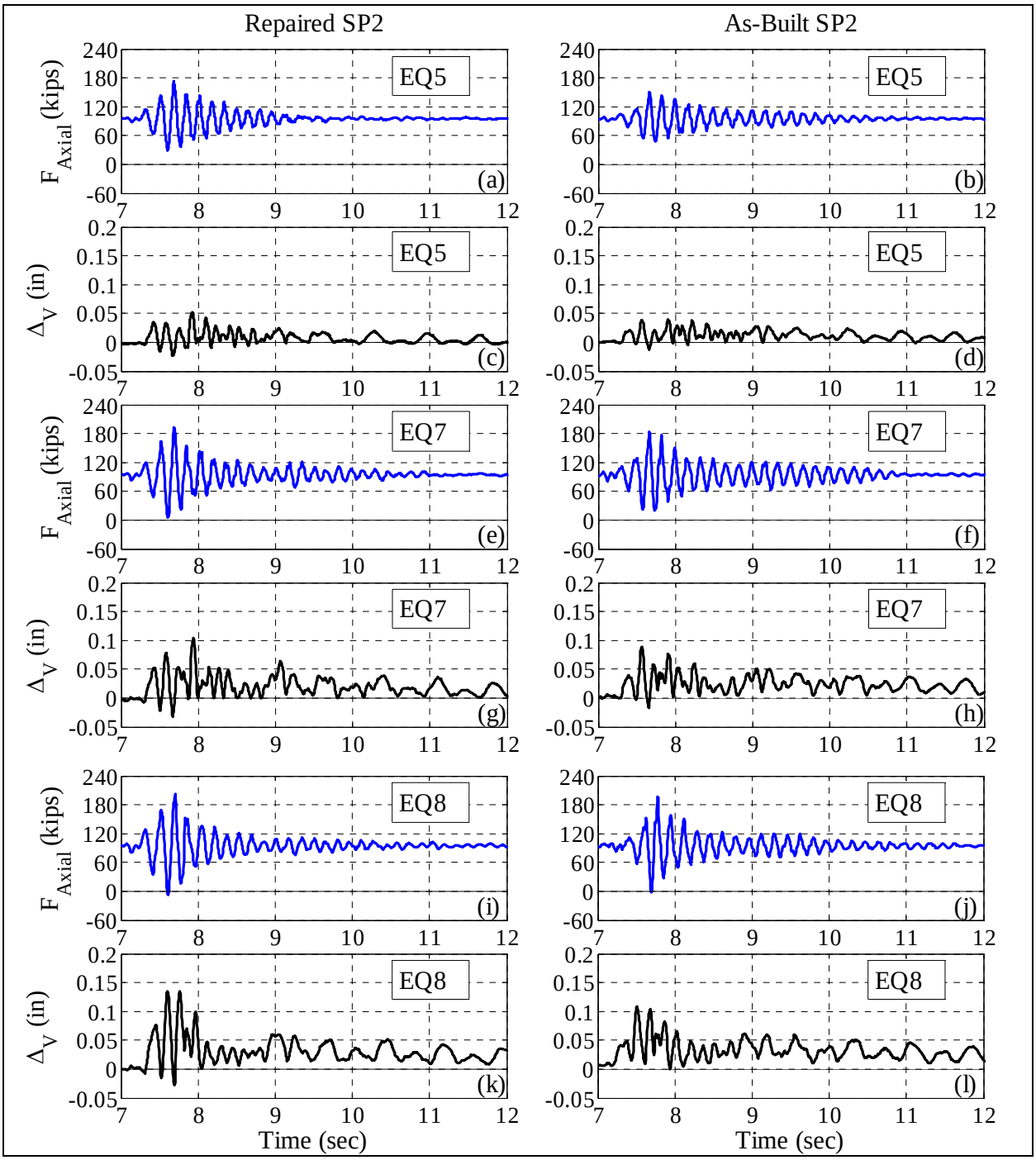

Figure 4.29 Axial load and vertical displacement time histories measured during 50%-, 70%- and 95%-scaled ground motions.

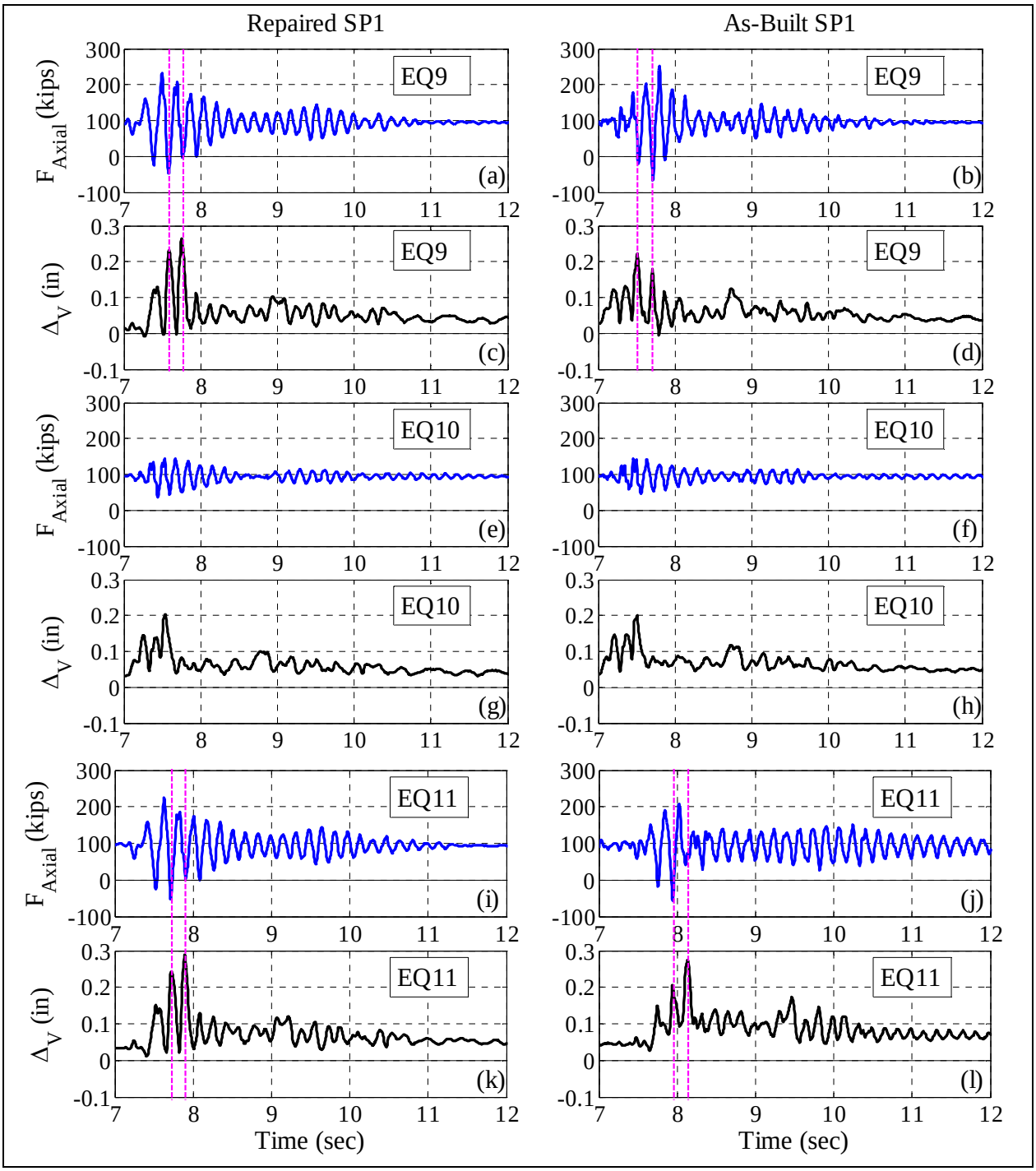

Figure 4.30 Axial load and vertical displacement time histories measured during 125%-scaled ground motions.

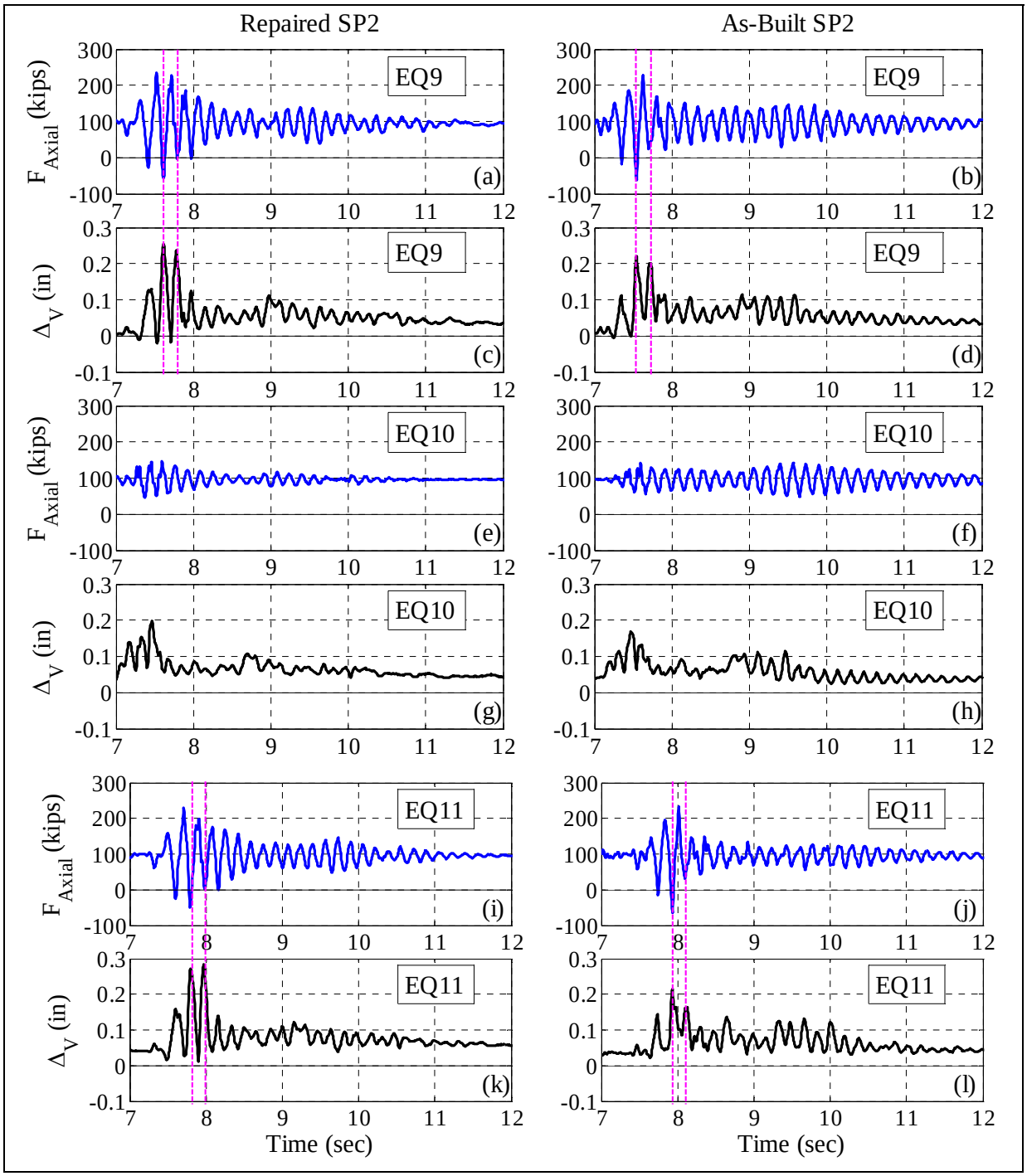

Figure 4.31 Axial load and vertical displacement time histories measured during 125%-scaled ground motions.

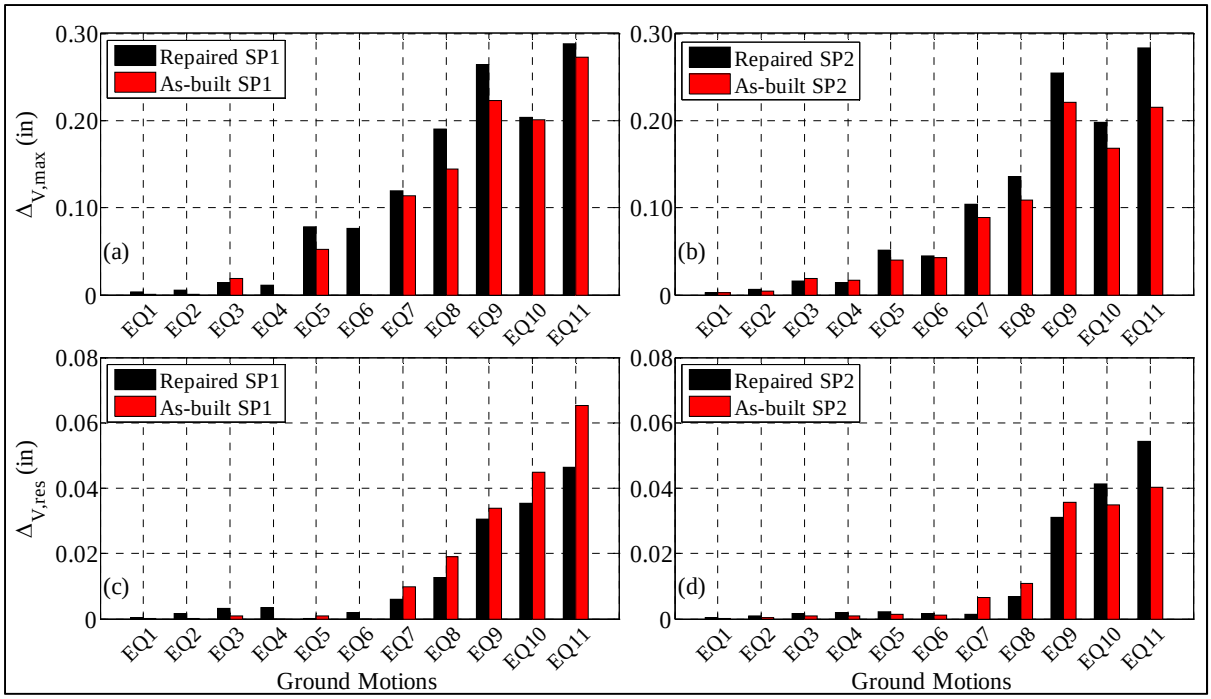

Figure 4.32 Maximum vertical displacements ($\Delta_{V,max}$) and residual vertical displacements ($\Delta_{V,res}$).

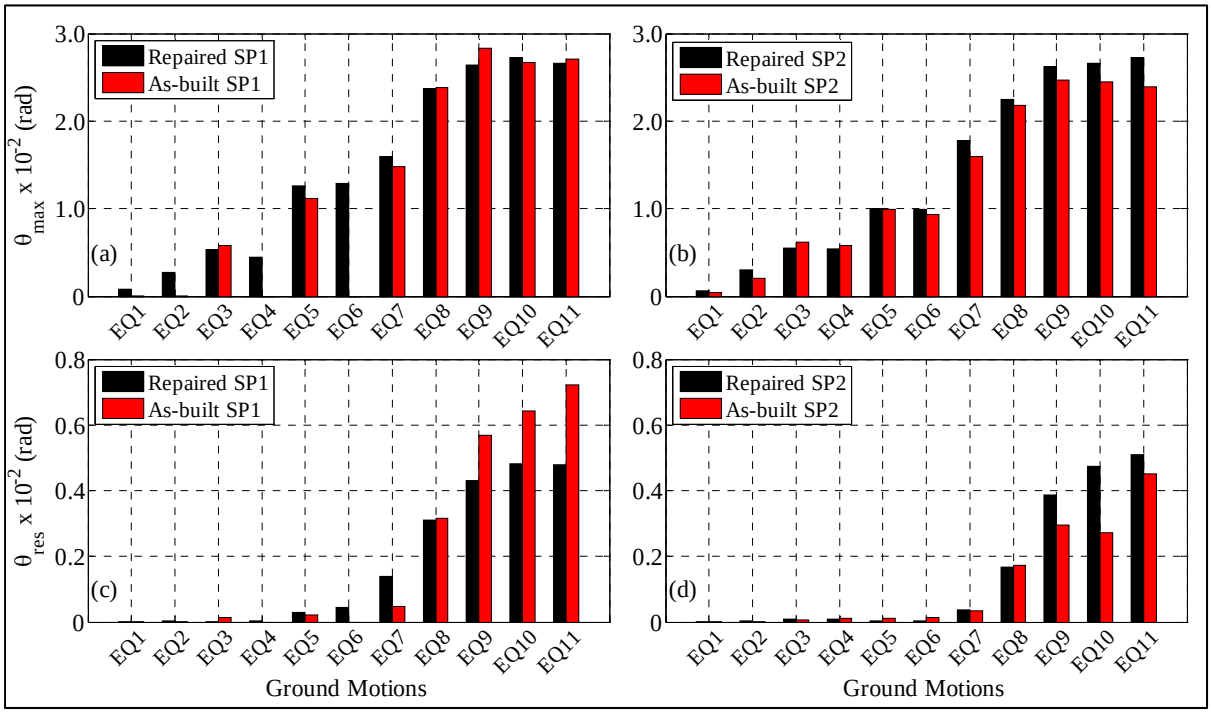

Figure 4.33 Absolute maximum top rotation (θ_{max}) and absolute residual top rotation (θ_{res}).

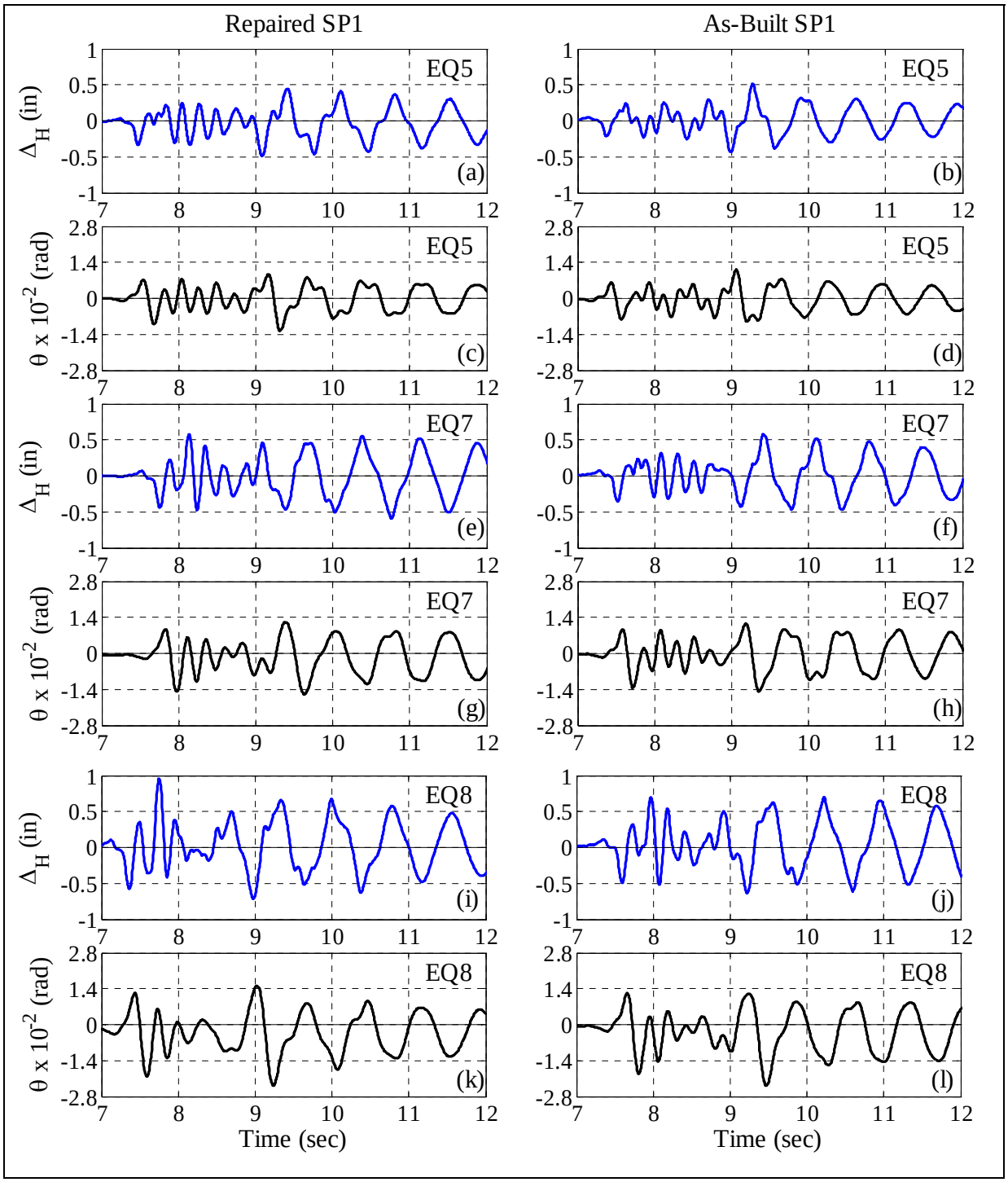

Figure 4.34 Horizontal displacement and top rotation time histories measured during 50%-, 70%- and 95%-scaled ground motions.

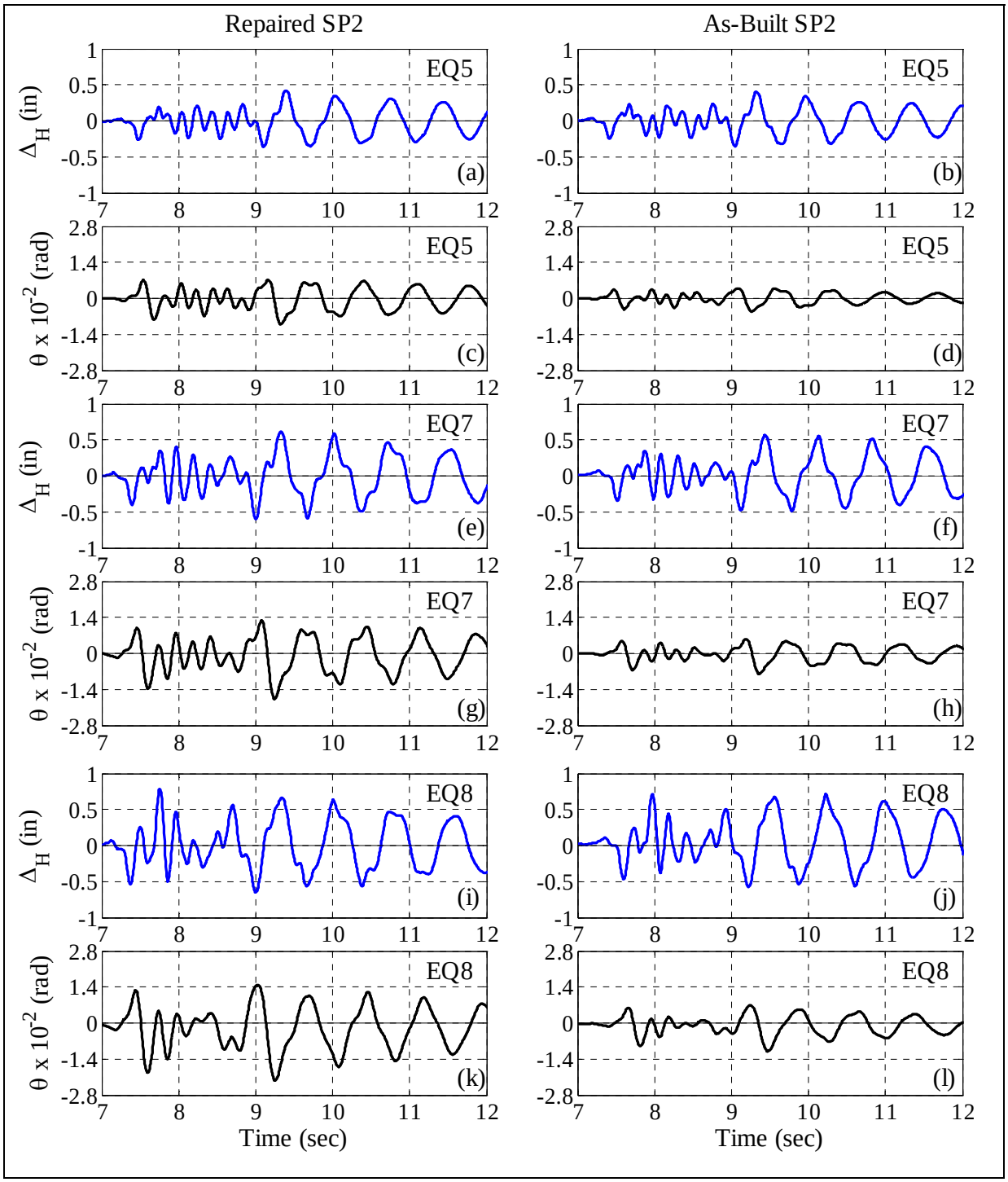

Figure 4.35 Horizontal displacement and top rotation time histories measured during 50%-, 70%- and 95%-scaled ground motions.

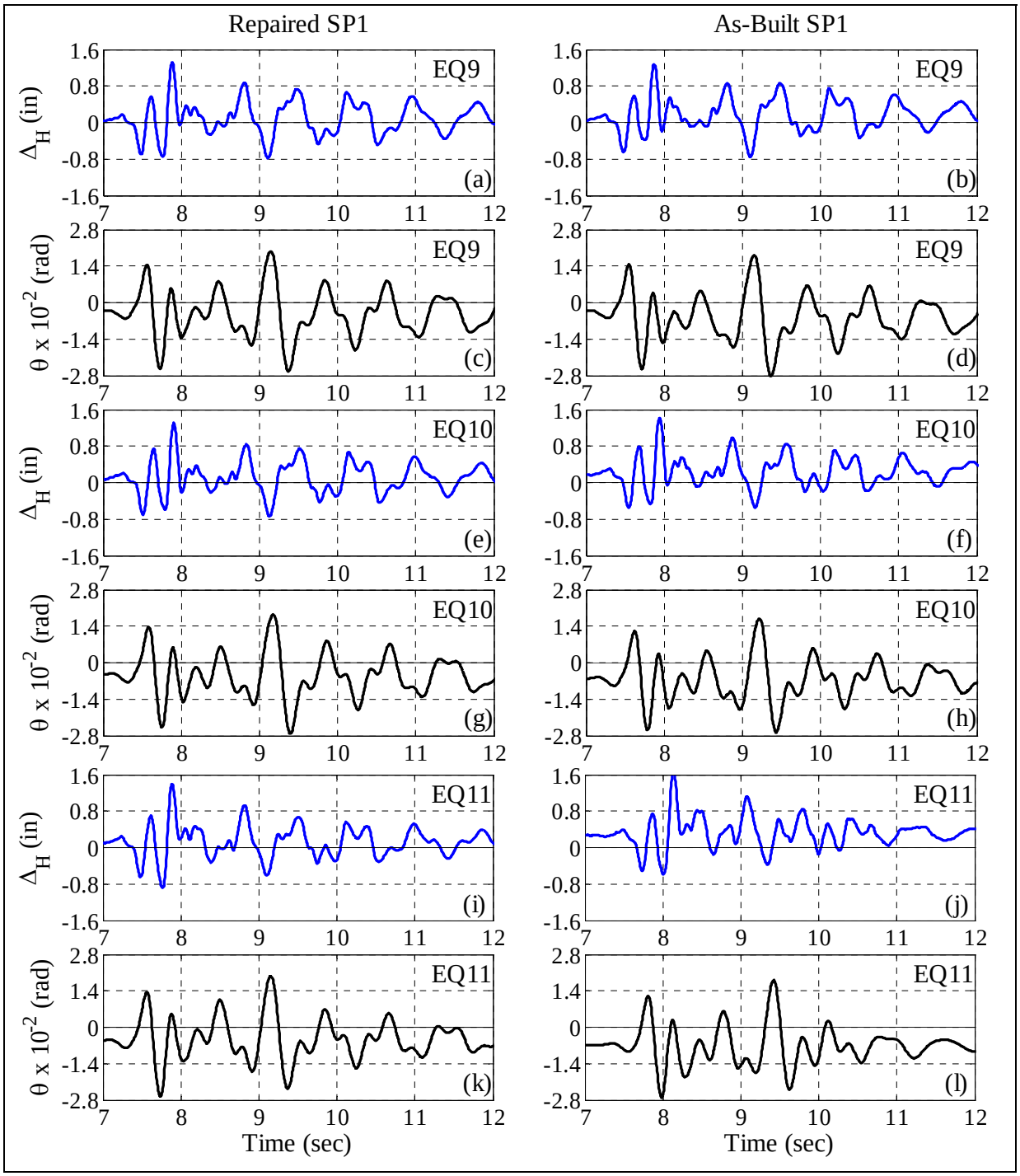

Figure 4.36 Horizontal displacement and top rotation time histories measured during 125%-scaled ground motions.

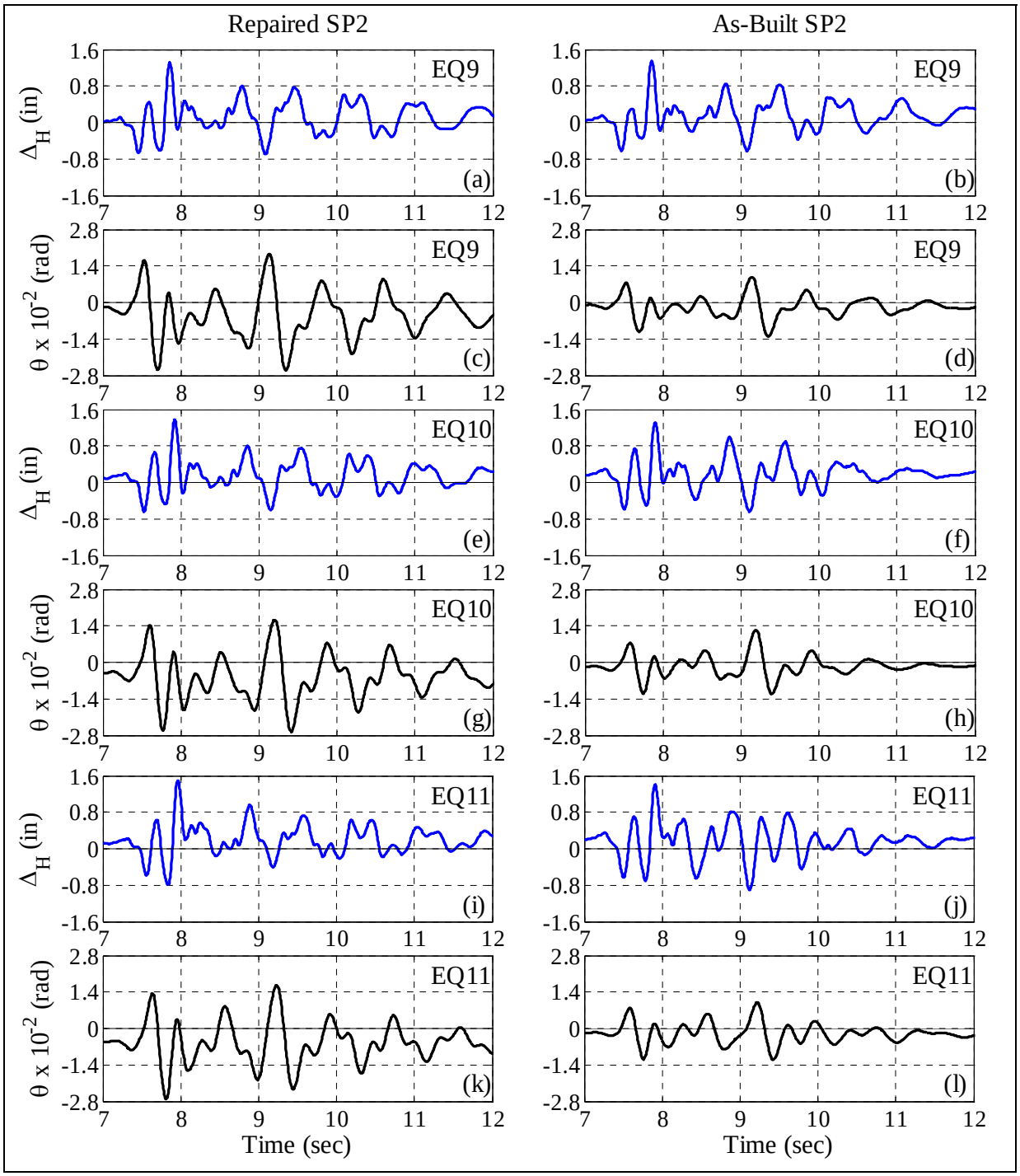

Figure 4.37 Horizontal displacement and top rotation time histories measured during 125%-scaled ground motions.

4.8 BENDING MOMENT RESPONSE

The bending moments at the specimens' column sections were computed by free-body diagram calculations using the horizontal and vertical reaction components measured by the four load cells. Figure 4.38 and Figure 4.39 compare the bending moments at the base and top of the two test specimens SP1 and SP2, respectively. The bending moment time histories of the repaired SP1 were different from the as-built SP1 during the 50%- and 70%-scaled ground motions. The magnitude and frequency of the successive peaks computed in the as-built SP1 were relatively higher than the case of the repaired SP1. This is attributed to the amount of accumulated damage in the repaired SP1 and the as-built SP1 during the 50% and 70%-scaled ground motions, which affected the flexural rigidity of the section. As the ground motion intensity increased to 95%- and 125%-scale, the difference in the bending moment response of the repaired SP1 and the as-built SP1 reduced. On the other hand, the bending moment response of the repaired and as-built SP2 was similar during the loading protocol.

During the strong part of ground motion, i.e. before 8.9 sec in the figures, the bending moment peaks at the base and top of the test specimens were out of phase, which indicated reverse bending. After the strong part of ground motion ended, the phase difference in the bending moment peaks at the base and top of the test specimens reduced until it became finally in-phase. The bending moment response at the top of the test specimens had a higher magnitude than the base due to the higher magnitude of top rotation. The magnitude of the peak strain (confining and longitudinal) and the peak curvature measured at the base of test specimens were lower than those measured at the top of the test specimens as discussed in more details in Chapter 5. This suggested that a relatively higher damage leading to higher flexibility in the concrete core took place near the top of the column.

Figure 4.40 compares the maximum magnitude of the bending moment at the base and the top of the test specimens. During the 125%-scaled ground motions, the maximum bending moment at top of the as-built SP1 and the as-built SP2 remained almost the same. The maximum bending moment at the top of the repaired test specimens increased as the intensity of the ground motions increased. During the 125%-scale ground motions, the maximum bending moment at the top of the repaired SP1 reduced in the absence of the vertical component of ground motion (EQ10). During EQ8, EQ9 and EQ11, the maximum top bending moments of the repaired SP1 were higher than those of the repaired SP2. This is attributed to the higher damage near the top of the as-built SP2 compared to the as-built SP1 prior to the FRP jacket repair, which contributed to the relatively higher flexural rigidity at the top of the repaired SP1 than the repaired SP2.

Figure 4.40c, d compares the maximum bending moment at the base of the test specimens. The difference in the magnitude of the maximum bending moment at the base of the two repaired test specimens was less than the difference at the top. The increment of maximum bending moment at the base of the repaired SP1 was almost linear from the 5%- to the 125%-scaled ground motions. This was not observed in the case of the repaired SP2. During 50%- and 125%-scaled ground motions, the maximum bending moment at the base of the repaired SP1 increased by 15% and 13%, respectively in the absence of the vertical component of ground motions (EQ6 and EQ10). On the other hand, the maximum bending moment at the base of the repaired SP2 remained almost the same during EQ5 and EQ6 and only increased by 10% from EQ9 to EQ10.

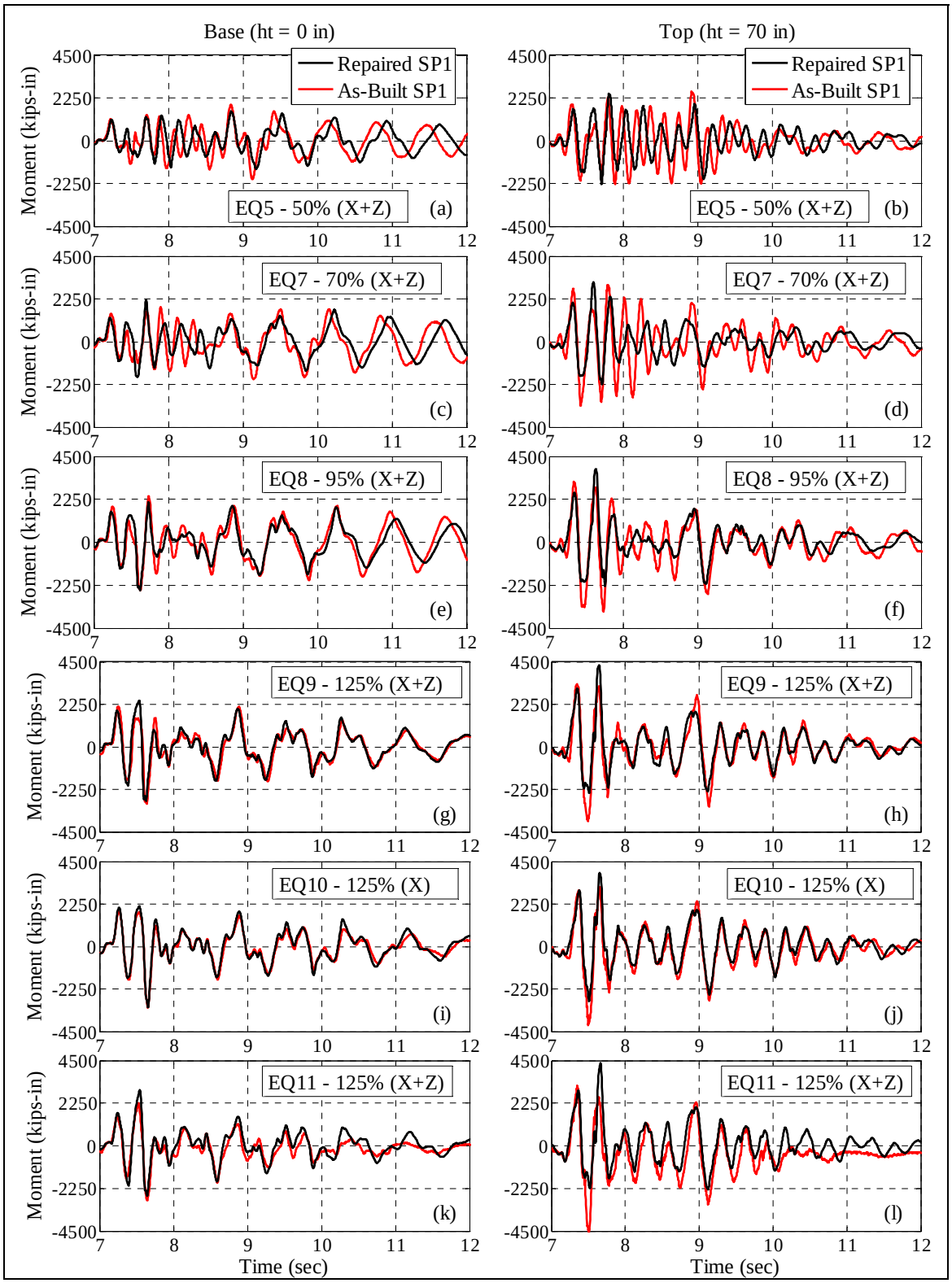

Figure 4.38 Bending moment time histories for SP1 tests.

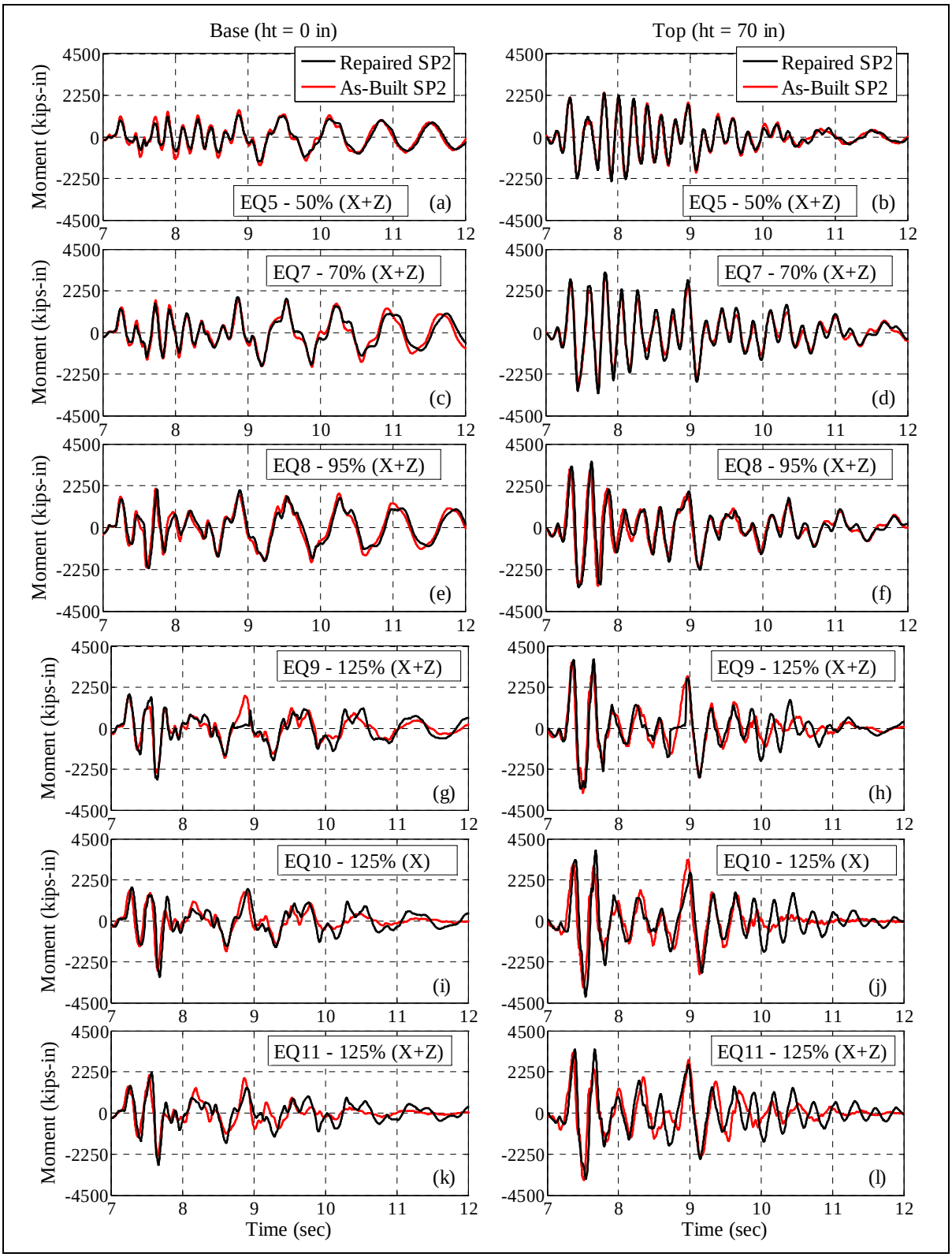

Figure 4.39 Bending moment time histories for SP2 tests.

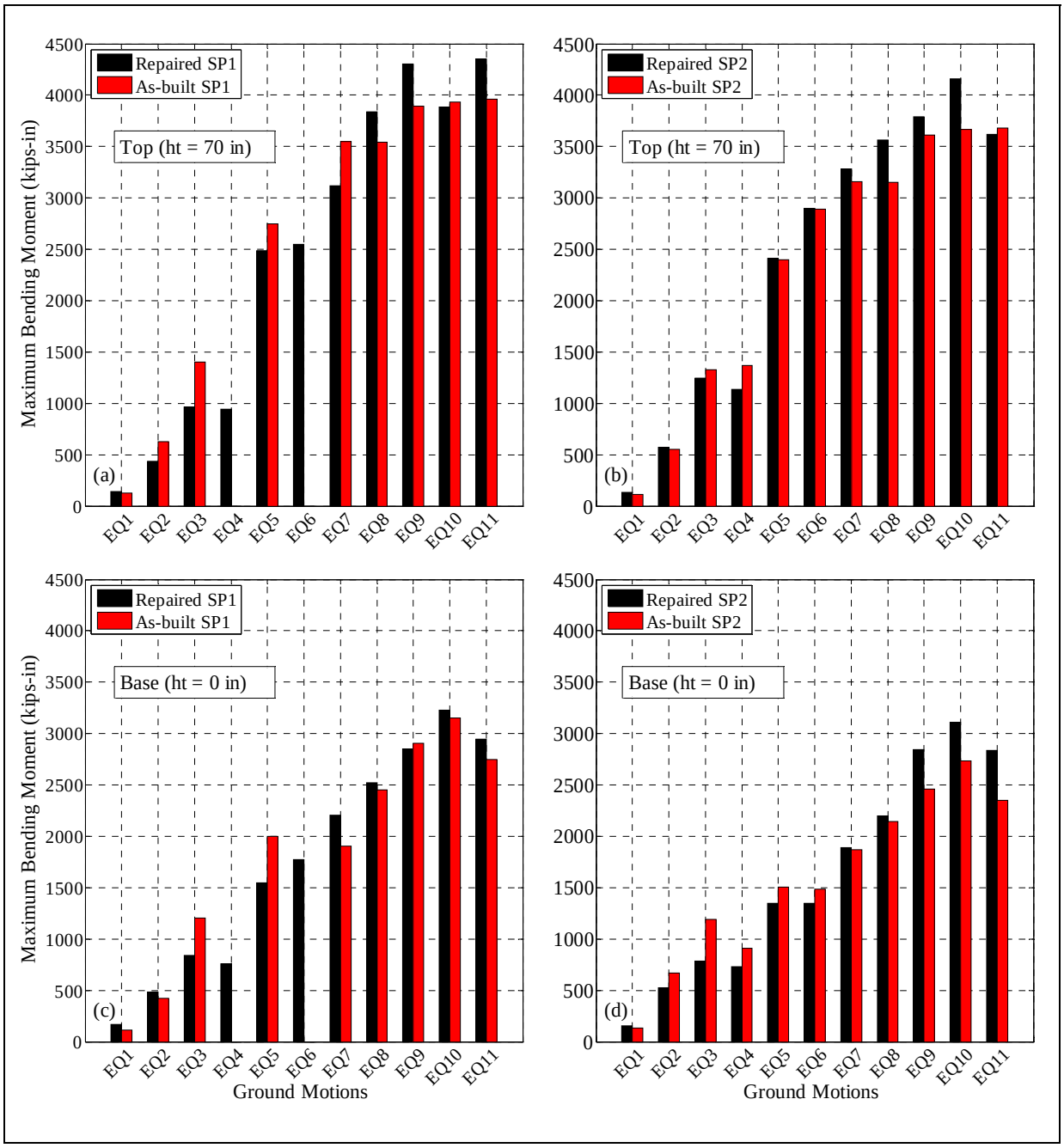

Figure 4.40 Maximum bending moment comparison.

4.9 FORCE-DISPLACEMENT RESPONSE

The shear force and the axial loads were computed by adding the reaction components measured by individual load cell in the X-direction and Z-direction, respectively. The lateral stiffness of the horizontal force-deformation response was computed as the ratio of the maximum shear force to the corresponding lateral displacement measured towards the North (or the South) side of the test specimen. It was observed that the average lateral stiffness of the test specimens (average of North and South side lateral stiffness) reduced as the intensity of ground motion increased.

Figure 4.41 and Figure 4.42 show the shear force-displacement relationship plots of the test specimens. The lateral stiffness of the repaired and the as-built SP1 was almost the same during the low intensity ground motions (5%- to 50% scale). During EQ7 and EQ8, the lateral stiffness of the repaired SP1 was less than that of the as-built SP1 (Figure 4.41). During the 125%-scaled ground motions, the stiffness of the repaired and as-built SP1 towards the North side was almost the same. The difference in the magnitude of the lateral stiffness measured to the North and South side of the force-displacement response of the repaired SP1 was lower than the as-built SP1. The lateral stiffness of the as-built SP1 had relatively higher reduction towards the North than the South side (Figure 4.42).

The force- displacement response of the repaired and as-built SP2 was almost similar during EQ5, EQ7 and EQ8 (Figure 4.41). During the 125%-scaled ground motions, the North side stiffness of the repaired SP2 was slightly higher than the as-built SP2. It is noted that the repair of the damaged as-built specimens was done mainly to improve the confinement of the column sections. The response of the repaired specimens was almost similar to the force-displacement response of their as-built counterparts, during the 50%-, 70%- and 95%-scaled ground motions. However, during the 125%-scaled ground motions (EQ9, EQ10 and EQ11), the force-displacement response of the repaired test specimens was better than the as-built specimens. This is due to the higher magnitude of the resisted base shear, relatively lower difference in maximum D.R. magnitudes measured towards the North and the South side, and the lower magnitude of the residual D.R. (Figure 4.42).

Figure 4.43 (a) through (d) show the cumulative force-displacement response of the test specimens. Based on the maximum shear force measured during each ground motion and the corresponding measured displacement, an idealized elasto-plastic envelope curve was obtained as shown in Figure 4.43e, f. The idealized curve of the repaired and the as-built SP1 was almost the same towards the North side. The response of the repaired SP1 towards the South end had lower stiffness than the as-built SP1. This is attributed to the higher damage on the South face of the as-built SP1 compared to the North face. The South side stiffness and the effective yield points on the envelope curve of the repaired and the as-built SP2 were almost the same. On the North side, the yield force and the corresponding displacement of the as-built SP2 was lower than the repaired SP2. The idealized displacement ductility was computed as the ratio of the maximum displacement to the effective yield displacement of the test specimens. Since the maximum displacement in all the test specimens was measured towards the North side (positive), the ductility values were computed using the positive plot data. The idealized displacement ductility of the repaired SP1 and SP2 was 3.48 and 3.85, respectively, while the idealized displacement ductility of the as-built SP1 and SP2 was 3.61 and 4.11, respectively. Only the displacement ductility of the as-built SP2 exceeded the design displacement ductility of 4.0 per the Seismic Design Criteria (SDC) [11],[12].

The last response quantity considered in studying the global response of the test specimens was the hysteretic energy adopted from the force-displacement relationships. Figure 4.44 and Figure 4.45 compare the input earthquake energy with the dissipated hysteretic energy for SP1 and SP2. The input energy was computed as follows,

$$E_{Input} = M \int_0^{t_D} a_g(t) v(t)\, dt \tag{4.8}$$

where M is the superstructure mass, $a_g(t)$ is the input acceleration measured at the base of the test specimen using averaged accelerometer data from the four 3D accelerometers mounted on the base steel plate, $v(t)$ is the relative velocity of the column top with respect to the foundation derived from the accelerometer data attached to the top mass block, and t_D is the total duration of the input ground motion.

The shaking table motions at the same intensity scale level had slightly different input energy as it depends on the relative velocity of the column top and the measured base accelerations. On the other hand, the dissipated hysteretic energy was computed as the area enclosed by the force-displacement relationship as follows,

$$E_{Hysteresis} = \int_0^{t_D} f_{shear}(t)\, du(t) \tag{4.9}$$

where $f_{shear}(t)$ is the shear force measured using the load cells at the base of the test specimen and $u(t)$ is the relative displacement of column top measured using the horizontal wire potentiometers. The repaired specimens were able to dissipate almost the same amount of energy as measured from the as-built specimens. For the 125%-scaled ground motions, the repaired specimens dissipated almost the same amount of energy. On the other hand, for the as-built specimens, the hysteretic energy values varied, which is attributed to more progression of damage for the as-built specimens than that for the repaired counterparts during this repeated part of the loading protocol.

Figure 4.46 and Figure 4.47 show the axial load-vertical displacement response of the repaired and as-built test specimens measured during EQ5 through EQ11. The difference in the magnitude of the maximum and minimum axial load measured at the base of the repaired specimens was higher than their as-built counterparts. The repair of the test specimens was done to improve the shear strength capacity of the damaged as-built test specimens without any significant improvement in the design axial response. The vertical displacements measured in the repaired test specimens were higher than the as-built test specimens. No significant tensile forces were measured in the test specimens before the 125%-scaled ground motions. Similar to the horizontal force-deformation response, the hysteretic energy dissipated during the vertical force-displacement response of the repaired specimens was higher or almost equal to the as-built specimens.

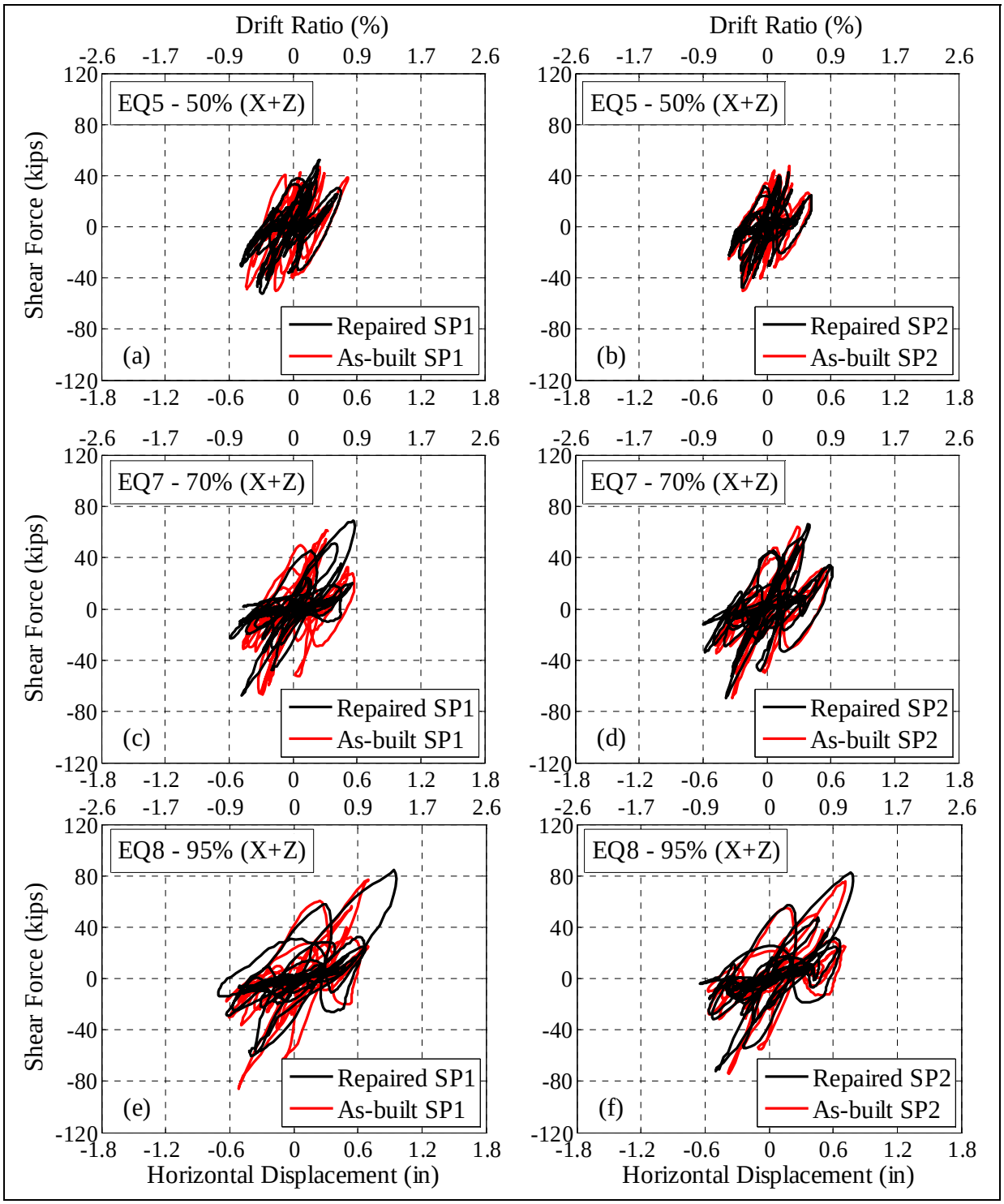

Figure 4.41 Shear force-top displacement response.

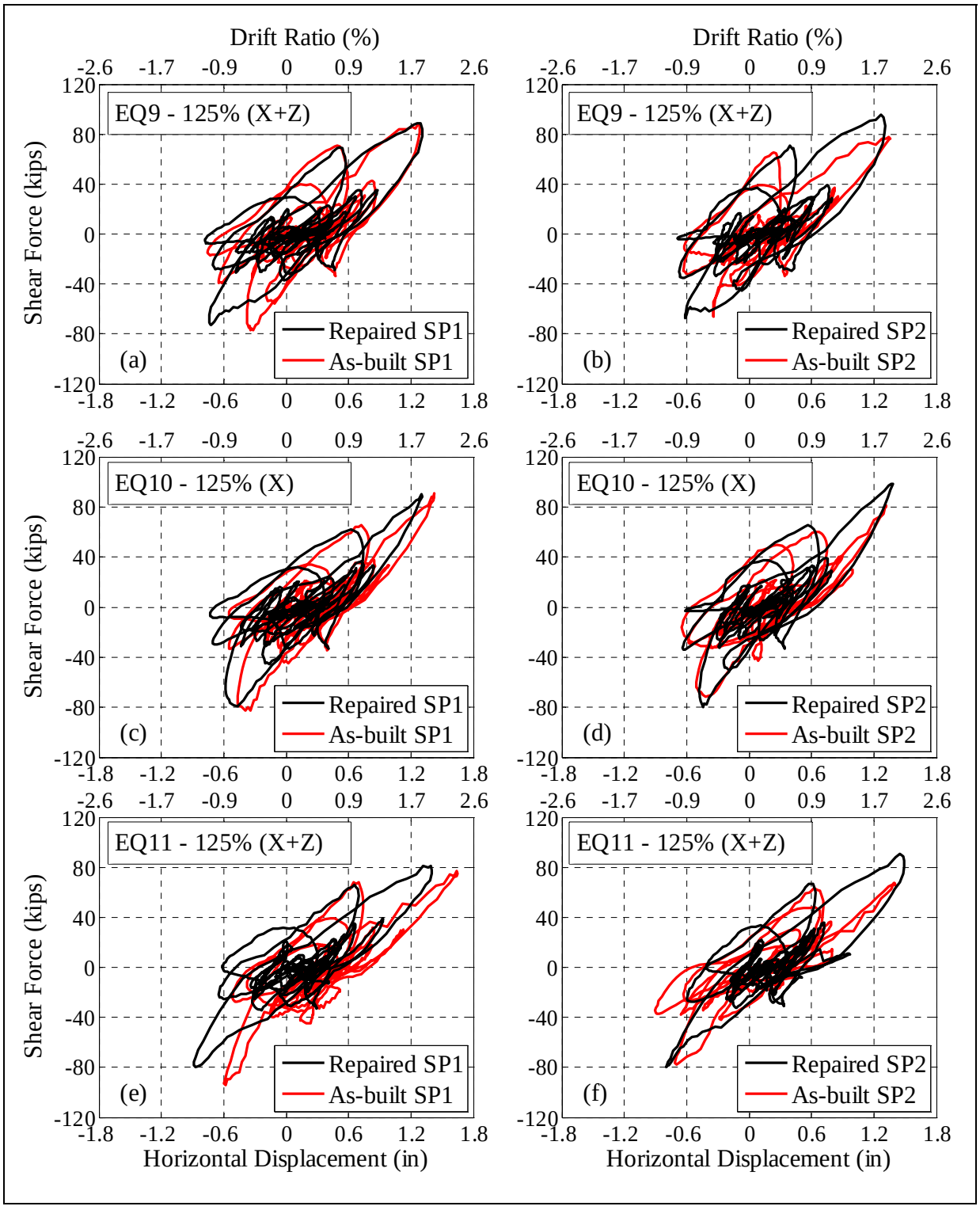

Figure 4.42 Shear force versus horizontal-top displacement response.

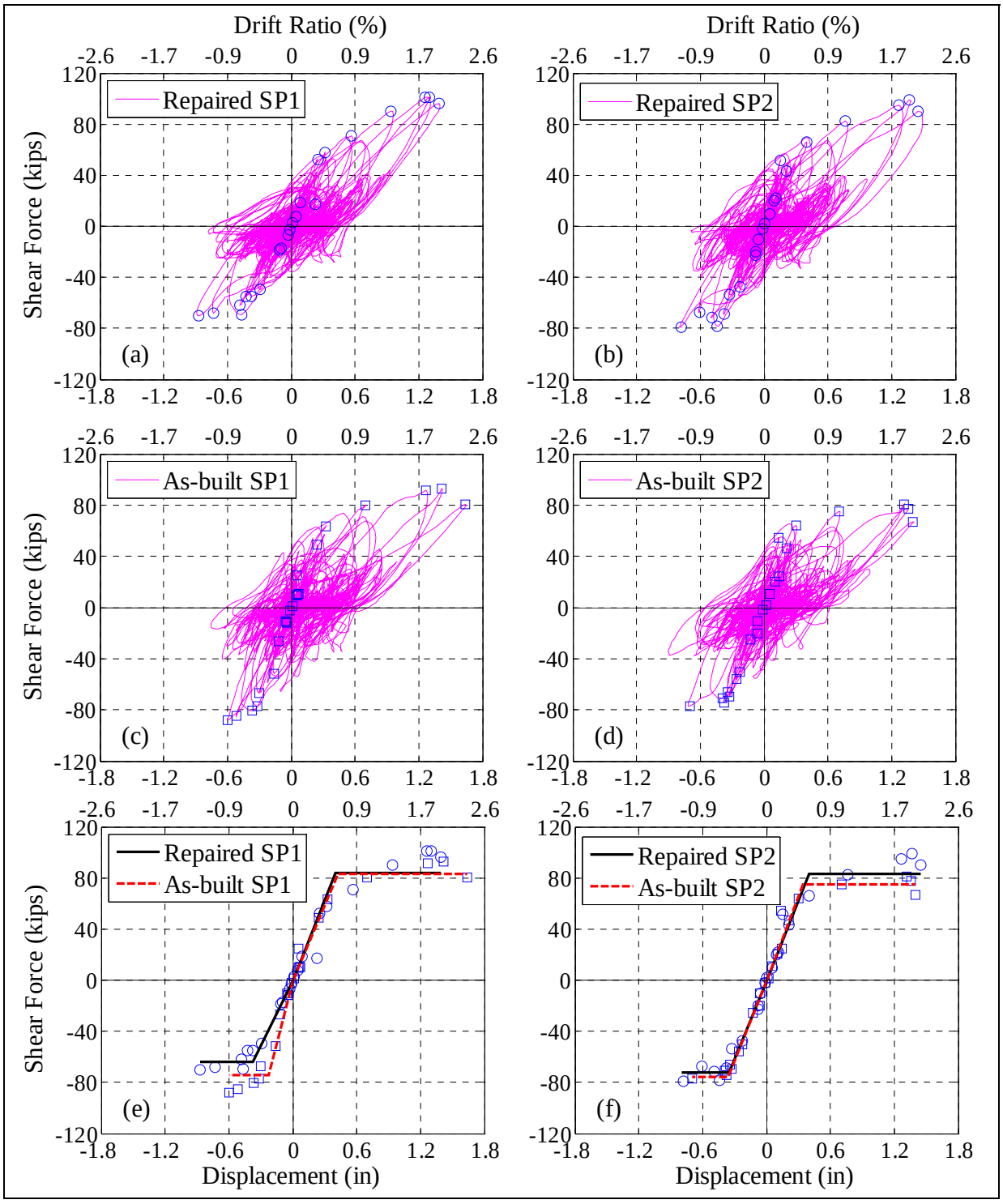

Figure 4.43 Cumulative shear force versus horizontal-top displacement response: (a) repaired SP1; (b) repaired SP1; (c) as-built SP1; (d) as-built SP2; (e) idealized envelop of repaired and as-built SP1; (f) idealized envelop of repaired and as-built SP2.

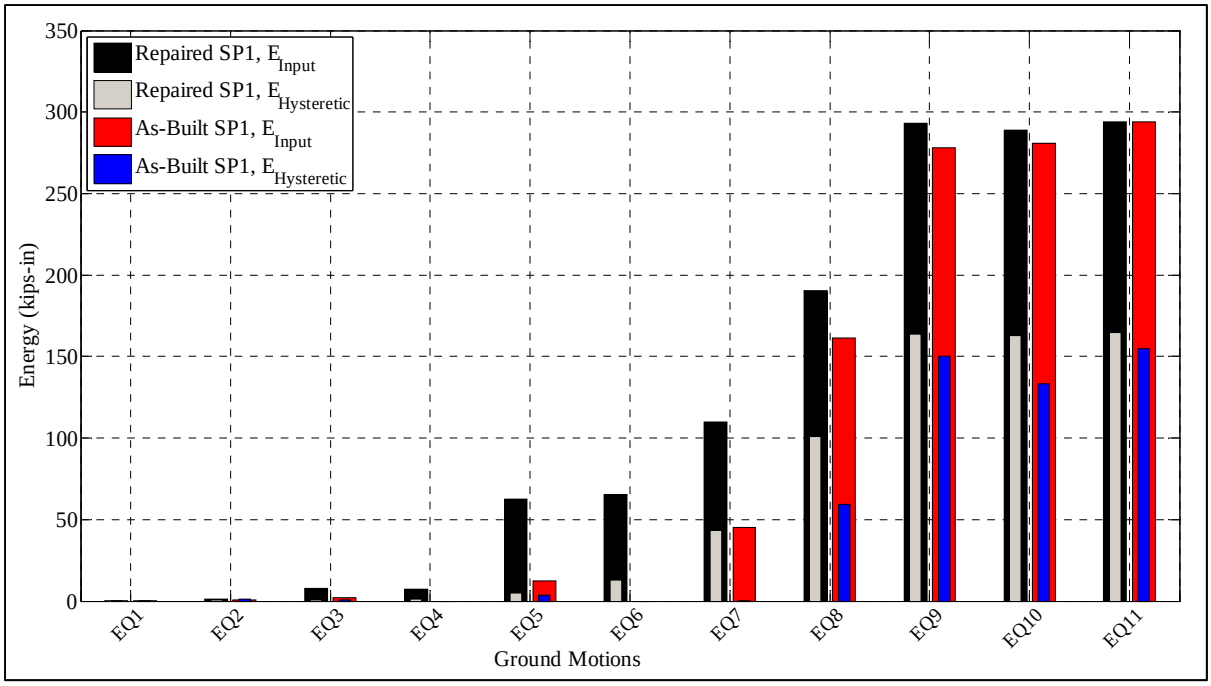

Figure 4.44 Input energy and hysteretic energy of the repaired and the as-built SP1.

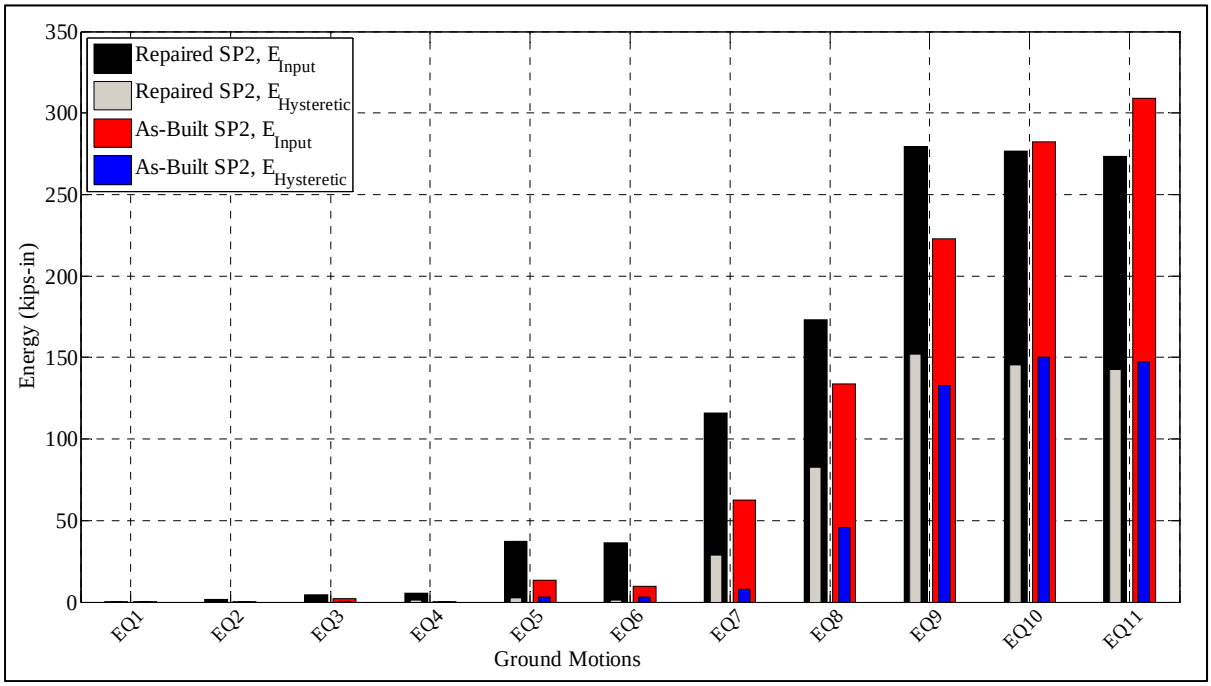

Figure 4.45 Input energy and hysteretic energy of the repaired and the as-built SP2.

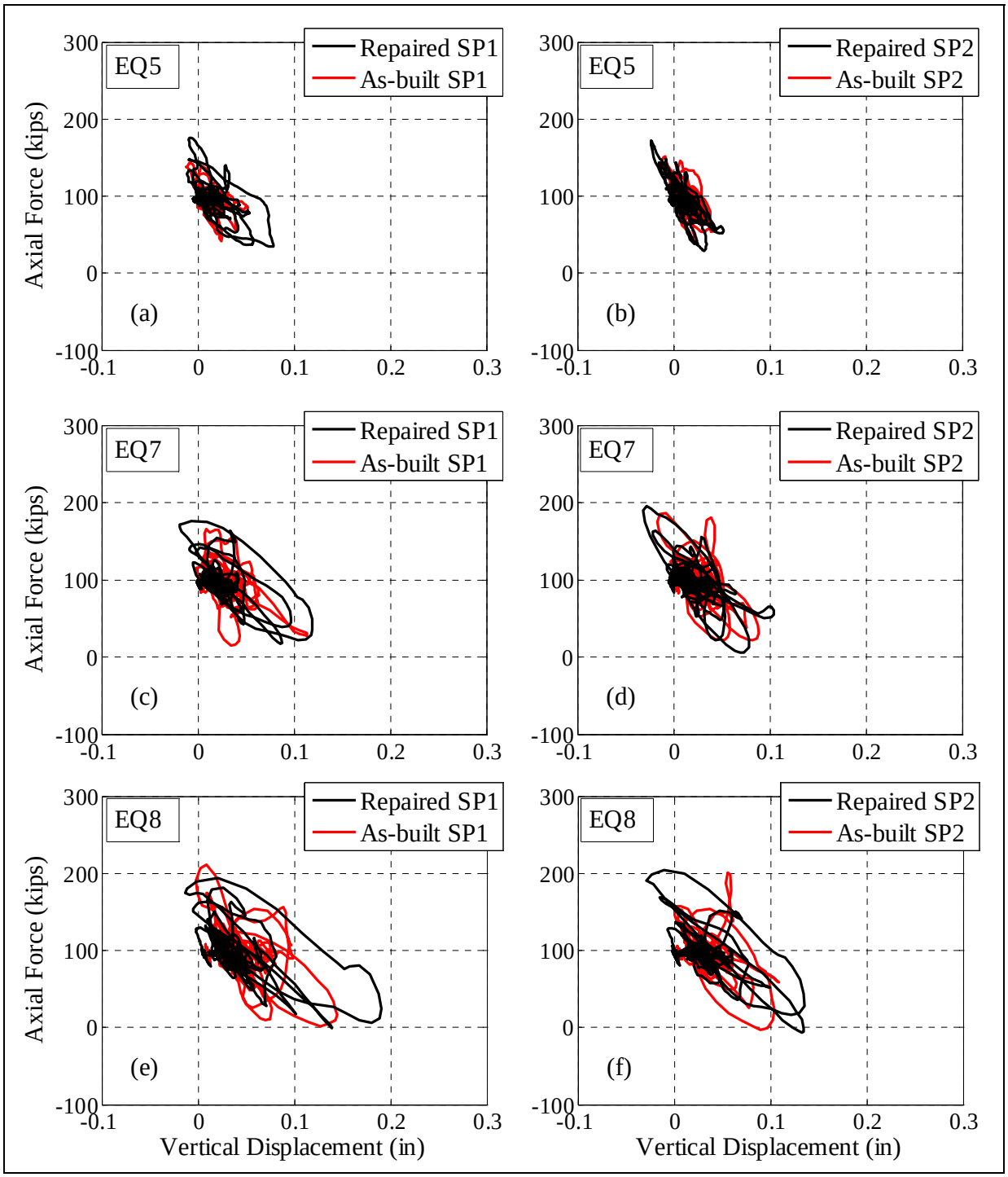

Figure 4.46 Axial force versus vertical displacement response.

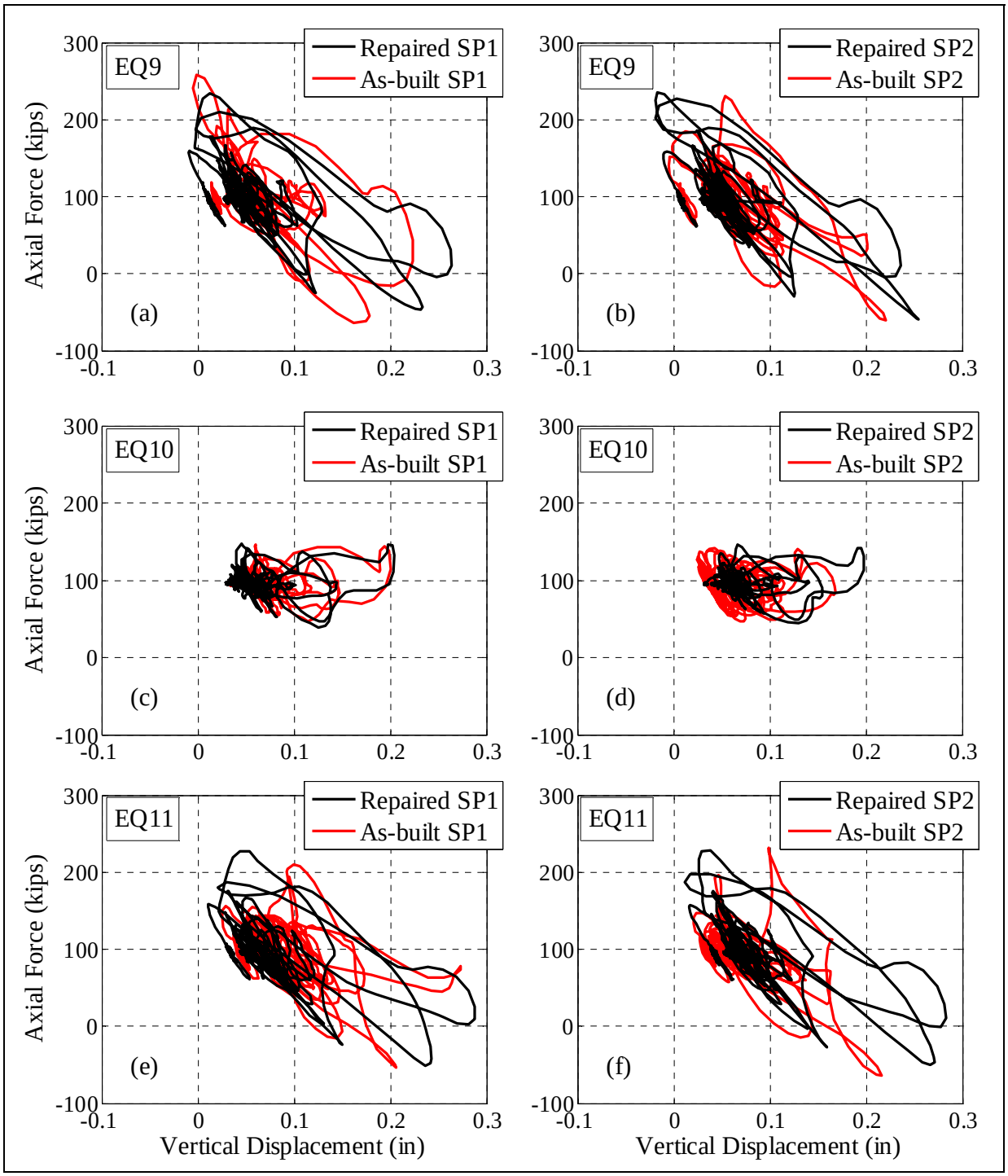

Figure 4.47 Axial force versus vertical displacement response.

Chapter 5. Local Response

5.1 INTRODUCTION

This chapter focuses on the local response of the test specimens measured during the shaking table testing of the repaired specimens. Strain gauges in both longitudinal and transverse directions were used to compute the strains and the curvatures at different column cross-sections. Section 5.2 discusses the longitudinal strains measured at the different locations along the column height. Some strain gauges were damaged during the dynamic testing of the as-built specimens and the repair that followed the as-built specimens' tests. In general, the longitudinal strains measured in the repaired test specimens were less than their as-built counterparts. The confining strains in the repaired test specimens were measured using strain gauges installed on the FRP jackets. Section 5.3 discusses the confining strains of the FRP jackets in more details. The confining strains in the GFRP jacket were less uniformly distributed around the circumference of the column cross-sections than the CFRP jacket as discussed later. The curvatures at the different sections of the test specimens were computed using Linear Vertical Displacement Transducers (LVDTs) and are discussed in Section 5.4. The curvature data showed that the test specimens were in double curvature during phase-I of a given run, which is the strong part of the ground motion. However, only single curvature was observed during the free vibration phase of a given run (phase-II). Section 5.5 discusses the Moment-Curvature (MC) response of the test specimens. Similar to the force-displacement response (Section 4.9), the MC response of the repaired test specimens suggested higher energy dissipations than the as-built test specimens. In this chapter, the locations of all instrumented sections are defined in terms of the height above the base of the cantilever columns.

5.2 LONGITUDINAL STRAINS RESPONSE

The longitudinal strains at the different cross-sections of the test specimens were measured using the strain gauges installed on the longitudinal steel bars prior to the casting of concrete. Some of the strain gauges were damaged during the construction, testing, and then, the repair of the as-built test specimens. This reduced the overall number of strain measurement locations in the repaired test specimens (Section 3.2). In this section, the tensile strains were assigned the positive sign and the compressive strains were assigned the negative sign. The yield strain (ε_y) of the longitudinal steel bars in the repaired test specimens was assumed 0.25%, which was the same as measured during the uniaxial material testing of the #5 rebar coupons (Section 2.6). It is to be noted that the yield strain of the reinforcing bars in the repaired test specimens was expected to be higher than the as-built test specimens due to the repeated stress-strain cycles

during the dynamic testing. In order to compare the strain response of the as-built and the repaired test specimens, the yield strain value was kept the same for a fixed benchmark. The strains measured on the East and West faces of the repaired test specimens, which was the orthogonal direction to the direction of loading, did not show any significant variation during the loading protocol and were less than the ε_y.

The longitudinal strains measured on the North and South face of the test specimens were out-of-phase during the testing. During the strong part of ground motions (phase-I, Section 4.6), the strains measured on the same face (North/South) near the base and top of the test specimens were out-of-phase. However, the phase difference was reduced during the free vibration phase (phase-II, Section 4.6). This suggested that the test specimens were in double (reverse) bending during phase-I and only single bending during phase-II. This was also verified by the curvatures measured along the column height of the test specimens as discussed in a following section (Section 5.4). From EQ1 through EQ4, the longitudinal strains measured along the column height of the test specimens were less than ε_y.

The first longitudinal strain peak exceeding ε_y in both test specimens was measured during the 50%-scaled ground motion (EQ5) as shown in Figure 5.1. It is noted that during EQ5 the maximum tensile strain measured on the North face of the repaired SP2 was $0.85\varepsilon_y$. The strain distribution trend of the repaired and the as-built SP2 was similar during the entire loading protocol at the common instrumented locations. Thus, it was assumed that near the column top of the repaired SP2, the longitudinal strain measured on the South face might be higher than those measured on the North face (closer to the ε_y). During EQ5 through EQ8, the longitudinal strain time histories measured at the height of 30 in (762 mm) and 40 in (1016 mm) above the column base of the repaired SP1 were almost similar (Figure 5.1 through Figure 5.3). During the same ground motion range, the strain histories measured in the repaired SP2 at the height of 20 in (508 mm), 30 in (762 mm), 40 in (1016 mm), and 50 in (1270 mm) were almost similar (Figure 5.1 to Figure 5.3). The maximum magnitude of the longitudinal strain near the top and the base of the column was observed during the phase-I in case of EQ5, and phase-II in case of EQ7 (Figure 5.1 and Figure 5.2).

Figure 5.4 through Figure 5.6 show the longitudinal strain time histories of the repaired and the as-built SP1 for comparison purposes. The strains are shown along with the three DOF defined in term of the horizontal drift ratio (D.R.), vertical displacement (Δ_v) and rotation (θ) measured at the column top during the 125%-scaled ground motions. The plotted strain time histories were measured at the height of 60 in (1524 mm) above the column base. The maximum magnitude of the strains on the North and the South faces of the repaired and as-built SP1 was measured during phase-I of a given ground motion. The maximum tensile strain on the South face, maximum D.R towards the South, the first significant Δ_v peak, and the maximum θ were all observed at the same time instant. Similarly, the maximum tensile strain on the North face, maximum D.R. towards North, and the second significant Δ_v peak (absolute maximum) were obtained at the same time instant. The magnitude of θ was relatively lower at the time instant of the maximum tensile strain on the North face than the South face. This resulted in higher damage (cracking and crack openings) on the South face, and thus, the magnitude of the tensile strains measured on the South face was higher than those measured on the North face. Moreover, the magnitude of the compressive strains measured in the repaired and as-built SP1 was less than ε_y, during the entire loading protocol.

Figure 5.7 through Figure 5.9 show the D.R., Δ_v, θ, and the longitudinal strain histories of the repaired and the as-built SP2 measured during the 25%-scaled ground motions. The strain data was measured on the North face of the test specimens about 60 in above the column base. Similar to the repaired SP1, the longitudinal strain response measured on the North face in case of the repaired SP2 was influenced by the magnitude and the orientation of the three DOFs. Due to the high residual strain in the as-built SP2, the magnitude of the strain measured in the repaired SP2 was lower than that measured in the as-built SP1. The maximum magnitude of the longitudinal strains in the repaired SP2 was measured during phase-I of the 125%-scaled ground motions. On the other hand, the significant longitudinal strain peaks in the as-built SP2 were measured during the phase-I and phase-II of the 125%-scaled ground motions. During EQ10 and EQ11, the maximum strain measured during the phase-II exceeded that measured during the phase-I.

Figure 5.10 and Figure 5.11 show the maximum longitudinal strains measured on the North and South face of the test specimens during 50%- through 125%-scaled ground motions. It is to be noted that the strain gauge data of the as-built SP1 at the height of 40 in (1016 mm) and 50 in (1270 mm) was not correct and is not shown in the figures. The maximum longitudinal strains measured in the repaired SP1 were higher than the repaired SP2 (at same locations). During the 125%-scaled ground motions, the maximum strains measured in the as-built test specimens were higher than the repaired test specimens.

During the entire loading protocol, the maximum longitudinal tensile strains measured in the as-built SP1 and SP2 was about $11.5\varepsilon_y$ and $7.8\varepsilon_y$, respectively. Moreover, for the repaired SP1 and SP2 tests, the maximum strains were $7.2\varepsilon_y$ and $4.1\varepsilon_y$, respectively. Due to the relatively higher tensile forces in the as-built test specimens, the shear and flexure cracks were accompanied by excessive spalling of the cover concrete near the column top, which led to reducing the aggregate-interlock action. This could have contributed to the higher magnitude longitudinal strains in the exposed longitudinal steel bars of the as-built specimens than the repaired specimens. That is because in the repaired specimens no concrete spalling was observed and the FRP jackets remained intact during the entire loading protocol. The higher magnitude of the residual D.R. could also have contributed to the relatively higher magnitude of the longitudinal strain in the as-built specimens than their repaired counterparts. Figure 5.12 and Figure 5.13 show the strain histories measured on the East and the West side of the test specimens during the 125%-scaled ground motions. The maximum strain magnitude measured during EQ9 and EQ11 was less than ε_y. The magnitude of the longitudinal strains measured on the East and West face of the repaired test specimens was lower than that measured in the as-built test specimens.

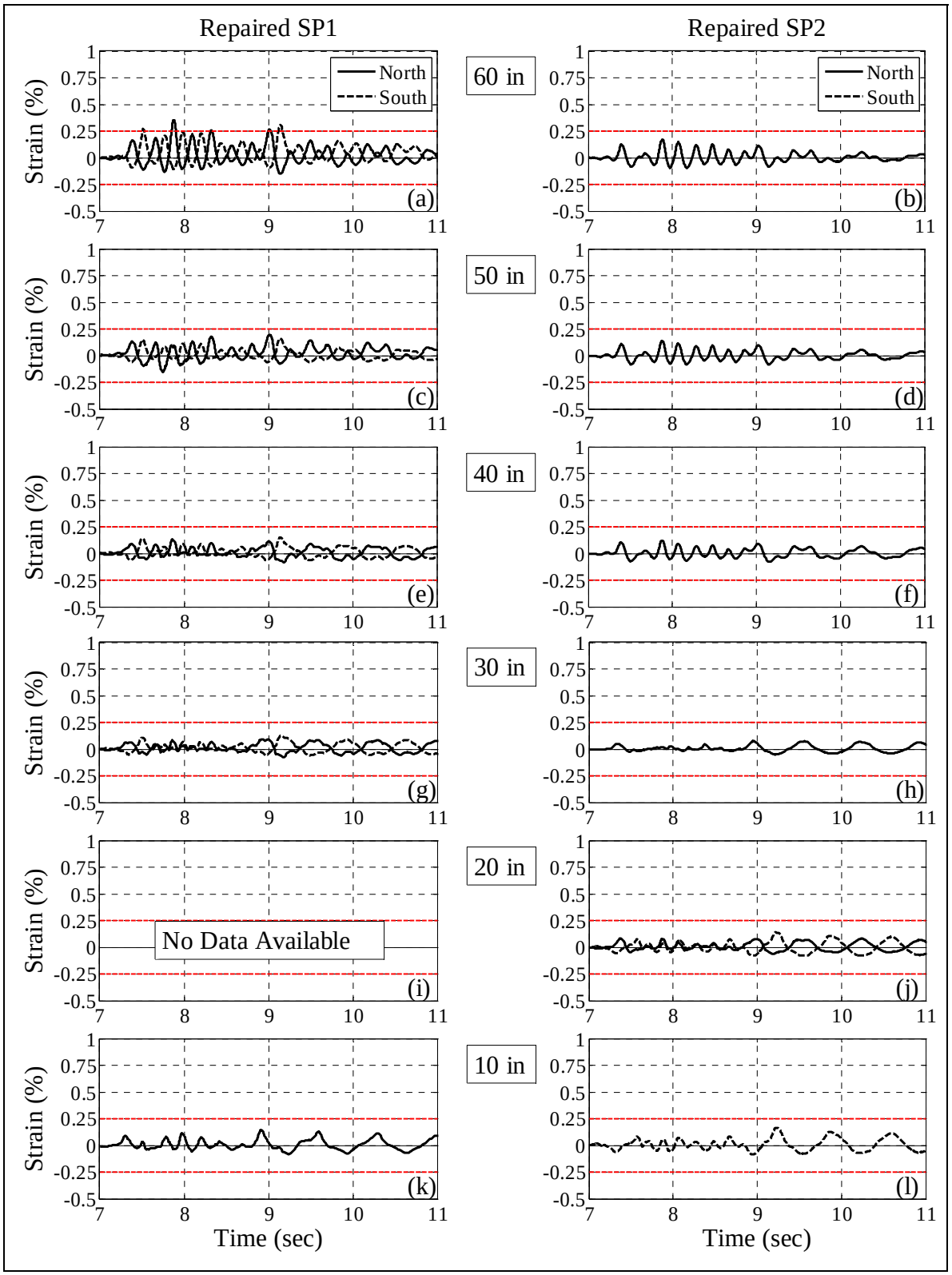

Figure 5.1 Longitudinal strain histories measured during EQ5.

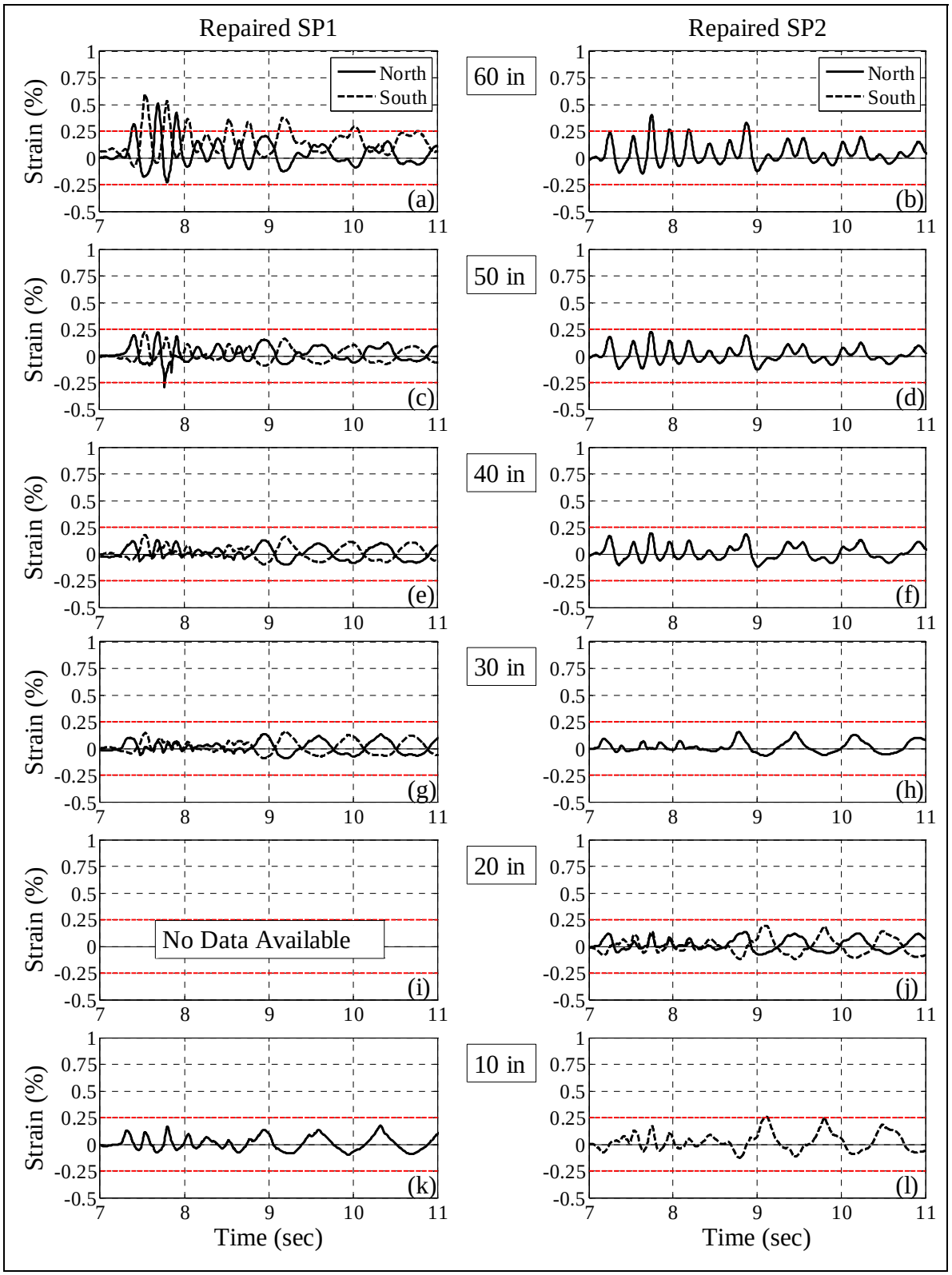

Figure 5.2 Longitudinal strain histories measured during EQ5.

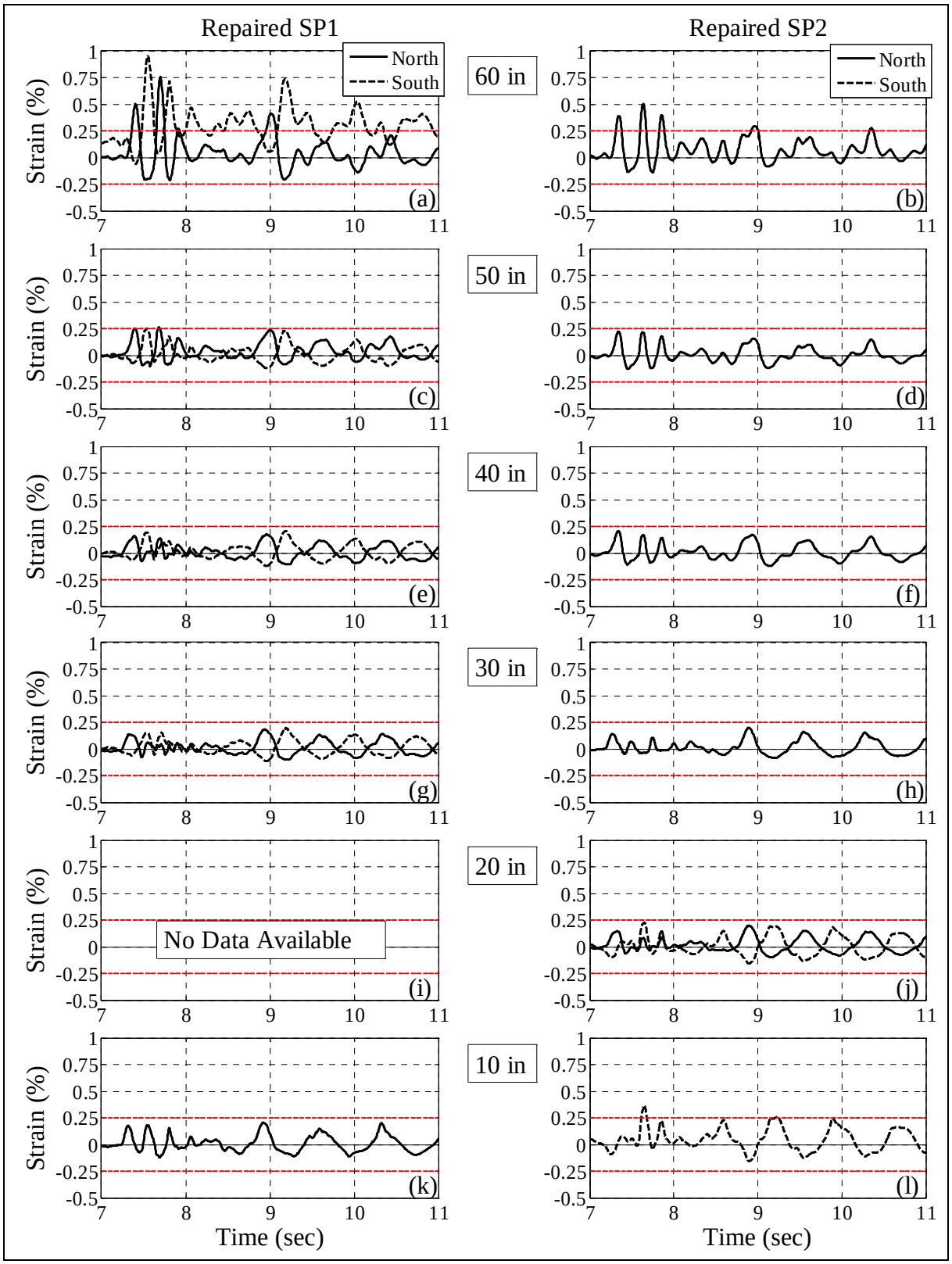

Figure 5.3 Longitudinal strain histories measured during EQ8.

.

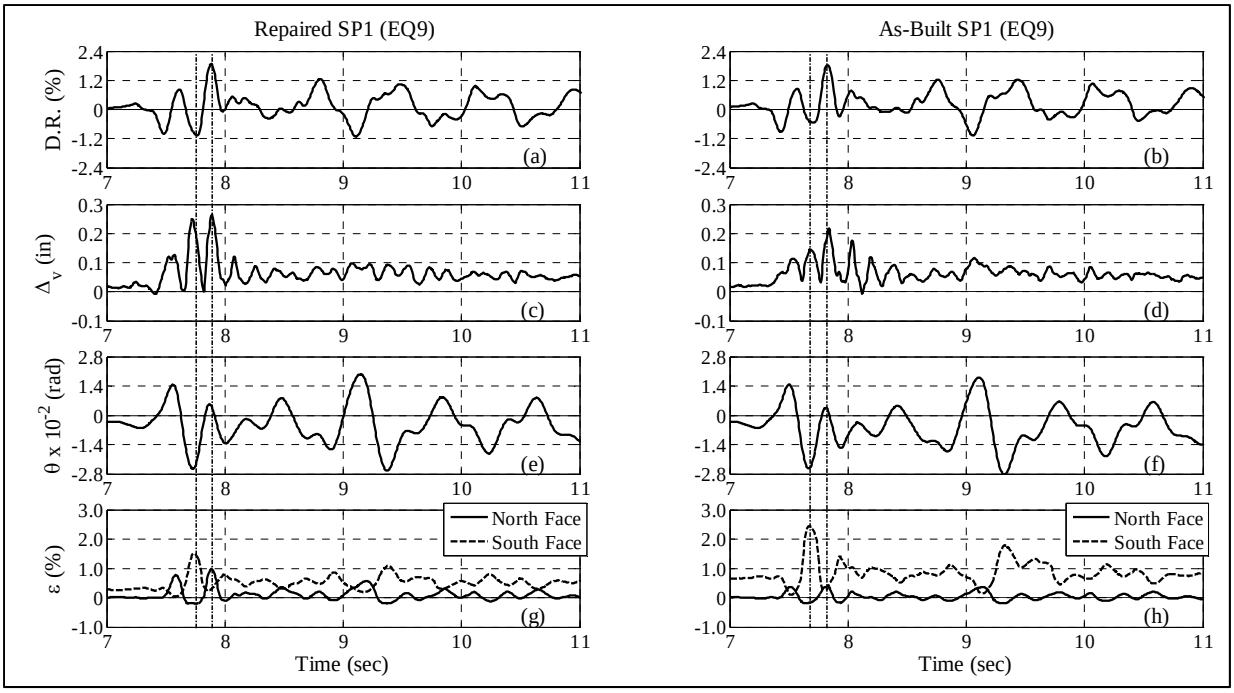

Figure 5.4 Drift ratio (D.R.), vertical displacement (Δ_V), top rotation (θ), and longitudinal strain (ε) measured near the top.

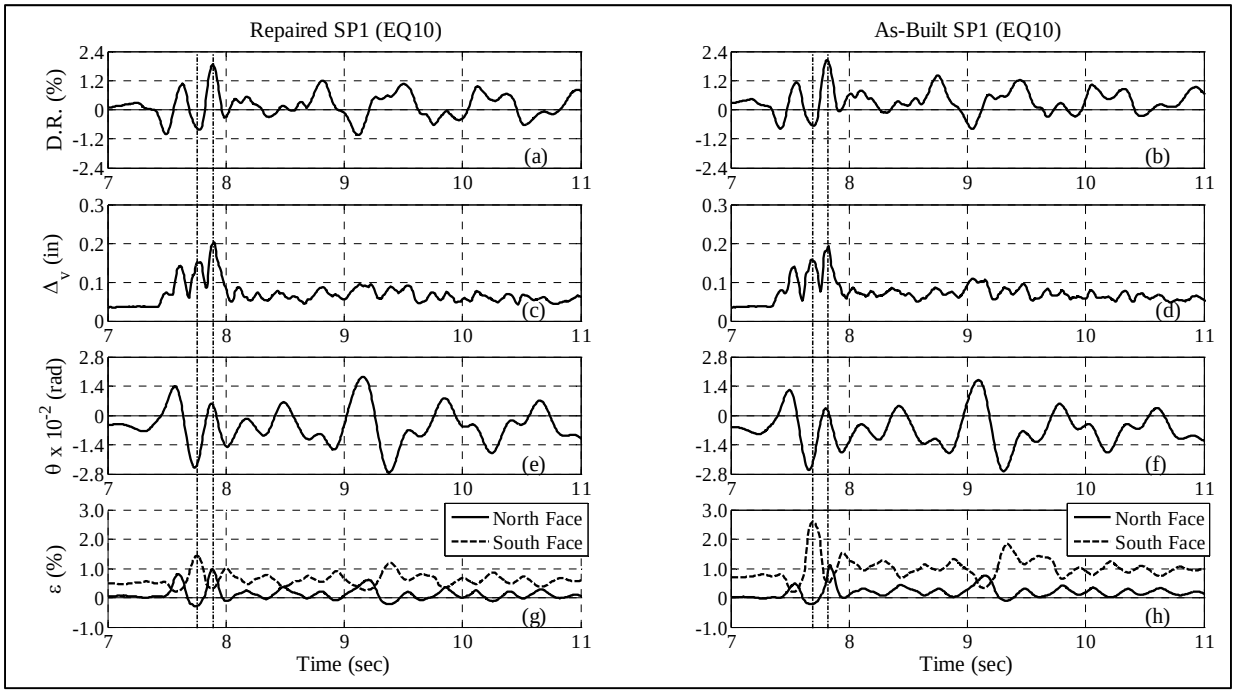

Figure 5.5 Drift ratio (D.R.), vertical displacement (Δ_V), top rotation (θ), and longitudinal strain (ε) measured near the top.

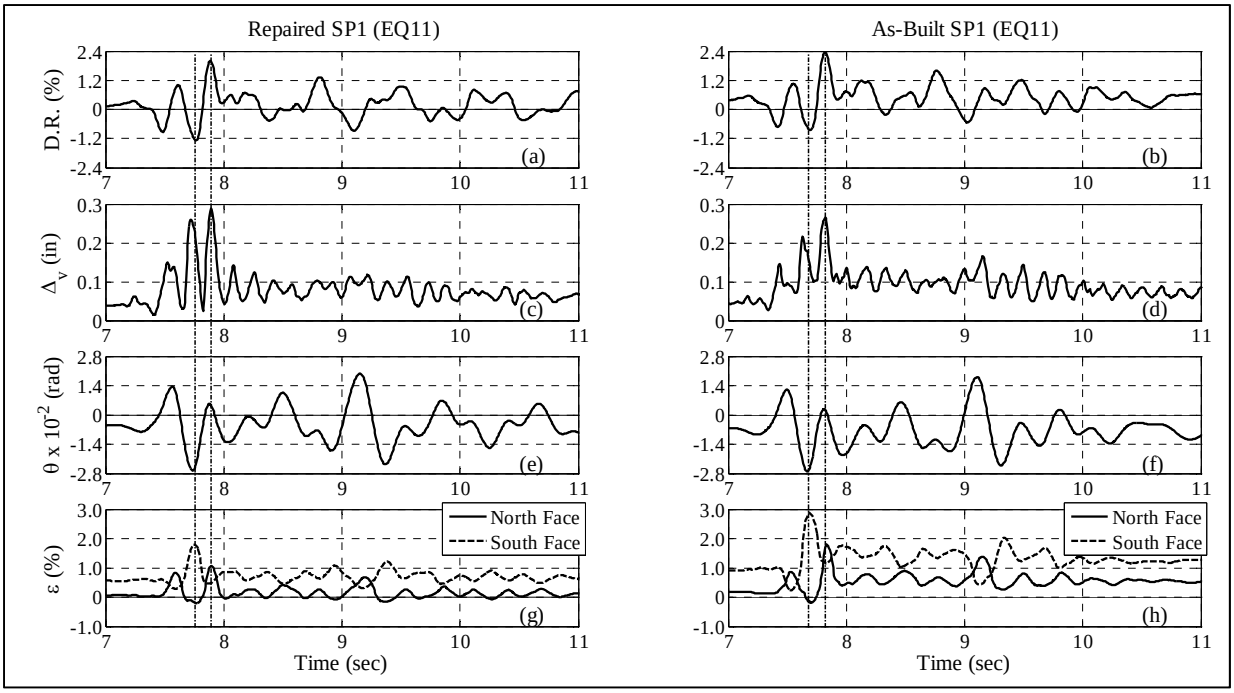

Figure 5.6 Drift ratio (D.R.), vertical displacement (Δ_V), top rotation (θ), and longitudinal strain (ε) measured near the top.

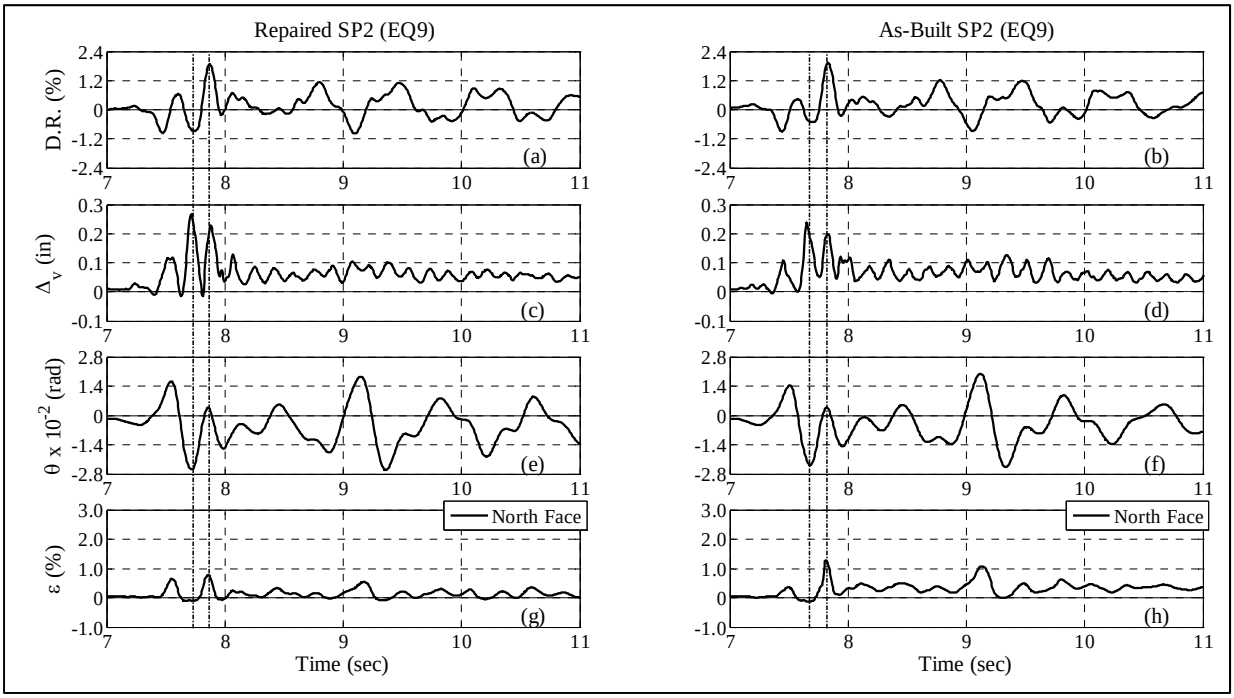

Figure 5.7 Drift ratio (D.R.), vertical displacement (Δ_V), top rotation (θ), and longitudinal strain (ε) measured near the top.

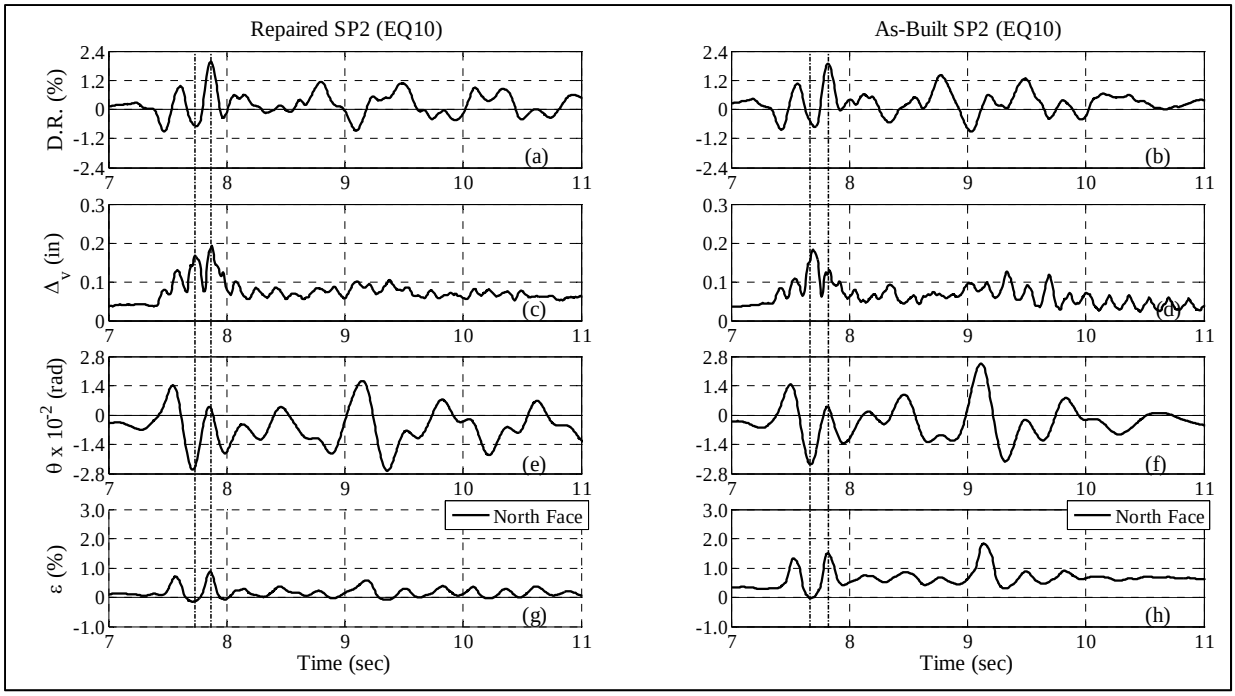

Figure 5.8 Drift ratio (D.R.), vertical displacement (Δ_V), top rotation (θ), and longitudinal strain (ε) measured near the top.

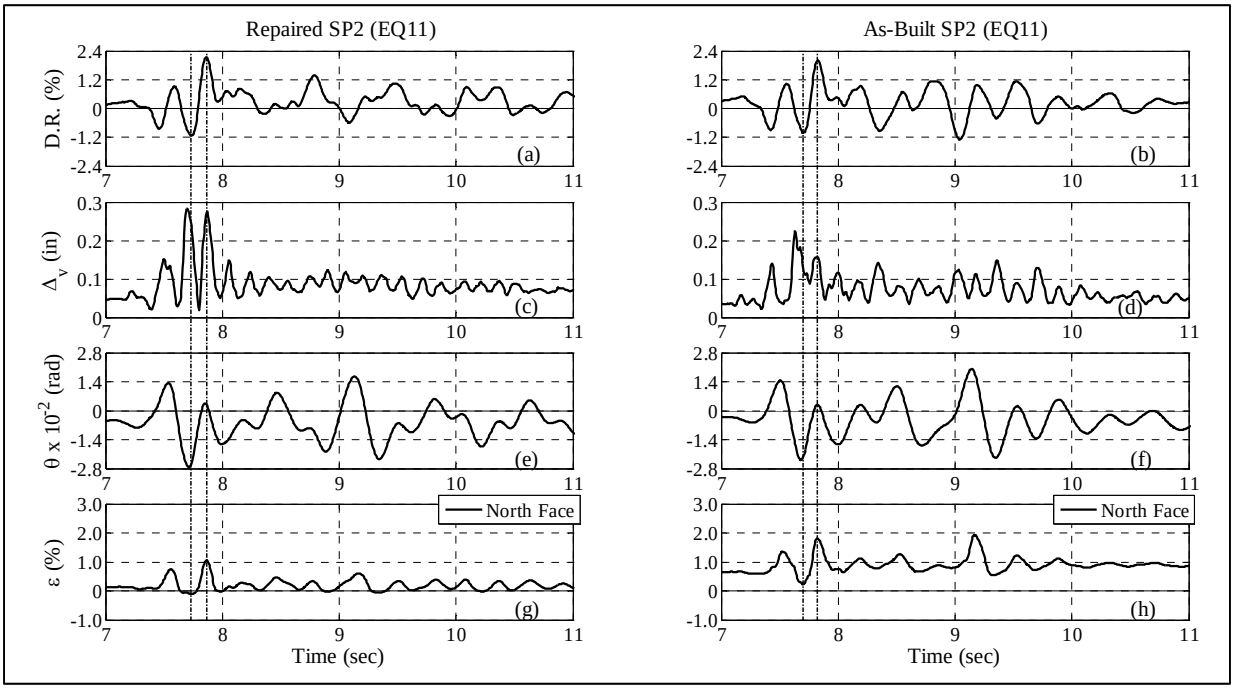

Figure 5.9 Drift ratio (D.R.), vertical displacement (Δ_V), top rotation (θ), and longitudinal strain (ε) measured near the top.

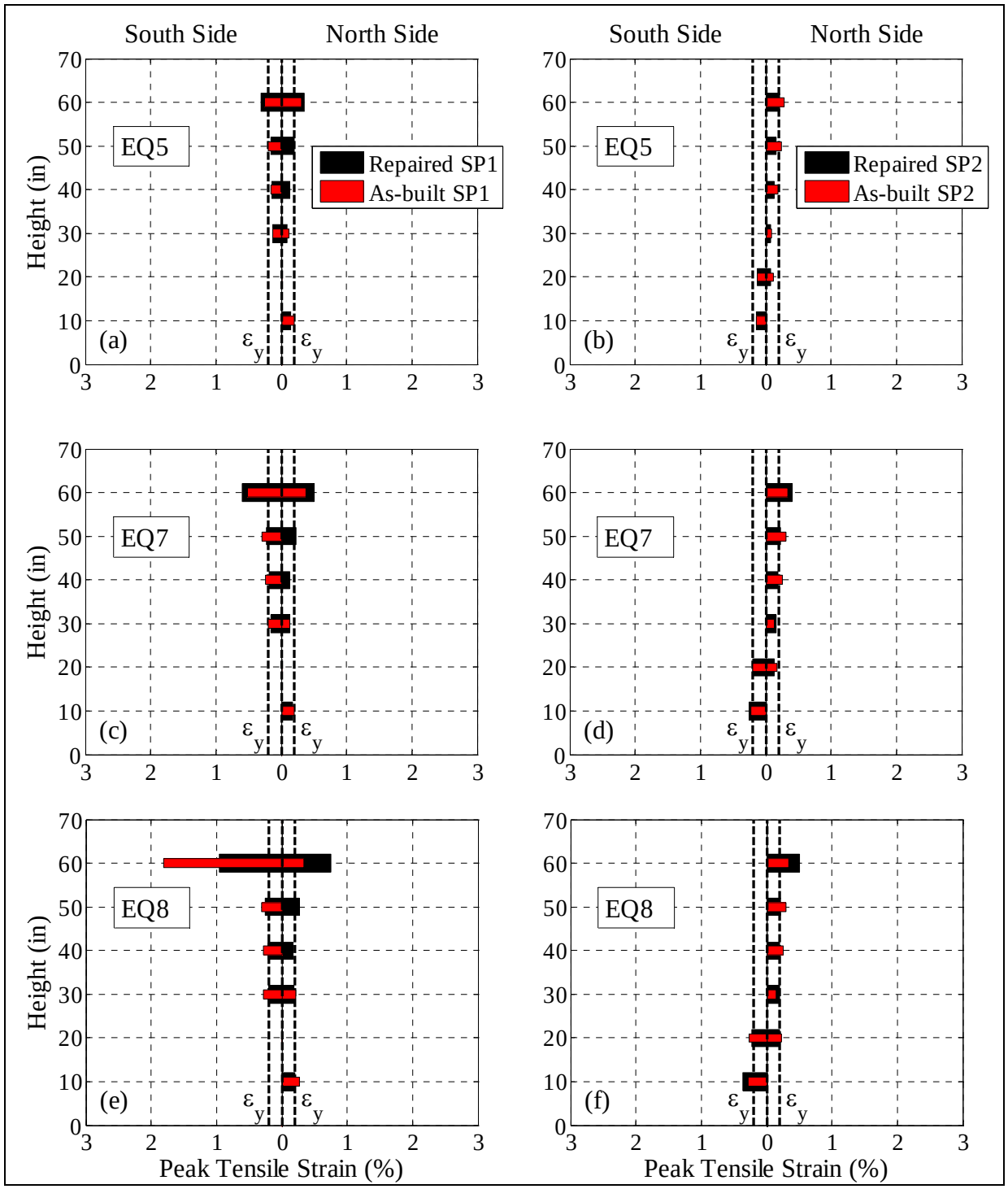

Figure 5.10 Peak longitudinal tensile strain profiles on the North and the South face.

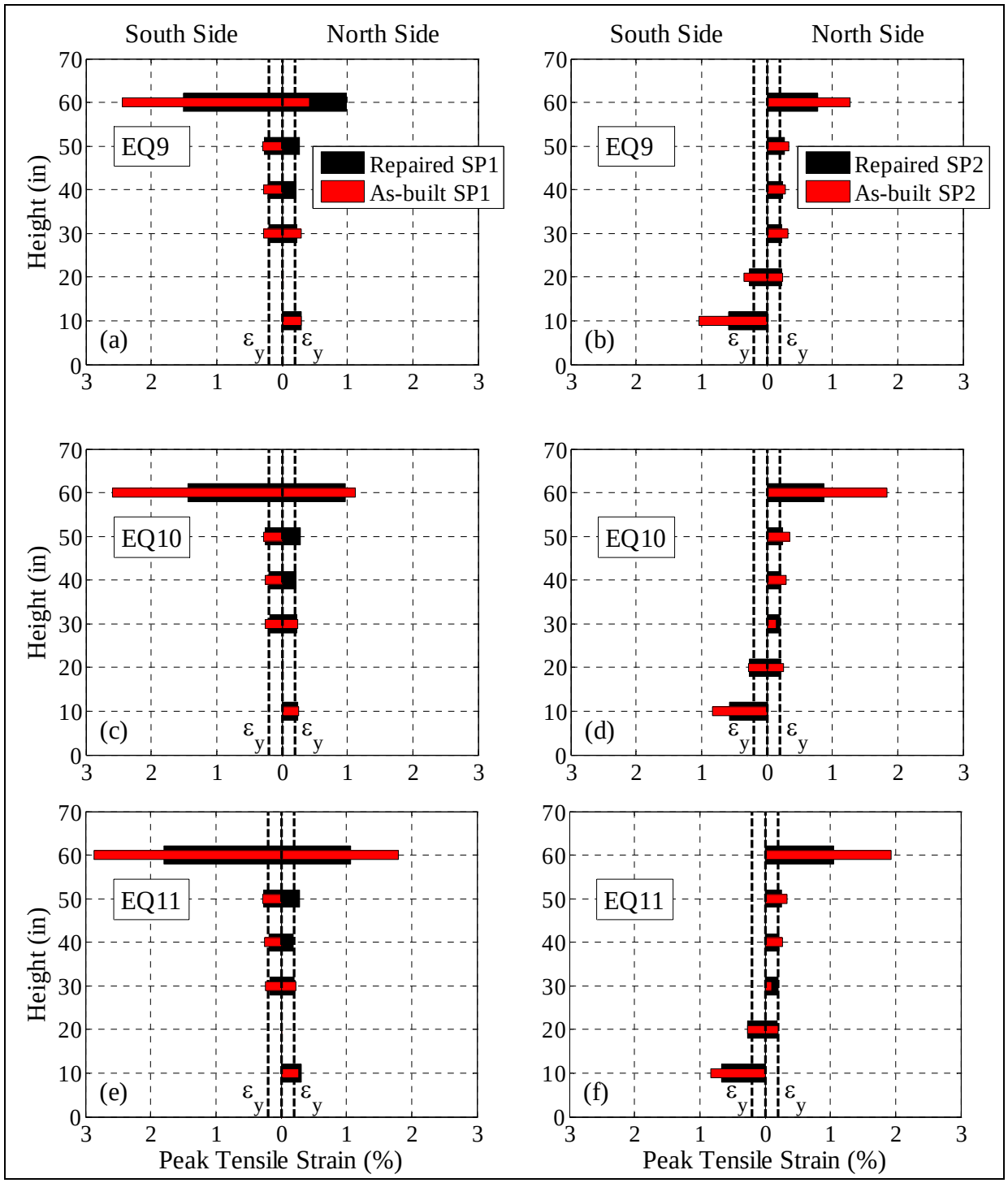

Figure 5.11 Peak longitudinal tensile strain profiles on the North and the South face.

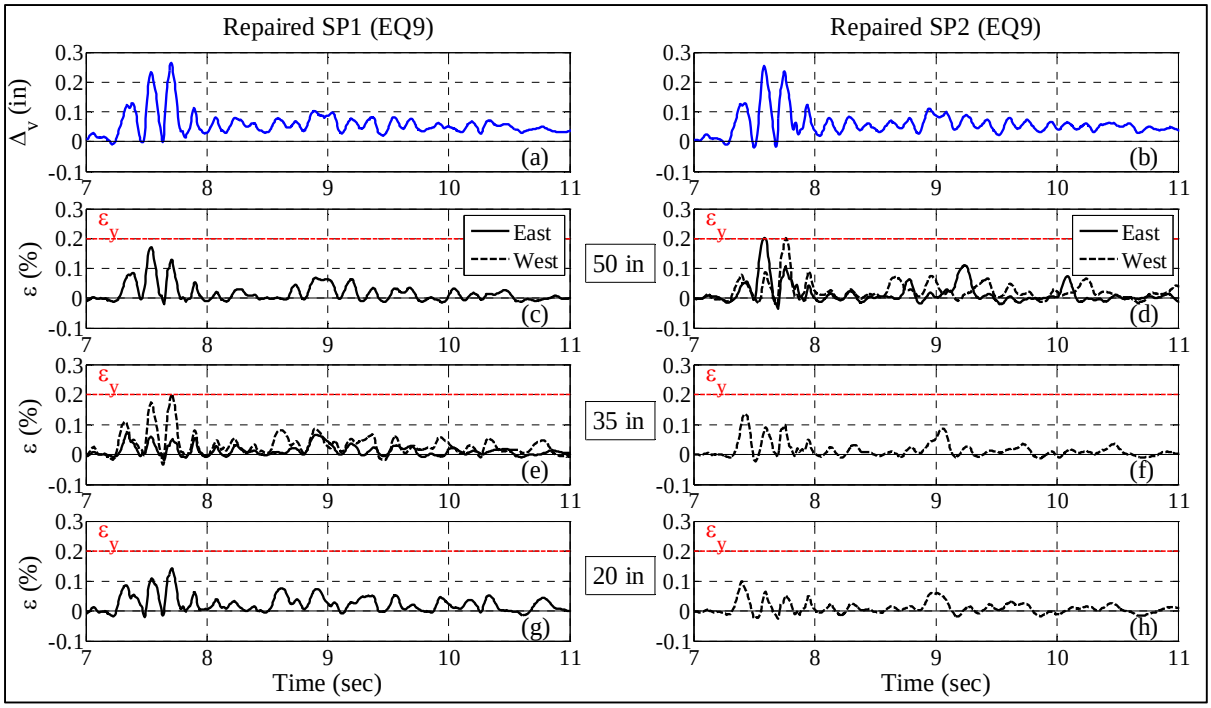

Figure 5.12 Longitudinal strain time histories measured on the East and the West face.

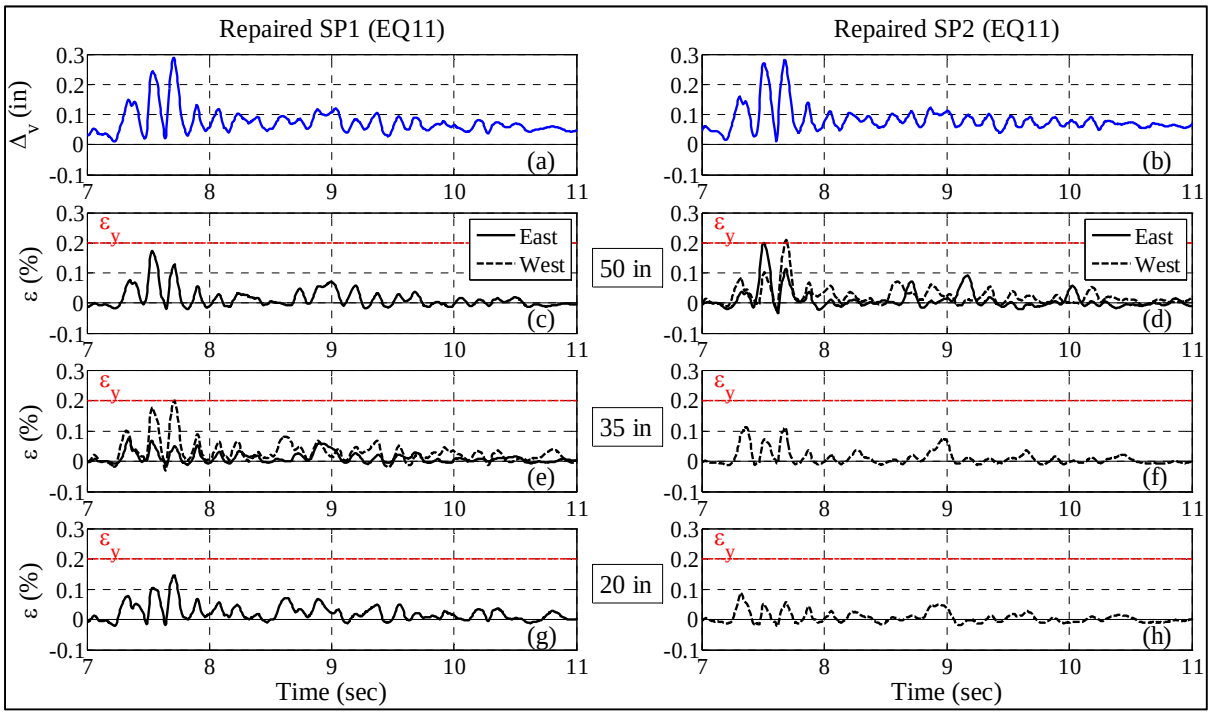

Figure 5.13 Longitudinal strain time histories measured on the East and the West face.

5.3 JACKET STRAINS RESPONSE

The as-built test specimens after they were tested were confined using unidirectional GFRP and CFRP jackets to improve the shear capacity and provide confinement to the damaged regions. Each test specimen was instrumented with 40 strain gauges installed on the FRP jacket along the column height. The locations and distribution of the jacket strain gauges were previously discussed in Section 3.2. The instrumented FRP jacket cross-sections at heights of 10 in (254 mm), 20 in (508 mm), 35 in (889 mm), 50 in (1270 mm), and 60 in (1524 mm) are designated as S10, S20, S35, S50 and S60, respectively for brevity. At any given section, the jacket strain gauges were labeled based on their location, e.g. a jacket strain in the North face at S20 is designated as N-S20 and a strain gauge installed on the South-East face at S60 is designated as SE-S60.

Figure 5.14 through Figure 5.16 show the confining (jacket) strain time histories of the repaired SP1 measured during the 125%-scaled ground motions. During EQ9 and EQ10, the jacket strain histories measured at different cross-sections remained almost the same and then increased during EQ11. The absolute maximum and minimum jacket strains in the repaired SP1 were measured at S60 and S35, respectively. The confining strain time histories of N-S10 (located at $D_{col}/2$ above the column base) and S-S20 (located at D_{col} above the column base) were almost the same during phase-I of the ground motions. A similar observation was valid for the confining strains measured by S-S10 (located at $D_{col}/2$ above the column base) and N-S20 (located at D_{col} above the column base). This suggested that the height of the compression strut near the base of the column was about $D_{col}/2$. The phase difference between the jacket strains measure on the North and South face was higher than the East and the West face of the repaired SP1.

The confining strain response measured on the CFRP jacket used in the repaired SP2 was different from the GFRP jacket used in the repaired SP1. Figure 5.17 through Figure 5.19 show the confining strain time histories of the repaired SP2 measured during the 125%-scaled ground motions. The confining strains measured on the North and South faces of the repaired SP2 had lower magnitude than the East and West faces. The maximum magnitude of the confining strains in the CFRP jacket was measured at S20 and S50 located at height D_{Col} above the base and below the top of the column, respectively, on the East-West face of the repaired SP2. This is attributed to the lower shear strength contribution of the concrete and the hoop steel in the repaired SP2, which resulted in higher shear strains (measured on the East and West face) in the CFRP jacket. On the other hand, the maximum strains in the repaired SP1 were measured at S10 and S60, respectively located at height $D_{Col}/2$ above the base and below the top of the cantilever column, and on the North face of the test specimen. This is attributed to the expansion on the damaged concrete resulting in higher confinement pressure. This suggested that the role of the FRP jacket was different in the two test specimens, which led to the different behavior of the confining strain time histories.

Figure 5.20 through Figure 5.23 show the elevation and cross-sectional view of the maximum jacket strain profiles measured in the repaired test specimens. As the ground motion intensity increased from 50% to 95%, the increment in the magnitude of the confining strains measured on the East and West face was higher than the North and South face. In the repaired SP1, the maximum magnitude of the confining strain was about 0.16%, measured during EQ11 (N-S60), which was about 7% of the rupture strain of the GFRP jacket and 40% of the design

confinement strain (Section 2.4). The confining strains near the column top had higher magnitude due to the rotation of the additional mass and the higher curvatures at the top section than the column base. This behavior of the confining strain variation at the top and bottom sections was not significant in the case of the repaired SP2 because the rotational stiffness at the top of the as-built SP2 reduced as the shaking intensity due to more shear damage caused by the larger hoop spacing. It is noted that maximum circumferential strain (0.13%) was measured at E-S20 in the repaired SP2 about 12% of rupture strain of the CFRP jacket and 33% of the design confining strain (Section 2.4). The CFRP jacket was effective in providing confinement, but the patch repair with high strength mortar and epoxy was not strong enough to fully strengthen the cracks formed during the testing of the as-built SP2, particularly for the high intensity shaking. In comparison to repaired SP1, the confining strain profiles measured at the base and top level of the repaired SP2 had lower magnitudes due to the higher magnitude of CFRP jacket stiffness compared to GFRP jacket. At both levels, the peak confining strain magnitudes were not measured in the direction of loading. The maximum magnitude of confining strains in the hoops steel, measured at 10 in (25.4 mm) above the column base, of the as-built SP1 and SP2 was about 0.57% and 0.34%, respectively. At same height, the maximum confining strains in the GFRP and CFRP jackets were 0.1% and 0.08%, respectively.

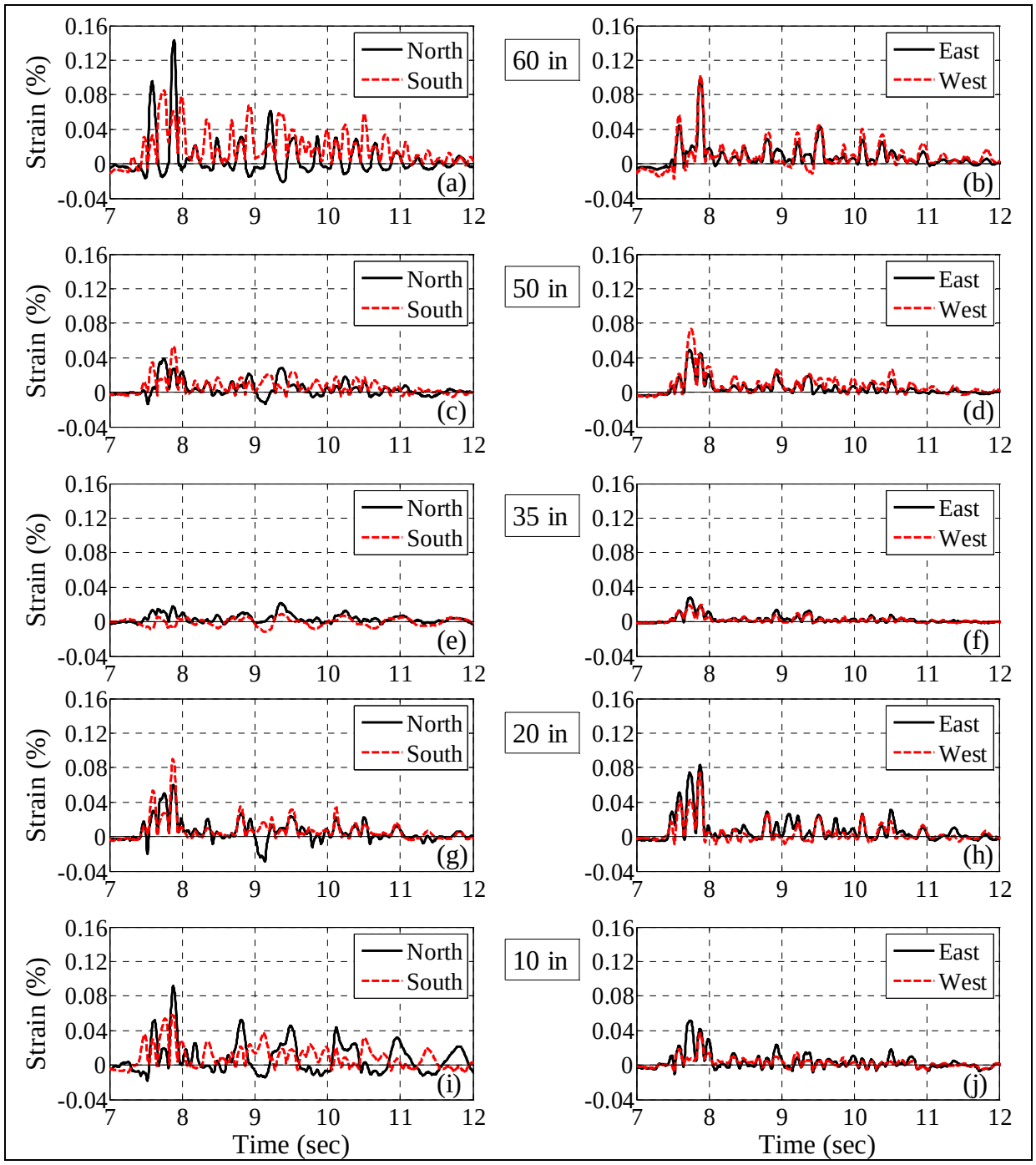

Figure 5.14 GFRP jacket strain time histories measured during EQ9.

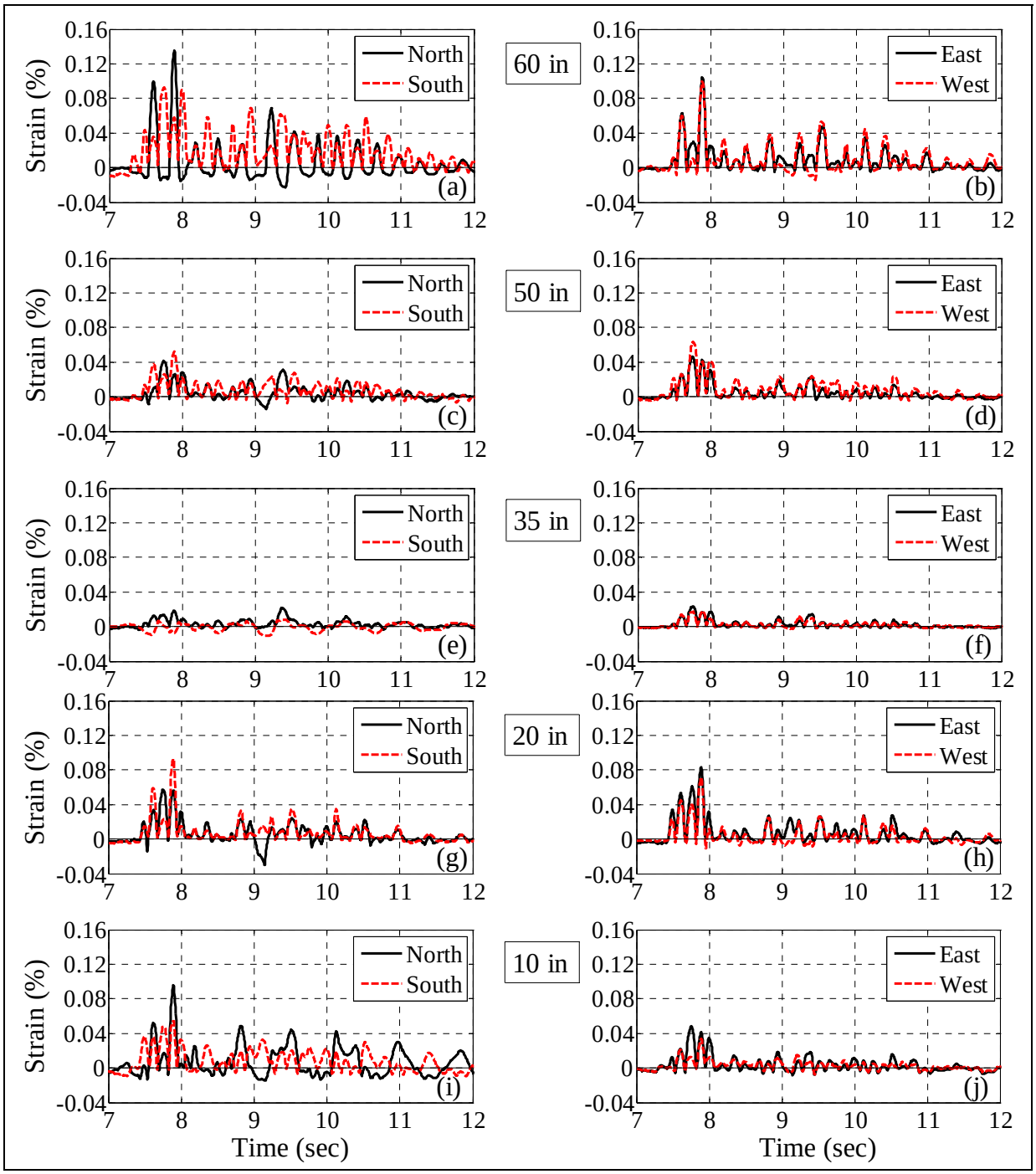

Figure 5.15 GFRP jacket strain time histories measured during EQ10.

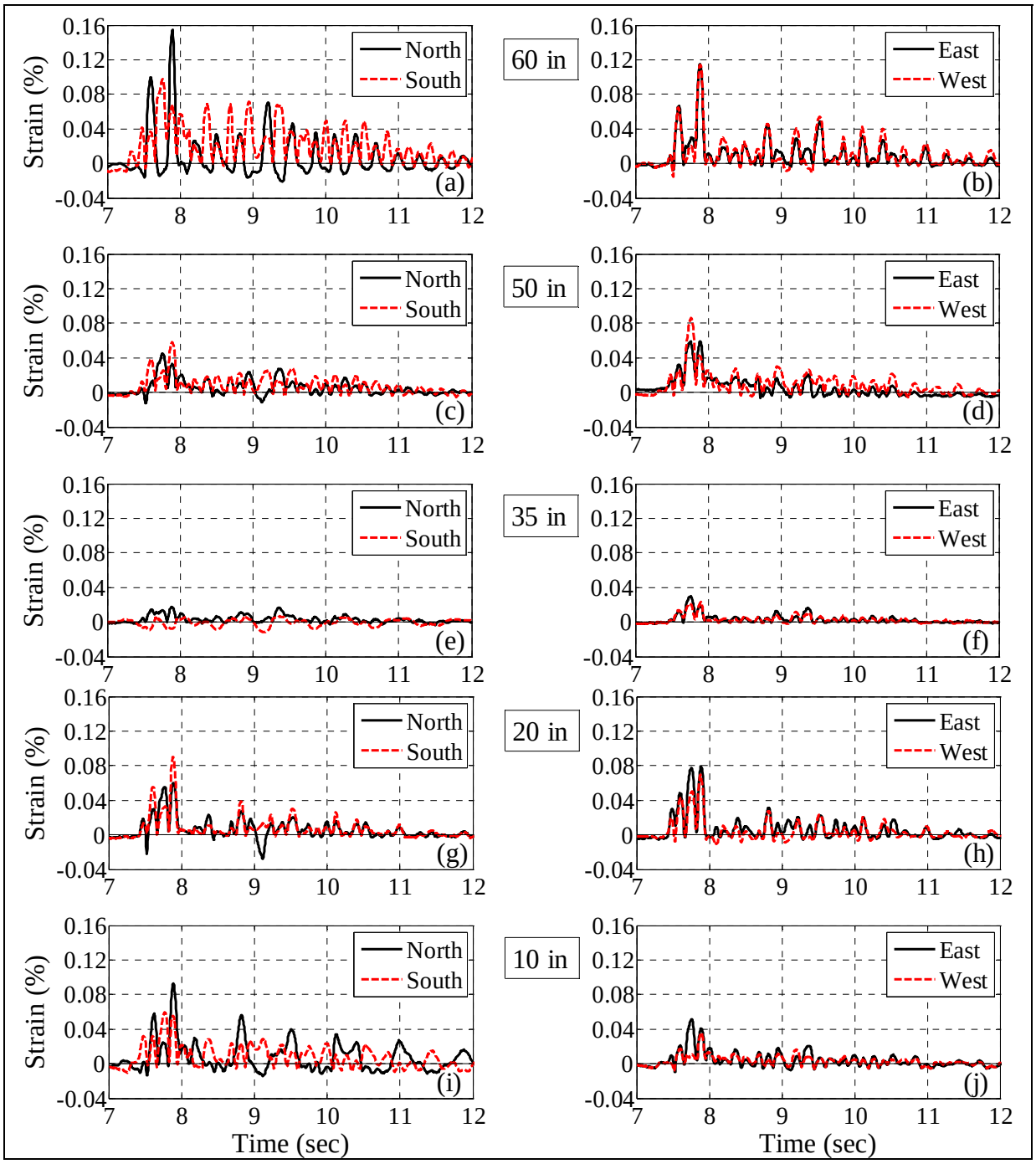

Figure 5.16 GFRP jacket strain time histories measured during EQ11.

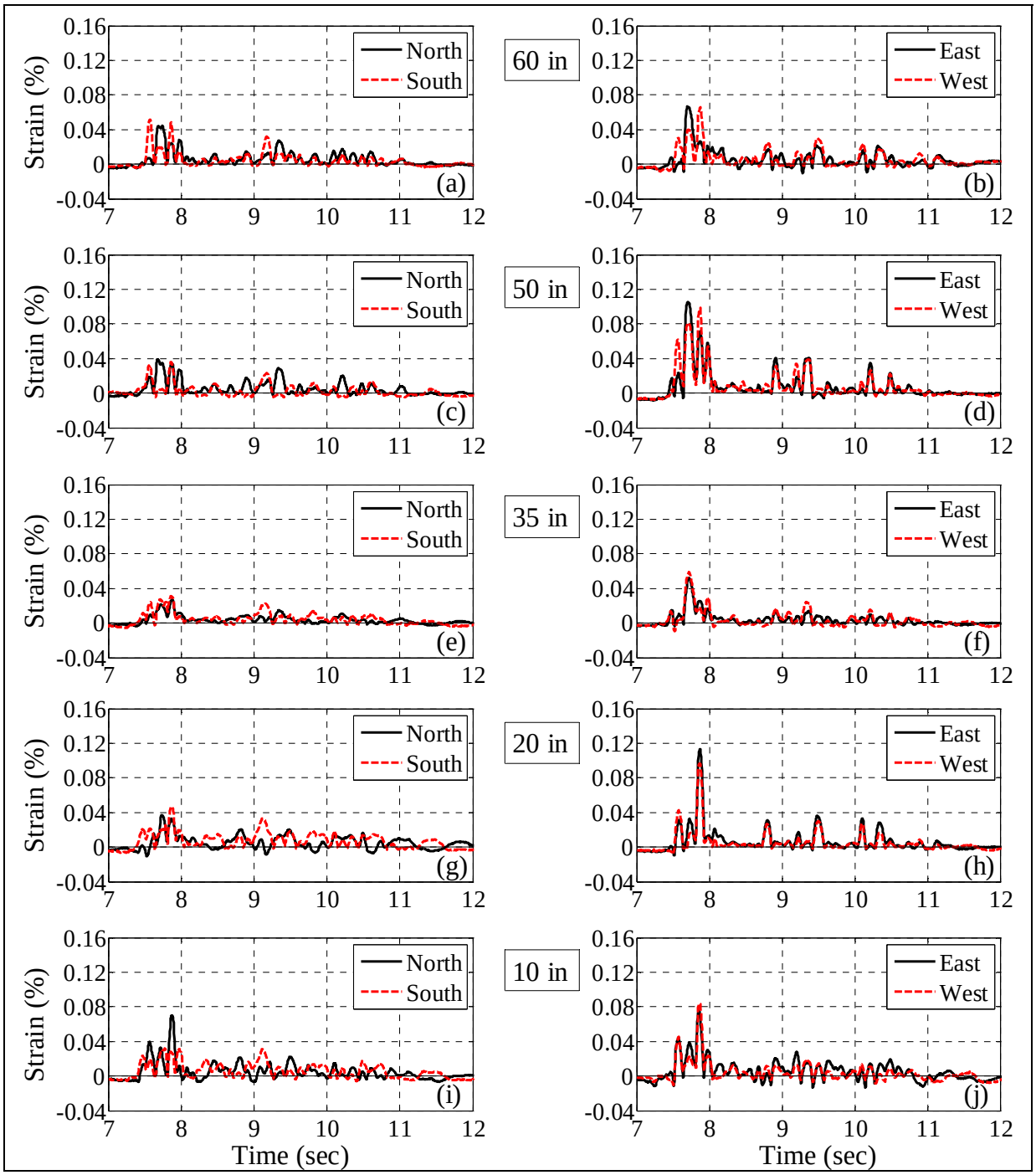

Figure 5.17 CFRP jacket strain time histories measured during EQ9.

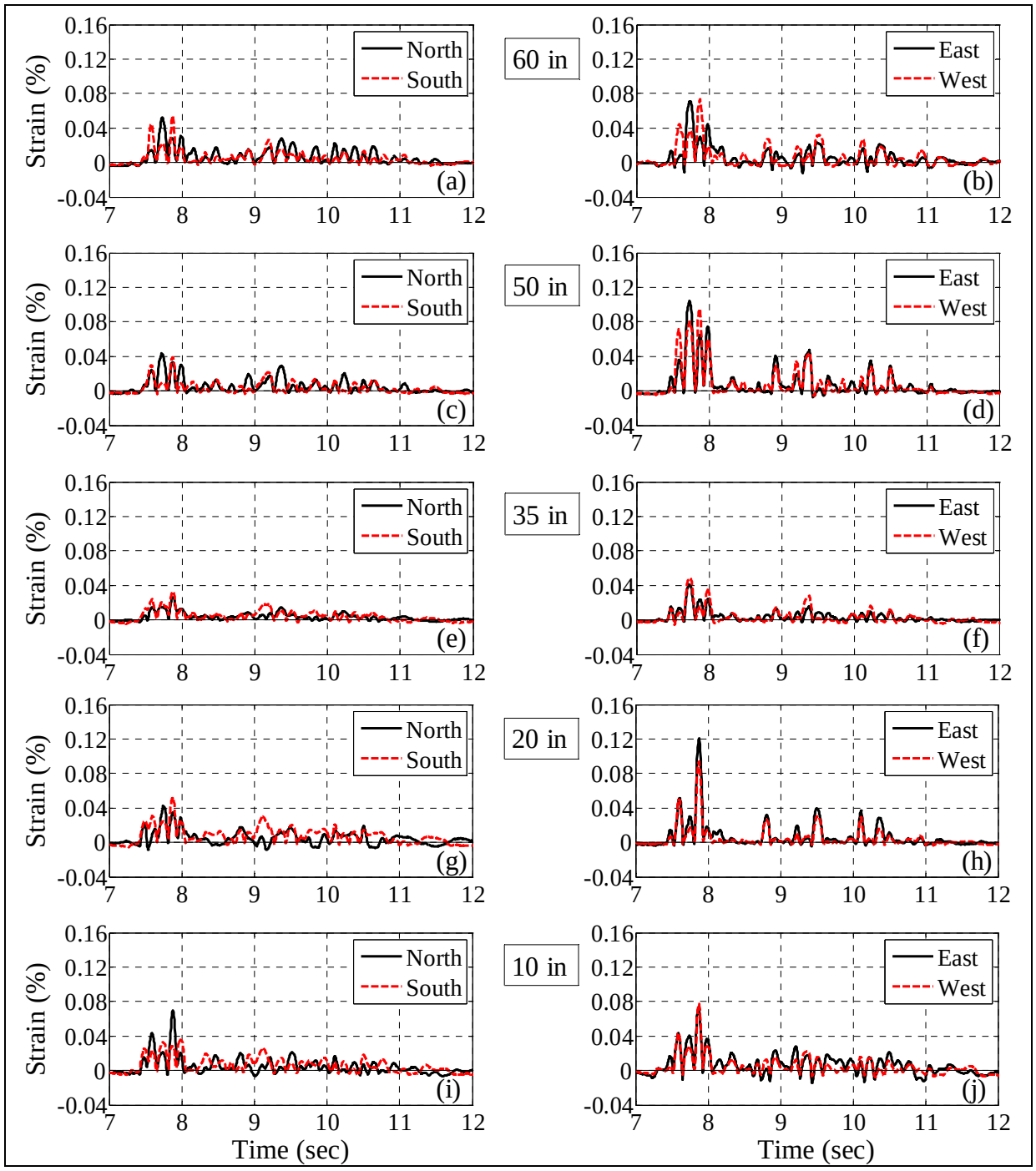

Figure 5.18 CFRP jacket strain time histories measured during EQ10.

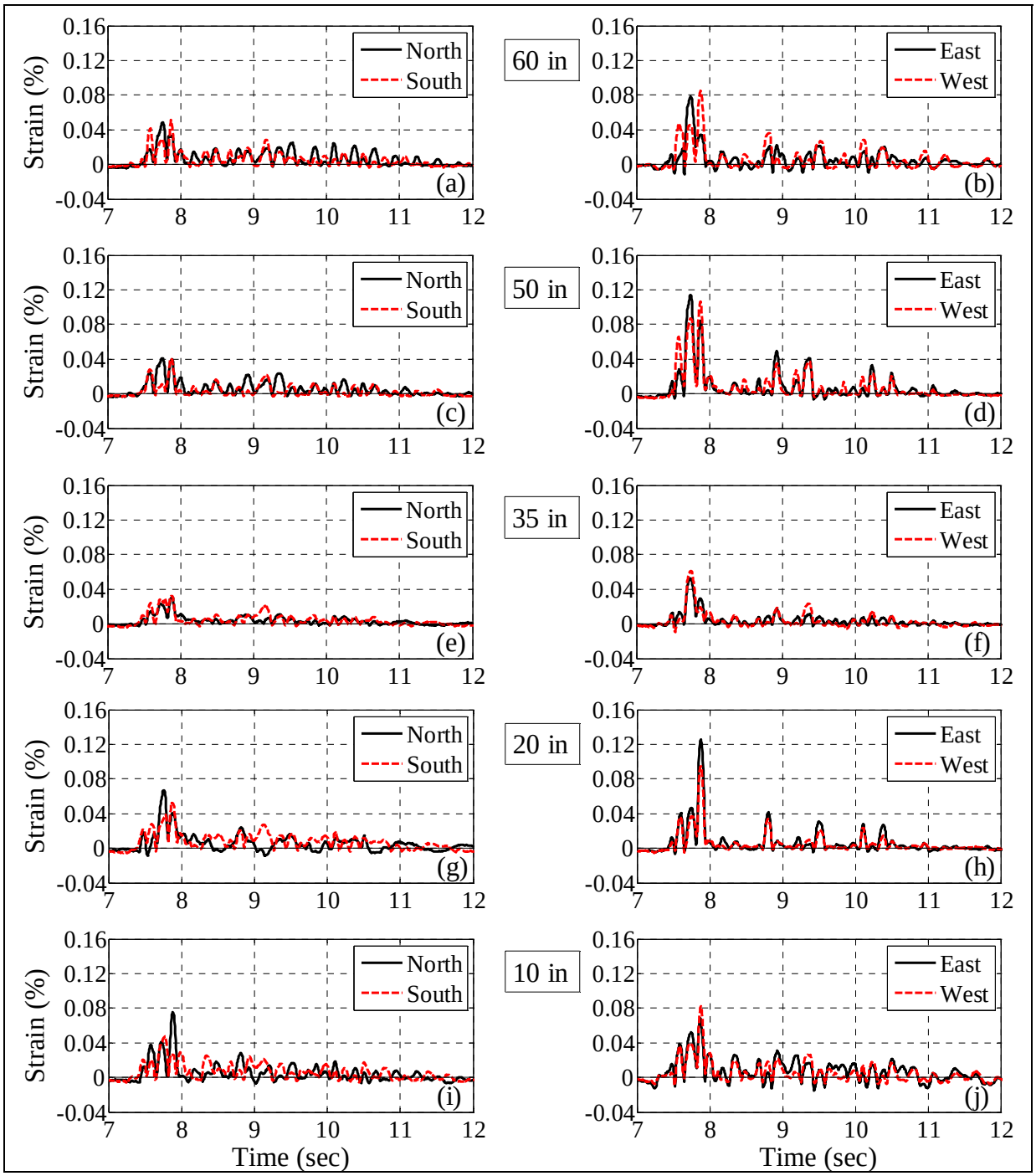

Figure 5.19 CFRP jacket strain time histories measured during EQ11.

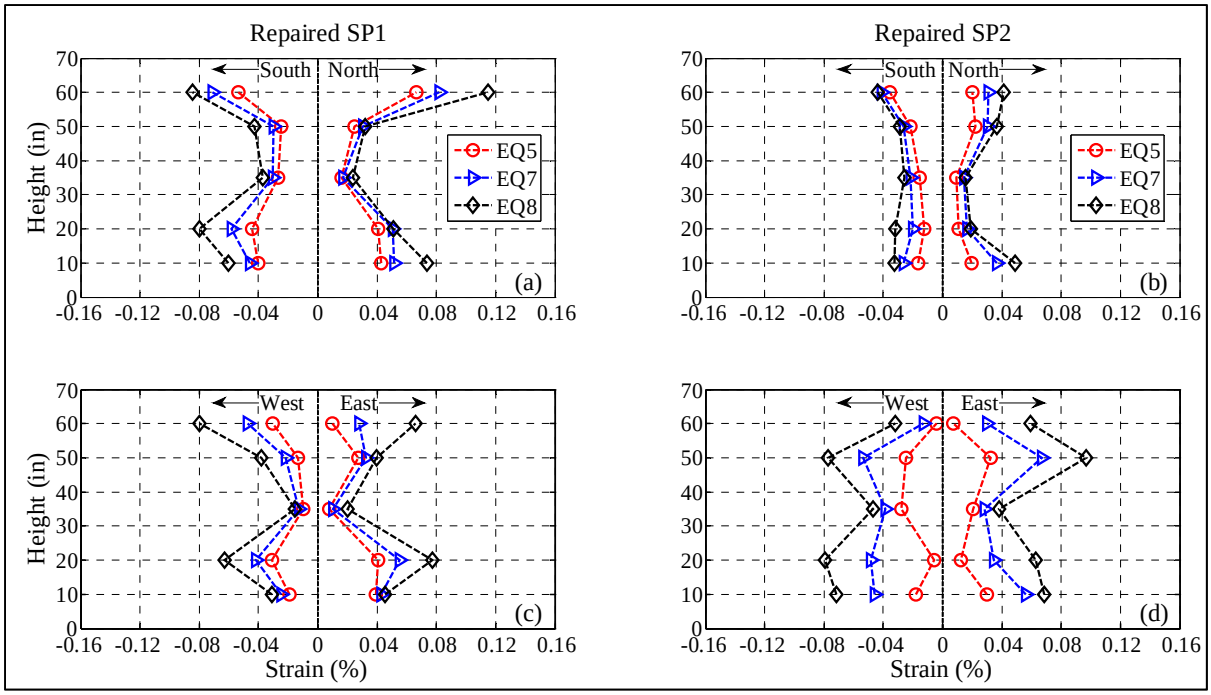

Figure 5.20 Peak confining strain profiles measured during 50%-, 70%- and 95%-scaled ground motions.

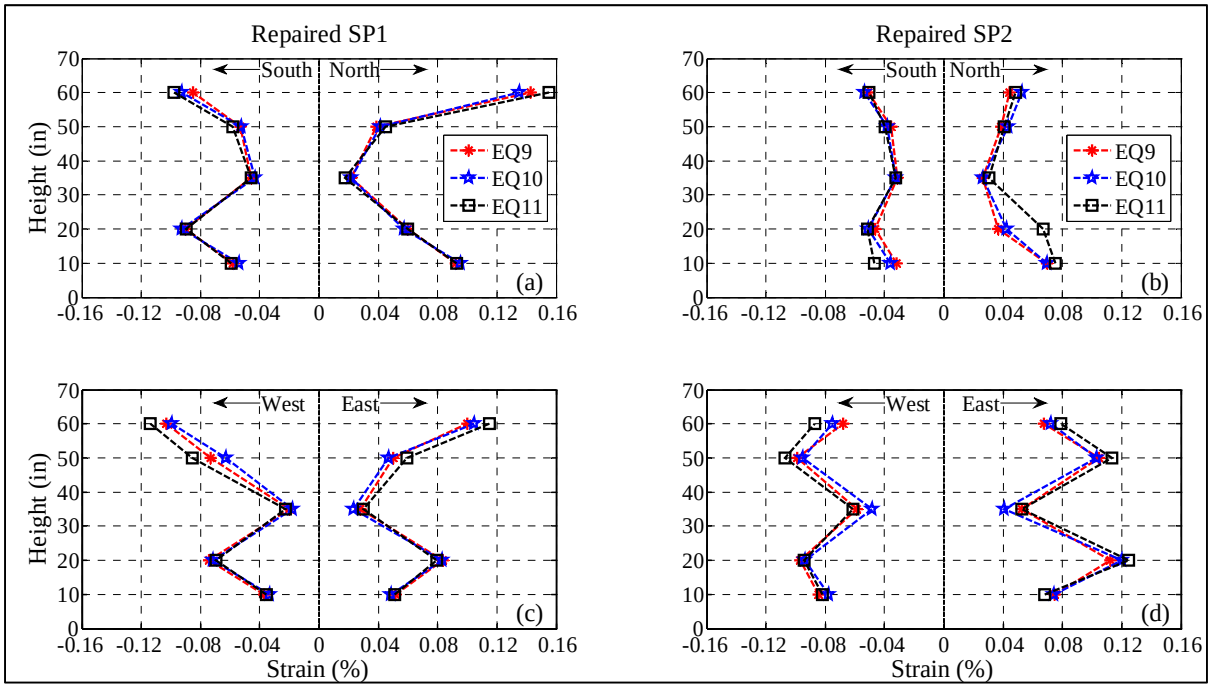

Figure 5.21 Peak confining strain profiles measured during 125%-scaled ground motions.

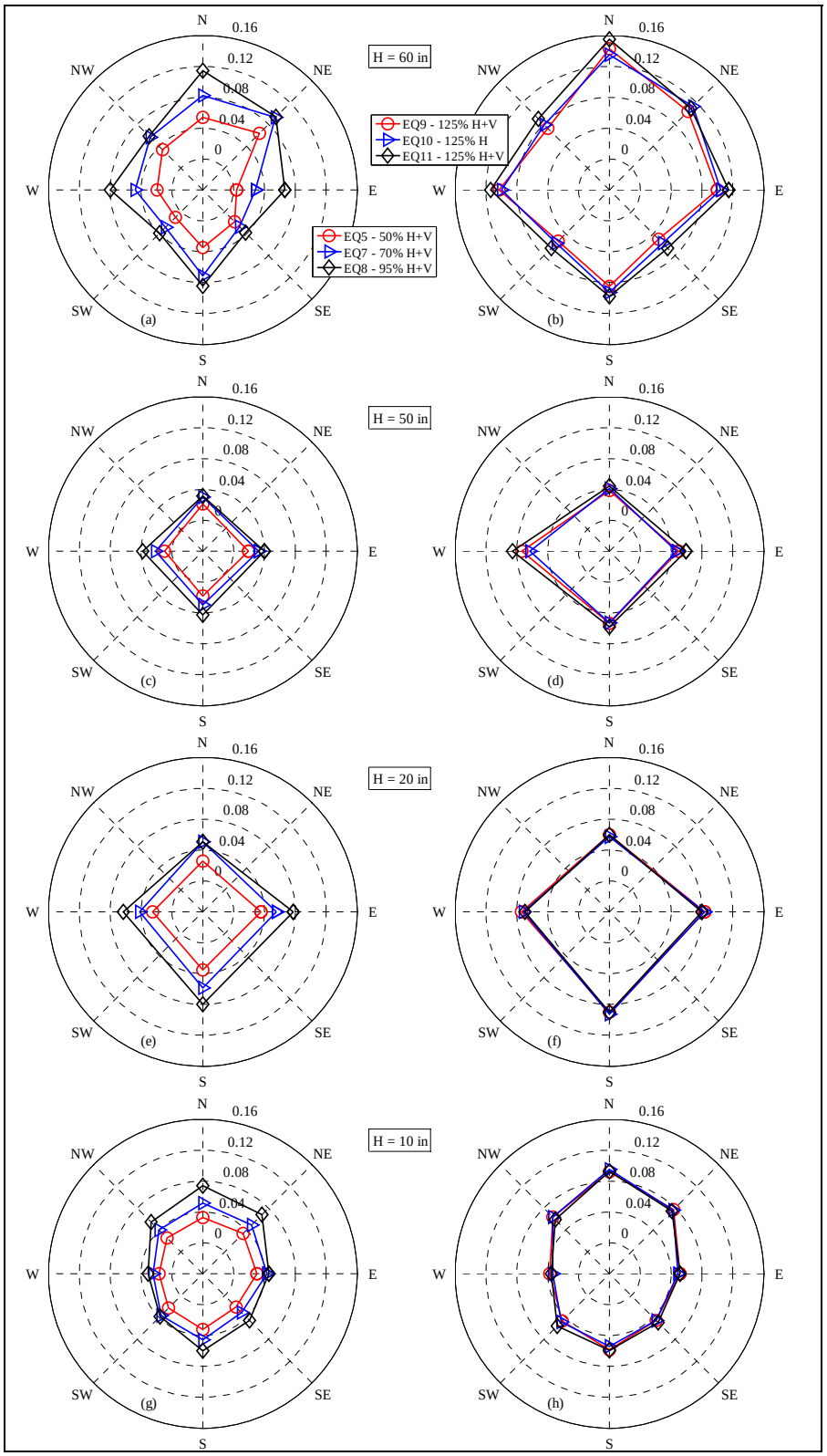

Figure 5.22 Peak GFRP jacket strain profiles (%).

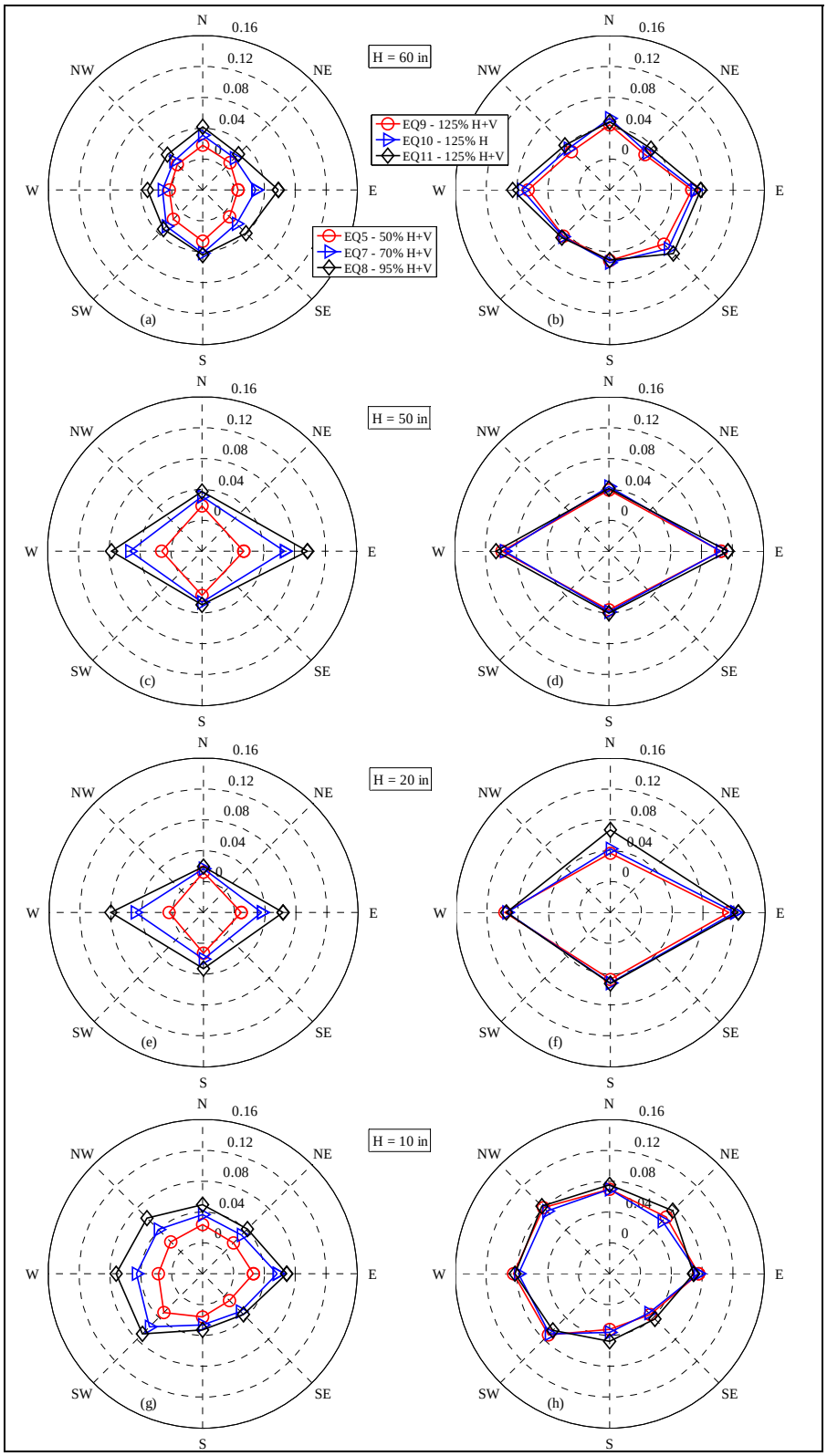

Figure 5.23 Peak CFRP jacket strain profiles (%).

5.4 CURVATURE RESPONSE

Fourteen LVDTs were installed on the North and South side of the test specimens to measure the curvatures in the horizontal loading plane (for detailed calculation, see Appendix C). The location, orientation, and gauge lengths of the LVDTs were previously discussed in Section 3.2. In this section, the positive and negative signs are assigned to the convex and concave bending of the north face (Appendix C). The location of sections, with respect to the column base, where the average curvatures were computed are labeled as C1 (2.5 in (63.5 mm)) , C2 (10 in (254 mm)), C3 (20 in (508 mm)), C4 (30 in (762 mm)), C5 (45 in (1143 mm)), C6 (60 in (1524 mm)) and C7 (67.5 in (1714.5 mm)).

The curvatures measured near the base (C1, C2 and C3) and the top (C5, C6 and C7) of the cantilever columns were out-of-phase during phase-I of the ground motions, which confirms that the test specimens were in double curvature. This was also verified by the longitudinal strain time histories measured on the North and South face of the test specimens (Section 5.2). The magnitude of the curvatures measured at C4 was significantly lower. During phase-II of the ground motions, the phase difference between the curvatures measured along the column height decreased and the test specimens were in single curvature. The highest magnitudes of curvature peaks were measured at C7. This could be attributed to the rotation of the superstructure mass and the relative higher displacement near the column top. As the intensity of ground motion increased, the magnitude of the curvatures measured in the test specimens increased as well. The rate of increase was higher near the top sections (C6 and C7). This suggested that the flexural stiffness reduced at a faster rate near the top section than the base. This was also verified by the moment curvature response of the test specimens as discussed in the next section (Section 5.5).

Figure 5.24 shows the D.R. and the curvature time histories measured at C1 and C7 during the 50%-, 70%- and 95%-scaled ground motions. The curvature histories of the repaired SP1 had higher magnitudes than the repaired SP2. During EQ8, the residual curvature of the repaired SP1 was higher than the repaired SP2. This could be attributed to the higher residual D.R. and rotation of the repaired SP1 than repaired SP2 (Chapter 4). Figure 5.25 and Figure 5.30 show the D.R., top rotation (θ) and curvatures (Φ) time histories of the repaired and as-built test specimens measured during the 125%-scaled ground motions. Due to the heavy mass and its configuration at the column top, the rotational mode of vibration governed the response during the strong motion part, with higher curvatures at the top compared to those at the column base. During phase-I of the 125%-scaled ground motions, the maximum D.R. towards the South (negative) side, the top rotation, and the curvatures at C7 (concave) were measured at the same time instants (Figure 5.25 to Figure 5.30). On the other hand, the maximum curvatures at C1 (concave) and the maximum D.R. (positive) were measured at the same time instant with negligible rotation of superstructure mass.

Figure 5.31 to Figure 5.34 show the curvature profile along the column height measured at the moment of the maximum concave and convex curvatures at C7. In comparison to the as-built SP1, the repaired SP1 showed a slight increase in the curvature magnitudes at C1 and C7 during the testing, while the curvatures measured in the repaired SP2 were lower than the as-built SP2. The difference in the curvatures of the repaired test specimens and their as-built counterparts measured at section C2, C3, C4, C5 and C6 was relatively lower. The repaired height, 69.5 in (1765.3 mm), for SP1 and SP2 was 0.25 in (6.35 mm) shorter than the 70 in (1778 mm) clear height from each end of the column. Therefore, the damage was concentrated at the unconfined

end sections where the GFRP (for SP1) and CFRP (for SP2) jackets were terminated, but no concrete spalling was observed.

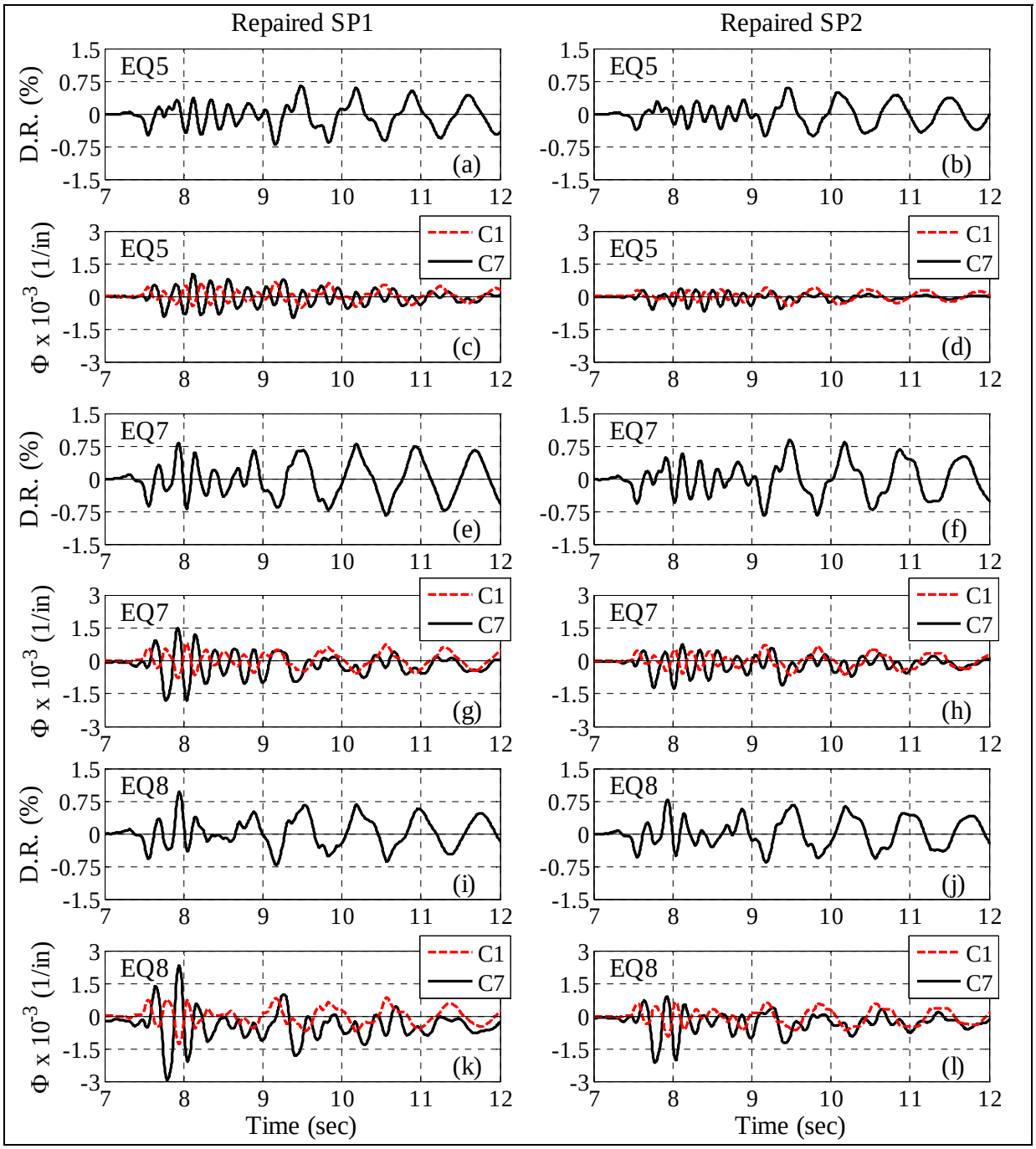

Figure 5.24 Curvature (Φ) time histories for repaired SP1 and SP2 tests.

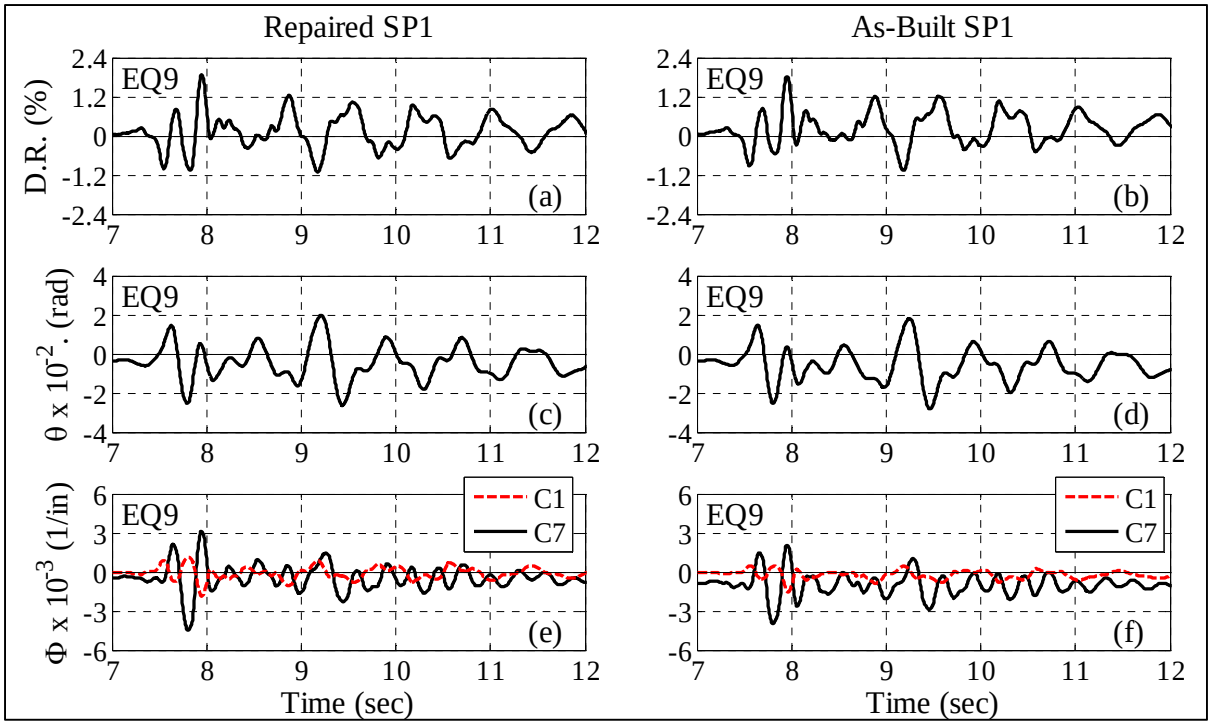

Figure 5.25 Drift ratio (D.R.), top rotation (θ) and curvature (Φ) time histories for repaired SP1 EQ9 tests.

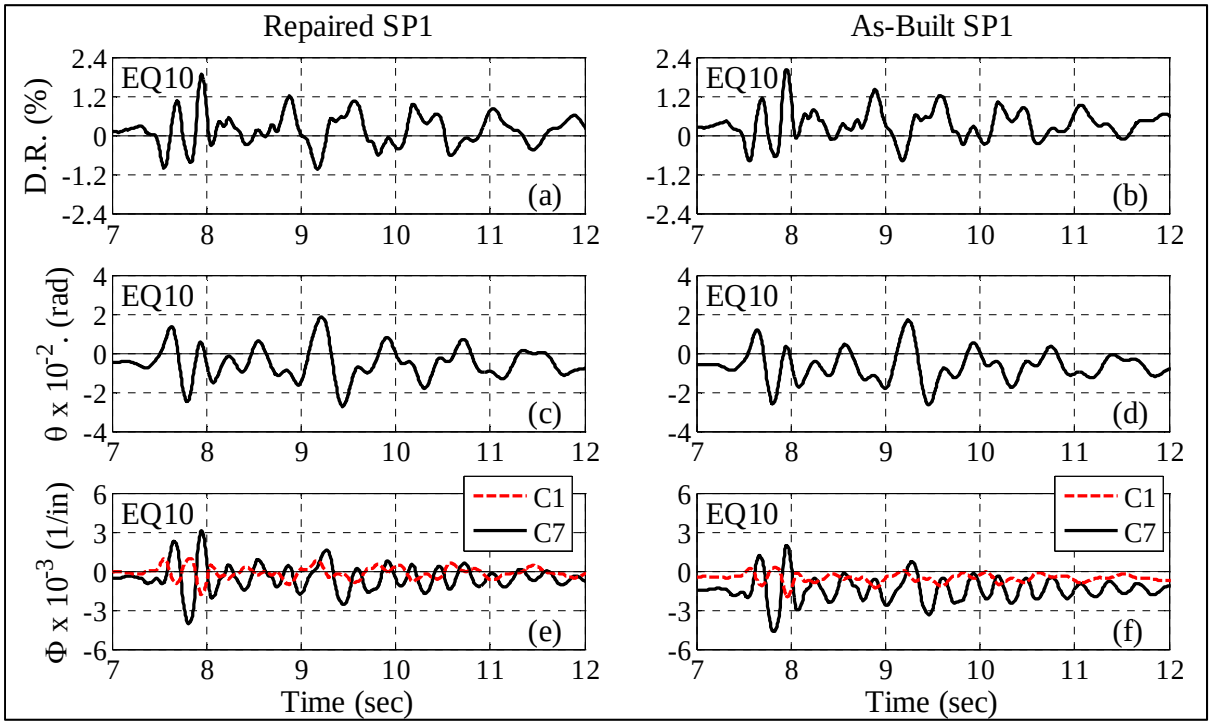

Figure 5.26 Drift ratio (D.R.), top rotation (θ) and curvature (Φ) time histories for repaired SP1 EQ10 tests.

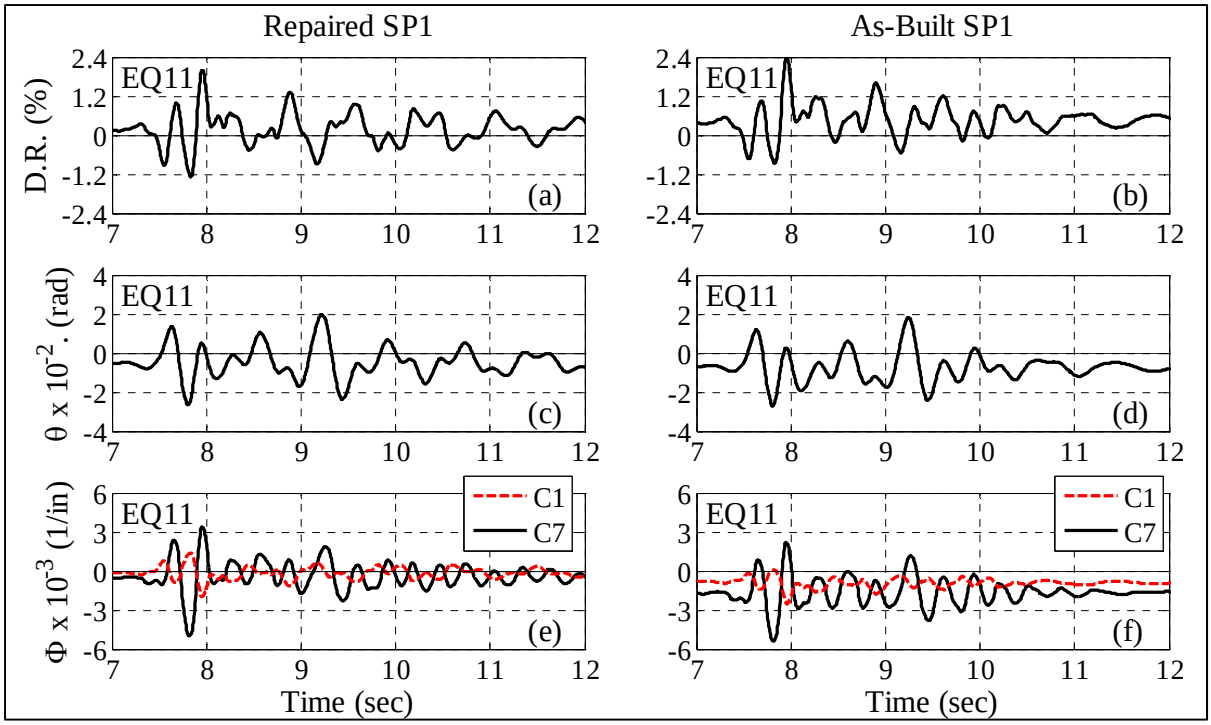

Figure 5.27 Drift ratio (D.R.), top rotation (θ) and curvature (Φ) time histories for repaired SP1 EQ11 tests.

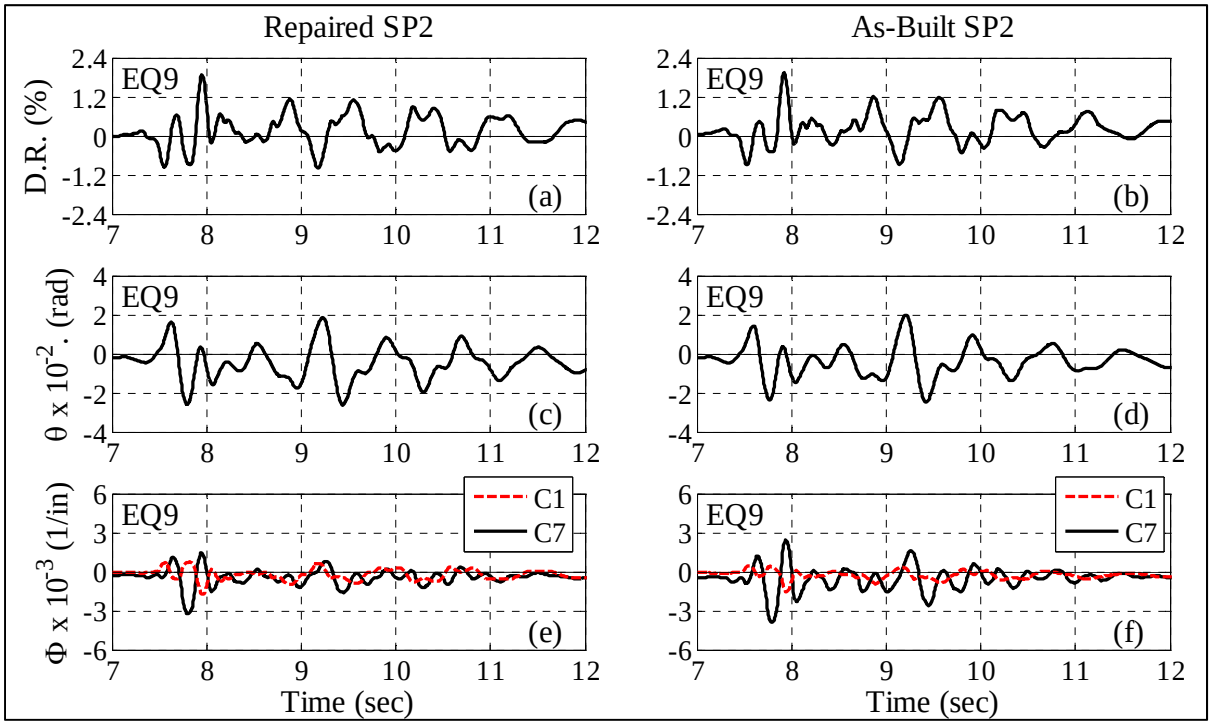

Figure 5.28 Drift ratio (D.R.), top rotation (θ) and curvature (Φ) time histories for repaired SP2 EQ9 tests.

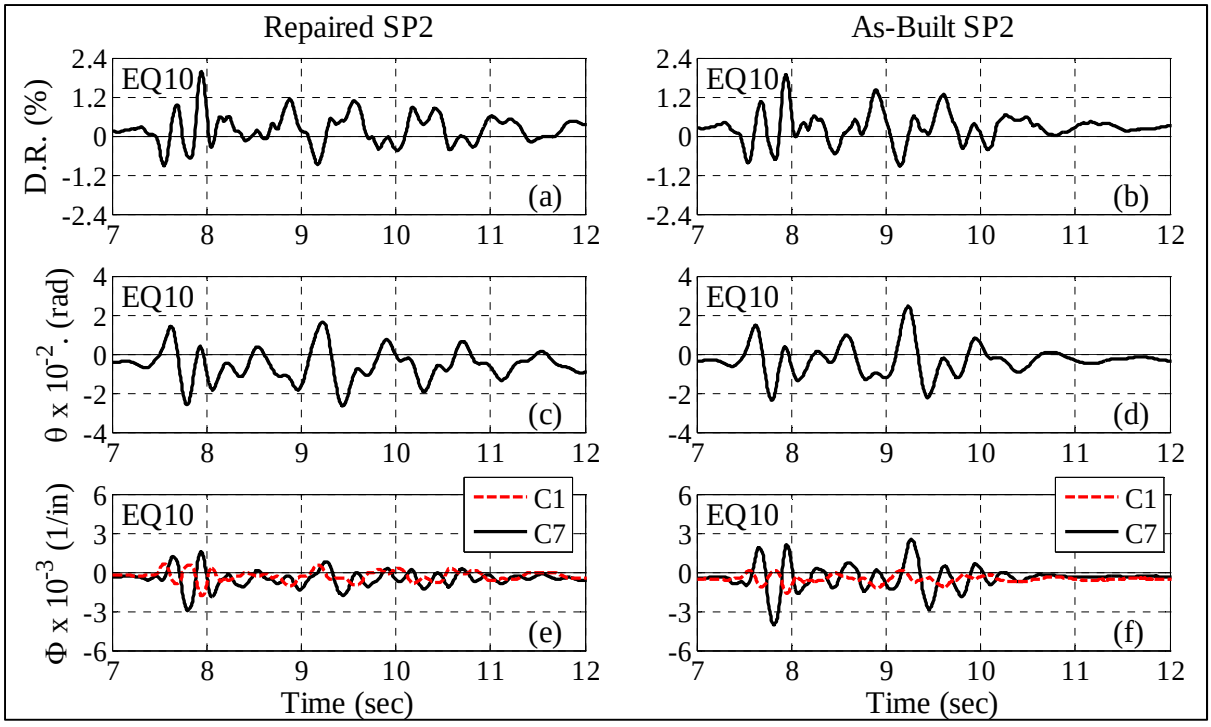

Figure 5.29 Drift ratio (D.R.), top rotation (θ) and curvature (Φ) time histories for repaired SP2 EQ10 tests.

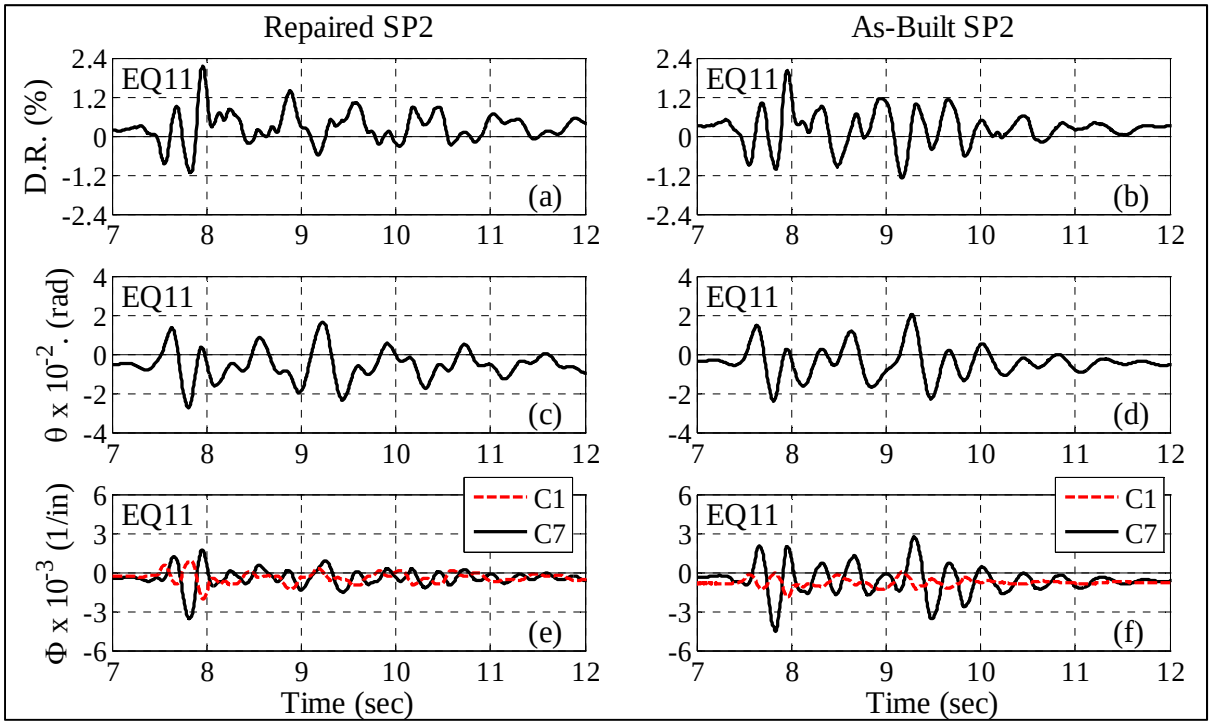

Figure 5.30 Drift ratio (D.R.), top rotation (θ) and curvature (Φ) time histories for repaired SP2 EQ11 tests.

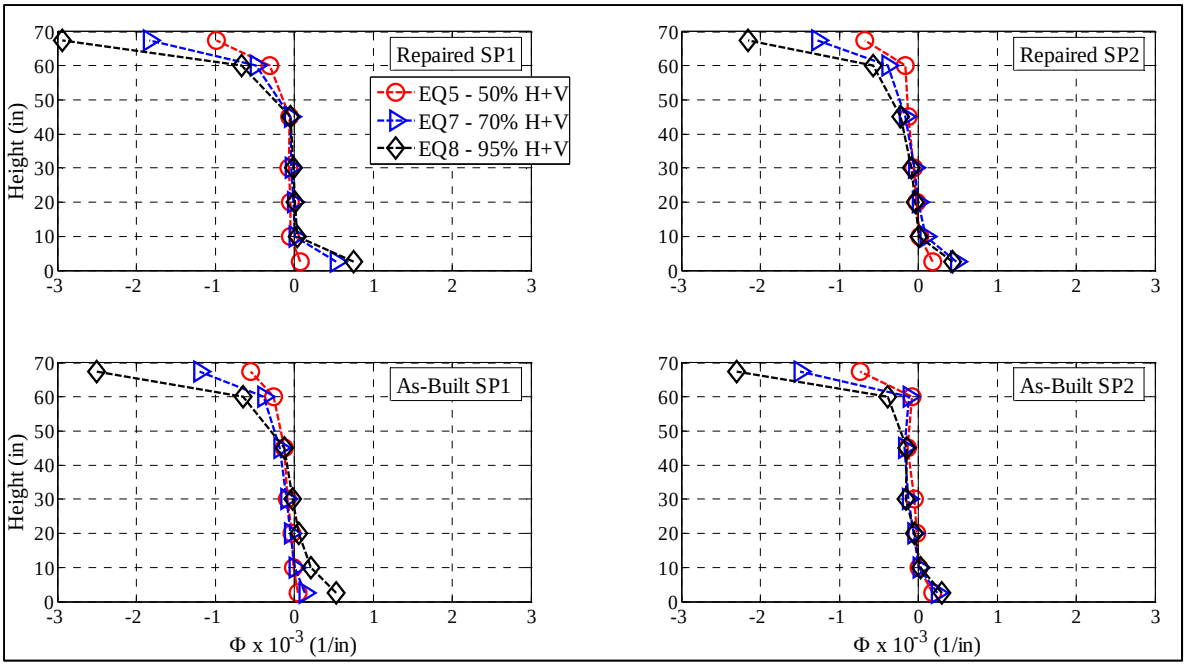

Figure 5.31 Curvature profiles measured at the time instant of peak concave curvatures at top.

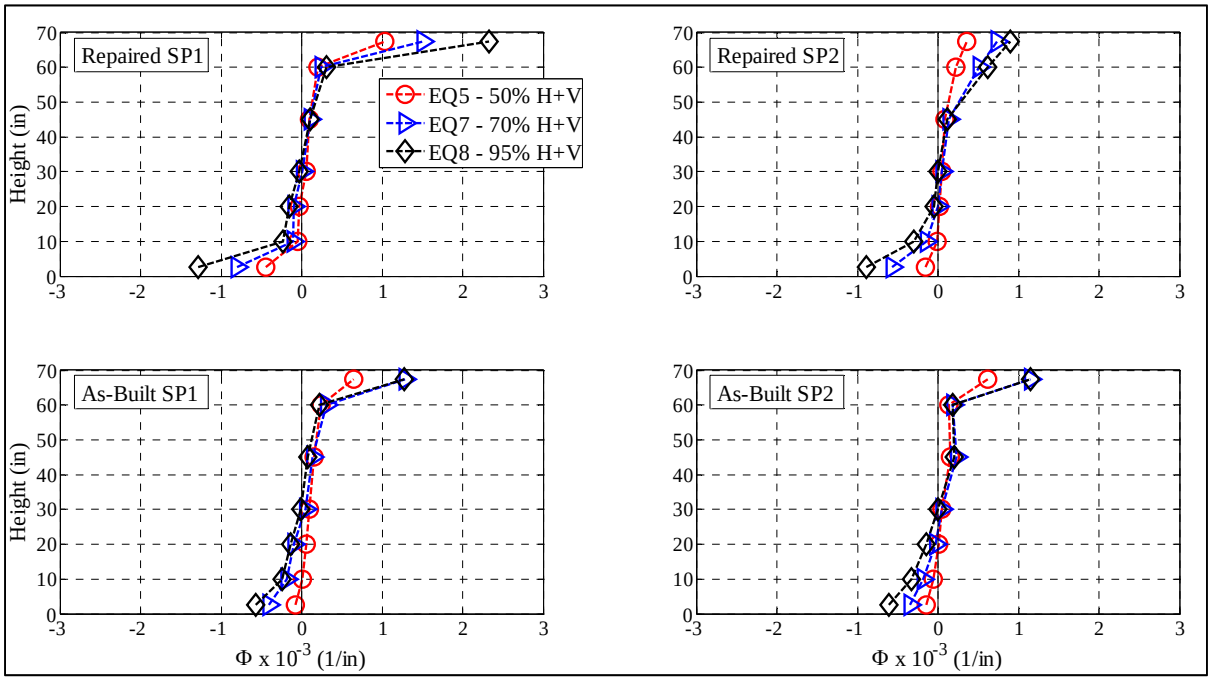

Figure 5.32 Curvature profiles measured at the time instant of peak convex curvatures at top.

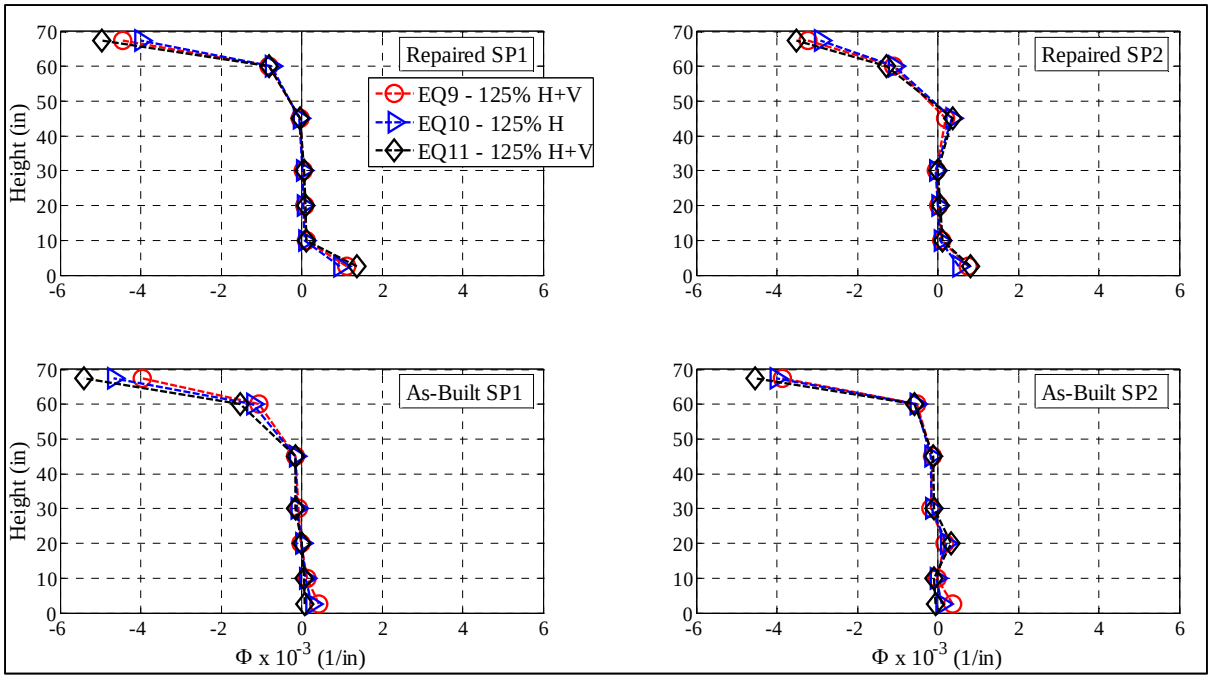

Figure 5.33 Curvature profiles measured at the time instant of peak concave curvatures at top.

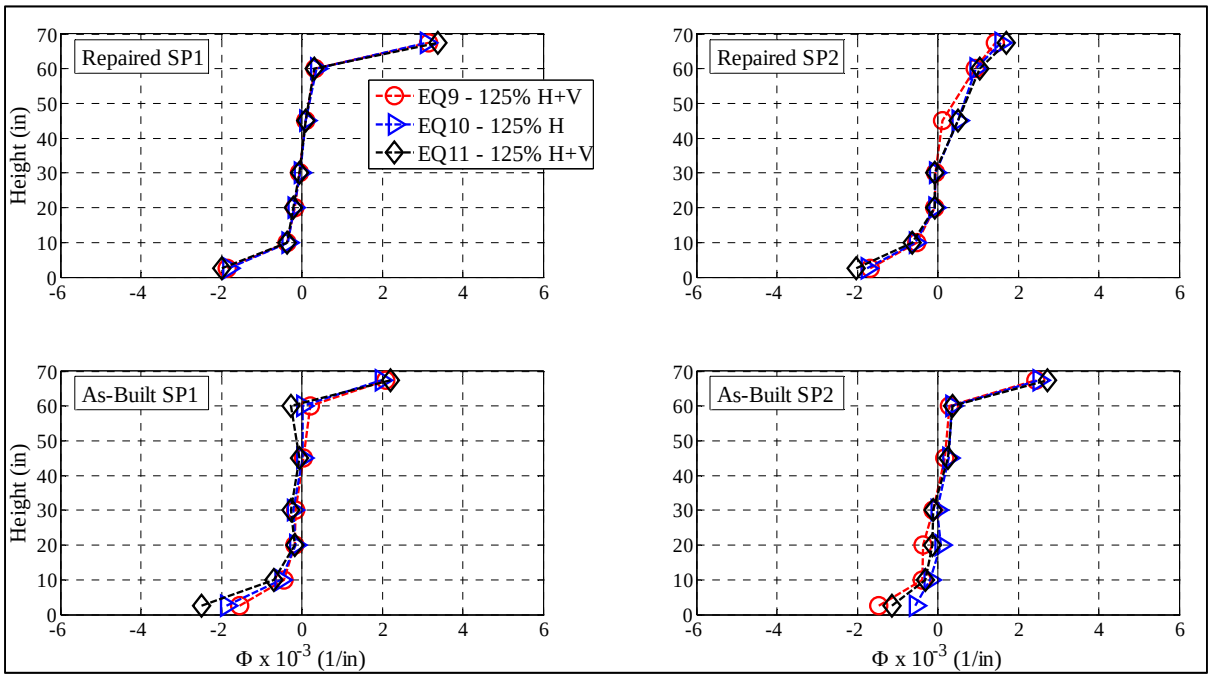

Figure 5.34 Curvature profiles measured at the time instant of peak convex curvatures at top.

5.5 MOMENT-CURVATURE RESPONSE

The last local response quantity considered in this study was the moment-curvature response. Figure 5.36 through Figure 5.38 show the Moment-Curvature (MC) plots near the base (2.5 in (63.5 mm)) and the top (67.5 in (1714.5 mm)) of the test specimens during EQ5through EQ11. The MC plots near the base of the repaired test specimens were almost linear with slightly higher stiffness than the as-built counterparts (Figure 5.36a, c and e). The maximum magnitude of the bending moment and curvatures near the base of the repaired SP1 were less than the as-built SP1 during the 50%-, 70%- and 95%-scaled ground motions. The MC response of the as-built specimens was almost linear near the top. On the other hand, the MC response of the repaired SP1 showed a reduction in the stiffness at the South side response (Figure 5.35b, d and f). The MC response of the repaired SP2 remained almost linear near the top, with a stiffness that was less than the as-built SP2, during the 5%- through 95%-scaled ground motions (Figure 5.36a, c and e). During EQ8 through EQ11, the MC hysteresis near the top of the repaired SP2 was wider than that of the as-built SP2, which illustrates that a relatively higher dissipation of energy occurred in the repaired specimen (Figure 5.36 and Figure 5.38).

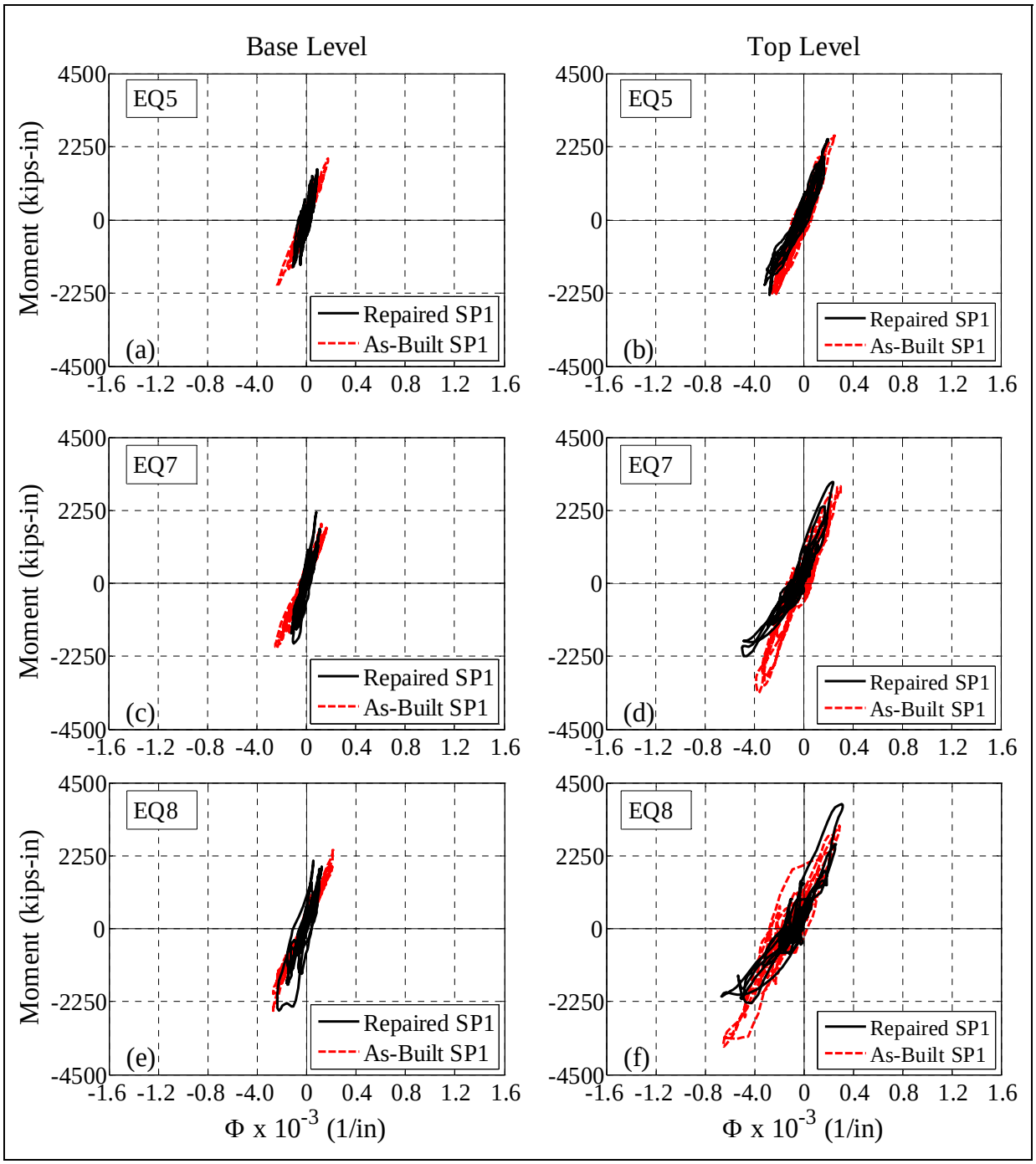

Figure 5.35 Moment-Curvature response during 50%-, 70%- and 95%-scaled ground motions.

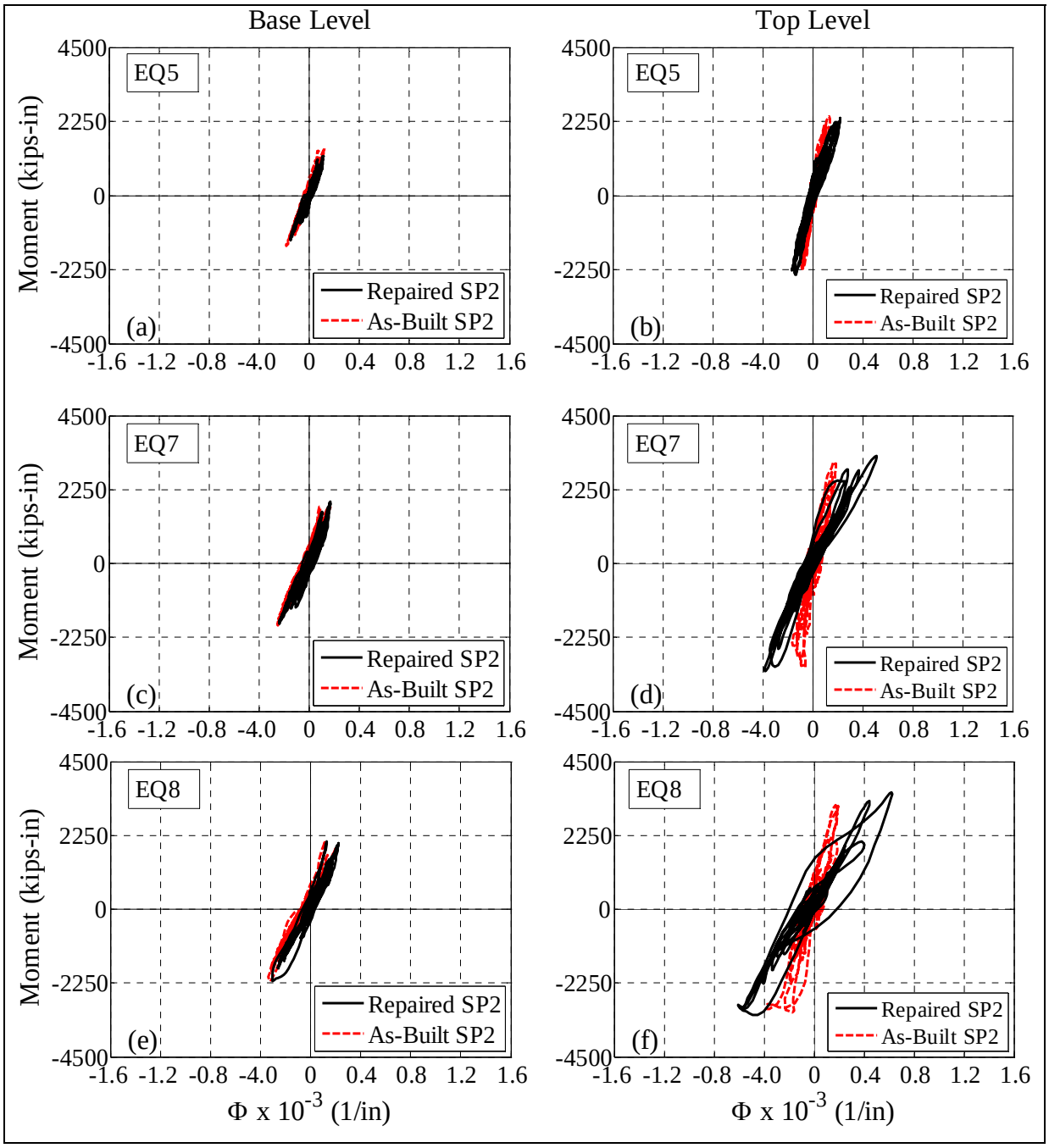

Figure 5.36 Moment-Curvature response during 50%-, 70%- and 95%-scaled ground motions.

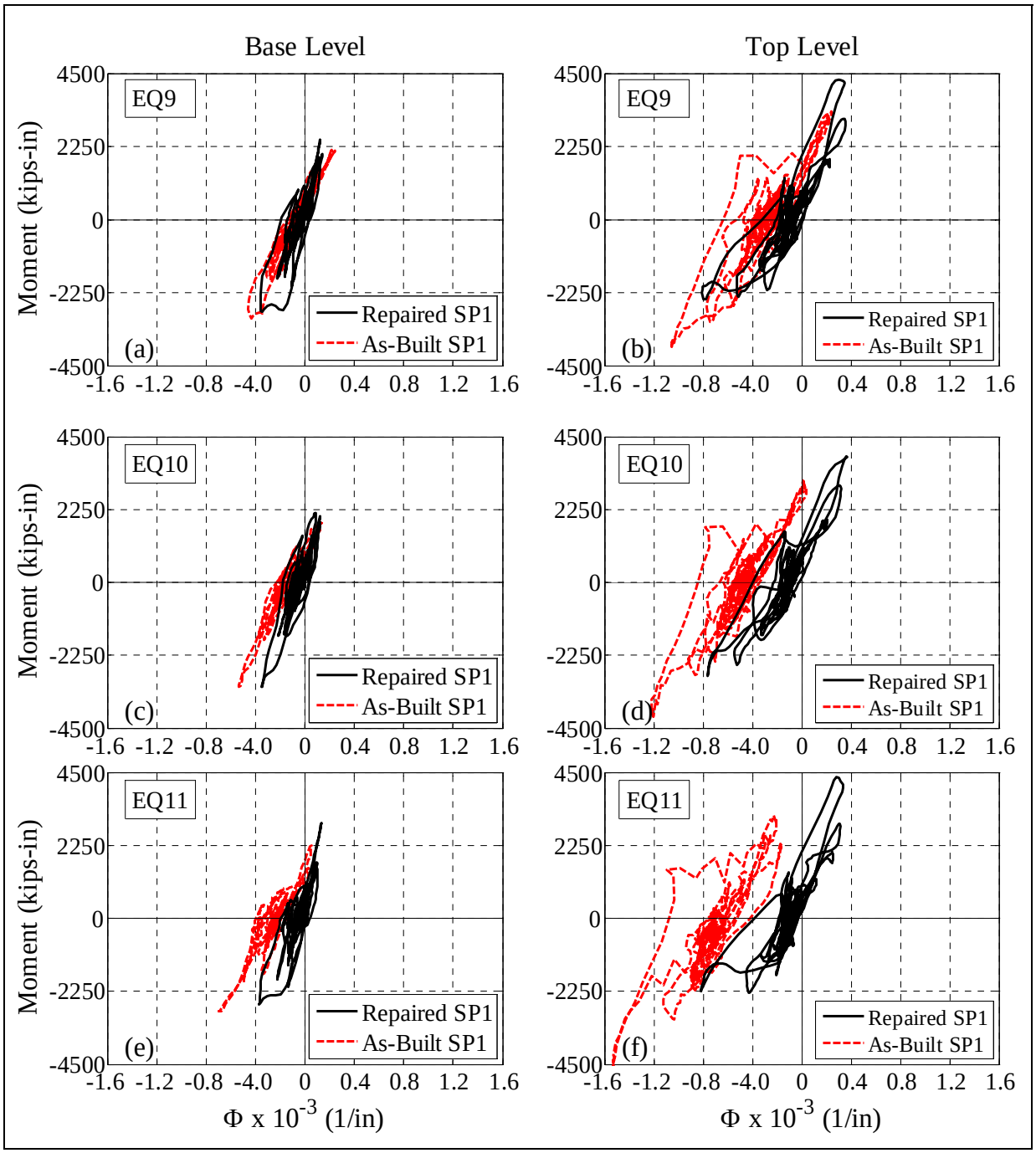

Figure 5.37 Moment-Curvature response during 125%-scaled ground motions.

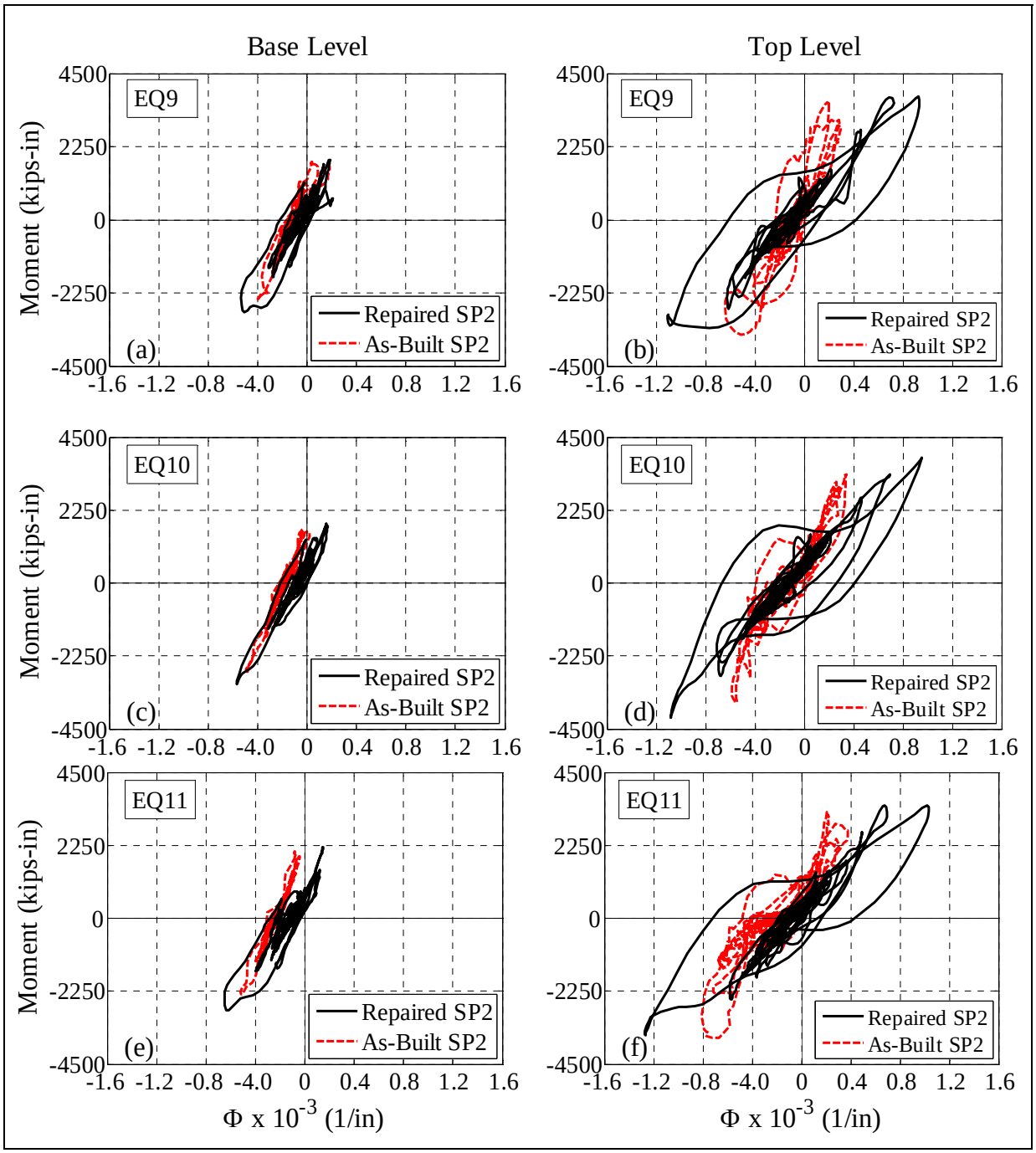

Figure 5.38 Moment-Curvature response during 125%-scaled ground motions.

Chapter 6. Computational Study

6.1 INTRODUCTION

A three-dimensional (3D) Finite Element (FE) model was developed to complement the experimental study and was calibrated using the shaking table test results. The main goal of the FE analysis is to calibrate and validate a set of nonlinear concrete constitutive material model parameters for possible future use and extended parametric study. The 3D model was created and tested using TNO DIANA (DIspalcement ANAlyser, 2011). DIANA is a FE analysis software package with modeling capabilities in 2D and 3D, and provides fast and accurate computations for linear and nonlinear models [58]. The following sections presents a brief background of 3D concrete and reinforcement modeling, and the nonlinear solution and the model development approach, and the output of the analytical model results versus the experimental results for the repaired test specimens.

6.2 CONCRETE MODELING

6.2.1 Mesh Type

Several options are available in DIANA for creating the mesh. However, only the auto-meshing algorithm was used in this study to generate the FE model using solid tetrahedron elements (TE12L) [58]. The TE12L is a 4 nodes and 3 side solid element with isoperimetric formulation (Figure 2.1). It is based on linear interpolation and 1-, 4- and 5-point Gauss integration. DIANA by default applies a 1-point integration scheme over the volume. Each node of the element has 3 DOFs and displacement (u_{XYZ}) of any point within the element is expressed using linear polynomial as follows,

$$u_i(\xi, \eta, \zeta) = a_0 + a_1\xi + a_2\eta + a_3\zeta \quad \textbf{(6.1)}$$

where ξ, η and ζ are the parametric coordinates of the TE12L element. The linear polynomial yield a linear stress and strain distribution over the element.

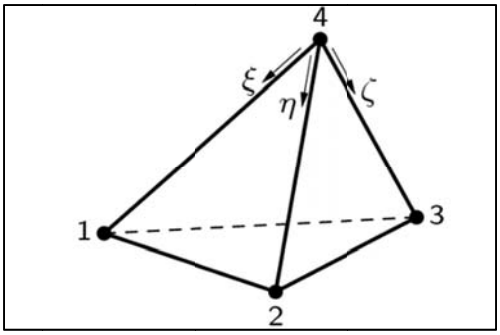

Figure 6.1 Solid tetrahedron element TE12L.

6.2.2 Total Strain Rotating Crack Model

Reinforced concrete is a heterogeneous material with markedly different response under compressive and tensile loading. Cracking of concrete has significant impact on the tensile and compressive strength of the material. Analytical modeling of cracked concrete is a challenging task due to the geometrical discontinuities caused by cracking. Rashid (1968) [45] proposed the modeling approach to consider cracking of concrete in FEA by adjusting the material stiffness, called the smeared crack approach and has been modified by several researchers [7], [21].Total Strain crack method was implemented in DIANA to model the behavior of cracked concrete based on the smeared crack approach. The model assumes that the cracks are always normal to the maximum principle strain and rotate as principle strain rotates [6], [24].

The stresses in the Total Strain Rotating crack model method are computed in the direction of the cracks. The strain vector, $\{\boldsymbol{\epsilon}\}$ in the element coordinate axis is updated with strain increment $\{\boldsymbol{\Delta\epsilon}\}$ at time step increment of Δt as follows,

$$\{\boldsymbol{\epsilon}\}_{i+1}^{t+\Delta t} = \{\boldsymbol{\epsilon}\}^{t} + \{\Delta\boldsymbol{\epsilon}\}_{i+1}^{t+\Delta t} \tag{6.2}$$

The updated strain vector is oriented in the direction of crack using the strain transformation matrix $[\boldsymbol{S}]$ to compute strains in the crack coordinate system $\{\boldsymbol{\varepsilon}\}$ as follows,

$$\{\boldsymbol{\varepsilon}\}_{i+1}^{t+\Delta t} = [\boldsymbol{S}]\,\{\boldsymbol{\epsilon}\}_{i+1}^{t+\Delta t} \tag{6.3}$$

The stress vector $\{\boldsymbol{\sigma}\}$ in the crack coordinate system is then computed using the constitutive relationship which is generally given by:

$$\{\boldsymbol{\sigma}\}_{i+1}^{t+\Delta t} = f\left(\{\boldsymbol{\epsilon}\}_{i+1}^{t+\Delta t}\right) \tag{6.4}$$

The updated stress vector $\{\boldsymbol{\Sigma}\}$ in the element coordinate system is computed as,

$$\{\boldsymbol{\Sigma}\}_{i+1}^{t+\Delta t} = [\boldsymbol{S}]^{T}\,\{\boldsymbol{\sigma}\}_{i+1}^{t+\Delta t} \tag{6.5}$$

To incorporate and monitor the cracking and the crushing of the concrete, six internal damage variable (D_k) are defined where, α_1, α_2, and α_3 were assigned to monitor the maximum strains (zero and above) and α_4, α_5, and α_6 were assigned to monitor the minimum strains (zero

and below). To model the stiffness degradation in tension and compression, additional unloading constraints (r_k) were defined. In tension,

$$C_k = \begin{cases} 0, \{\boldsymbol{\varepsilon}_k\}_{i+1}^{t+\Delta t} > \alpha_k \\ 1, \{\boldsymbol{\varepsilon}_k\}_{i+1}^{t+\Delta t} \leq \alpha_k \end{cases}, \; k = 1, 2 \text{ and } 3 \tag{6.6}$$

and in compression,

$$r_k = \begin{cases} 0, \{\boldsymbol{\varepsilon}_{k-3}\}_{i+1}^{t+\Delta t} < \alpha_k \\ 1, \{\boldsymbol{\varepsilon}_{k-3}\}_{i+1}^{t+\Delta t} \geq \alpha_k \end{cases}, \; k = 4, 5 \text{ and } 6 \tag{6.7}$$

The stress in any direction *x* is computed as follows,

$$\sigma_x = f_x(\alpha_1, \alpha_2, \ldots \alpha_6, \boldsymbol{\varepsilon}) \times g_x(\alpha_1, \alpha_2, \ldots \alpha_6, \boldsymbol{\varepsilon}) \tag{6.8}$$

where f_x is the constitutive function and g_x is the loading and unloading function (Figure 6.2). In this study, a secant stiffness matrix approach is adopted. This approach has proven to be robust and stable in RC structures with extensive cracking. The loading and unloading branches were modeled by computing the maximum and minimum strain in each crack direction. The function g_x was computed as follows,

$$g_x = \begin{cases} 1 - \dfrac{\alpha_x - \varepsilon_x}{\alpha_x}, \; \varepsilon_x > 0 \\ 1 - \dfrac{\alpha_{x+3} - \varepsilon_x}{\alpha_{x+3}}, \; \varepsilon_x < 0 \end{cases} \tag{6.9}$$

In an incremental-iterative solution scheme, equilibrium between the internal and external force vectors is achieved with an iterative procedure. For this purpose, the secant stiffness of the constitutive model is utilized to achieve equilibrium (Figure 6.2). The secant stiffness in the *x*-direction is given as follows,

$$\bar{E}_{sec,x} = \begin{cases} \dfrac{f_x(\alpha_1, \alpha_2, \ldots \alpha_6, \boldsymbol{\varepsilon})}{\alpha_x}, Tension \\ \dfrac{f_x(\alpha_1, \alpha_2, \ldots \alpha_6, \boldsymbol{\varepsilon})}{\alpha_{x+3}}, Compression \end{cases} \tag{6.10}$$

The secant stiffness matrix (in all directions) for an orthotropic material (with zero Poisson's ratio) in crack coordinates system is given by a diagonal matrix as,

$$[\bar{E}_{sec}] = Diag[\bar{E}_{sec,1}, \bar{E}_{sec,2}, \bar{E}_{sec,3}, \bar{G}, \bar{G}, \bar{G}] \tag{6.11}$$

where $\bar{G} = \beta_S G$ and the parameter β_S ($0 \leq \beta_S \leq 1$) is a non-dimensional shear retention factor that reduced the elastic shear modulus G of concrete to constant value $\bar{G}$ after cracking. DIANA offers pre-defined compressive behavioral models for use with the total strain crack models. The tensile relationship is based on linear tension softening. The tensile behavior depends on the concrete tensile strength f_t and the fracture energy G_f^I from crack opening mode (mode I). The areas under the compressive and tensile stress-strain relationships control the ultimate compressive strain and the crack strain beyond which the concrete loses its entire respective

capacities. These areas depend on the band-width (h), i.e. localization size, of plasticization or damage due to cracking which is expressed as $h = \sqrt[3]{V_e}$ where V_e is the volume of the FE.

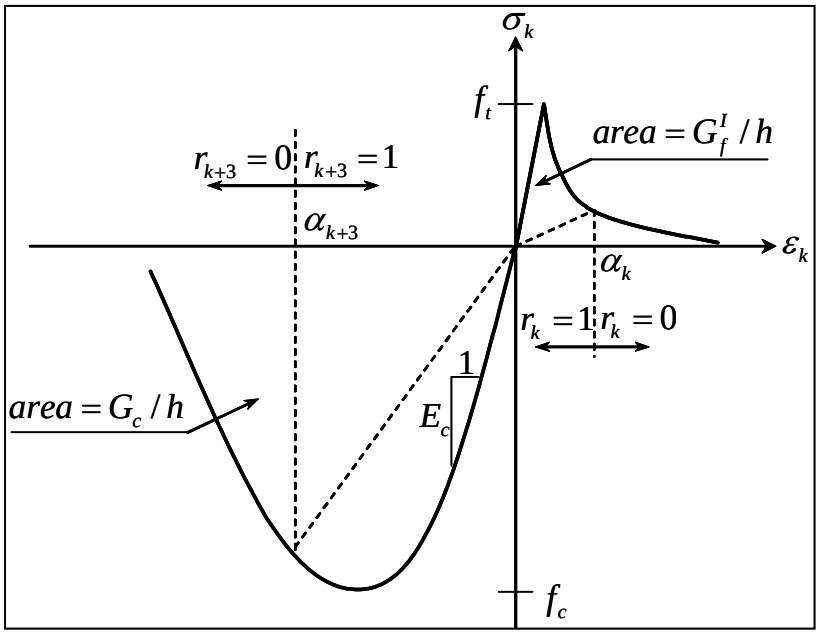

Figure 6.2 Unidirectional concrete material model in the principal directions.

6.2.3 Constitutive Relationship

For the present study the stress-strain response of the concrete under compression was assumed to be bilinear [31], [39], [56], [61]. The bilinear constitutive relationship proposed by Saiidi et al. (2005) [56] was used to compute the concrete properties (Figure 6.3a). The stress at the break point corresponding to a strain (ε_c) of 0.002 was computed as follows,

$$f_c = f_{co} + 0.003\rho_{cf}E_j \tag{6.12}$$

$$\rho_{cf} = 4n_j t_j / D \tag{6.13}$$

where f_c is the stress at the break point, f_{co} is the strength of unconfined concrete, ρ_{cf} is volumetric ratio of FRP jacket, E_j is the tensile modulus of the FRP composite jacket, n_j is number of FRP plies, t_j is the thickness of each ply and D is the diameter of the column. The ultimate stress and strain of concrete in compression is computed as follows,

$$f_{cu} = f_{co} + 3.5f_l^{0.7} \tag{6.14}$$

$$\varepsilon_{cu} = \varepsilon_j / \left(0.1 - 0.25ln(f_l/f_{co})\right) \tag{6.15}$$

where f_l is the confinement pressure, ε_j is the jacket strain. The confinement pressure was computed considering effect of hoop steel and the FRP composite jackets. Jacket strain was assumed to be 50% of the ultimate FRP jacket strain [56].

The tensile stress-strain response of concrete was assumed to be linear until the maximum tensile strength followed by a linear softening branch (Figure 6.3b). The initial stiffness of the constitutive model under compression and tension was assumed to be equal and was one of the parameters used for calibrating the analytical model along with the maximum tensile strength and ultimate tensile strain of the concrete.

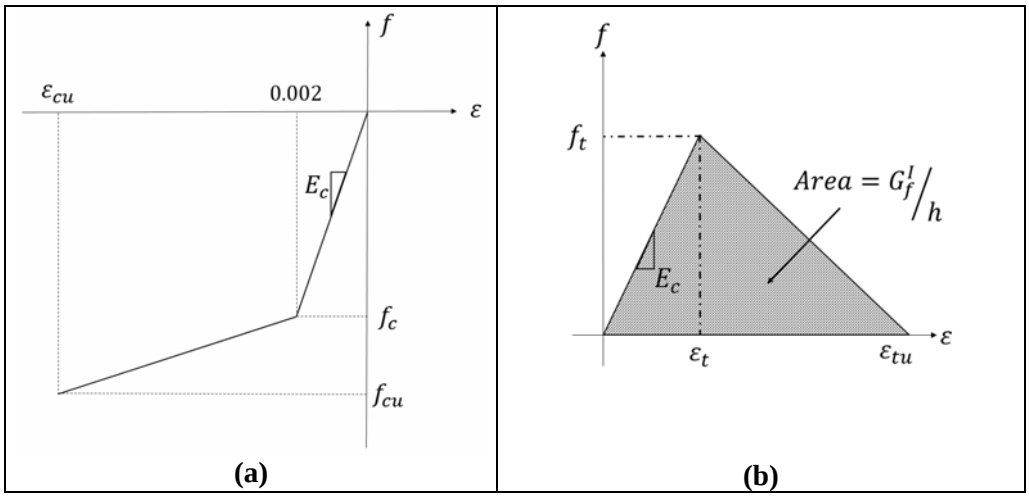

Figure 6.3 Constitutive relationship of concrete in: (a) compression; (b) tension.

6.3 STEEL MODELING

Steel reinforcement can be modeled using a discrete or smeared model in 3D solid elements. For this study, all FE models of the test specimens used the embedded (or smeared) steel reinforcement element available in DIANA (Figure 6.4a) for modeling the reinforcements. The embedded reinforcement modifies the stiffness and strength properties of the concrete element (also called the parent element) that it passes through while assuming a perfect bond between the concrete and the steel. DIANA (2011) [58] also offer the discreet reinforcement steel element that takes into account the bond slip behavior of the steel bars. The discretized steel model is computationally demanding and requires additional interface nodes. No bond slip was observed during the dynamic testing of the repaired specimens. Thus, the embedded reinforcement model was used.

In case of the embedded steel element the reinforcement displacements $\{u_R\}$ are computed using the same shape functions ($[N]$), which are used to compute the displacement in the concrete elements as follows,

$$\{u_R\} = [N]\{d\} \tag{6.16}$$

$$\{\varepsilon_R\} = [B]\{d\} \tag{6.17}$$

However, the reinforcement displacements are evaluated at the isoparametric coordinates of the reinforcement integration points, e.g. using 2-point Gauss integration scheme. Therefore, the strain vector in the reinforcement $\{\varepsilon_R\}$ is computed using the strain-displacement matrix ($[B]$) evaluated at the reinforcement integration points (Equation 6.17). Making use of transformation, constitutive equations, and FE procedure, one can obtain the contribution of the reinforcement to the stiffness of the concrete elements and the corresponding internal forces. Accordingly, the stiffness and internal force contributions of the reinforcement are accounted for in a similar manner as the concrete element stiffness and internal forces with only the exception that integration is performed at the reinforcement integration points rather than at the element integration points.

The reinforcement steel was modeled using the Voce hardening rule along with the Von-Mises yield criterion as follows (Figure 6.4b) [58]:

$$\sigma(\varepsilon) = \begin{cases} \varepsilon E_s \leq \sigma_y\,, & \varepsilon < \varepsilon_y + \varepsilon_{pl} \\ \sigma_y + (\sigma_u - \sigma_y)\left(1 - exp\left(-\dfrac{\varepsilon - \varepsilon_y - \varepsilon_{pl}}{\varepsilon_{po}}\right)\right), & \varepsilon \geq \varepsilon_y + \varepsilon_{pl} \end{cases} \tag{6.18}$$

where σ_y is the yield stress, σ_u is the ultimate stress, E_s is the modulus of elasticity of steel, ε_y is the yield strain, ε_{pl} the yield plateau strain and ε_{po} is a parameter to adjust the strain-hardening regime. All parameters in Equation 6.18 were calibrated against the actual reinforcement steel properties obtained from the material tests (Section 2.6).

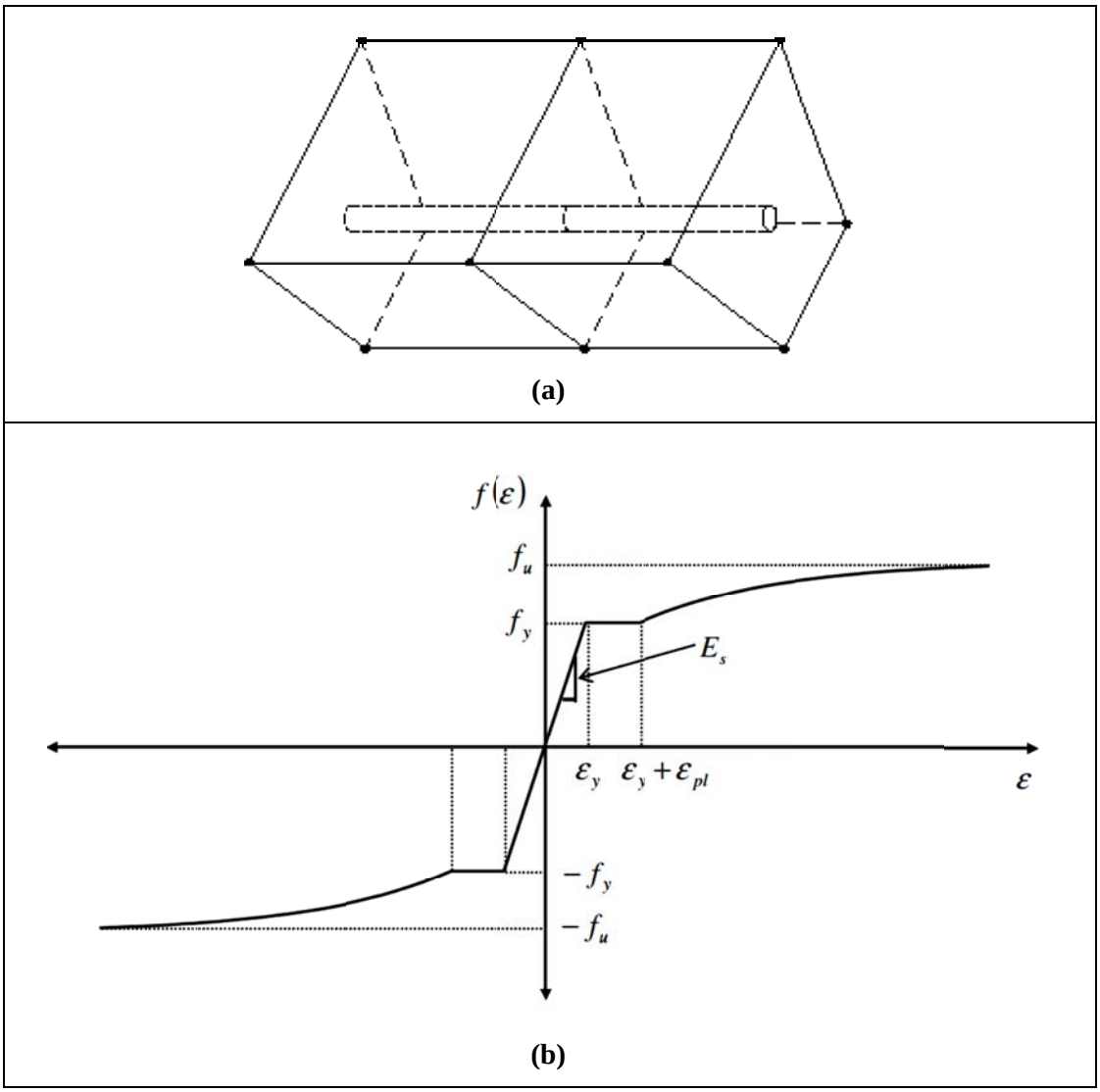

Figure 6.4 (a) Embedded reinforcement element; (b) Constitutive relationship of steel in compression and tension.

6.4 INCREMENTAL-ITERATIVE PROCEDURE

In case of nonlinear FE analysis, the state of equilibrium is determined by discretization of space (finite dimensional) and time employed in the incremental-iterative solution procedures. The time increment used for the case of dynamic analysis is the real time increment. The equilibrium at each time step is achieved by adopting suitable iterative algorithms. The iterative solution methods are based on the concept of generating a sequence of approximation for the desired solution (e.g. displacement vector) using the following state recovery formula,

$$\{u_{i+1}\} = \{u_i\} + \gamma_i \left(P_f - [K]\{u_i\}\right) \tag{6.19}$$

where P_f is the force vector, $\{u_i\}$ & $\{u_{i+1}\}$ are respectively the displacement vectors at time step i & $i+1$, and γ_i is defined as the iterative solver such that the residual $\left(P_f - [K]\{u_i\}\right)$ converges to zero. DIANA offers several iterative solution methods such as Newton-Raphson method, Quasi-Newton method and the Linear Stiffness method. Quasi-Newtown method was used for the iterative solution procedure in this study.

The Quasi-Newton method (also known as the Secant Method) used the information of the previous solution vectors and the out-of-balance force vectors during the increment to achieve a better approximation (Figure 6.5). The stiffness of the structure is determined from the known positions at the equilibrium path. Three different methods are available in DIANA for assembling the Quasi-Newton stiffness matrix. These are the Broyden, the Broyden-Fletcher-Goldfarb-Shanno (BFGS), and the Crisfield methods. Only the Broyden method was used in this study as it demonstrated the least rate of divergence in runs with large number of DOF.

For the time step increments, the initial choice of the step size for every increment is an important factor in the incremental-iterative process. There are several methods that can be used to determine the step sizes, e.g. fixed time increment method and arc-length method. Only fixed time step incremental methods that used fixed steps either in load control or displacement control were used in this study.

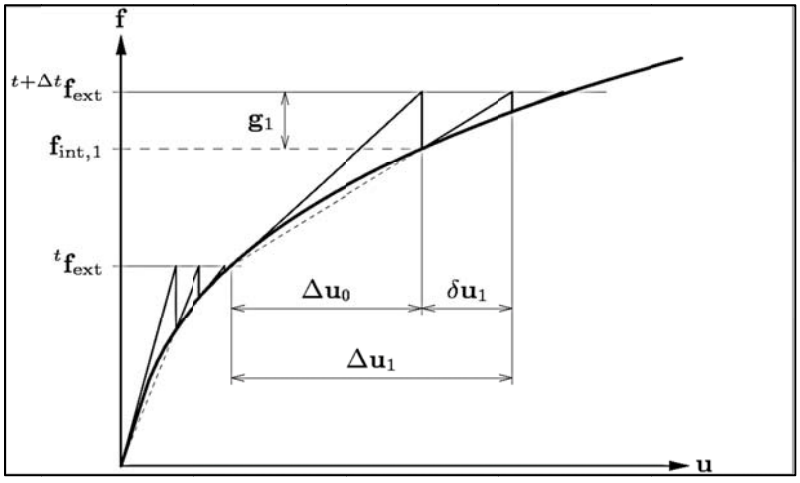

Figure 6.5 Quasi-Newton iterations.

6.5 DIANA MODEL

The analytical model was created using the auto-mesh algorithm as previously mentioned to generate a model that had 2187 nodes and 4092 TE12L (solid tetrahedron) elements (Figure 6.6). In order to replicate the superstructure mass configuration four rigid elastic beams were added to the model. The dead weight of the superstructure mass was applied as point mass at the end of each of the four rigid elastic beams (Figure 6.6 and Figure 6.7a). The length of the elements was adjusted such that the point mass location at the end of the beams matched the actual test specimen. Additional 162 elements (for the repaired SP1) and 140 elements (for the repaired SP2) were created for the embedded bar reinforcement (Figure 6.7b). As discussed in the previous sections the total crack rotating strain model was used for the concrete elements. The analytical FE model was developed based on the material properties of the as-built specimens and the relevant material models to incorporate the effect of the FRP jackets as previously discussed.

Table ***3.2*** lists the concrete properties used for the first trial DIANA model. The confinement pressure was computed using two different cases: confinement provided by the hoop steel and FRP jacket, and the confinement provided by FRP jacket only. However, the results of the analytical models were almost the same for both cases. The tensile strength and strain of the epoxy and the mortar used for the repair of the test specimens was higher than the tensile strength of the concrete (Appendix A). However, it was assumed that the tensile strength of the repaired concrete was the same as the tensile strength of the concrete coupons (Section 2.6). For the final analysis runs, the stiffness of the tensile softening branch was about 20% the stiffness of the elastic branch. The final elastic stiffness of the concrete constitutive relationship of the DIANA model was about 40% of the initial stiffness (E_C) (as computed in Table ***3.2***). The final stiffness of the longitudinal steel bars in the analytical model was about 70% of the stiffness measured from the steel coupons material tests (Section 2.6).

Table 6.1 Concrete properties for the DIANA model.

Test Specimens	ρ_{cf} **(%)**	f_c **ksi [MPa]**	E_c **ksi [MPa]**	f_l **ksi [MPa]**	f_{cu} **ksi [MPa]**	ε_{cu} **(%)**	f_t **ksi [MPa]**
Repaired SP1	0.032	4.34 [29.92]	2170 [14961.63]	0.25 [1.72]	5.34 [36.82]	0.51	0.47 [3.24]
Repaired SP2	0.016	4.49 [30.96]	2245 [15478.73]	0.32 [2.21]	5.59 [38.54]	0.55	0.47 [3.24]

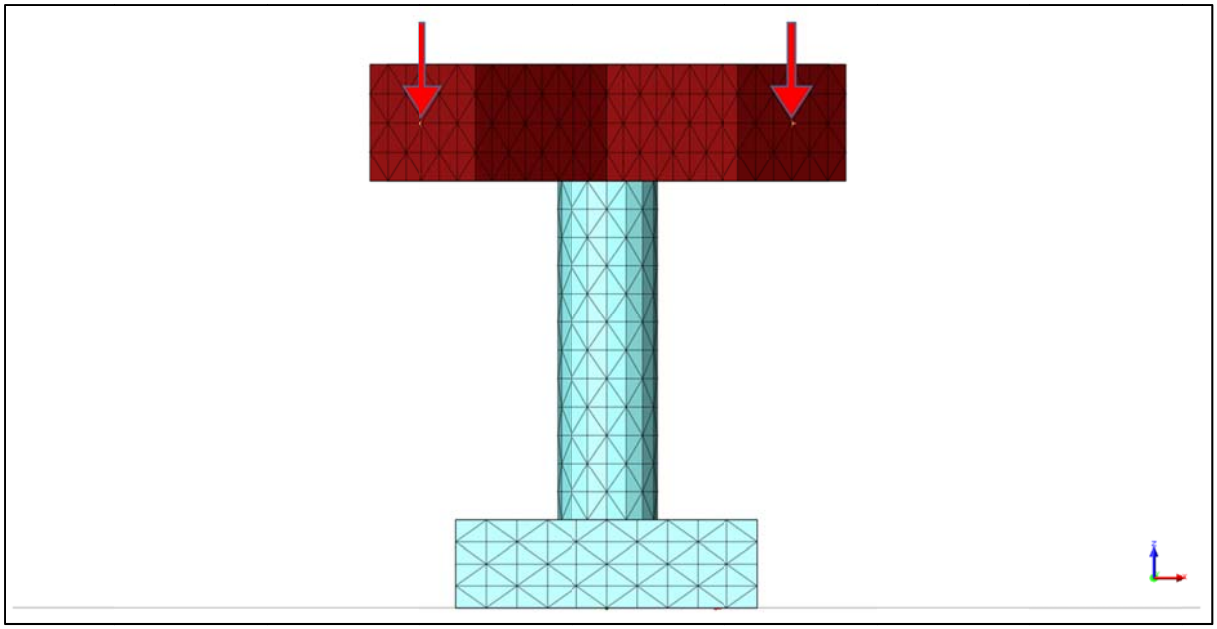

Figure 6.6 Elevation view of the analytical model.

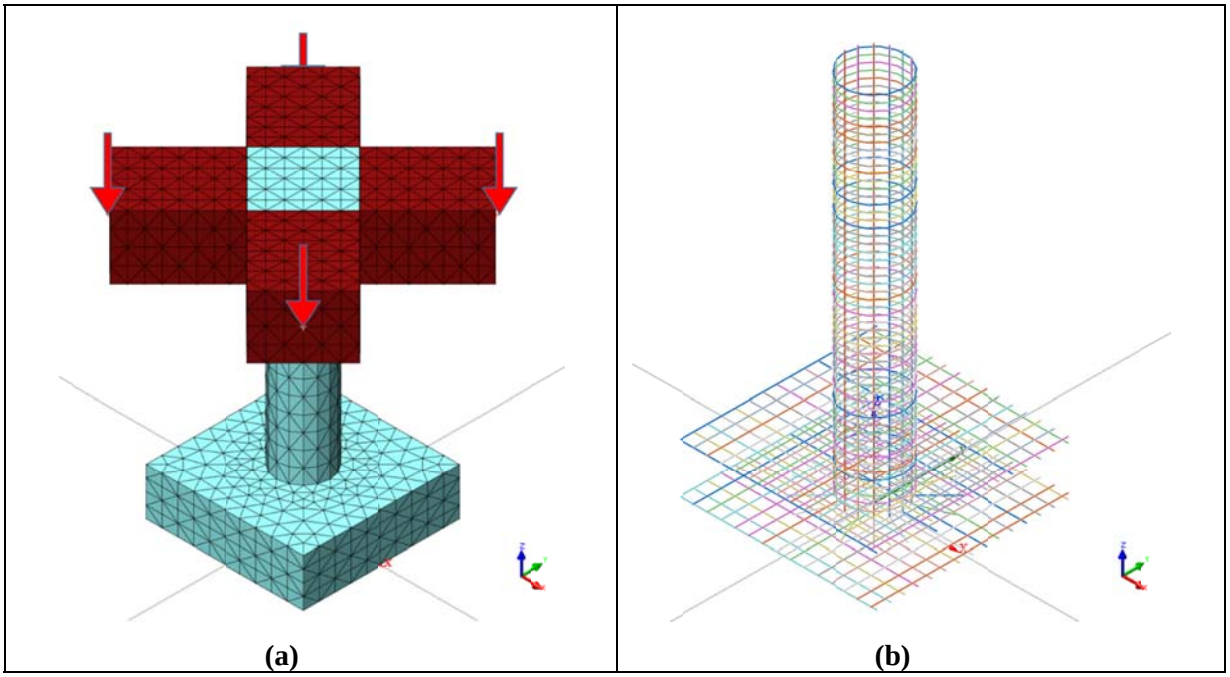

(a) **(b)**

Figure 6.7 (a) Loading and isotropic view of the analytical model; (b) embedded reinforcement cage.

6.6 BOUNDARY CONDITIONS

One parameter of the model calibration was the FE model boundary conditions at the base of the footing. The boundary conditions at the base were calibrated primarily such that the natural period of the analytical models matched the initial vibration periods of the repaired test specimens measured during the free vibration testing (Section 4.3). The natural period of the analytical models was checked by performing the Eigenvalue analysis in DIANA. Two different boundary conditions were considered for the DIANA model as described next.

For the first boundary condition (BC-I), four supports were defined under the footing at the locations (centerline) of the load cells (Figure 6.8). A zero-length spring with axial stiffness that is similar to the axial stiffness of the load cell, but rigid in the other two perpendicular directions was used to model the load cell support. Based on the results obtained from the Eigenvalue analysis, the natural period of the test specimens modeled with the 4 zero-length spring supports was 0.33 sec for the repaired SP1 model, and 0.3 sec for the repaired SP2. These values were slightly less than the period measured from the free vibration tests of the repaired specimens (Section 4.3). Figure 6.9 through Figure 6.11 show the first three vibration modes of the repaired SP1 modeled in DIANA with 4 spring supports. The results show that the axial stiffness of the spring was not high enough to reproduce the experimentally determine vibration periods. Thus, a mode stiff case considered for the boundary conditions.

For the second boundary condition (BC-II), all the nodes of the footing base were fixed to represent a fixed base scenario (Figure 6.12). The natural period of the analytical models, as obtained from the eigenvalue analysis, was 0.51 sec for the repaired SP1, and 0.48 sec for the repaired SP2. These values were close to 0.53 sec and 0.51 sec, the natural periods of the repaired SP1 and SP2, respectively, estimated from the free vibration testing (Section 4.3). The vertical period of both analytical models (with BC-II) was 0.045 sec, which reasonably compared to the experimentally measured vertical period of the repaired test specimens (0.032 sec). Figure 6.13 through Figure 6.15 show the most three relevant horizontal and vertical vibration modes of the repaired SP1 modeled in DIANA with fixed base. The model with fixed base was chosen for the final dynamic analysis due to its better dynamic properties match with the actual test specimens.

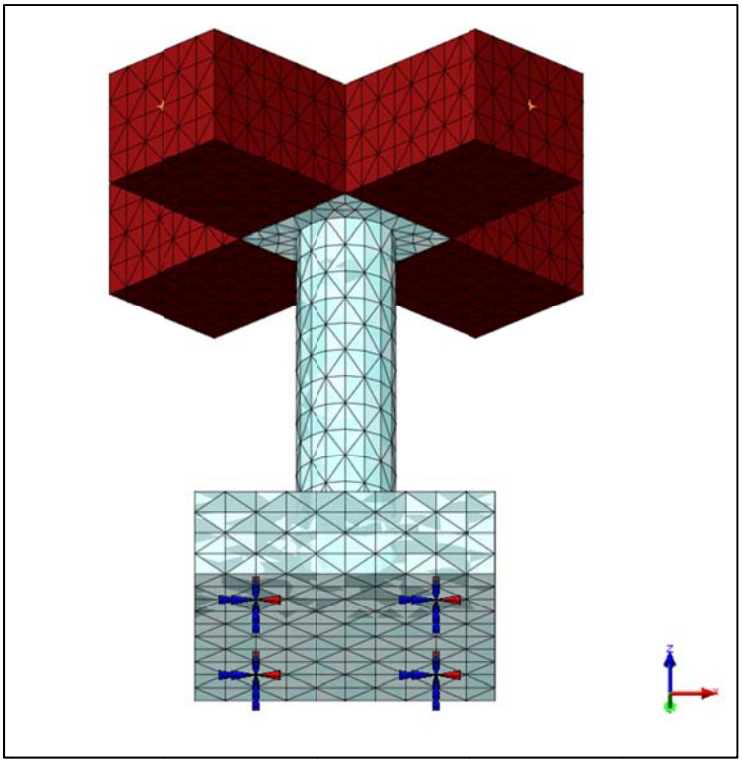

Figure 6.8 Zero-length spring supports, BC-I.

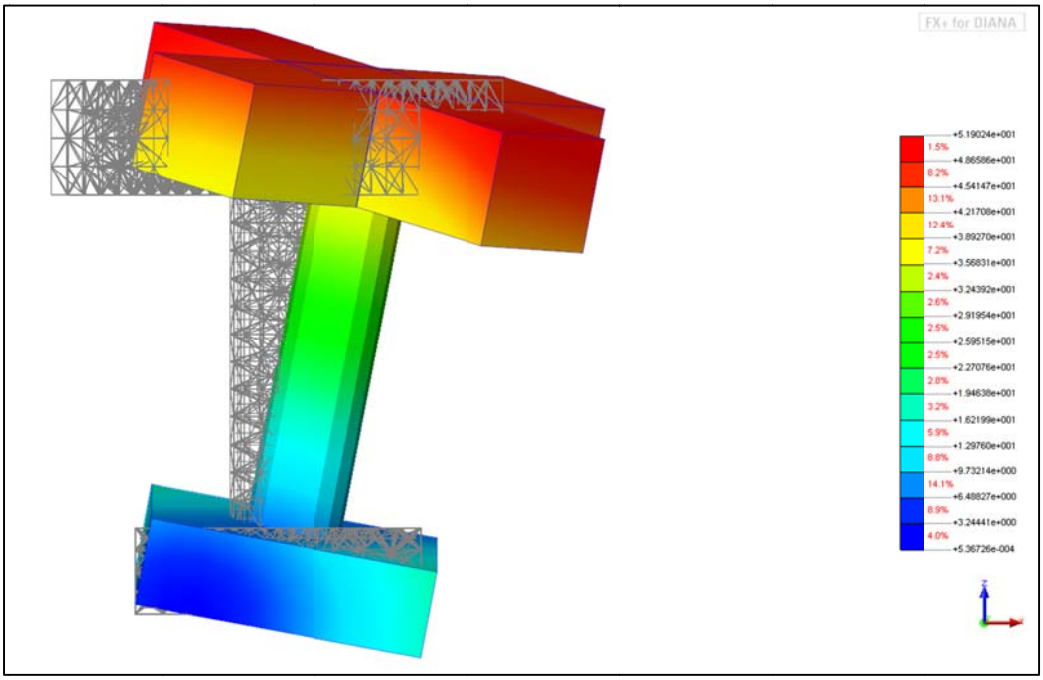

Figure 6.9 First vibration mode for the case of BC-I.

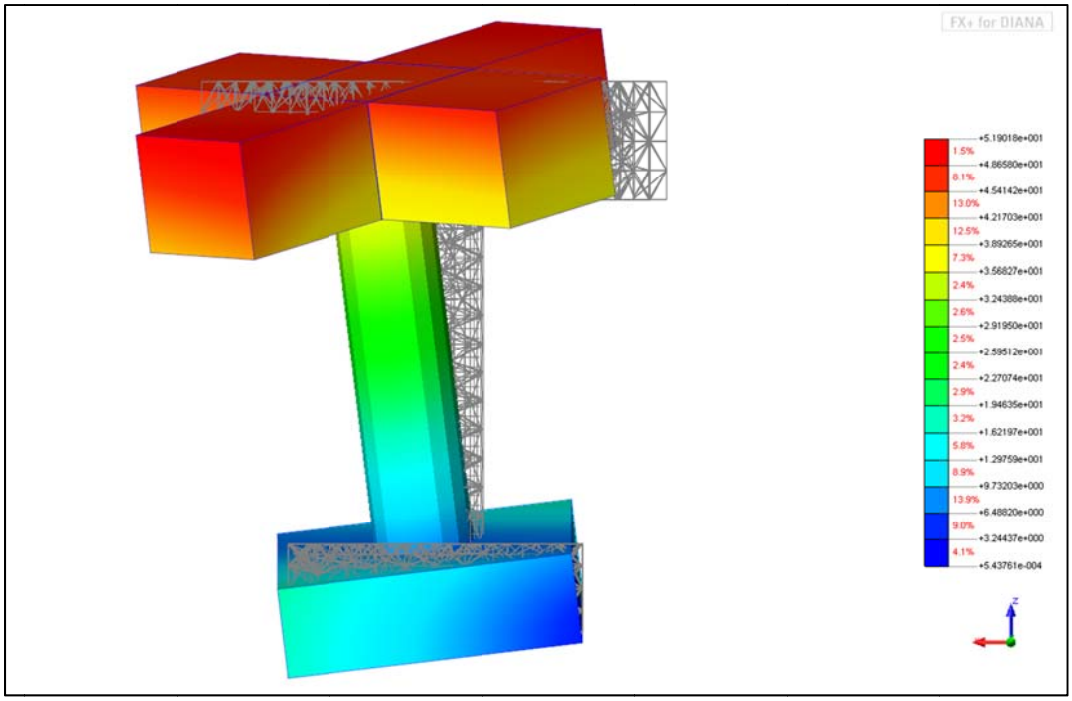

Figure 6.10 Second vibration mode for the case of BC-I.

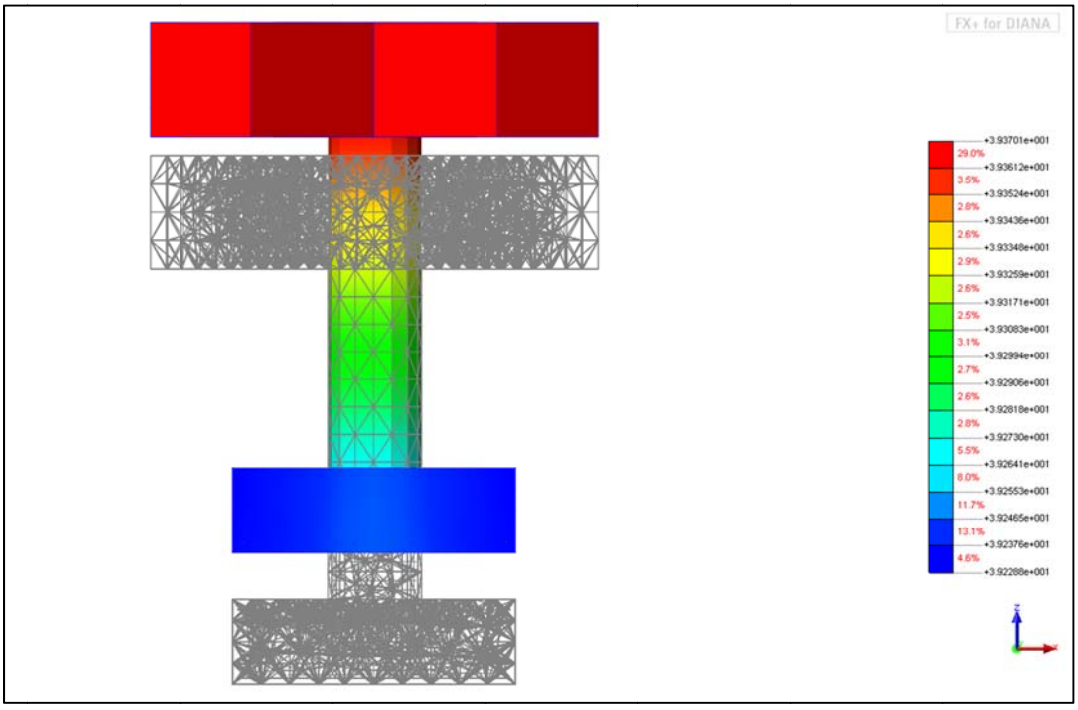

Figure 6.11 Third vibration mode for the case of BC-I.

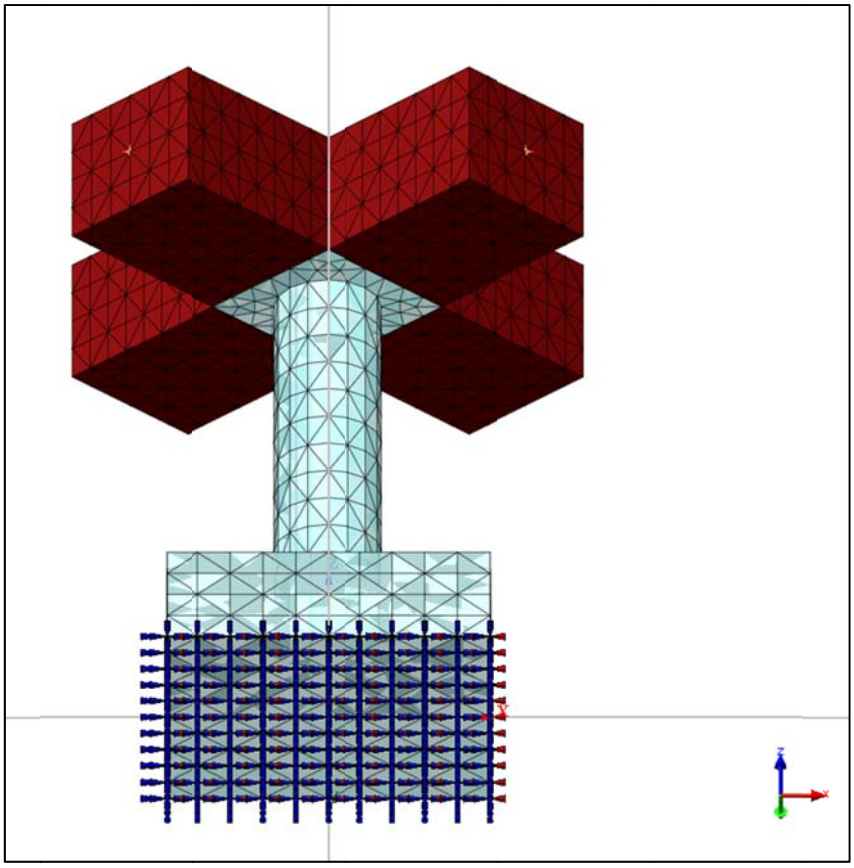

Figure 6.12 Fixed base supports, BC-II.

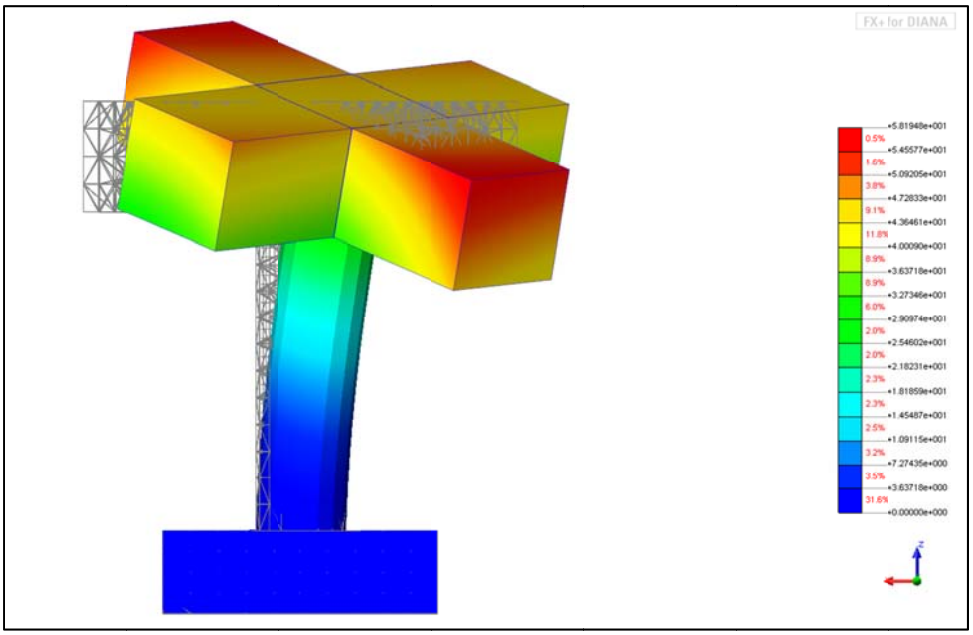

Figure 6.13 First vibration mode for the case of BC-II.

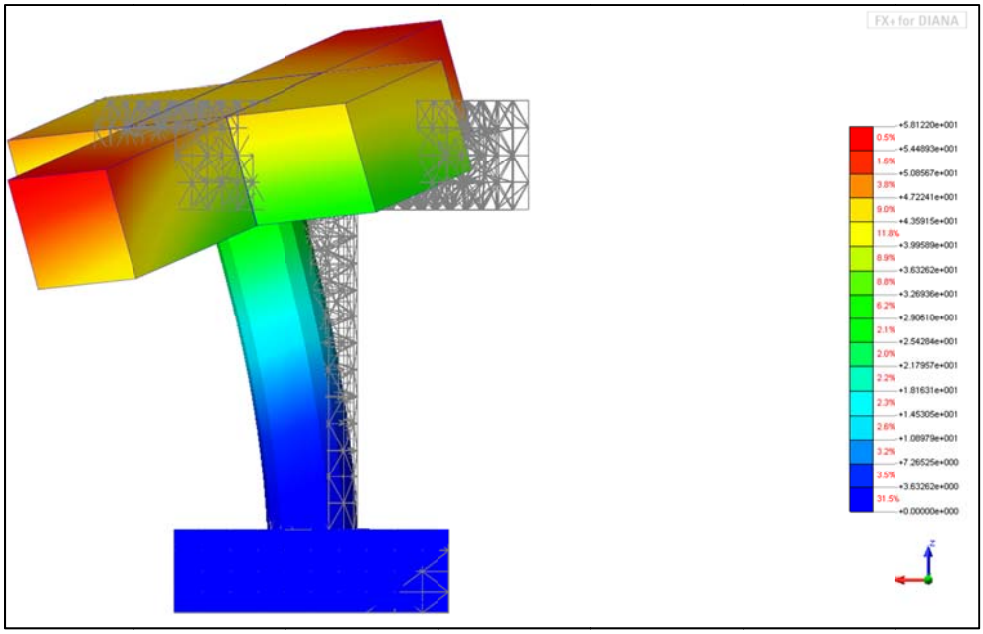

Figure 6.14 Second vibration mode for the case of BC-II.

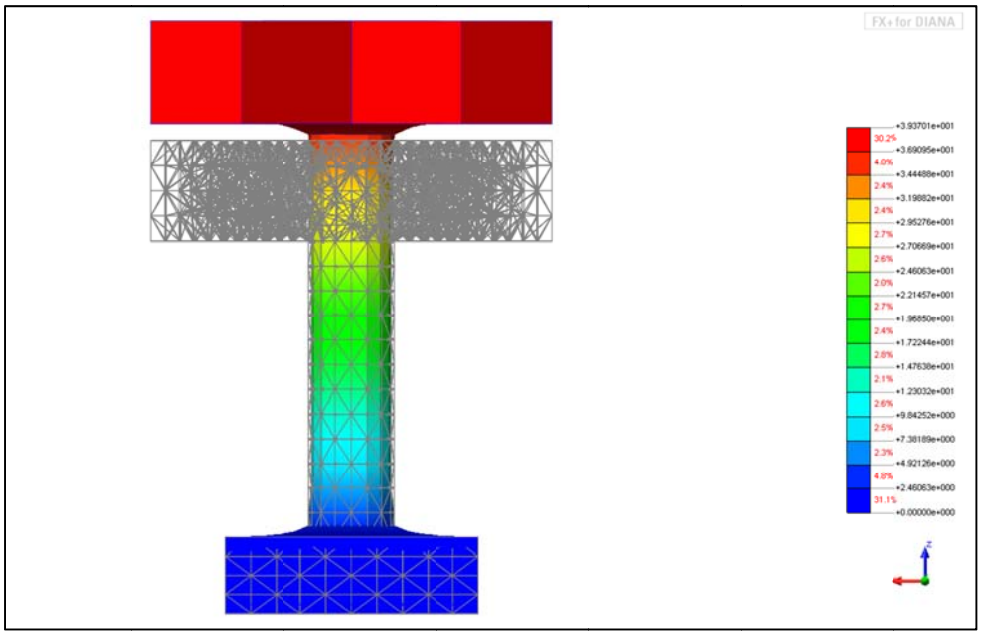

Figure 6.15 Third vibration mode for the case of BC-II.

6.7 DYNAMIC ANALYSIS

To conduct a nonlinear time history analysis using the repaired specimens DIANA models, the ground motion accelerations measured at the steel plate level (base accelerations) during the experimental testing (Section 4.3) were used as the input loading. The acceleration data measured in the X- and Z-directions during the 11 dynamic tests was combined into a single ground motion input for the analysis. In order to reduce the computation time, the ground motions were curtailed in terms of total time such that the 12 second record with the significant experimental response (e.g. displacement, forces, etc.), was used for each test specimen. Overall the analytical and experimental global response of the test specimens showed a better match during the phase-I (strong ground motion phase) than the phase-II (free vibration phase). On the other hand, the local behavior, such as the curvatures and strains, obtained from the DIANA analysis was not very accurate as it was sensitive to the mesh element types and sizes. Thus, for the lack of accurate comparison of the local behavior from the experiments and the FE analysis, only the global response is presented and discussed.

The comparison between the experimental and FE dynamic analysis results included the shear and axial forces histories, the lateral and vertical displacements histories, force-displacement relationships, and moment histories. Figure 6.16 compares the experimental and analytical shear force data measured at the base of the test specimens. It is noted that the shear force measured at the base of the footing and the base of the cantilever column was almost the same from both the experimental and analytical results. The analytical model was able to replicate the experimental shear forces reasonably. The maximum magnitude of the shear forces (negative) toward the South side was slightly higher in the case of the DIANA models than the experimental data. The maximum shear force (positive) computed by the analytical models was almost the same as the experimental results. Unlike the shear force comparison, the axial forces computed from the DIANA model fewer matches with the experimental data as shown in Figure 6.17. However, the analytical model was able to capture the experimentally measured maximum magnitude of compressive and tensile forces during EQ9 and EQ11, within less than 15% error (Figure 6.17).

Figure 6.18 compares the relative top displacement from the experimental and analytical data. The maximum displacement measured towards the South side (negative) obtained from the analytical model was comparable or slightly higher than the North side. The maximum top displacements (positive) computed by the analytical models were less than the experimental displacement magnitudes. However, the DIANA model captured the maximum magnitude of the vertical displacements with an error margin of ±20% as compared to the experimental results, given that the time instant when the maximum vertical displacement occurred was different in the experimental and analytical time histories as shown in Figure 6.19. It was also observed that the residual horizontal and vertical displacements computed from the analytical models were less than those measured from the experimental data. Figure 6.20 compares the experimental and analytical lateral shear force-displacement relationships measured during the 125%-scaled ground motions (EQ9 through EQ11). During EQ9, the, secant stiffness (ratio of maximum shear force and the corresponding displacement) measured from the North (positive) and South (negative) response of the experimental results was lower than the those computed using the DIANA model. On the other hand, the secant stiffness (positive) of the analytical model towards the North end was higher than the values during EQ10 and EQ11. This stiffer FE solution could be attributed to the fully fixed foundation base that led to lower magnitude of horizontal

displacement relative to the experimental results. However, the negative secant stiffness obtained from the analytical model and the experimental data was almost same. Additionally, the bending moments estimated at the top of the column section from the analytical FE model did not show a very with the experimental results. As observed from Figure 6.21. However, the analytical model was able to compute the maximum moments only within an error margin of ±35%.

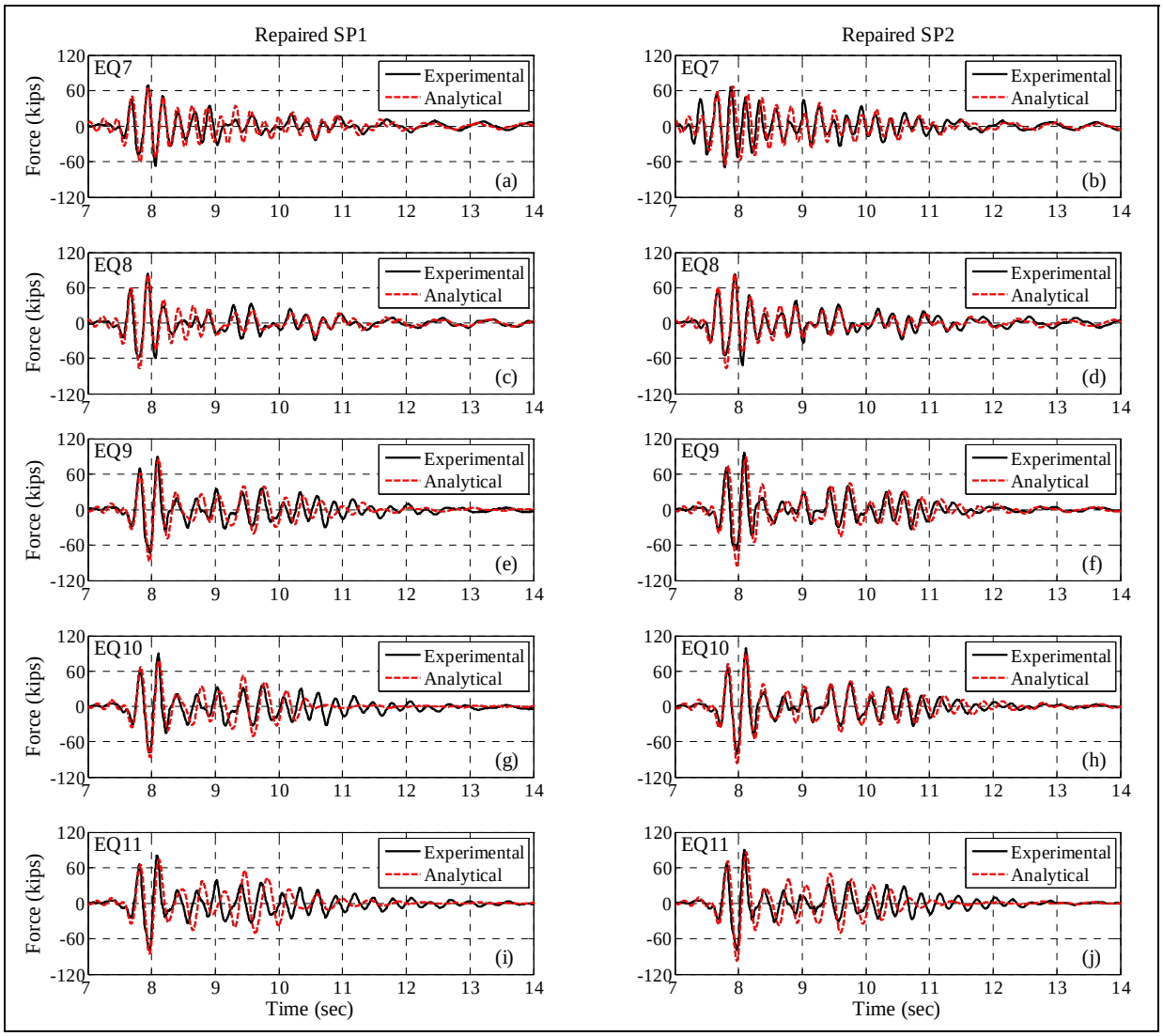

Figure 6.16 Shear force time histories.

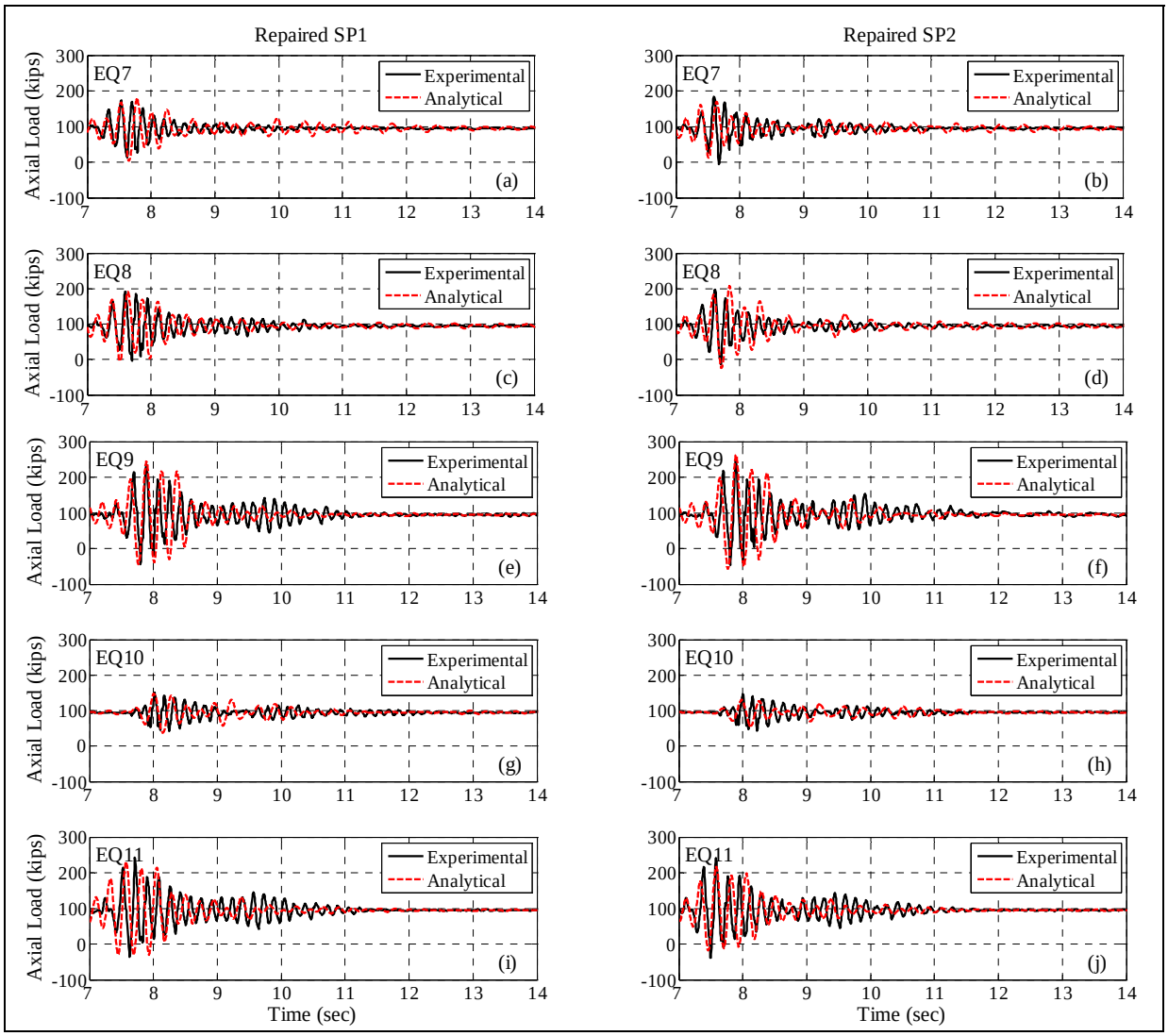

Figure 6.17 Axial load time histories.

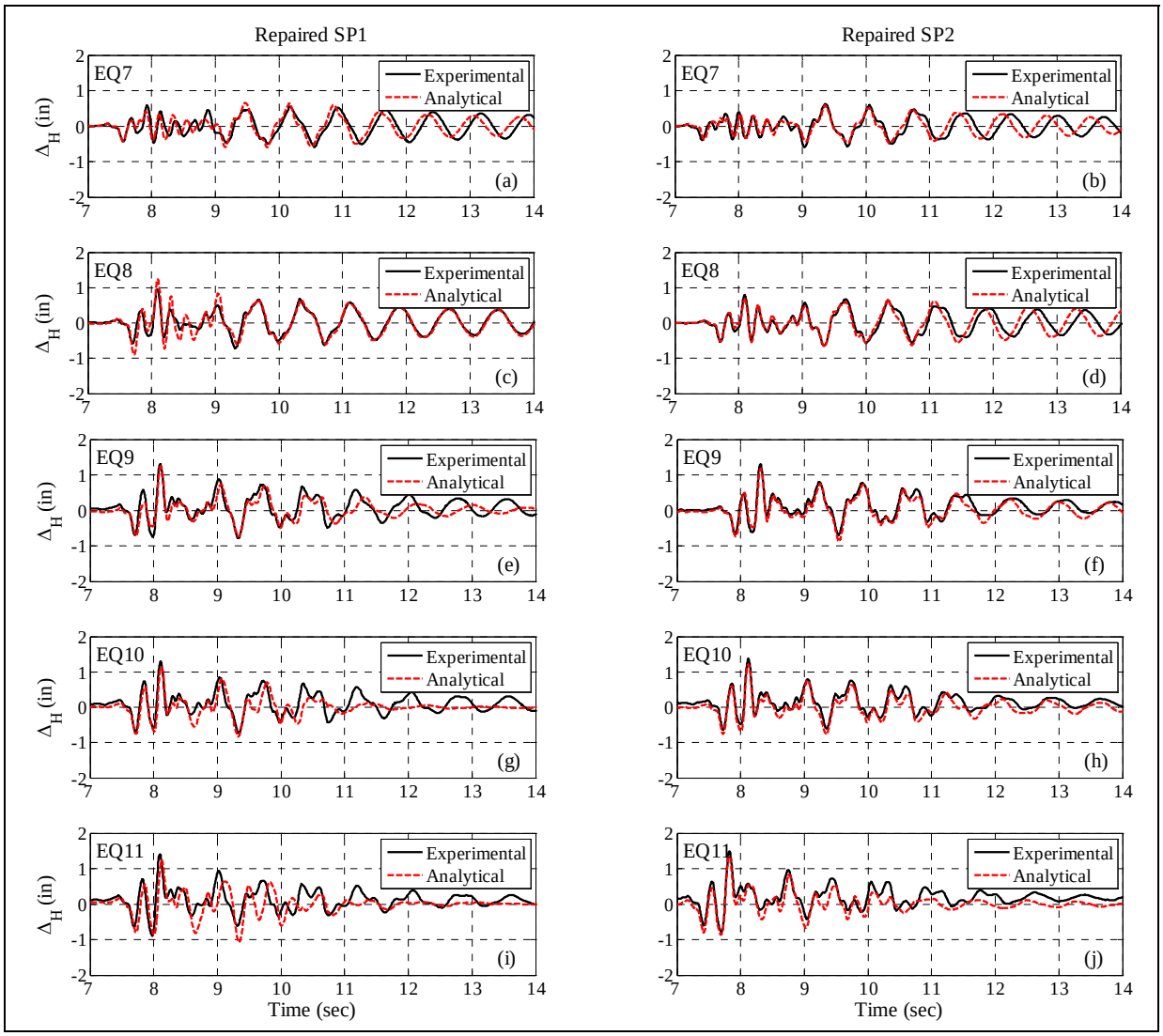

Figure 6.18 Displacement time histories.

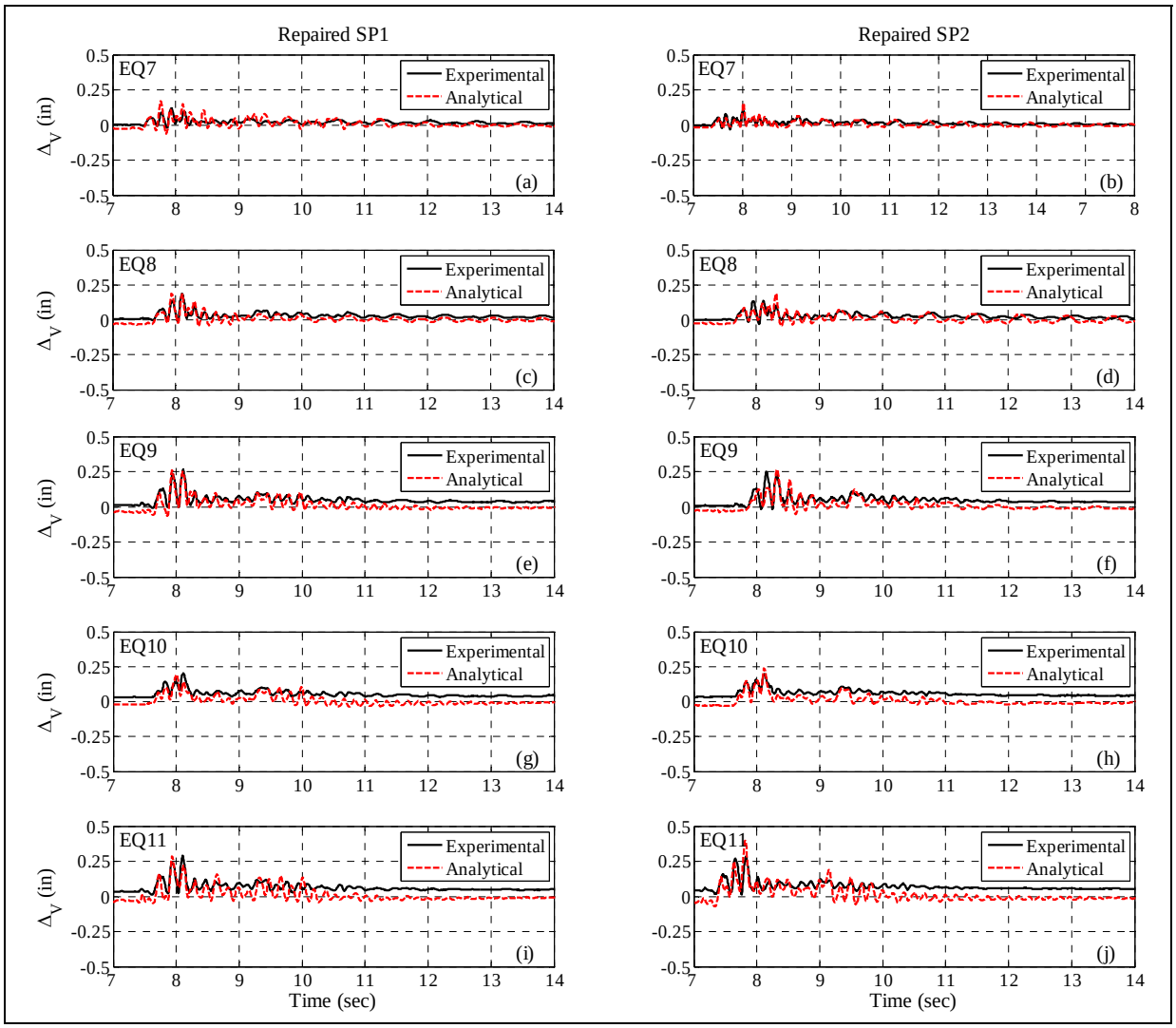

Figure 6.19 Vertical displacement time histories.

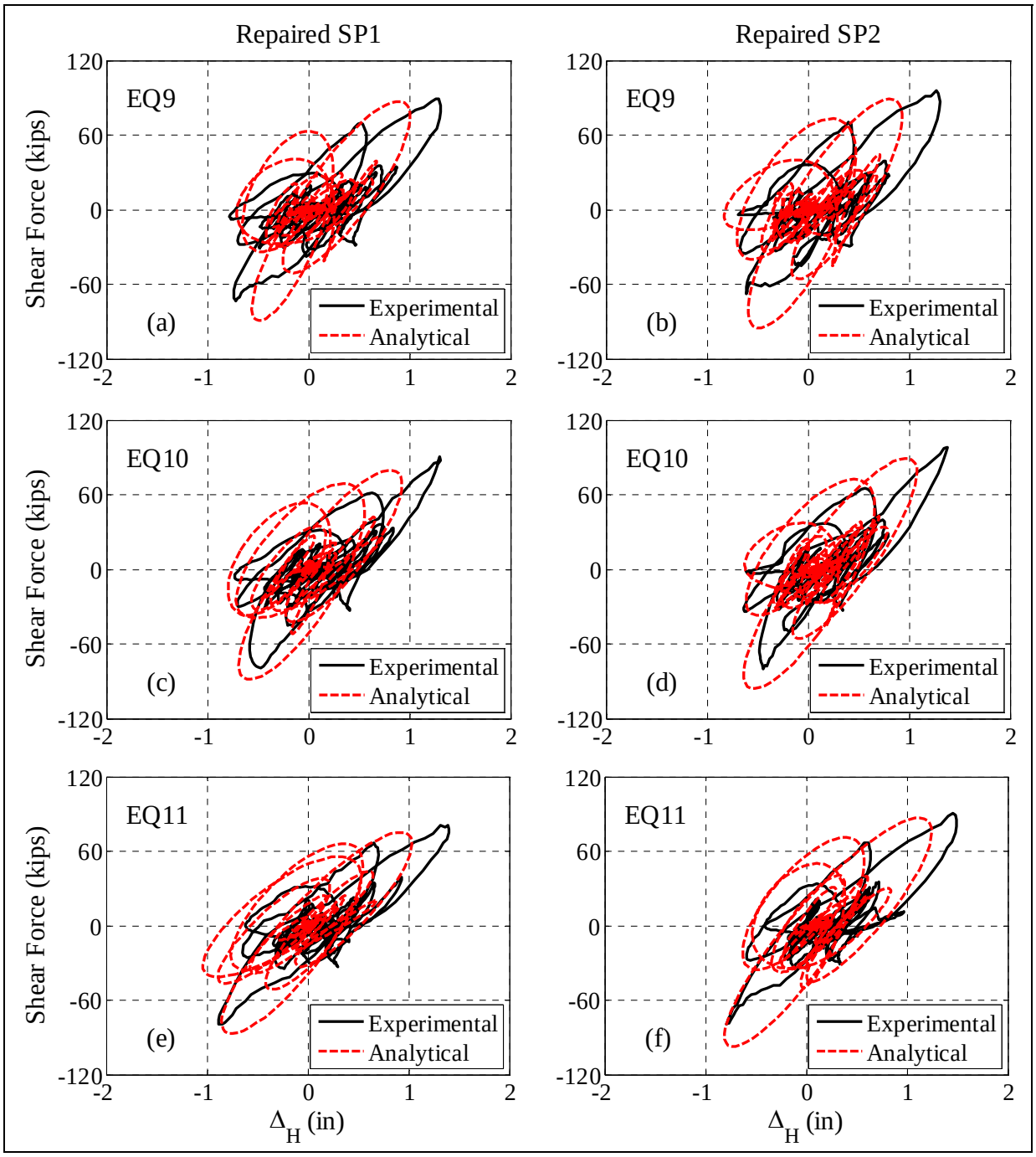

Figure 6.20 Force displacement response measured during 125%-scaled ground motions.

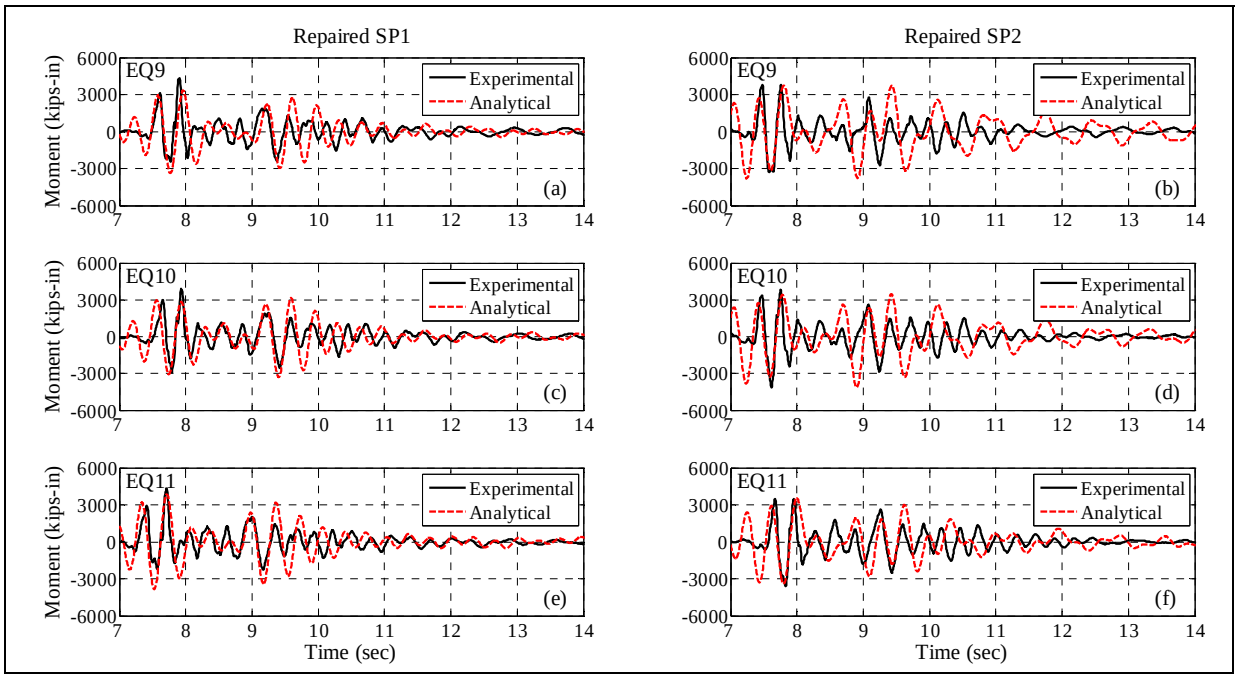

Figure 6.21 Moment time histories near the column top measured during 125%-scaled ground motions.

6.8 PARAMETRIC STUDY

After validation of the 3D FE model with the experimental test results of the repaired test specimens, the scope of the analytical model was expanded to preform a parametric study of the retrofitted columns investigating the effect of the jacket thickness on the lateral force-deformation response (global response) and confining hoop strains (local response). For the case of retrofitted column specimens it was assumed that the core concrete was not cracked.

Three 3D FE models of the RC bridge column specimens were modeled in DIANA. As-built specimens SP2 was chosen as the prototype for the computational model. The geometry, reinforcement details, superstructure mass configuration, concrete and steel properties (based on the coupon tests) of the three computational models were the same as the as-built SP2, but had different jacket thickness (Table ***6.2***). The confining strain response measured during the shaking table testing of the repaired and the as-built test specimens were not significantly affected by the vertical component of the base excitations (Section 5.3) as also discussed in, [33]. Thus, for the dynamic analysis of the FE models, the horizontal ground motion component (010), measured at the Pacoima Dam station during the 1994 Northridge earthquake, was selected.

The horizontal force-deformation response of the FE models from the dynamic analysis is shown in Figure 6.22. It was observed that the three plots were almost similar in terms of stiffness, maximum shear and displacement magnitude. The response was almost linear with negligible residual drift. This suggested that the number of plies in the FRP jacket did not have a significant effect on the lateral shear force-deformation response. This is mainly attributed to the unidirectional FRP jacket contributing to the confinement effect

The confining hoop strains obtained from the computational model with different jacket thickness differed. Figure 6.23 shows the peak confining hoop strain profiles computed from a column cross-section, located at a height of 65 in (1651 mm) above the column base. In all three models, peak confining strains computed on the North and South faces were higher than those computed on the East and West faces, suggesting higher influence of the flexure than the shear response in the composite column system. This is attributed to the strong component of the horizontal ground motion towards the North side. In comparison to M1 and M2, the confining strains computed in M3 were more uniformly distributed and had lower peak magnitudes. Peak confining strain computed using M1 was 4 times higher than M3. The difference in the confining strain response of the 4-ply and 2-ply cases was higher than the difference between the cases of 4-ply and 6-ply. Thus, the effectiveness of the jacket is not linearly dependent on the number of plies in the FRP jacket, i.e. up to a certain number of plies, 4 in this study, increasing the jacket thickness has little effect on the structural response.

Table 6.2 Concrete properties for the parametric study.

FE Model	n_j	ρ_{cf} (%)	f_c ksi [MPa]	E_c ksi [MPa]	f_l ksi [MPa]	f_{cu} ksi [MPa]	ε_{cu} (%)	f_t ksi [MPa]
M1	2	0.016	4.19 [28.88]	2170 [14961.63]	0.13 [0.87]	4.82 [33.35]	0.42	0.47 [3.24]
M2	4	0.032	4.34 [29.92]	2170 [14961.63]	0.25 [1.72]	5.34 [36.82]	0.51	0.47 [3.24]
M3	6	0.048	4.57 [31.50]	2170 [14961.63]	0.38 [2.61]	5.78 [39.84]	0.58	0.47 [3.24]

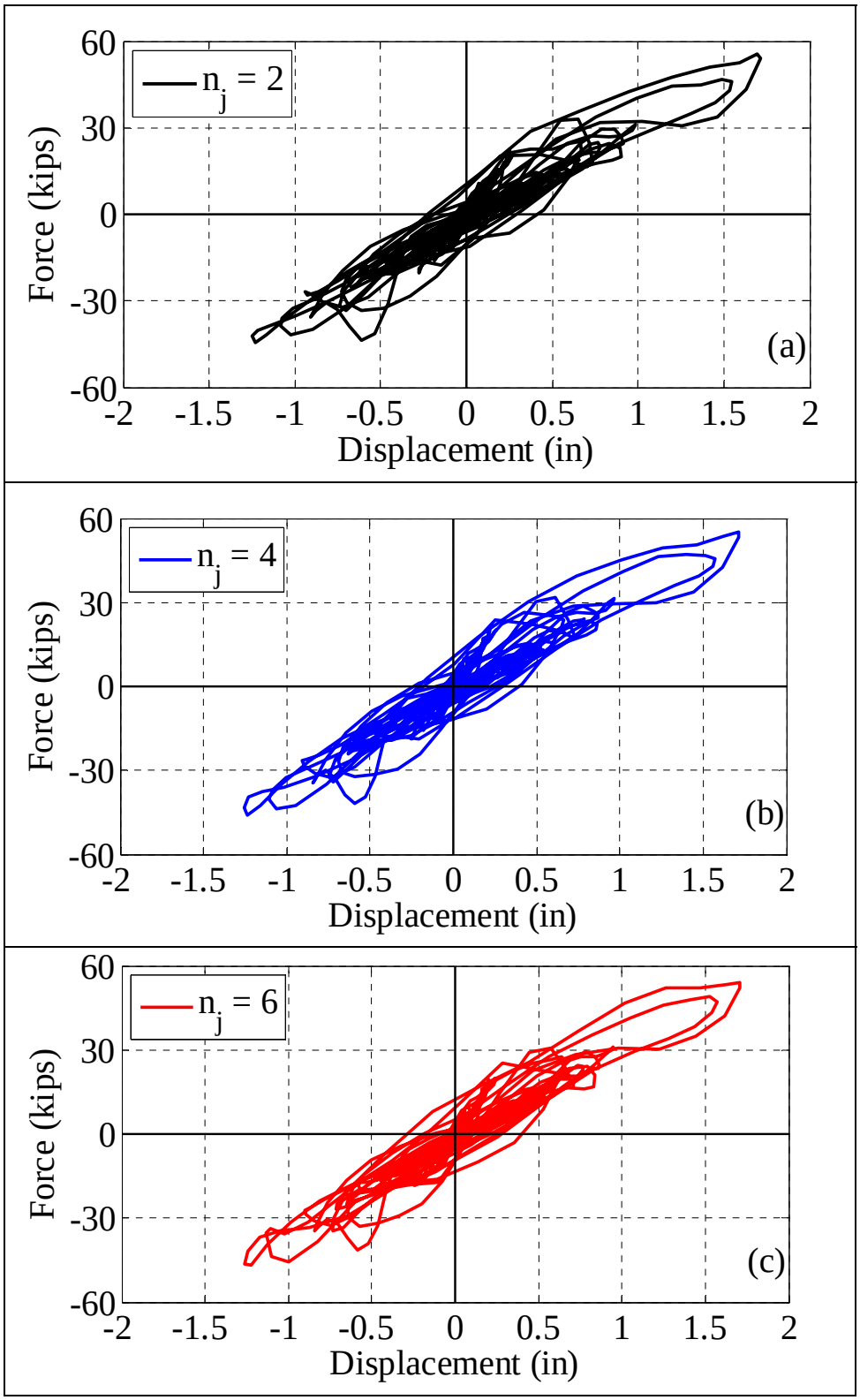

Figure 6.22 Horizontal force-deformation response of FE models.

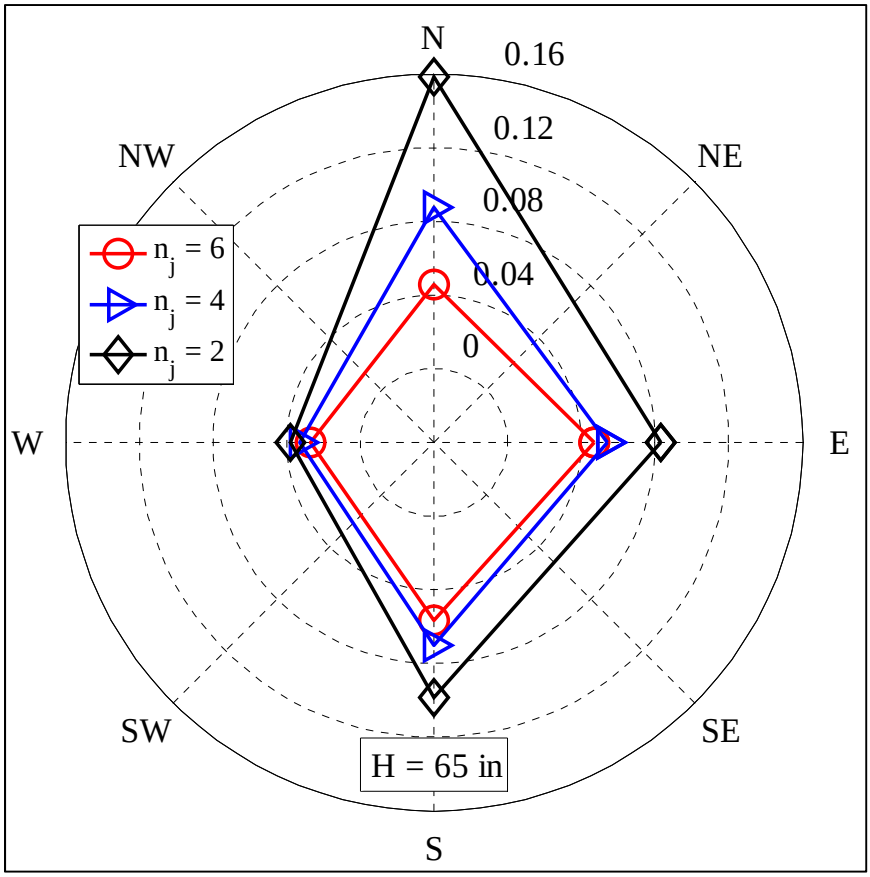

Figure 6.23 Confining (hoop) strain profile in (%).

Chapter 7. Summary and Conclusions

7.1 SUMMARY

Current seismic bridge design codes allow repairable level damage to the bridge columns during more “frequent” earthquakes. Damage to a bridge column depends on different factors, such as, soil conditions, magnitude and duration of the ground motion, and force and displacement drift demands imposed on the structure during a seismic event. A rapid restoration of the damaged bridges is crucial to avoid traffic congestions during the evacuation hours and to minimize the delays in arrival of emergency vehicles for sustainable dispatch and distribution. Under such circumstances, it is the responsibility of the engineers to access the ability of the bridge structure to support the traffic flow and to decide if the structure is repairable or requires a complete replacement. If the structure can be repaired, the engineers should choose repair methods that are effective in supporting the demand and can be completed within a reasonable time period.

The current study investigated the effectiveness of the Fiber Reinforced Polymer (FRP) jackets as a rapid and effective repair option to restore the shear capacity of damaged Reinforced Concrete (RC) bridge columns. Two pre-damaged RC bridge columns with circular cross-sections were experimentally investigated in this research. Both test specimens were identical except for the volumetric transverse reinforcement ratio due to different spacing of the hoop reinforcement in the two specimens. The test specimens had moderate to high damage at the end of the loading protocols without any ruptured steel reinforcement. Subsequently, the two columns were repaired using unidirectional FRP composite jackets. Assuming that the damage level was similar to the damage of bridge columns after a frequent earthquake, the design of the FRP jacket repair was performed to improve the shear capacity of the damaged column specimens and to provide better confinement. Test specimen SP1 was repaired using 4 plies of E-Glass FRP, i.e. GFRP, jacket and test specimens SP2 was repaired using 2 plies of Carbon FRP, i.e. CFRP. jacket. The repaired specimens were tested on a shaking table under the same series of horizontal and vertical ground motions used for testing the as-built test specimens.

A three dimensional (3D) computational model using the Finite Element (FE) method was developed to complement the experimental study and was calibrated using the shaking table test results. The FRP jackets were not modeled explicitly in the analytical study but rather a bilinear constitutive confined concrete model was used to include the effect of the GFRP and CFRP jackets. A parametric study to understand the global and local response quantities of retrofitted bridge columns was conducted using the calibrated 3D FE model.

7.2 CONCLUSIONS

The force-deformation response of the GFRP-repaired specimen was very similar to its as-built counterpart. Considering that the as-built specimen was code compliant in terms of transverse reinforcement and accordingly did not experience severe damage during testing, the improvement provided by the GFRP repair by upgrading the response of the damaged as-built specimen to its original undamaged response state is beneficial. On the other hand, the CFRP-repaired specimen showed an improved force-deformation response compared to its as-built counterpart, especially in terms of strength. The effect of the CFRP repair on enhancing the shear capacity of a column with relatively large hoop spacing was remarkable. The repaired specimens were able to dissipate almost the same amount of energy as measured from the as-built specimens.

During the high intensity ground motions, the repaired columns were able to resist higher shear forces with slightly lower magnitude of tensile forces due to the vertical component of the ground motion. Hence, reductions in shear capacity due to any axial tension forces were less than the as-built counterparts. The tensile strains measured in the repaired specimens were lower than those in the as-built specimen due to the confining action of the FRP jacket in holding the concrete from spalling. The CFRP repaired specimen had relatively lower magnitudes of longitudinal strains and curvatures in comparison to the GFRP repaired specimen, due to the higher tensile strength of the CFRP than the GFRP which also contributed to lower confining strains.

Overall, the nonlinear dynamic analysis results show great potential for 3D modeling of confined concrete using FRP jackets in applications of shear-governed modes of failure. A good match was obtained between the analytical and experimental force and deformation time histories. The FE model was also able to determine the maximum magnitude of axial load, tensile forces, vertical displacements, and bending moments within reasonable error margin. The results also verify the practical modeling approach of altering the total crack strain model parameters to reflect the FRP-confined concrete without the need for the computationally-intensive explicit jacket modeling or introduction of interface elements in the computational model. Effect of confinement contribution from the hoop transverse steel reinforcement did not show any significant variation in the results in the analytical study. Based on the parametric study it was concluded that the confining strain response was significantly affected by reducing the number of the plies in the FRP jacket lower than certain value, namely 4 plies, but increasing the jacket thickness further does not improve the response significantly. The parametric study also demonstrated that the effect of the thickness of the unidirectional FRP jacket on the lateral force-deformation was almost negligible.

Both repaired test specimens were successful in providing the required passive confinement and remaining intact during the entire test protocol. Under the applied ground motions, no failure of the FRP jackets was observed, which was also justified by the strain measurements on the jackets. In comparison to the repaired specimen SP1, the confining strain profiles measured at the base and top level of the repaired specimen SP2 had lower magnitudes and were relatively more uniformly distributed across the column circumference, due to the higher magnitude of the CFRP jacket stiffness compared to the GFRP jacket. At the same cross-section level, the magnitude of confining strains measured in the repaired test specimens was lower than those of the as-built test specimens. Near the column base, the maximum confining

strain in the as-built SP1 and SP2 were about 5.5 times and 4.3 times higher than the repaired SP1 and the repaired SP2, respectively. In addition, residual displacements after all tests were much lower for both of the repaired specimens compared to their as-built counterparts. This is indicative of the effectiveness of the investigated FRP repair technique to produce resilient bridge columns when subjected to severe earthquake loading. Finally, the FRP repair is clearly a viable repair solution for enhancing the shear strength of bridge columns under the combined effect of vertical and horizontal ground motion excitation.

7.3 SUGGESTED FUTURE EXTENSIONS

The current study demonstrated the effectiveness of the FRP confinement in restoring the shear strength capacity of damaged RC bridge columns. Based on the experimental and analytical results, several future extensions can be suggested.

A similar experimental study but with higher ground motion intensity to the point of FRP rupture can be conducted. An insight into such damage state can provide valuable information about the design limits and accurate modeling of the FRP confined concrete sections. Despite the availability of various computational models for the analysis and design of FRP confined concrete structures, the guidelines on the practical application of FRP jacket repair of members subjected to multi-directional earthquake loading are still limited. More experimental studies are required to confirm the effectiveness of the design models, and to propose reliable and comprehensible guidelines for the engineers.

The 3D computational model developed in this study utilizes a bilinear confined concrete model. The used FE platform DIANA also offers a saturation hardening model which has much closer representation to the measured stress-strain response of the FRP confined concrete section. An analytical study can be conducted to compare the variation in the results of the two constitutive models. Further enhancement of the 3D FE model and comparison with the dynamic test results can be achieved and utilized for an extended parametric study of this work. For example a detailed parametric study exploring the effect of thickness of FRP jackets and concrete strength on the different local response parameters (e.g. longitudinal strains and curvatures) can be conducted.

References

[1] AASHTO. (2005). *LRFD Bridge Design Specifications, 3rd Edition, 2005 Interim Revisions.* American Association of State and Highway Transportation Officials, Washington, DC.

[2] AASHTO. (2010). *LRFD Bridge Design Specifications, 5th Edition, 2005 Interim Revisions.* American Association of State and Highway Transportation Officials, Washington, DC.

[3] Aboutaha, R. S., Engelhardt, M. D., Jirsa, J. O., & Kreger, M. E. (1999). Rehablitation of Shear Critical Columns by Use of Rectangular Steel Jackets. *ACI Structural Journal, 96*(1), 68-78.

[4] ACI Committee 318. (2008). *Building Code Requirements for Structural Concrete and Commentary.* ACI 318-08, American Concrete Institute, Farmington Hills, MI.

[5] Bakis, C. E. (1993). FRP Reinforcement: Materials and Manufacturing. Fiber Reinforced-Plastic (FRP). In *Reinforcements fo Concrete Structures: Properties and Applications.* (pp. 13-58). Elsevier Science.

[6] Bazant, Z. P., & Lin, F.-B. (1988). Nonlocal Smeared Cracking Model for Concrete Fracture. *Journal of Structural Engineering, 144*(11), 2493-2510.

[7] Bazant, Z. P., & Planas, J. (1998). *Fracture and Size Effect in Concrete and other Quasibrittle Materials.* CRC Press, Boca Raton, Florida, and London, U.K.

[8] Beausejour, P. (2000). *Seismic Retrofit of Concrete Columns with Splice Deficiences by External Prestressing.* M. A. Sc. Thesis, Department of Civil Engineering, University of Ottawa, Ottawa, Ontario, Canada.

[9] Binici, B., & Mosalam, K. M. (2007). Analysis of Reinforced Concrete Columns Retrofitted with Fiber Reinforced Polymer Lamina. *Composites Part B: Engineering, 38*(2), 265-276.

[10] Button, M. R., Cronin, C. J., & Mayes, R. L. (2002). Effect of Vertical Motions on Seismic Response of Bridges. *ASCE Journal of Structural Engineering, 128*(12), 1551-1564.

[11] California Department of Transportation (Caltrans). (2006). *Seismic Design Criteria (SDC).* Sacramento, California.

[12] California Department of Transportation (Caltrans). (2010). *Seismic Design Criteria (SDC).* Sacramento, California.

[13] Chai, Y. H., Priestly , M. J., & Seibel, F. (1991). Seismic Retrofit of Circular Bridge Columns for Enhanced Flexural Performance. *ACI Structural Journal, 88*(5), 572-584.

[14] Chamber, R. E. (1992). Composite Performance in the Infrastructure. *Proceedings of Material Science Conference, ASCE,* (pp. 532-545). Atlanta.

[15] Chang, S., Li, Y., & Loh, C. (2004). Experimental Study of Seismic Behavior of As-Built and Carbon Fiber Reinforced Plastics Repaired Reinforced Concrete Bridge Columns. *ASCE Journal of Bridge Engineering,* 391-402. doi:10.1061/(ASCE)1084-0702(2004)9:4(391)

[16] Chopra, A. K. (2006). *Dynamics of Structures - Theory and Applications to Earthquake Engineering, 3rd Ed.* Upper Saddle River, New Jersey: Pearson Prentice Hall.

[17] Chopra, A. K. (2011). *Dynamics of Structures, Theory and Applications to Earthquake Engineering* (4th ed.). Pearson Pretince Hall, Upper Saddle River, NJ.

[18] Chung, H. W. (1981). Epoxy Repair of Bond in Reinforced Concrete Members. *ACI Structural Journal, 78*(7), 79-82.

[19] Cooper, J. D., Nimis, R. B., & Bobb, N. M. (1994). The Northridge Earthquake: Progress Made, Lessons learned in Seismic Resistant Bridge Design. *Pubic Roads, Summer 1994, 58*(1).

[20] Database, PEER-NGA. (2012). *http://peer.berkeley.edu/nga/.*

[21] De Borst, R., & Nauta, P. (1985). Non-orthogonal cracks in a smeared finite element model. *Enigeering Computations, 2*(1), 35-46.

[22] Ersoy, U., Tankut, A. T., & Suleiman, R. (1993). Behavior of Jacketed Columns. *ACI Structural Journal, 90*(3), 288-293.

[23] French, C. W., Thorp, G. A., & Tsai, W. (1990). Epoxy Repair Techniques for Moderate Earthquake Damage. *ACI Structural Journal, 87*(4), 416-424.

[24] Gupta, A. K., & Akbar, H. (1983). *Cracking in reinforced concrete analysis.* Reinforced Concrete Shell Research Report, Civil Engineering Department, North Carolina State University, Raleigh, NC.

[25] Harajili, M. (2008). Seismic Behavior of RC Columns with Bond-Critical Regions: Criteria for Bond Strengthening Using External FRP Jackets. *ASCE Journal of Composite Construction,* 69-79. doi:10.1061/(ASCE)1090-0268(2008)12:1(69)

[26] Haroun, M. A., Mosallam, A. S., Feng, M. Q., & Elsanadedy, H. M. (2003). Experimental Investigation of Seismic Repair and Retrofit of Bridge Columns by Composite Jackets. *Journal of Reinforced Plastics and Composites, 22*(14), 1243-1268.

[27] Ilki, A., Peker, O., Karamuk, E., Demir, C., & Kumbasar, N. (2006). Axial Behavior of RC Columns Retrofitted with FRP Composites. *Advances in Earthquake Engineering for Urbas Risk Reduction,* pp. 301-316.

[28] Jirawattanasomkul, T., Dai, J., Zhang, D., Senda, M., & Ueda, T. (2013). Experimental Study on Shear Behavior of Reinforced-Concrete Members Fully Wrapped with Large Rupture-Strain FRP Composites. *ASCE Journal of Composites for Construction, 18*(3). doi:10.1061/(ASCE)CC.1943-5614.0000442

[29] Kunnath, S., Abrahamson, N., Chai, Y. H., Erduran, E., & Yilmaz, Z. (2008). *Development of Guidelines for Incorportation of Vertical Ground Motion Effects in Seismic Design of Highway Bridges.* Techincal Report - CA/UCD-SESM-08-01, University of California, Davis.

[30] Lam, L., & Tang, J. G. (2003). Design-Oriented Stress-Strain Model for FRP Confined Concrete. *Journal of Construction and Building Materials, 17*(6-7), 471-489.

[31] Lam, L., & Teng, J. G. (2001). A New Stress-Strain Model for FRP-Confined Concrete. *Proceedings of the International Conference on FRP Composite in Civil Engineering*, (pp. 283-292). Hong Kong, China.

[32] Lee, H. (2011). *Experimental and Analytical Inversitgation of Reinforced Concrete Columns Subjected to Horizontal and Vertical Ground Motions.* Dissertation, Civil and Environmental Engineering Department, Univeristy of California, Berkeley.

[33] Lee, H. (2011). *Experimental and Analytical Investigation of Reinforced Concrete Columns Subjected to Horizontal and Vertical Ground Motions.* Dissertation, Civil and Environmental Engineering Department, University of California, Berkeley.

[34] Lee, H., & Mosalam, K. M. (2014). *Effect of Vertical Acceleration on Shear Strength of Reinforced Concrete Columns.* PEER Report 2014/04, Pacific Earthquake Engineering Research Center, University of California, Berkeley.

[35] Lee, H., & Mosalam, K. M. (2014). Seismic Evaluation of the Shear Behavior in Reinforced Concrete Bridge Columns Including Effect of Vertical Acceleration. *Earthquake Engineering and Structural Dynamics, 43*(3), 317-337.

[36] Lehman, D. E., Gookin, S. E., Nacamuli, A. M., & Moehle, J. P. (2001). Repair of Earthquake Damaged Bridge Columns. *ACI Structural Journal, 98*(2), 233-242.

[37] Ma, G., Li, H., & Wang, J. (2013). Experimental Study of the Seismic Behavior of an Earthquake-Damaged Reinforced Concrete Frame Structure Retrofitted with Basalt Fiber-Reinforced Polymer. *ASCE, Journal of Composites for Construction*. doi:10.1061/(ASCE)CC.1943-5614.0000413, 04013002.

[38] Mahin, S. A., Bertero, V. V., Chopra, A. K., & Collins, R. G. (1976). *Response of Olive View Hospital Main Building During the San Fernando Earthquake.* Techincal Report No. EERC 76-22, Earthquake Engineering Research Center, University of California, Berkeley.

[39] Mirmiran, A., Shahawy, M., Samaan, M., Echary, H., Mastrapa, J., & Pico, O. (1998). Effect of Column Parameters on FRP-Confined Concrete. *(ASCE) Journal of Composite Construction, 2*(4), 175-185.

[40] Mosalam, K. M., Talaat, M., & Binici, B. (2007). A Computational Model for Reinforced Concrete Members Confined with Fiber Reinforced Polymer Lamina:

Implementation and Experimental Validation. *Composite Part B: Engineering, 38*(5-6), 598-613.

[41] Papazoglou, A. J., & Elnashai, A. S. (1996). Analytical and Field Evidence of the Damaging Effects of Vertical Earthquake Ground Motion. *Earthquake Engineering and Structural Dynamics, 25*, 1109-1137.

[42] Priestly, M. J. N. (1990). *Flexural Test of High-Strength Fiber Retrofitted Column.* SEQAD Consulting Engineers, Report No. 90-06, Nov 1990. Solano Beach, California.

[43] Priestly, M. J. N.; Seibel, F.; Xiao, Y.; Verma, R. (1994). Steel Jacket Retrofitting of Reinforced Concrete Bridge Columns for Enhanced Shear Strength - Part 1: Theoretical Considerations and Test Design. *ACI Structural Journal, 91*(5), 394-405.

[44] Priestly, M. J. N.; Seibel, F.; Xiao, Y.; Verma, R. (1994). Steel Jacket Retrofitting of Reinforced Concrete Bridge Columns for Enhanced Shear Strength - Part 2: Test Results and Comparison with Theory. *ACI Structural Journal, 91*(5), 537-551.

[45] Rashid, Y. R. (1968). Analysis of prestressed concrete pressure vessels. *Nuclear Engineering Design, 7*(4), 334-355.

[46] Robert, J. E. (1991). *Recent Advances in Seismic Design and Retrofir of Bridges.* Transposrtation Research Record, No. 1290, National Research Council, Washington, D.C.

[47] Rodriguez, M., & Park, R. (1994). Seismic Load Tests in Reinforced Concrete Columns Strengthened by Jacketing. *ACI Structural Journal, 91*(2), 154-159.

[48] Rots, J. (1991). Numerical Simulation of Cracking in Structural Masonary. In R. De Borst, & D. G. Roddeman (Ed.), *In Computational Mechanics: Recent Developments in DIANA, 36(2).* Heron.

[49] Saadatmanesh, H., Ehsani, M. R., & Jin, L. (1996). Seismic Strengthening of Circular Bridge Pier Models with Fiber Composites. *ACI Structural Journal, 93*(6), 639-647.

[50] Saadatmanesh, H., Ehsani, M. R., & Jin, L. (1997). Repair of Earthquake-Damaged RC Columns with FRP Wraps. *ACI Structural Journal, 94*(2), 206-215.

[51] Saadatmanesh, H., Ehsani, M. R., & Jin, L. (1997). Seismic Retrofitting of Rectangular Bridge Columns with Composite Straps. *Earthquake Spectra, 13*(2), 281-304.

[52] Saadatmanesh, H., Ehsani, M. R., & Li, M. W. (1994). Strength and Ductility of Concrete Columns Externally Reinforced with Fiber Composite Straps. *ACI Structural Journal, 91*(4), 434-447.

[53] Saadeghvaziri, M. A., & Foutch, D. A. (1991). Dynamic Behavior of R/C Highway Bridges Under the Combined Effect of Vertical and Horizontal Earthquake Motions. *Earthquake Engineering and Structural Dynamics, 20*, 535-549.

[54] Saatcioglu, M., & Elnabelsy, G. (2001). Seismic Retrofit of Bridge Columns with CFRP Jackets. *Proceedings of the International Conference on FRP Composites in Civil Engineering, 12-15 December 2001,* pp. 833-838. Hong Kong, China.

[55] Saatcioglu, M., & Yalcin, C. (2003). External Prestressing Concrete Columns for Improved Seismic Resistance. *ASCE Journal of Structural Engineering, 129*(8), 1057-1070.

[56] Saiidi, M., Sureshkumar, K., & Pulido, C. (2005). Simple Carbon-Fiber-Reinforced-Plastic-Confined Concrete Model for Moment Curvature Analysis. *Journal of Composites for Construction, 9*(1), 101-104.

[57] Seible, F.; Priestly, M. J. N.; Hegemier, G.; Innamorato, D. (1997). Seismic Retrofit of RC Columns with Continuous Carbon Fiber Jackets. *Journal of Composite Construction*, 52-62. doi:10.1061/(ASCE)1090-0268(1997)1:2(52)

[58] TNO DIANA. (2011). *DIANA.* Retrieved from TNO DIANA - A TNO Company: http://tnodiana.com

[59] Veletzos, M. J., Restrepo, J. I., & Seible, F. (2006). *Seismic Response of Precast Segmental Bridge Superstructures.* Technical Report- CalTrans - SSRP-06/18, Univeristy of California, San Diego.

[60] Vosooghi, A., & Saiidi, M. (2010). *Post-Earthquake Evaluation and Emergency Repair of Damaged RC Bridge Columns using CFRP Materials.* Report No. CCEER-10-05, Center for Civil Engineering Earthquake Research, Department of Civil Engineering, University of Nevada, Reno, Nevada.

[61] Wu, G., Wu, Z. S., & Lu, Z. T. (2007). Design-Oreinted Stress-Strain Model for Concrete Prisms Confined with FRP Composites. *(ScienceDirect) Construction and Building Materials, 21,* 1107-1121.

[62] Xiao, Y., Wu, H., & Martin, G. (1999). Prefebricated Composite Jacketing of RC Columns for Enhanced Shear Strength. *ASCE Journal of Structural Engineering*, 255-264. doi:10.1061/(ASCE)0733-9445(1999)125:3(255)

[63] Yarandi, M. S. (2007). *Seismic Retrofit and Repair of Existing Reinforced Concrete Bridge Columns by Transverse Prestressing.* Ph.D. Thesis, Department of Civil Engineering, Univeristy of Ottawa, Ottawa, Ontario, Canada.

[64] Yoshimura, K., Kikuchi, K., & Kuroki, M. (1991). Seismic Shear Strengthening Method for Existing Reinfroced Concrete Short Columns. *Proceedings of ACI Conference on Evalutation and Rehabilitation of Concrete Structures and Innovations in Design. SP-128*, pp. 1065-1079. American Concrete Institute: Farmington Hills, Michigan.

[65] Yu, C. P., Broekhuizen, D. S., Roesset, J. M., Breen, J. E., & Kreger, M. E. (1997). Effect of Vertical Ground Motion on Bridge Deck Response. *Workshop on Earthquake Engineering Frontiers in Transportation Facilities, Technical Report No. NCEER-97-0005* (pp. 249-263). New York: National Center for Earthquake Engineering Research, State University of New York at Buffalo.

Appendix A Repair-Material Properties

The properties of the repair materials (mortar, epoxy, FRP jackets, etc.) were provided by the manufacture and are detailed in this appendix.

Table A.1 BC020 Bonding and corrosion protection system.

Physical Properties (based on ratio mix at 70ºF)	
Bond Strength (ASTM C882)	1800 psi (2 hours), 2100 psi (24 hours)
Tensile Strength (ASTM C190)	800 psi (28 days)
Flexural Strength (ASTM C78)	2000 psi (28 days)
Chlorine Ion Permeability (ASTM C1202)	Less than 150 Coulombs (28 days)
Mixing Ratio	1 gallon of Component A with 1 bag of powder.
Pot Life	Approximately 90 minutes
Shelf Life	One year if unopened
Open Time	Up to 24 hours
Coverage	70 - 80 ft^2 per gallon, 175 – 200 ft^2 per unit
VOC Content	< 50 g/L. SCAQMD 1113 (US EPA 40 CFR 59)

Table A.2 High strength structural mortar.

Physical Properties	
Compressive Strength (ASTM C109)	3 ksi (1 day), 5 ksi (7 days), 6.3 ksi (28 days)
Tensile Strength (ASTM 496)	485 psi (7 days), 565 psi (28 days)
Modulus of Elasticity	2260 ksi (28 days)
Flexural Strength (ASTM C293)	1100 psi (7 days), 1500 (28 days)
Bond Strength (ASTM D4541)	500 psi (28 days); Failure in substrate
Mixing Ratio	6.5-7.0 pints of water per 55 lbs bag.
Shelf Life	One year if unopened
Yield	0.42 ft^3 per 55 lbs bag
Time to coat or seal	3 to 7 days

Table A.3 High strength structural epoxy.

Physical Properties	
Compressive Strength (ASTM D695)	10.5 ksi; After 7 days of curing at 75ºF
Tensile Strength (ASTM D638)	7200 psi (14 days)
Rupture Strain (ASTM D638)	0.85%
Flexural Strength (ASTM D790)	5800 psi (14 days)
Bond Strength (ASTM C882)	Minimum 1800 psi (14 days)
Working Time	55-64ºF: 1.5-2.5 hours
Gel Time	Approximately 60 minutes
Track Free time	16-18 hours at 40ºF

Appendix B Sign Conventions

Figure B.1 shows the sign conventions used in the current report. Shear forces, displacement, and accelerations towards North were considered positive. Axial load in compression was assigned positive sign while tensile forces were assigned negative signs. Convex and concave bending of the North face (and corresponding curvatures) were assigned positive signs. Using right hand rule and looking from the West side (as the elevation view in the figure below) counterclockwise rotation of superstructure mass was assigned a negative sign and clockwise rotation was considered positive. Tensile strain and vertical displacement causing extension were assigned positive signs.

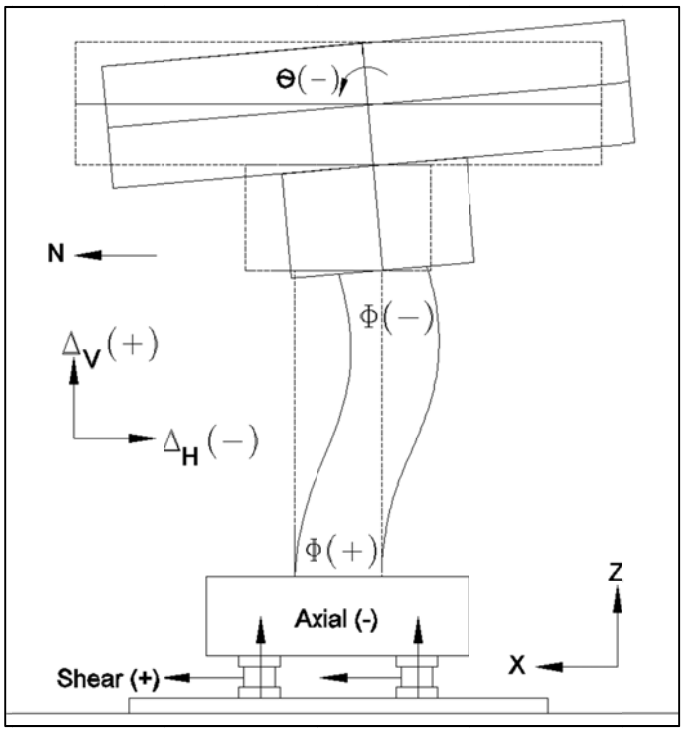

Figure B.1 Sign conventions.

Appendix C Curvature Measurements

The curvatures were calculated by dividing the net rotation of the instrumented section with the horizontal distance between the LVDTs (Figure C.1). Net rotation of section was the ratio of relative displacement of one side (North or South) to the length of instrumented section. For example, if at any instant of loading, reading (relative displacement of two end of a LVDT) on the North and South side of the test specimen is α_N and α_S, the relative displacement (δ_r) of North side with respect to South side is ($\alpha_N - \alpha_S$). Net rotation (ψ) of this section is ratio of relative displacement (δ_r) to the initial length of instrumented section (L_{inst}). If the horizontal distance between the two instrumented locations is D_{inst}, then the curvature (Φ) of instrumented section can be computed as,

$$\Phi = \frac{\psi}{D_{inst}} = \frac{\delta_r}{(D_{inst} \times L_{inst})} = \frac{(\alpha_N - \alpha_S)}{(D_{inst} \times L_{inst})} \quad \textbf{(C.1)}$$

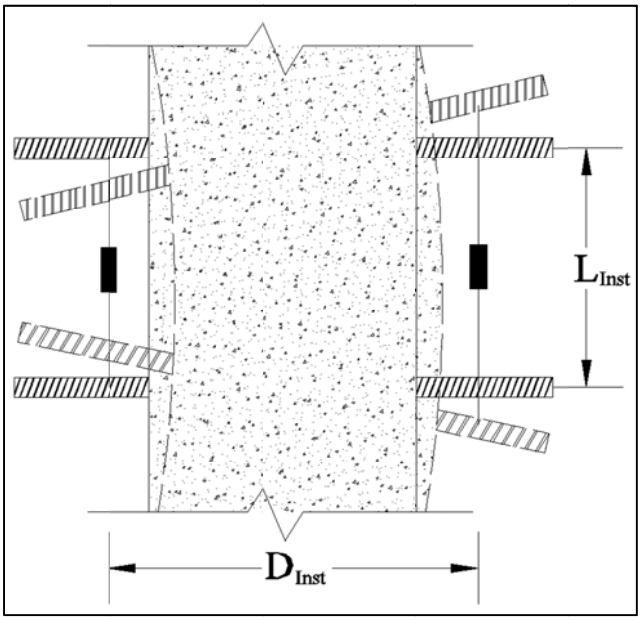

Figure C.1 Curvature calculations using LVDTs.

Figure C.2 and Figure C.3 shows the curvature time histories measured near the base of top of the repaired test specimens and their as-built counterparts during 50%-, 70%- and 95%-scaled ground motions.

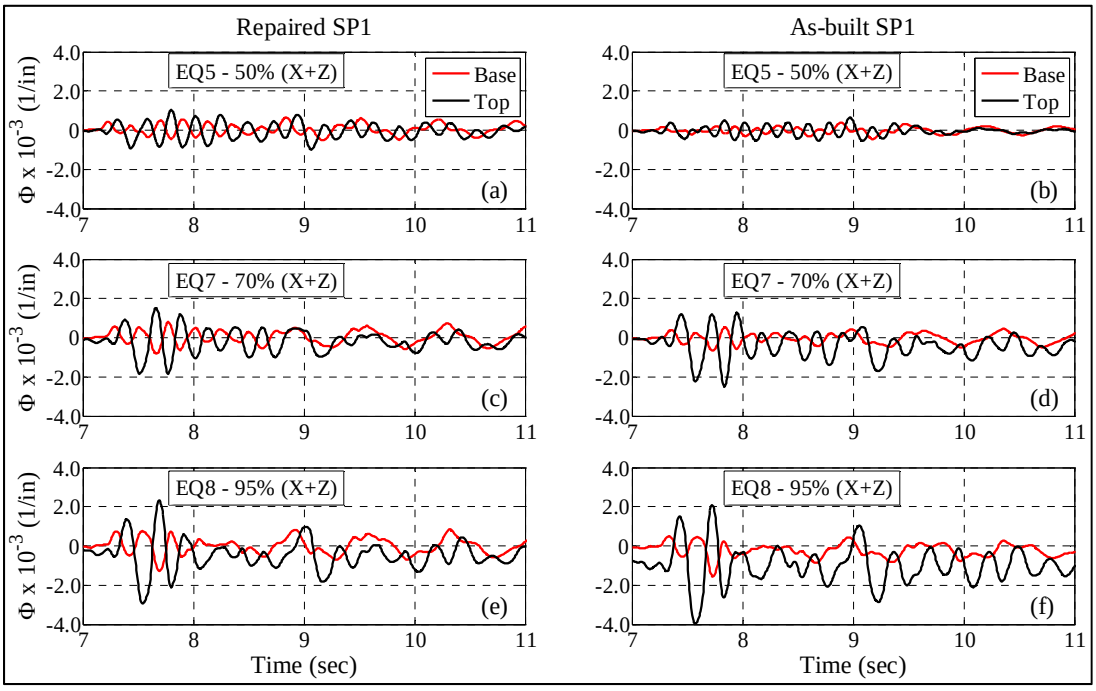

Figure C.2 Curvature (Φ) time histories.

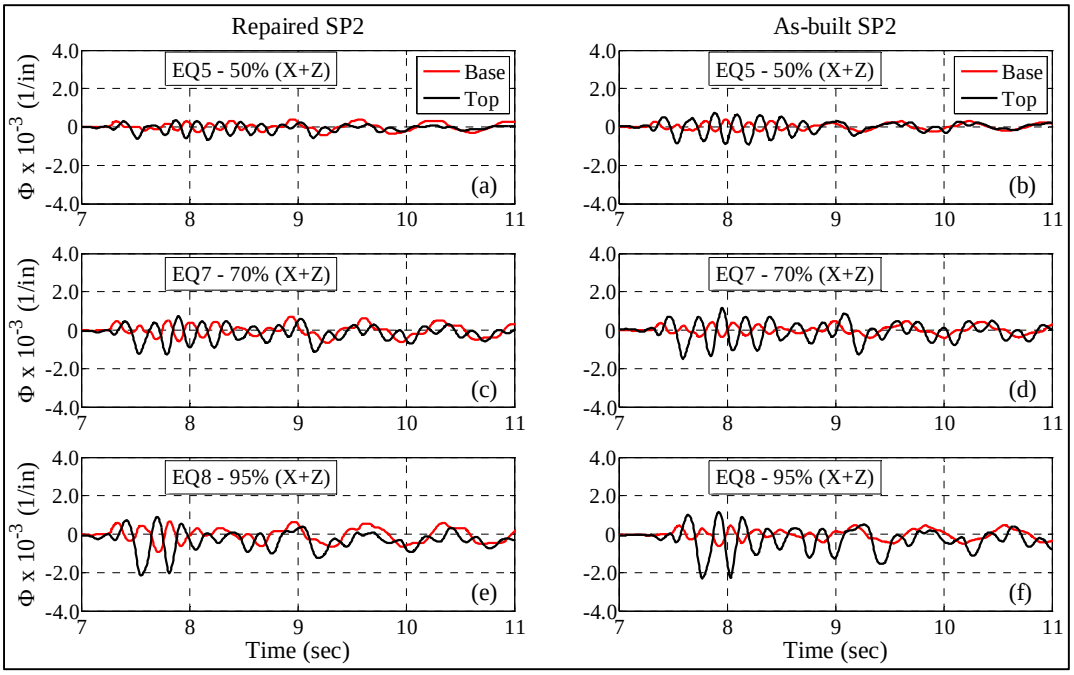

Figure C.3 Curvature (Φ) time histories.

Appendix D Maximum Global Response

Maximum magnitude of acceleration, input cumulative energy, force and displacement response of the repaired test specimens are tabulated in this appendix.

Table D.1 Measured peak acceleration of the repaired specimens.

Test Specimen	Test	X-direction (g)			Z-direction (g)		
		Steel Plate	Mass Block	Conc. Slab	Steel Plate	Mass Block	Conc. Slab
Repaired SP1	EQ5	0.96	0.84	0.20	0.85	0.83	0.95
	EQ7	1.34	1.04	0.25	1.02	1.06	1.09
	EQ8	1.78	1.29	0.33	1.25	1.26	1.33
	EQ9	1.88	1.44	0.37	1.39	1.57	1.69
	EQ10	2.15	1.45	0.35	0.90	0.60	0.65
	EQ11	1.70	1.33	0.33	1.38	1.58	1.79
Repaired SP2	EQ5	0.86	0.67	0.22	0.75	0.82	0.88
	EQ7	1.36	0.98	0.27	0.91	1.11	1.21
	EQ8	1.67	1.14	0.35	1.08	1.28	1.40
	EQ9	1.90	1.41	0.38	1.38	1.65	1.85
	EQ10	2.17	1.45	0.32	0.87	0.61	0.66
	EQ11	1.78	1.45	0.31	1.37	1.58	1.77

Table D.2 Measured input cumulative energy based on steel plate accelerations.

Test	$E_{cum,x}^{max}$		$E_{cum,z}^{max}$	
	Repaired SP1	**Repaired SP2**	**Repaired SP1**	**Repaired SP2**
EQ1	0.001	0.001	0.001	0.001
EQ2	0.007	0.005	0.006	0.006
EQ3	0.027	0.022	0.012	0.020
EQ4	0.024	0.023	0.002	0.001
EQ5	0.102	0.097	0.109	0.133
EQ6	0.102	0.095	0.027	0.021
EQ7	0.206	0.187	0.175	0.214
EQ8	0.380	0.322	0.274	0.234
EQ9	0.579	0.571	0.562	0.594
EQ10	0.612	0.610	0.132	0.115
EQ11	0.577	0.569	0.560	0.555

Table D.3 Maximum shear forces.

Test	Repaired SP1	Repaired SP2	As-Built SP1	As-Built SP2
EQ1	2.85	2.25	2.29	1.73
EQ2	7.83	10.05	11.78	10.79
EQ3	17.15	22.43	26.53	25.35
EQ4	18.75	20.03	NA	20.42
EQ5	52.27	47.57	51.53	50.39
EQ6	57.73	53.75	NA	56.02
EQ7	71.06	69.10	67.13	69.29
EQ8	90.43	82.36	84.96	75.17
EQ9	100.9	94.91	91.40	77.39
EQ10	101.1	98.81	92.58	80.85
EQ11	96.21	90.23	88.30	77.24

Table D.4 Maximum relative horizontal displacements.

Test	Repaired SP1, in (mm)		Repaired SP2	
	North Side	South Side	North Side	South Side
EQ1	0.037 (0.934)	0.035 (0.893)	0.030 (0.762)	0.031 (0.796)
EQ2	0.128 (3.243)	0.117 (2.972)	0.135 (3.418)	0.127 (3.216)
EQ3	0.229 (5.812)	0.229 (5.812)	0.230 (5.837)	0.205 (5.198)
EQ4	0.215 (5.346)	0.211 (5.357)	0.216 (5.492)	0.199 (5.043)
EQ5	0.448 (11.383)	0.491 (12.470)	0.421 (10.695)	0.358 (9.092)
EQ6	0.368 (9.349)	0.459 (11.670)	0.367 (9.326)	0.359 (9.107)
EQ7	0.579 (14.712)	0.591 (15.022)	0.618 (15.688)	0.597 (15.170)
EQ8	0.962 (24.426)	0.709 (18.009)	0.787 (19.995)	0.652 (16.568)
EQ9	1.307 (33.190)	0.780 (19.810)	1.309 (33.242)	0.692 (17.571)
EQ10	1.307 (33.200)	0.733 (18.609)	1.379 (35.026)	0.639 (16.224)
EQ11	1.404 (35.652)	0.889 (22.592)	1.494 (37.935)	0.793 (20.142)